2015-02-09

Polarimetric C-band Microwave Scattering Properties of Snow Covered First-Year Sea Ice

Gill, Jagvijay P. S.

UNIVERSITY OF CALGARY

Polarimetric C-band Microwave Scattering Properties of Snow Covered First-year Sea Ice

by

Jagvijay Pratap Singh Gill

A THESIS

SUBMITTED TO THE FACULTY OF GRADUATE STUDIES

IN PARTIAL FULFILMENT OF THE REQUIREMENTS FOR THE

DEGREE OF DOCTOR OF PHILOSOPHY

GRADUATE PROGRAM IN GEOGRAPHY

CALGARY, ALBERTA

JANUARY, 2015

Abstract

In this thesis, the physical, dielectric, and C-band polarimetric microwave properties of snow covered first-year sea ice (FYI) at different temperature conditions, largely encompassing late winter to melt onset period are investigated. First, a set of polarimetric parameters derived using different decomposition and synthesis techniques are analyzed at cold temperature conditions by relating them to pre-identified sea ice types. These parameters are further analyzed for their sea ice classification potential. This analytical scheme is extended to warmer temperature conditions and their stability for ice type signature response and classification potential is assessed. Second, the polarimetric SAR response from snow covered FYI at cold temperature conditions is analyzed to investigate the sensitivity of polarimetric backscatter to snow thickness. The backscatter sensitivities are examined as a function of change in surface air temperature through the changes manifested in snow geophysical properties. Lastly, *in-situ* measured geophysical and dielectric properties of thick and thin snow cover over smooth FYI and the corresponding C-band scatterometer measurements are analyzed at diurnal time scales during the transition from early melt to melt onset. A simple, multi-layer surface and volume scattering model of snow covered FYI is adopted. Using *in-situ* snow properties for model parameterization, corresponding C-band backscatter response is evaluated and scattering mechanisms are theorized. The findings indicate additional information is provided from fully polarimetric C-band backscatter data for sea ice classification and snow thickness retrieval purposes. Results also suggest that these parameters are best estimated at low radar incidence angles and during the late winter to early melt timeframe.

Acknowledgements

First and foremost, I would like to thank my supervisor Dr. John Yackel for allowing me choose my path freely, for allowing me to learn by experimenting and above all for inspiring me to think different. John, you have been extremely supportive and a great teacher.

I also thank all my colleagues and seniors who spared their time and brain to help me out at every obstacle of my journey of research. The friendship, collaboration and assistance of Torsten Geldsetzer, Randall Scharien, Chris Fuller, Carina Butterworth and Musharraf Hussain are highly valued.

The contribution of my committee members is greatly appreciated. These include: Dr. Mryka Hall-Beyer (Geography), Dr. Darren John Bender (Geography), Dr. Shelley Marie Alexander (Geography), Dr. Bryan JB Mercer (Geomatics Engineering), Dr. Xin Wang (Geomatics Engineering), and Dr. Christian Haas (York University).

I extend my sincere thanks to the Department of Geography, University of Calgary for taking me as a graduate student. Within the Department of Geography I thank Catherine Avramenko and Paulina Medori for their assistance and help. I also thank the U of C Faculty of Graduate Studies (FGS) for providing me with financial assistance. Canadian Ice Service, Science and Operational Applications Research (SOAR) Program of the Canadian Space Agency and ArcticNet- a Network Centres of Excellence of Canada are thanked for their data and financial support. Churchill Northern Studies Centre (CNSC) and Polar Continental Shelf Program (PCSP) are thanked for their logistical support.

Science and language of this thesis has been refined considerably through peer review and through peer suggestions at numerous conferences. I thank the reviewers of *Canadian Journal of Remote Sensing* and *IEEE Transactions on Geoscience and Remote Sensing*. I also thank the *Canadian Association of Geographers*, *SOAR Program of the Canadian Space Agency*, the organizers of *Multi-temporal Conference* and the organizers of *International Symposium on Sea Ice in a Changing Environment* for allowing me to showcase my work.

Lastly, I wish to thank my wife Nidhi Bishnoi and my brother Navneet Singh Gill for their unconditional and unwavering support throughout my academic career.

This thesis is dedicated to my mother Upkar Kaur Gill

(It wouldn't have been possible without you)

Table of Contents

List of Tables

List of Figures

List of symbols and abbreviations

Symbol	Definition
$[S]$	Scattering matrix
$[M]$	Mueller matrix
$[C]$	Covariance matrix
$[T]$	Coherency matrix
$\vec{k}$	Pauli target vector
θ_i	Radar incidence angle
E_p^s	Scattered wave electric field
E_q^i	Incident wave electric field
σ_{HH}^0	Normalized radar cross-section – horizontal co-pol
σ_{VV}^0	Normalized radar cross-section – vertical co-pol
σ_{HV}^0	Normalized radar cross-section – cross-pol
γ_{co}	Co-polarization ratio
γ_{cr}	Cross-polarization ratio
ϕ_{HH-VV}	Co-polarized phase difference
σ_{SPAN}^0	Total power
ρ_{co}	Co-polarized correlation coefficient
H	Entropy
α	Alpha angle
β	Beta angle
A	Anisotropy
P_s	Surface scattering
P_d	Double bounce scattering
P_v	Volume scattering
α_s	Alpha parameter
ϕ_s	Phase parameter
ψ	Orientation angle
τ_s	Helicity
λ_s	Dominant eigenvalue
p	Degree of polarization
P_{max}	Maxima of degree of polarization
P_{min}	Minima of degree of polarization
$\langle\vec{P}\rangle$	Completely polarized component
$\langle\vec{U}\rangle$	Completely un-polarized component
R_0^{opt}	Scattered intensity
P_r^{max}	Maximum received power
P_r^{min}	Minimum received power
γ_{var}	Coefficient of variation
f_p	Fractional polarization
φ_{bs}	Brine volume fraction of snow

φ_{bsi}	Brine volume fraction of sea ice
ρ_s	Density of snow
ρ_b	Density of brine
ρ_i	Density of pure ice
T_s	Temperature of snow
S_b	Salinity of brine
S_S	Salinity f snow
δ_p	Vertical penetration depth
Ke	Extinction coefficient
L_C	Correlation length
ε^*	Complex dielectric constant
ε'	Dielectric permittivity
ε''	Dielectric loss
PPT	Parts per Thousand

Abbreviations

GARP	Global Atmosphere Research Programme
WMO	World Meteorological Organization
OSA	Ocean-sea ice atmosphere
PAR	Photosynthetic active radiation
GCMs	Global Circulation Models
SAR	Synthetic Aperture Radar
FYI	First-year sea ice
SYI	Second-year sea ice
MYI	Multi-year sea ice
SFYI	Smooth first-year sea ice
RFYI	Rough first-year sea ice
DFYI	Deformed first-year sea ice
OW	Open water
NRCS	Normalized radar cross section
SOAR	Science and Operational Applications Research
MSC	Meteorological Service of Canada
IPY	International Polar Year
CFL	Circumpolar Flaw Lead
MLC	Maximum likelihood classifier
SVP	Surface validation points
ERS	European Remote Sensing Satellite
PCSP	Polar Continental Shelf Program
CARS	Canada Aviation Regulations Station
RMS	Root mean square
SAT	Surface atmospheric temperature
PDF	Probability density function

Research is what I am doing when I don't know what I am doing.

- Wernher Von Braun,

New York Times, 16 December 1957

CHAPTER ONE:

INTRODUCTION

1.1 Rationale

Global Atmosphere Research Programme (GARP) of the World Meteorological Organization (1975) regarded sea ice as one of the five important components of the earth's climate system (McGuffie et al., 2000). This is primarily due to (1) the large areal extent of sea ice covering roughly 7% of the Earth's oceans (Parkinson et al., 1979); (2) its highly dynamic extent and thickness, seasonally and inter-annually (Parkinson et al. 1979); (3) its reflective properties that reduces the absorption of solar radiation by the earth's surface (Tremblay and Nivsak, 1997); (4) its strong insulation effect affecting the amount of heat, moisture and momentum flux between the ocean and the atmosphere (Tremblay and Nivsak, 1997); (5) its positive feedback mechanism, where high albedo of the sea ice results in reduced intake of solar energy, thereby cooling the atmosphere, which in response freezes the ocean waters (Ledley, 1991; Feltham, 2008); and (6) its thermohaline effect on the ocean circulation system, by altering the salinity of water during freeze-up and meltdown (Feltham, 2008).

Similarly, snow cover on Arctic sea ice has also been regarded as an important component of the ocean-sea ice-atmosphere (OSA) system. This is due to the physical and thermodynamic controls it exhibits on the radiation and chemical fluxes between the OSA layers. The physical properties of snow, i.e. conductivity, thermal diffusivity, reflection, absorption and transmission determine the conductive, radiative and turbulent energy exchanges between the atmosphere and underlying sea ice. This makes the snow cover act as a barrier between the two, thus impeding the energy transfer and regulating the accretion and ablation of sea ice (Geiger, 1957; Barry, 1996). During freeze-up, snow cover retards the process of ice growth and in the spring it increases the melting period by insulating the sea ice from cold and warm atmosphere (Mellor, 1964). These effects of snow are dependent on the distribution of snow cover in space, time and vertical dimension and can range from micro to meso scales affecting local habitats and global climate system. At micro scales, the absorption properties of snow for photosynthetic active radiation (PAR) determines the life cycle of epontic algal communities. The epontic communities survive in a highly balanced and stable environmental conditions determined by the snow thickness. Too thick or too thin snow cover hinders the algal growth by either starvation or access of light, thus reducing the primary productivity of the organisms (Cota and Horne, 1989). At local to regional scales, snow cover plays a major role in the life cycle of arctic seals and polar bears. It provides protection to the seals from predators through the accumulation of snow on ice ridges during storm events (Smith and Stirling, 1977). At global scales, snow cover dominates the energy balance of the OSA due to its low thermal diffusivity, low transmissivity and high albedo making it one of the most important variables in the climate system.

A steady decline in Arctic sea ice thickness due to loss of thick multiyear ice (MYI) relative to first-year (FYI) has been reported (Kwok et al., 2009). The decrease in MYI and relatively increase in FYI, which melts during the summer months has exposed the Arctic to incoming solar radiation. The ratio of reflected solar radiation to incident radiation for ocean water is 0.06 whereas for FYI is between 0.3-0.6 (Serreze and Barry, 2005). Disappearance of FYI during summer months decreases the overall albedo of the Arctic thereby allowing more absorption of solar energy, which in turn further reduces the sea ice due to ocean warming. The change in Arctic sea ice cover from MYI to FYI has thus resulted in an intensification of sea-ice-albedo-feedback.

1.2 Scientific Rationale

Decline in sea ice extent (Parkinson et al., 1999; Cavalieri et al., 2003) and thickness (Rothrock et al., 1999) in response to variations in the global climate and its inclusion in Global Circulation Models (GCMs) necessitates increased information on its geophysical properties for model parameterization. Additionally, information on sea ice at a variety of spatial and temporal scales is highly important for the circumpolar Arctic economy and for safe and efficient marine navigation. This information is primarily gained through a combination of *in-situ* observations and satellite based remote sensing. *In-situ* data collection methods are considered impractical because of their incapacity to provide information at the necessary spatial and temporal scales. Active microwave sensors onboard satellites have advantages in this regard, given their all-weather day and night capability, continuous repetitive coverage and various operational configurations.

Multi-frequency multi-polarized Synthetic Aperture Radar (SAR) has been increasingly applied to the study of snow covered sea ice during the past three decades. Initially, both image tone and texture have been exploited for this purpose (eg. Barber et al., 1992). Several techniques, such as neural networks (Karvonen, 2004), image segmentation (Simila et al., 2006), wavelet transformation (Simila and Helminen, 1995), backscatter inversion (Carlstrom and Ulander, 1995), integration of SAR with ice models (Shih el at., 1998) and lookup tables (Kwok et al., 1992) have been developed and tested to utilize SAR data for geophysical inversion. However, the focus of a majority of these studies has been (1) classification of ice types (Karvonen, 2004; Carlstrom and Ulander, 1995; Simila et al., 2006; Shih el at., 1998); (2) Thin ice-open water discrimination (Geldsetzer and Yackel, 2009; Lundhaug 2002; Gill, 2003; Mäkynen, 2007); (3) Sea ice thickness estimation (Winebrenner et al., 1995; Ngheim el at., 1997; Shih et al., 1998 and Simila et al., 2006); (4) Determination of thermodynamic state of sea ice (Barber and Ngheim, 1999; Yackel and Barber, 1998; Barber et al., 1995; Yackel and Barber, 2000; Yackel et al., 2000 & 2007) and (5) Extraction of information on sea ice dynamics (Lepparanta et al., 1998; Kwok et al., 1998). Although most studies have successfully inverted single and dual co-polarized backscatter to retrieve sea ice geophysical information, many others have shown that single polarized backscatter signatures provide limited information for, (1) Sea ice type classification (Sanden, 2004); (2) Discrimination of water from very thin ice (Geldsetzer and Yackel, 2009); (3) Estimation of melt pond fraction under wind conditions (Yackel and Barber, 2000) and (4) Calculation of sea ice concentration (Sanden, 2004). On the other hand, dual and multi-polarized backscatter has more strongly been related to sea ice characteristics (Dierking and Askne, 1998).

Studies on snow cover on Arctic sea ice have followed a similar pace. All kinds of characteristic properties of snow on sea ice have been studied through an array of *in-situ* based (Barber et al., 1994, 1995, 1996; Iacozza and Barber, 2010; Sturm et al., 2002), laboratory based (Lytle et al., 1993; Bredow and Gogineni, 1990), active microwave imagery based techniques (Barber and Nghiem, 1999; Yackel and Barber, 2007). With regard to snow and sea ice morphological properties, Shokr and Sinha (1994) have investigated micro scale snow structural properties. Similarly, dielectric properties of dry snow and brine-wetted snow were investigated by Frolov and Macheret (1999) and Geldsetzer et al., (2009), respectively. A detailed statistical analysis on snow physical properties was conducted by Barber et al. (1995). Snow cover depositional pattern were explored by Iacozza and Barber (2010). Seasonal co-evolution of snow physical, thermal, electrical and radiative properties from winter freeze-up to spring melt were investigated by Strum and Holmgren (2002), Barber et al. (1995), Barber et al. (1994). The effects of snow cover on scattering and emissive properties of OSA were more intricately analyzed by Barber and Nghiem (1999), Barber et al., (1998) and Tjuatja et al. (1995). With regard to microwave scattering properties of snow covered sea ice, studies conducted by Beaven et al. (1995), Lytle et al. (1993), Bredow and Gogineni (1990) present detailed analysis. On the use of SAR data for retrieval of snow physical, electrical and thermal properties (hereafter referred to electro-thermo-physical properties) is demonstrated by Yackel and Barber (1998, 2007) and Barber and Nghiem (1999). Estimation of snow thickness has been attempted using passive microwave techniques (Wang et al., 1992); direct backscatter inversion techniques (Beaven et al., 1995) and using the thermal dependence of backscatter (Barber et al., 1999; Yackel and Barber, 2007).

However, very little research using the full polarimetry of SAR data has been exploited for any of the purposes. This is partly due to the relative newness of fully polarimetric SAR sensors with Radarsat-2 operational only since 2007, TerraSAR-X since 2008 and ALOS PALSAR since 2006. Therefore, fully polarimetric SAR data must be investigated as an alternate or complementary approach to providing additional or improved information regarding snow cover properties on sea ice.

1.3 Research Objectives

The overarching goal of this research is to enhance our understanding of snow and sea ice polarimetric microwave (C-band) scattering properties of snow covered FYI for the purpose of improving geophysical inversion algorithms to retrieve unambiguous ice type and snow cover information. *In-situ* collected snow-sea ice property observations coincident to surface based C-band scatterometer data and Radarsat-2 SAR satellite overpass imagery will allow accomplishing the following objectives.

1) Determine C-band SAR polarimetric signatures of sea ice types at different geophysical and temperature conditions.
2) Evaluate the ice type classification potential of C-band SAR polarimetric parameters at different geophysical and temperature conditions.
3) Determine C-band SAR polarimetric signatures of snow cover on smooth FYI for different snow thickness and geophysical conditions.
4) Quantify SAR polarimetric parameter sensitivity to snow thickness on smooth FYI.
5) Quantify and assess the co-variation in coincident electro-thermo-physical properties of snow cover over smooth FYI and associated C-band microwave backscatter at diurnal time scales during the late winter to melt onset transition.
6) Quantify and assess the seasonal co-variation in coincident electro-thermo-physical properties of snow cover over smooth FYI and associated C-band microwave backscatter from early melt to melt onset period.

1.4 Research Structure

To address these research objectives, the thesis is split into seven chapters. Most chapters in the thesis are adopted from peer-reviewed research articles or manuscripts submitted for publication. Minimal modifications to the original manuscripts are made. Considering the manuscript driven nature of this thesis, some redundancy in the introductory and methods sections of the chapters is introduced.

Chapter 2 provides a background on selected definitions and fundamentals. It also establishes a nomenclature used in this thesis. More specifically, the definitions and terms related to electro-thermo-physical processes of snow covered sea ice and the microwave polarimetry are described.

Chapter 3 presents the C-band polarimetric microwave signatures of snow covered FYI types at cold atmospheric temperatures. The chapter also investigates the classification potential of polarimetric parameters derived after Cloude-Pottier (1997) decomposition, Touzi (2007) decomposition, Freeman-Durden (1998) decomposition, normalized radar cross section (NRCS) measurements, phase differences and statistical SAR correlation measures by relating them to three pre-identified sea ice types and wind roughened open water. A combined approach that constitutes visual inspection of estimated probability densities of the polarimetric parameters and quantitative analysis using supervised classifications (k-means and maximum likelihood) is adopted. Polarimetric parameters are iteratively combined in pairs and triplets to test for their ice type discrimination potential. Sensitivity of polarimetric parameters to radar incidence angle is also examined. The material in this chapter has undergone peer review and the results are published in the *Canadian Journal of Remote Sensing.* Parts of this chapter have also been presented and published in the *Canadian Association of Geographers conferences.* References can be found below.

***Gill, Jagvijay. P. S** & Yackel, J.J., "Evaluation of C-band SAR polarimetric parameters for discrimination of first-year sea ice types", Canadian Journal of Remote Sensing, Vol 38, No. 3, PP. 306-323, 2012.*

***Gill, Jagvijay. P. S.,** Fuller, M.C., Yackel, J. "Examination of C-band Polarimetric SAR Backscatter Response of Snow covered First-Year Sea Ice", The Prairie Summit, Regina, Saskatchewan, Canada, June 1-7, 2011.*

***Gill, Jagvijay. P. S.,** Yackel, J. "Evaluation of SAR Polarimetric Parameters for Sea Ice Classification", Canadian Association of Geographers Conference, Calgary, Alberta, Canada, May 31 - June 5, 2010.*

Chapter 4 extends the analysis conducted in Chapter 3 using the same dataset to investigate the thermal dependence of snow on polarimetric microwave backscatter. Ice type signatures of the same selected twenty polarimetric parameters are presented for warm atmospheric conditions and the consistency in FYI classification potential of these polarimetric parameters is analyzed by comparing the results of two studies conducted for the same ice types under different geophysical settings. Probability density functions, grey level parameter images and classification statistics derived using k-means classifier are used in the comparative analysis**.** The material in this chapter is published in the *Canadian Journal of Remote Sensing.* Parts of this chapter have also been presented at the *SOAR Program Mini Workshop.* References can be found below.

Gill, Jagvijay. P. S., *Yackel, J.J. and Geldsetzer, T., "Analysis of consistency in first-year sea ice classification potential of C-band SAR polarimetric parameters*", *Canadian Journal of Remote Sensing, Vol 39, No. 2, PP. 101-117, 2013.*

Gill, Jagvijay. P. S., *Yackel, J. "Polarimetric Microwave Investigations of Snow Covered First Year Sea Ice" SOAR Program Mini Workshop, Calgary, Alberta, Canada, October, 26, 2012.*

Chapter 5 investigates the sensitivity of C-band linear and polarimetric parameters derived from synthesis and decomposition of Radarsat-2 SAR data with respect to snow covers of variable thickness on smooth FYI. The study is conducted for two selected temperature conditions: 1) cold and 2) warm. First, the polarimetric SAR response from the snow cover under cold conditions is analyzed with an objective to investigate the sensitivity of linear and polarimetric backscatter to snow thickness. Second, the changes in these sensitivities are examined as a function of change in surface air temperature through the changes manifested in snow geophysical properties. The dependence of linear and polarimetric backscatter response on radar incidence angle for different snow thicknesses is also evaluated. The material in this chapter has been peer reviewed by the *Journal of IEEE Transactions on Geoscience and Remote Sensing.* The suggestions provided by the reviewers have been addressed and are included in chapter 5. The paper has been resubmitted. Parts of this chapter have also been presented at the *3rd Radarsat-2 Workshop* and *34th Canadian Symposium on Remote Sensing.*

Gill, Jagvijay. P. S., *Geldsetzer, T., Yackel, J.J., Christopher Fuller, M., and M. Hussain, "Sensitivity of C-band synthetic aperture radar polarimetric parameters to snow thickness over first-year sea ice",* IEEE Transcations on Geoscience and Remote Sensing, *2014 (in review).*

Fuller, M. Christopher., ***Gill., Jagvijay. P. S.,*** *Geldsetzer, T.,Yackel, J.J., and Derksen, C. "Observations of complexely-layered snow on first-year sea ice using microwave remote sensing", Hydrological Processes, Vol. 28, No. 16, PP. 4614-4625.013, 2014.*

Gill, Jagvijay. P. S., *Geldsetzer, T., Yackel, J.J. and Fuller, M. Christopher., "Limitations to estimating snow thickness on first-year sea ice using thermodynamics and C-band microwave backscatter", 34 Canadian Symposium on Remote Sensing, Victoria, Canada. 27-29 Aug, 2013.*

Gill, Jagvijay. P. S., *Yackel, J. "C and X-band multi-polarized SAR response from Snow Covered First Year Sea Ice during Spring Melt", 3rd Radarsat-2 Workshop, Saint-Hubert, Quebec, Canada, Sept 27 - Oct 2, 2010.*

Chapter 6 presents observations of diurnal and time series coincident geophysical and dielectric properties of thick and thin snow covers over smooth FYI sea ice and the polarimetric backscatter response at C-band. First part of the chapter presents an analysis of the diurnal observations of snow properties and the associated microwave backscatter is assessed for two temperature regimes: 1) early melt and 2) melt onset period - using measurements acquired every two to three hours. Second part of the chapter presents observations of C-band microwave signatures of thick and thin snow cover over smooth FYI, coincident to *in-situ* measured snow properties for a 15 day temporal scale starting early melt to melt onset. Parts of this chapter have been presented in the *International Symposium on Sea Ice in a Changing Environment and Multi-temporal Conference.* The chapter will be submitted for publication following this thesis.

Gill, Jagvijay. P. S., *Yackel, J.J., and Geldsetzer, T., "Diurnal observations of coincident C-band microwave backscatter and snow geophysical properties over smooth first-year sea ice - Implications for SAR remote sensing", International Symposium on Sea Ice in a Changing Environment. Hobart, Tasmania, Australia, 9-14 March, 2014*

Gill, Jagvijay. P. S., *Yackel, J.J., Geldsetzer, T., Bishnoi, N., Fuller, M. Christopher., Butterworth, C. "Analysis and modelling of multi-temporal polarimetric microwave signatures of snow covered first-year sea ice" Multi-temporal Conference, Banff, Alberta, Canada, June, 25-26, 2013.*

Chapter 7 presents a summary of the results of the preceding four chapters and provides concluding remarks. It also provides suggestions and recommendations for future work.

Appendix A provides a discussion on the implications of violation of data normality for classifications where classification algorithms assume data to be normally distributed. The chapter also provides a comparison of the classification results produced using normalized and un-normalized data.

Appendix B describes the contributions of the collaborators and a list of software used to process polarimetric SAR data.

CHAPTER TWO:
BACKGROUND AND FUNDAMENTALS

2.1 Abstract

This chapter provides a brief review of four important components pertinent to the current research. First, a description of snow and sea ice is provided. Second, SAR polarimetric remote sensing theory and polarimetric parameters are presented. Next, a theoretical basis of microwave remote sensing of snow covered sea ice is presented. Finally, a section on evolution of snow and sea ice electro-thermo-physical properties and corresponding microwave scattering is presented.

2.2 Sea ice

2.2.1 Sea ice types

The freezing of saline sea water results in the formation of sea ice. At the initial stage, when the ocean water temperature falls to -1.8°C, *ice spicules* appear in large quantity on the sea surface. These *ice spicules* are called *frazil ice*. On further cooling, these spicules merge together to evolve into *grease ice*. *Frazil ice* is distinguished from the *grease ice* as the *grease ice* has a matt look to it while *frazil ice* is oily. Another form of sea ice called *slush* is formed when fresh snow falls on the sea surface at freezing temperatures. Furthermore, the wind and the wave action on these ice types give rise to yet another form of ice known as *shuga*. *Frazil ice, grease ice, slush* and *shuga* are all forms of *new ice*. Most forms of new ice are largely unconsolidated. The thickness of *new ice* is less than 10 cm (WMO, 2007).

On further cooling the ice becomes consolidated and results in the formation of *nilas*. Depending upon the thickness, *nilas* can be divided into *dark nilas* (< 5 cm) or *light nilas* (≥ 10 cm). The consolidated ice with no or very little salinity is called *ice rind.* It is usually ≤5cm in thickness. *Ice rind, dark nilas* and *light nilas* are all considered as *nilas ice*. However, the presence of waves or wind action prevents the formation of *nilas,* instead *grease ice* coalesce to form small clumps. With further cooling and increase in ice thickness (>1cm), these clumps harden to form *pancakes*. These floating *pancakes* constantly collide with each other under the influence of wind action and grow up to 3m in diameter. Ice that originates from the *pancakes* has a very rough surface unlike *nilas.* The slush between the pancakes finally consolidates to form solid ice. As the temperature falls, the thickness of sea ice increases. Until sea ice reaches a thickness of 30 cm it is called *new / young ice*. Based on the thickness, the *new ice* is categorized as follows: *nilas* (~10 cm), *grey ice* (10-15cm) and *grey-white ice* (15-30cm). All these ice types are considered as *young ice* (Shuchman et al., 2004; WMO, 2007; MSC, 2005). After the formation of *young ice*, *first-year sea ice* (FYI) appears. Thickness of FYI can vary from 30cm to 2m. Based on the thickness, FYI is divided in *thin first-year ice* (30 – 70cm), *medium first-year ice* (70 – 120cm) and *thick first year ice* (120cm - 2m) (WMO, 2007; MSC, 2005). The topmost layer of FYI is composed of randomly-oriented ice crystals of *frazil ice*. Below the top layer exists vertically-oriented *columnar ice* (Shokr and Sinha, 1994). FYI is also described by its state of deformation. If the ice develops under calm / low wind conditions, it is termed as *Smooth FYI.* If the ice develops under moderate wind conditions and exhibits roughness up to few centimeters it is *Rough FYI*. *Deformed FYI* originates under extreme wind conditions when recently formed FYI collides with older and landfasted FYI or older, harder sea ice or landmasses giving rise to rafts or ridges (Dierking and Dall, 2007).

If thick FYI survives one melt season, it becomes *second-year ice* (SYI) and if it survives more than one melt season it becomes *multi-year ice* (MYI). Both SYI and MYI can be referred to as *old ice* with their thickness ranging from 1.2 - 5m (WMO, 2007; MSC, 2005).

2.2.2 Seasonal evolution of sea ice

Sea ice is a multiphasic alloy composed of liquid brine, ice and solid salts (Weeks and Ackley, 1986). Barber et al., 1994, following Livingstone et al. (1991), divided the annual cycle of sea ice growth into thermodynamic regimes, based on average processes operating across the OSA interface. These regimes are sequentially ordered by thermodynamic season as, *freeze up, winter, early melt, melt onset* and *advanced melt.*

The initial freezing of Arctic sea water in the months of October and November marks beginning of *freeze-up*. During the month of December, with further decrease in atmospheric temperature due to reduced solar energy, FYI starts growing thicker and becomes covered with meteoric snow. This is the start of *winter*. From January to March, with almost no solar input, the Arctic does not experience much change. From mid-April the solar input starts to increase and marks the beginning of *early melt season*. Solar radiation increases rapidly from late April through May, increasing the snow temperature and resulting in the *early melt season*. Mid to late June usually marks the start of *advanced melt*, when most of the surface snow melts to form ponds on the surface of sea ice (Holt and Digby, 1985). During the latter point of Advanced Melt, the sea ice volume becomes isothermal thereby allowing surface melt ponds to drain from the surface to the underlying ocean surface.

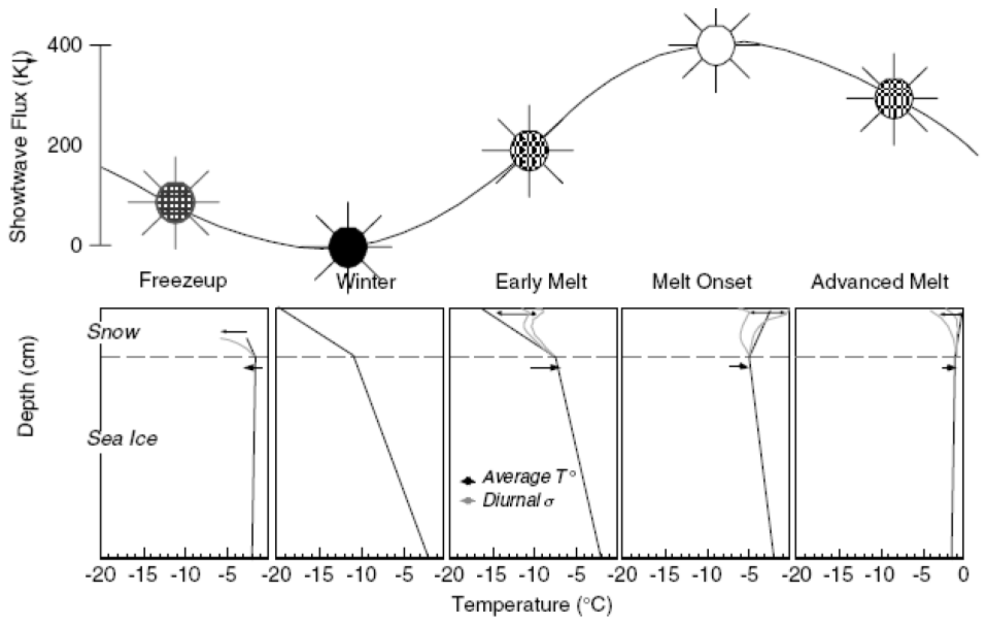

Figure 2.1. Seasonal shortwave flux, snow and ice vertical temperature profiles and thermodynamic regimes from freeze-up to advanced melt for FYI. (From Barber et al., 2001). Note the characteristic diurnal temperature swings in the snow profile during the early melt and melt onset regimes

2.3 Snow cover on sea ice

2.3.1 Snow types

Snow is a mixture of water, ice and air, all existing at the same time. Snow begins to deposit on sea ice as soon as the ice consolidates on the ocean surface. During winter , snow cover on sea ice can largely be categorized into three primary types (Barber et al., 1995): 1) New or fresh snow consisting of small randomly oriented snow grains (~1 mm) and very low density (0.19g/cm3), 2) Wind slab consisting of very small (∼0.5 mm) closely packed, randomly oriented snow grains and high density ranging from 0.4g/cm3 to 0.6g/cm3, 3) Depth hoar consisting of large (1-5 mm), flat, cup-shaped or columnar snow grains and a density of 0.28g/cm3.

During the early melt stage, snow cover in general has larger grain size and spherical shapes. This is the result of diurnal heating and cooling that produce melt-freeze cycles in the upper snow layers and allow snow grains to coalesce together (Colbeck et al., 1990). At times, during the freezing cycle, the presence of water in the voids between snow grains can freeze to form non spherical poly-aggregate crystals (Colbeck et al., 1990). The snow grains in the depth hoar during the early melt period also become rounded as a result of reduced vertical thermal gradient. Although their faceted shapes may still be present but their edges are smoothed.

Snow cover on FYI wicks brine from the underlying saline sea ice creating a layer of *brine-wetted snow*. *Brine-wetted* snow usually constitutes the bottom 10 cm of snow cover. The salinities in the brine wetted snow range from 1-20‰ (Drinkwater and Crocker, 1988; Barber et al., 1995). Brine wetted snow is the result of brine entrapment in sea ice during the initial freeze-up which on further drop in temperature, due to increase in pressure inside the brine pockets, is expelled to the sea ice surface and into the ocean waters underlying sea ice (Tucker et al., 1992). A thin layer of brine is usually accumulated on the sea ice surface (Martin, 1979). This brine layer is highly saline. The salinities in the brine layer can be on the order of 100‰ (Martin, 1979; Drinkwater and Crocker, 1988). Due to the presence of salts, brine is in liquid form, even at temperatures <0°C (Assur, 1960). As soon as the snow cover accumulates on sea ice surface, brine is wicked up through capillary action (Barber and Thomas, 1998; Barber et al., 2003). This brine resides in the voids between the snow grains as brine inclusions.

2.3.2 *Snow thickness variability*

The thickness of snow cover is highly dependent on the sea ice type, its roughness and the amount of meteoric snow that occurs from freeze-up until the sea ice completely ablates during Advanced Melt. Snow thickness can range from 0-60 cm on both FYI and MYI (Iacozza and Barber, 2001; Sturm et al., 2002; Sturm et al., 2006) and can vary at a scale 10-20 m for both FYI and MYI types? (Iacozza and Barber, 1999). With an increase in FYI surface roughness, snow thickness increases (Iacozza and Barber, 1999).

2.4 Polarimetric SAR

Fully polarimetric SAR remote sensing of natural targets is accomplished using single antenna transmitted and received radar pulse and measuring the returned amplitude and phase of the scattered signal at all linear polarizations (HH, VV, HV and VH). This is represented by complex scattering matrix $[S]$.

2.4.1 *Scattering polarimetry*

The relationship between incident wave electric field $\vec{E}^i$ and the scattered wave electric field $\vec{E}^s$ is represented in terms of scattering matrix $[S]$ by equation 1.1. Analogous to the scattering matrix, Mueller matrix $[M]$ represents the same by relating incident and scattering stokes vectors through equation 1.2.

$$\vec{E}^s = \frac{e^{jkr}}{r}[S]\vec{E}^i \tag{1.1}$$

$$\vec{R} = [M]\vec{T} \tag{1.2}$$

where, *r* is the distance between target and antenna, *k* is the wave number and *j* denotes receiving polarization. $\vec{T}$ and $\vec{R}$ are incident and scattered Stokes vectors, respectively.

Equations 1.1 and 1.2 are true only for completely polarized waves. Random scattering phenomenon is better represented by the covariance matrix $[C]$ which is the ensemble averaged complex outer product of lexicographic scattering vector, shown by equation 1.3.

$$[C] = \begin{pmatrix} \langle S_{HH}S_{HH}^*\rangle & \langle S_{HH}S_{HV}^*\rangle & \langle S_{HH}S_{VH}^*\rangle & \langle S_{HH}S_{VV}^*\rangle \\ \langle S_{HV}S_{HH}^*\rangle & \langle S_{HV}S_{HV}^*\rangle & \langle S_{HV}S_{VH}^*\rangle & \langle S_{HV}S_{VV}^*\rangle \\ \langle S_{VH}S_{HH}^*\rangle & \langle S_{VH}S_{HV}^*\rangle & \langle S_{VH}S_{VH}^*\rangle & \langle S_{VH}S_{VV}^*\rangle \\ \langle S_{VV}S_{HH}^*\rangle & \langle S_{VV}S_{HV}^*\rangle & \langle S_{VV}S_{VH}^*\rangle & \langle S_{VV}S_{VV}^*\rangle \end{pmatrix} \tag{1.3}$$

where, the diagonal elements represent backscatter intensities and the off diagonal elements represent complex covariance of polarizations. An alternate to the lexicographic scattering vector, Pauli target vector $\vec{k}$ (equation 1.4) produces coherency matrix $[T]$ (equation 1.5). $[T]$ and $[C]$ are consimilar with same eigenvalues but different eigenvectors.

$$\vec{k} = \frac{1}{\sqrt{2}}\big(S_{HH} + S_{VV}\ S_{HH} - S_{VV}\ S_{HV} + S_{VH}\ j(S_{HV} - S_{VH})\big)^T \tag{1.4}$$

$$[T] = \langle \vec{k} \cdot \vec{k}^{*T} \rangle \tag{1.5}$$

2.4.2 Normalized radar cross section (NRCS) parameters

2.4.2.1 Radar backscattering coefficient

Radar backscattering coefficient is the ratio of the statistically averaged total received signal power to the illuminated area transmitted power represented by equation 1.6.

$$\sigma_{pq}^{0}(\theta_0) = \frac{4\pi r^2 \langle \left| E_p^s \right|^2 \rangle}{a \left| E_q^i \right|^2} \tag{1.6}$$

where, θ_0 is the incidence angle measured with respect to vertical, p is the received polarization, q is the transmitted polarization, E_p^s is the scattered wave electric field, E_q^i is the incident wave electric field, a is the area illuminated by the radar and r is the distance between target and antenna.

2.4.2.2 Co-polarization ratio

The ratio of horizontally transmitted and received σ_{HH}^{0} to vertically transmitted and received σ_{VV}^{0} or vice versa is termed as co-polarization ratio (γ_{co})(Cloude and Pottier, 1997).

$$\gamma_{co} = \frac{\sigma_{HH}^{0}}{\sigma_{VV}^{0}} = \frac{|S_{HH}|^2}{|S_{VV}|^2} \tag{1.7}$$

2.4.2.3 Cross-polarization ratio

The relationship between σ^0_{HH} and σ^0_{HV} is defined by cross-polarization ratio (γ_{cr}) (Cloude and Pottier, 1997; Nghiem et al., 1997). γ_{cr} describes the scattering mechanism and orientation of the scattering elements, categorizing the target media as isotropic or anisotropic.

$$\gamma_{cr} = \frac{\sigma^0_{HH}}{\sigma^0_{HV}} = \frac{|S_{HH}|^2}{|S_{HV}|^2} \tag{1.8}$$

2.4.2.4 Phase difference

The difference of time measured as angle between the transmitted and received vertical and horizontal waves is phase difference. Co-polarized phase difference as described by Drinkwater et al. (1992) is shown in equation 1.9.

$$\phi_{HH-VV} = tan^{-1}\left(\frac{Im(S_{HH}S^*_{VV})}{Re(S_{HH}S^*_{HH})}\right) \tag{1.9}$$

2.4.2.5 SPAN

It is the sum of the intensities at all polarizations and is represented by the equation 1.10.

$$\sigma^0_{SPAN} = \sigma^0_{HH} + 2\sigma^0_{HV} + \sigma^0_{VV} \tag{1.10}$$

2.4.2.6 Co-polarized correlation coefficient

Co-polarized correlation coefficient (ρ_{co}), equation 1.11, describes the correlation magnitude of polarized backscattered intensity.

$$\rho_{co} = \left| \frac{S_{HV}\, S_{VV}^{*}}{\sqrt{(S_{HH}S_{HH}^{*})(S_{VV}S_{VV}^{*})}} \right| \tag{1.11}$$

If $\rho_{co} = 1$, the backscatter is considered fully polarized and if $\rho_{co} = 0$, the backscatter is fully depolarized. ρ_{co} is inversely related to incidence angle and directly related to the salinity of sea ice (Drinkwater et al., 1992). It also depends on the wave frequency, shape and orientation of scatterers (Nghiem et al., 1995).

2.4.3 Cloude and Pottier decomposition parameters

Cloude and Pottier (1997) developed a technique to decompose target coherency matrix [T] to extract parameters of target characterization defined by eigenvectors and eigenvalues. The decomposition is described by equation 1.12, under the assumption of reciprocal scattering and collocated SAR transmitter and receiver.

$$[T] = [U_3] \begin{pmatrix} \lambda_1 & 0 & 0 \\ 0 & \lambda_2 & 0 \\ 0 & 0 & \lambda_3 \end{pmatrix} [U_3]^{*T} \tag{1.12}$$

Where, λ_1, λ_2 and λ_3 are eigenvalues of [T] and [U_3] is given by equation 1.13:

$$[U_3] = \begin{pmatrix} cos(\alpha_1) & cos(\alpha_2) & cos(\alpha_3) \\ sin(\alpha_1)\, cos(\beta_1)\, e^{i\delta_1} & sin(\alpha_2) cos\,(\beta_2) e^{i\delta_2} & sin(\alpha_3)\, cos(\beta_3) e^{i\delta_3} \\ sin(\alpha_1)\, sin(\beta_1) e^{i\gamma_1} & sin(\alpha_2)\, sin\,(\beta_2) e^{i\gamma_2} & sin(\alpha_3)\, sin\,(\beta_3) e^{i\gamma_3} \end{pmatrix} \quad (1.13)$$

In equation 1.13, the columns are the orthogonal eigenvectors of $[T]$. α_i and β_i are the target scattering mechanism and orientation angles, respectively. γ_i is the phase difference between $(S_{HH} + S_{VV})$ and S_{HV}. δ_i is the phase difference between $(S_{HH} + S_{VV})$ and $(S_{HH} - S_{VV})$.

Decomposition of target coherency matrix $[T]$ allows the computation of several polarimetric parameters.

2.4.3.1 Scattering entropy

Entropy (H) describes the degree of randomness of target scattering. It is computed by decomposing the target symmetric coherency matrix and measuring its eigenvalues and complex eigenvectors. Each eigenvector represents an orthogonal scattering mechanism derived from equation 1.14.

$$H = \sum_{i=1}^{3} -P_i\, log_n(P_i) \quad (1.14)$$

where, P_i is given by equation 1.15 and λ_i are the eigenvalues of [T].

$$P_i = \frac{\lambda_i}{\sum_{i=1}^{3} \lambda_i} \quad (1.15)$$

Entropy quantifies the magnitude of mixing between the three scattering mechanisms and is normalized between 0 and 1. *H*=0 indicates one dominant scattering mechanism (pure single bounce or pure double bounce) with a single non-zero eigenvalue. *H*=1 indicates an equal mixture of the three scattering mechanisms with the three eigenvalues equal.

2.4.3.2 Alpha angle

Alpha angle describes the dominant scattering mechanism for the target. It is computed as the weighted average of the α_i values of the equation 1.16.

$$\alpha = P_1\alpha_1 + P_2\alpha_2 + P_3\alpha_3 \tag{1.16}$$

where, α_i are target scattering mechanisms derived from equation 1.13 and P_i is given by equation 1.15. Alpha angle (α) ranges from $0^\circ - 90^\circ$. α=0° indicates a trihedral isotropic scattering or a smooth surface scattering where $|\mathrm{HH}| = |\mathrm{VV}|$. With increase in α, the surface becomes anisotropic where $|\mathrm{HH}| \neq |\mathrm{VV}|$. $\alpha = 45^\circ$ indicates dipole scattering where either HH or VV is zero. $\alpha = 90^\circ$ indicates anisotropic dihedral scattering.

2.4.3.3 Beta angle

Beta angle represents the orientation of the scatterers with respect to the radar line of sight. It is computed as the weighted average of the β_i values using equation 1.17.

$$\beta = P_1\beta_1 + P_2\beta_2 + P_3\beta_3 \tag{1.17}$$

where, β_i is the orientation angle derived from equation 1.13 and P_i is given by equation 1.15.

2.4.3.4 Anisotropy

Anisotropy (A) defines the scatterer's shape and composition (dielectric constant). A can be derived from the eigenvalues of $[T]$ using equation 1.18.

$$A = \frac{\lambda_1 - \lambda_2}{\lambda_1 + \lambda_2} \tag{1.18}$$

where, λ_1 and λ_2 are the eigenvalues of $[T]$. $A = 1$ denotes, either the scatterers are spherical in shape or have low dielectric constant. $A < 1$ denotes that the scatterers are needle like shaped and $A > 1$ denotes that the scatterers are oblate shaped.

2.4.4 Freeman-Durden decomposition parameters

The Freeman Durden (1998) decomposition is based on a three component scattering model and yields three parameters that describe the contributions due to rough surface scattering (P_s), double bounce scattering (P_d) and volume scattering (P_v). The full description of the algorithm is presented in Freeman Durden (1998).

2.4.5 *Touzi's decomposition parameters*

Similar to eigenvalue decomposition, the projection of the scattering matrix on to the Pauli basis using Kennaugh-Huyen, con-diagonalization results in a scattering vector model that allows the derivation of basis invariant target parameters (Touzi, 2007). The five computed parameters describe the magnitude (α_s) and the phase (ϕ_s) of scattering type and the orientation angle (P_{si}), helicity (τ_s) and the dominant eigenvalue (λ_s) of the maximum polarization response (Touzi, 2007). The full description of the algorithm can be found in Touzi, 2007.

2.4.6 *Wave synthesized parameters*

The Polarimetric synthesized parameters used in this thesis are computed after Touzi et al. (1992) and the nomenclature in the following sections is adopted from Van Zyl et al. (1987), Zebker et al. (1987), Evans et al. (1988) and Touzi et al. (1992).

2.4.6.1 Degree of polarization

Degree of polarization (p) can either be derived from Stokes vectors or from eigenvalues of the covariance matrix $[C]$, using the equation 1.19.

$$p = \frac{\lambda_1 - \lambda_2}{\lambda_1 + \lambda_2} = \frac{\sqrt{\langle s_1^2 \rangle + \langle s_2^2 \rangle + \langle s_3^2 \rangle}}{\langle s_0 \rangle} \tag{1.19}$$

where, λ_1 and λ_2 are the real positive eigenvalues of $[T]$, given by equations 1.20 and 1.21. $\langle s_0 \rangle$, $\langle s_1 \rangle$, $\langle s_2 \rangle$ and $\langle s_3 \rangle$ are the elements of Stokes vector. The denominator in equation 1.19 represents the total wave power and numerator represents the polarized wave power.

$$\lambda_1 = \frac{1}{2}\left\{\langle s_0 \rangle + \sqrt{\langle s_1^2 \rangle + \ \langle s_2^2 \rangle + \langle s_3^2 \rangle}\right\} \tag{1.20}$$

$$\lambda_1 = \frac{1}{2}\left\{\langle s_0 \rangle - \sqrt{\langle s_1^2 \rangle + \ \langle s_2^2 \rangle + \langle s_3^2 \rangle}\right\} \tag{1.21}$$

The range of values for p lies between 0 and 1. $p = 1$ denotes complete polarization and $p = 0$ denotes complete un-polarization. The extrema of p are important parameters for target characterization and are derived by computing p for all values of ellipse orientation angle (ψ) and ellipticity angle (χ), the process known as synthesis.

2.4.6.2 Extrema of polarized and un-polarized components

Completely polarized $\langle \vec{P} \rangle$ and completely un-polarized $\langle \vec{U} \rangle$ components sum up to produce a partially polarized wave and can be expressed in the form of Stokes vector components by equation 1.22 and Stokes vector elements and degree of polarization by equation 1.23. Synthesis as an optimization technique is used to enhance or depress the two components in the radar backscatter. This is performed by processing the Stokes vector for all values of ψ and χ, until the combination produces a maximum or minimum of the desired component.

$$\langle \vec{s} \rangle = \langle \vec{P} \rangle + \langle \vec{U} \rangle \tag{1.22}$$

$$\langle \vec{s} \rangle = \begin{pmatrix} p\langle s_0 \rangle \\ \langle s_1 \rangle \\ \langle s_2 \rangle \\ \langle s_3 \rangle \end{pmatrix} + \begin{pmatrix} (1-p)\langle s_0 \rangle \\ 0 \\ 0 \\ 0 \end{pmatrix} \tag{1.23}$$

where, $\langle \vec{P} \rangle$ is the completely polarized component and $\langle \vec{U} \rangle$ is the completely un-polarized component. The two components are highly dependent on the property of the target to depolarize the wave.

2.4.6.3 Extrema of scattered intensity

The incident $(\vec{R})$ and scattered $(\vec{T})$ Stokes vectors are related by Mueller matrix (M) as shown in equation 1.2. Total intensity of the scattered wave is computed by determining the Stokes vector of incident wave and measuring the scattering behavior of the target using (M). This is represented by the equation 1.24.

$$R_0 = M_{00}T_0 + M_{01}T_1 + M_{02}T_2 + M_{03}T_3 \tag{1.24}$$

where, M_{ij} are the elements of M and T_i are the elements of transmitted wave Stokes vector. The extrema of the scattered intensity can be calculated by optimization of the equation 1.25, under the assumption that the transmitted wave is completely polarized.

$$R_0^{opt} = M_{00} \pm \sqrt{M_{01}^2 + M_{02}^2 + M_{03}^2} \quad (1.25)$$

2.4.6.4 Extrema of received power

Extrema of received power provides important information on the type of scattering and its homogeneity. Total received power (P_r) is represented by equation 1.26.

$$P_r = \frac{1}{2} R_0(1-p) + pR_0 cos^2\left(\frac{\delta}{2}\right) \quad (1.26)$$

where, R_0 denotes received intensity, p denotes degree of polarization and δ is the angular distance (on Poincare Sphere) between the polarization states of scattered wave and receiving antenna. Received power is maximum when $\delta = 0$ and minimum when = 90. In other words P_r is maximum when polarization of receiving antenna is matched to the polarization of scattered wave and P_r is minimum when polarization of receiving antenna is orthogonal to the polarization of scattered wave. The extrema of the received power can be determined from the equations 1.27 and 1.28.

$$P_r^{max} = \left(\frac{R_0}{2}\right)(1+p) \quad (1.27)$$

$$P_r^{min} = \left(\frac{R_0}{2}\right)(1-p) \quad (1.28)$$

2.4.6.5 Coefficient of variation and fractional polarization

Coefficient of variation (γ_{var}) and fractional polarization (f_p) are obtained by synthetically varying co- or cross polarized radar signals and measuring their maximum P_{max} and minimum P_{min} intensities, equation (1.29) & (1.30). γ_{var} indicates heterogeneity in the scattering mechanism and f_p describes the percentage of polarized returned pulse.

$$\gamma_{var} = \frac{P_r^{min}}{P_r^{max}} \tag{1.29}$$

$$f_p = \frac{P_r^{max} - P_r^{min}}{P_r^{max} + P_r^{min}} \tag{1.30}$$

2.5 Active microwave remote sensing of snow and sea ice

2.5.1 Theoretical scattering model

Radar backscatter is a function of surface and volume scattering originating from different layers of the OSA system (Figure 2.2). Depending upon the penetration depth, backscatter response could be the contribution of one, two or all of the following scattering types.

1) Surface scattering from snow-air interface.
2) Volume scattering from snow.
3) Scattering from snow-ice interface.
4) Surface scattering from ice.
5) Volume scattering from ice layer.

6) Scattering from ice-water interface.

7) Scattering from sea ice bottom surface.

Numerous theoretical backscatter models describe the scattering mechanisms for different combinations of sea ice dielectric and geometric properties. The simplest one-dimensional model was presented by Fung, 1994 whereas more complicated models for level ice (Carlström and Ulander, 1995; Dierking et al., 1997 and 1999), rough ice (Carlström and Ulander, 1995; Carlström, 1997), for snow covers on smooth ice (Barber and Nghiem, 1999), for melt ponds on FYI (Yackel et al., 2000) are also reported in the literature.

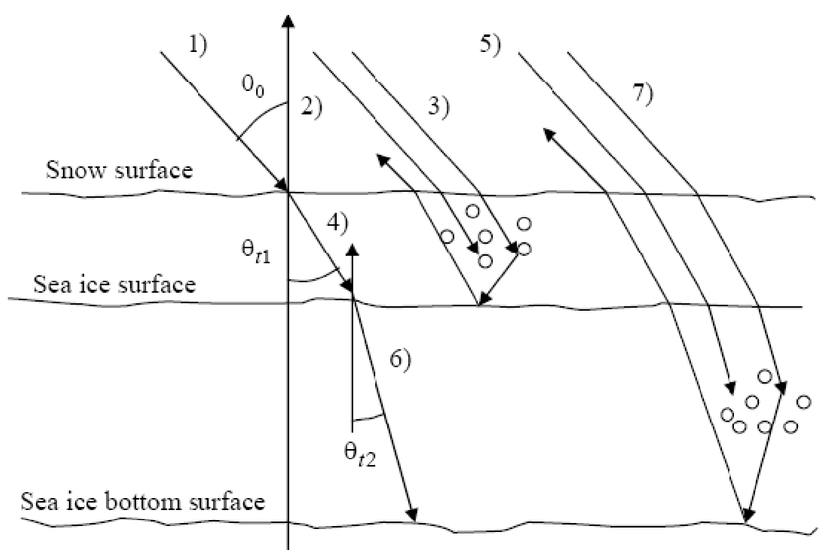

Figure 2.2. Backscatter mechanisms from snow covered sea ice. $\boldsymbol{\theta_0}$ is the radar incidence angle and $\boldsymbol{\theta_{t1}}$, $\boldsymbol{\theta_{t2}}$ and transmitted angles in snow and ice. The numbers correspond to the scattering mechanisms mentioned in section 2.5.1. (Adopted from Mäkynen, 2007)

In general, microwave remote sensing of snow covered sea ice depends on radar parameters (frequency, incidence angle and polarization), geophysical properties of snow and sea ice and dielectric properties of snow and sea ice.

2.5.2 Radar parameters and microwave scattering

The wavelength of the transmitted and received radar pulse (radar frequency) largely determines the penetration depth of electromagnetic waves. Penetration depth is longer for low frequencies. Backscatter response from rough surfaces is a function of radar frequency and incidence angle? (Barry, 1964; Hibler and Tucker, 1977).

The angle between the radar beam and the perpendicular on the snow-ice surface is called incidence angle. Mean backscattering coefficient (σ°) in decibels (dB), exhibits a negative linear relationship with radar incidence angle in the range between 20˚ and 40˚ over smooth FYI (Nghiem et al, 1997). The relation between backscatter and incidence angle is also a function of target geophysical and dielectric properties. The dependence of radar backscatter on incidence angle is lower for deformed ice than level ice (Ulaby et al., 1984). Radar polarimetric parameters can exhibit negative, positive or no relationship to incidence angle. Ngheim et al., 1997 showed that incidence angle had no significant effect on co-pol correlation coefficient and phase of correlation coefficient.

Amplitude of electromagnetic transverse wave in vertical or horizontal direction defines the polarization. If the wave traverses and forms an ellipse only in X-axis, it is termed as linear horizontally-polarized wave. And if the wave traverses only in Y-axis, it is linear vertically-polarized wave. Snow and sea ice are sensitive to polarization to the extent that at C-band VV co-polarization, mean backscatter difference between level ice and water is 3 dB higher than at C-band VH cross-polarization (Carlström, 1990). Similarly, the mean backscatter difference between level ice and deformed ice is 10 dB higher at C-band VH cross-polarization than at C-band VV co-polarization (Hyyppa and Hallikainen, 1992). In general, classifications performed using cross-polarization achieves higher accuracies than using co-polarization and the best results are found with their combination (Hyyppa and Hallikainen, 1992; Hallikainen and Toikka, 1992).

2.5.3 Snow and sea ice dielectric properties and microwave scattering

The dielectric properties of a material are described by its complex dielectric constant. Complex dielectric constant constitutes dielectric constant or permittivity, and dielectric loss. The dielectric constant and loss are known as the real and the imaginary components of the complex dielectric constant. The complex dielectric constant ε^* is defined in equation 1.31.

$$\varepsilon^* = \varepsilon' - i\varepsilon'' \tag{1.31}$$

where ε' is the dielectric constant, ε'' is the dielectric loss, i states that ε'' is an imaginary number.

Following Mäkynen (2007), total radar backscatter depends on the volume absorption and scattering coefficients of snow and ice. In general, radar backscatter is inversely related to the dielectric constant. Bulk relative dielectric constant of snow and sea ice determines the volume absorption coefficient. The dielectric constant of snow depends on snow density, snow wetness, snow temperature and brine volume fraction, whereas the dielectric constant of sea ice depends on brine volume fraction, which further depends on ice density, salinity and temperature. The volume scattering coefficient of snow and ice is governed by dielectric constant of scatterers. Ice crystals and brine pockets (air bubbles) are the principal scatterers in snow and sea ice, respectively (Mäkynen, 2007). Temperature controls the dielectric constant in ice crystals, whereas brine salinity, sea water salinity and temperature collectively govern dielectric constant in brine pockets.

2.5.4 Snow and sea ice geophysical properties and microwave scattering

Surface and volume scattering is governed by the following geophysical characteristics of snow and sea ice.

(a) Small and large scale surface roughness of snow and sea ice**.** Surface roughness is the root mean square (RMS) height deviation of a surface. For microwaves, surface roughness is defined by the equation 1.32 (Woodhouse, 2006). A smooth surface produces a coherent backscatter. A rough surface results in less coherent scattering, more random phase differences, low polarization differences and generally higher backscatter.

$$RMS_{smooth} < \frac{\lambda}{32cos\theta} \tag{1.32}$$

(b) Volume fraction and size of ice crystals in snow, where volume fraction depends on snow density and wetness. Large snow grain size decreases the backscatter (Barber and Nghiem, 1999).

(c) Brine volume fraction and size in sea ice, where volume fraction depends on sea ice density, salinity and temperature. Increase in brine volume increases the radar backscatter (Barber and Nghiem, 1999)

2.6 Microwave backscatter from snow and sea ice

2.6.1 Sea Ice

Sea ice exhibits a very complex and dynamic cycle of changing electro-thermo-physical and morphological properties, beginning with fall accretion and concluding with summer decay (Barber et al., 1999). During the initial stages of freeze up, *new ice* (thin ice) is formed with primary components as *frazil* and *slush*, which later aggregate to form *shuga* (grease ice) and *nilas* (dark ice) (Barber et al., 1999). Thin new ice exhibits a direct relationship of C-band backscatter signatures to ice thickness in the range of 0-12 cm (Kwok et al., 1998). Presence of slushy layers reduce the microwave backscatter responses by 4-5 dB and 4-8 dB at VV and HH polarizations, respectively (Kwok et al., 1998). With further cooling, ice grows into crystals with brine pockets, which are either extruded to the surface resulting in frost flowers or expelled into the ocean (Drinkwater and Crocker, 1988; Hollinger et al., 1984). Frost flowers cause sudden increase in backscatter by 3-5 dB owing to their high dielectric constant and micro-scale roughness (Kwok et al., 1998; Barber et al., 2014). Throughout the growth process, surface and bottom ice salinities are higher than in the bulk of the interior.

Snow/ice decay begins with the appearance of liquid water and grain growth within the snow cover, followed by the development of ice lenses and ice layers due to metamorphic processes. This causes a decline in density from newly fallen snow (~0.05

g/cm^3) to crustal snow layers (~0.5 g/cm^3). Temperature within the ice volume rises, consequently inducing an increase in brine volume and growth of brine pockets (Barber et al., 1999). With the increase in bulk ice temperature backscatter also increases, therefore, during the freeze-up and ablation period (spring and fall), variations in backscatter could be a response to thermal environment and should be interpreted with care (Kwok et al., 1998). Liquid water is slowly drained from the saturated snow through the interconnected brine pockets leaving behind polycrystalline aggregates. Salinities at the sea ice surface decrease rapidly as the freshwater infiltrates. Snow/ice melt and drainage begins with shallower inter-drift patches through seal holes, cracks, leads and brine channels forming melt ponds (Barber et al., 1999). Melt ponds or flooding on sea ice increases the backscatter by ~ 1.7 dB at normal incidence (Kwok et al., 1998). Due to surface ponding, multiyear ice can show significant reduction in backscatter signatures, sometimes lower than younger ice, causing reversal in backscatter contrast of these ice types (Kwok et al., 1998). Break-up occurs, which is the final ablation process, leaving behind mechanically weak pans of sea ice. These pans can exist for extended period of time as decayed ice or transform into second year/multiyear ice type (Barber et al., 1999).

2.6.2 Snow

A review of interaction between electro-thermo-physical and scattering properties of snow is presented through two theories: (1) the effect of variable snow thickness on radar backscatter and (2) the response in radar backscatter as a function of temperature change. Barber and Nghiem (1999) found that total scattering from a smooth snow covered sea ice surface is largely a function of snow grain size (which can subsequently act as large scattering centers once they become brine coated at warmer temperatures), brine volume (brine inclusions and brine pockets) and small scale roughness at the snow-ice interface (Figure 2.3).

Under dry snow conditions and air (and snow) temperatures < -15° C, scattering at C-band is mainly due to the sea ice roughness as dry cold snow is transparent to electromagnetic waves. With an increase in snow basal temperature, brine volume at snow-ice interface increases (Cox and Weeks, 1983) following the empirically derived sea ice phase proportion calculations originally developed by Assur, 1958. As a result, backscatter also increases. This increase is attributed to several factors, such as (1) enhanced contrast (effective permittivities) between the basal snow layer and ice surface, (2) larger brine-coated snow grain scatterers and (3) overall higher brine volume in snow and ice layers (Barber and Nghiem, 1999). The increase in backscatter as a function of increase in temperature is less for thick snow covers (24cm) and rougher ice surfaces underlying snow covers (Barber and Nghiem, 1999). This is because the thicker snow cover insulates the sea ice interface temperature from the warming air and snow temperatures. The rougher ice surface contributes an ice surface roughness scattering term to the total backscatter thereby masking/diluting the relatively subtle thermal effect of detecting an increased brine volume. With regard to the relationship between variable snow thickness over smooth FYI and microwave scattering, at snow temperatures <-10°C, radar backscatter generally increases with increasing snow thickness for similar snow and ice surface temperature (Barber and Nghiem, 1999). Small scale roughness and dielectric contrast between snow and ice have been identified as primary factors contributing to backscatter increase when snow thickness increases from 0 to 12 cm (Beaven et al., 1995). With further increase in snow thickness, snow thermodynamics begin to play a role in contributing to total backscatter. Thick snow results in a smaller vertical temperature gradient in snow pack and relatively higher temperature at the snow-ice interface. On the contrary, thin snow exhibits a larger vertical temperature gradient in snow pack and lower temperature at the snow-ice interface. The increased snow-ice interface temperature in thick snow induces an increase in brine volume in the basal snow and adjacent sea ice layer (Nakawo and Sinha, 1981, Barber and Nghiem, 1999). As a consequence, radar backscatter increases.

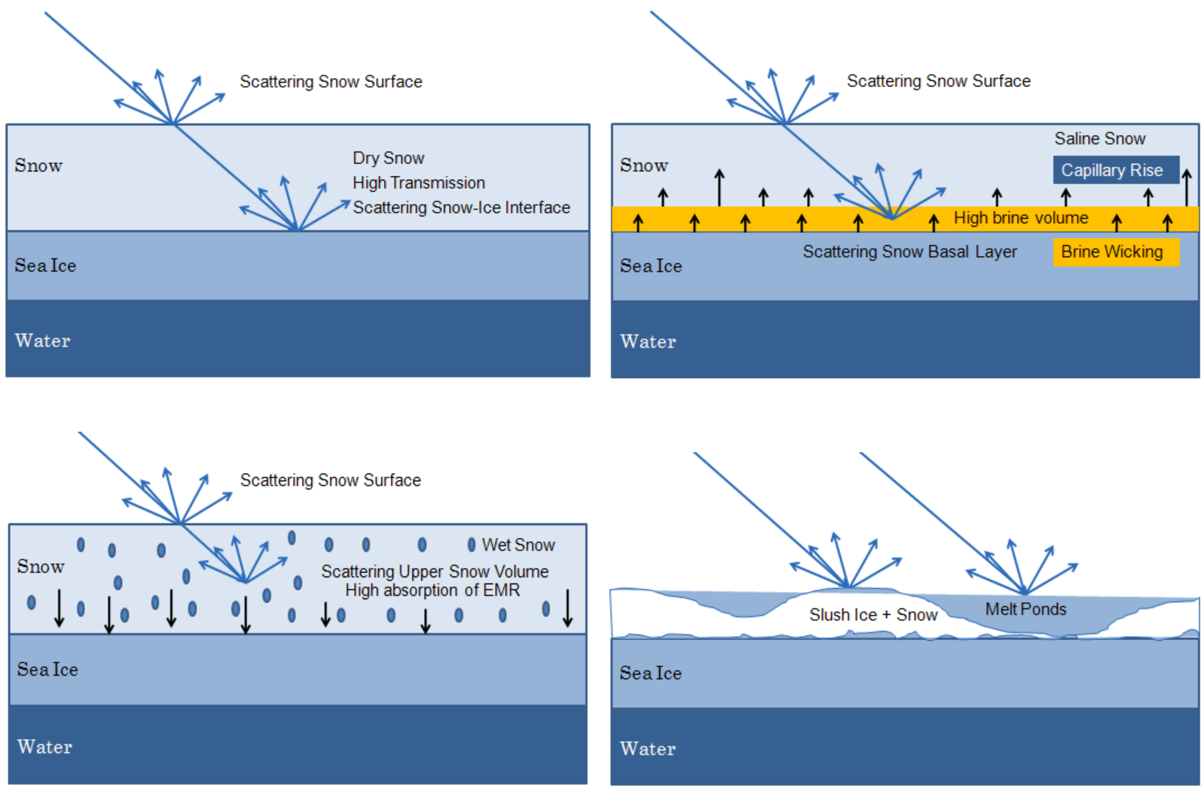

Figure 2.3: Scattering mechanisms operating at different stages of snow covered smooth thick FYI. Top-left figure demonstrates scattering during the winter season and the other three figures (top-right, bottom -left and bottom-right) represent scattering during early-melt, melt-onset and ponding stages, respectively.

CHAPTER THREE:
EVALUATION OF C-BAND SAR POLARIMETRIC PARAMETERS FOR DISCRIMINATION OF FIRST-YEAR SEA ICE TYPES AT COLD ATMOSPHERIC CONDITIONS

3.1 Abstract

In this chapter, polarimetric signatures and the classification potential of polarimetric parameters derived after Cloude-Pottier (1997) decomposition, Touzi (2007) decomposition, Freeman-Durden (1998) decomposition, normalized radar cross section (NRCS) measurements, phase differences and statistical SAR correlation measures is evaluated by relating them to three pre-identified sea ice types and wind roughened open water. A combined approach that constitutes visual inspection of estimated probability densities of the polarimetric parameters and quantitative analysis using supervised classifications (k-means and maximum likelihood) is adopted. Polarimetric parameters are iteratively combined in pairs and triplets to test for their ice type discrimination potential. Sensitivity of polarimetric parameters to radar incidence angle is also examined.

3.2 Introduction

Over the past three decades, multi-frequency multi-polarized synthetic aperture radar (SAR) data have been extensively applied to sea ice classification using a variety of approaches. Some of the successful applications of SAR have focused on (1) classification of ice types (Dierking et al., 2003; Scheuchl et al., 2003a; Nghiem and Bertoia, 2001; Carlström and Ulander, 1995) (2) thin ice-open water discrimination (Geldsetzer and Yackel, 2009; Lundhaug 2002; Mäkynen, 2007); (3) sea ice thickness estimation

(Winebrenner et al., 1995; Nghiem el at., 1997; Shih et al., 1998 and Nakamura et al., 2005); (4) and determination of thermodynamic state of sea ice (Barber and Nghiem, 1999; Yackel and Barber, 1998). Both polarimetric intensity and texture has been exploited for classification purpose. Several techniques, such as neural networks (Karvonen, 2004), image segmentation (Simila et al., 2006), wavelet transformation (Simila and Helminen, 1995), backscatter inversion (Dierking et al., 2003; Scheuchl et al., 2003a, Scheuchl et al., 2005), integration of SAR with ice models (Shih et al., 1998) and lookup tables (Kwok et al., 1992) have been developed and tested to utilize SAR data for sea ice classification.

Although most studies have successfully inverted single and dual co-polarized HH and VV backscatter to retrieve sea ice geophysical information, many others have highlighted the shortcomings of single polarized data (van der Sanden, 2004; Geldsetzer and Yackel, 2009; Yackel and Barber, 2000). Multi and fully polarimetric backscatter has more strongly been related to sea ice characteristics (Dierking and Askne, 1998, Scheuchl et al., 2003b) and has yielded better classification results. With the launch of Radarsat-2 in 200x, the trend has evolved to utilize parameters computed from different forms of fully polarimetric matrix decompositions and synthesis. However, full polarimetric data at present is not used for operational sea ice monitoring due to the small satellite image swaths available with this type of data. Most commonly used polarimetric parameters are derived after Cloude-Pottier (1997) eigenvalue decomposition (Scheuchl et al., 2003b; Scheuchl et al., 2001; Rodrigues et al., 2003; Ferro-Famil et al., 2001) and the Freeman-Durden (1998) three component scattering decomposition (Scheuchl et al., 2002). Many other polarimetric decomposition techniques exist. The result is an increased number of polarimetric parameters have evolved that could be utilized for sea ice classification and must be investigated. Although in most cases the parameters are derived from single algorithm and are used to seed classifications. The inter-algorithm parameter combinations have not been tested. We expect that combining parameters derived from different algorithms may result in better classification as opposed to parameters from a single algorithm.

3.3 Objectives

This chapter investigates polarimetric signatures and evaluates the classification potential of polarimetric parameters derived after Cloude-Pottier (1997) decomposition, Touzi (2007) decomposition, Freeman-Durden (1998) decomposition, normalized radar cross section (NRCS) measurements, phase differences and statistical SAR correlation measures by relating them to three pre-identified sea ice types and wind roughened open water. By conducting the analysis we intend to answer the following questions;

(1) What kind and strength of relationship exists between the polarimetric parameters and the considered sea ice types?

(2) How does the relationship change with radar incidence angle?

(3) Which polarimetric parameters can be combined to produce higher sea ice type classification accuracy?

These research questions are answered using a multi-method approach that constitutes visual inspection of estimated probability densities of the polarimetric parameters and quantitative analysis using supervised classifications (k-means and maximum likelihood), defined in section 3.5. The study area, dataset used, methods and techniques adopted to evaluate the polarimetric parameters are also described in section 3.5. Section 3.6 presents the results on incidence angle dependence of the SAR polarimetric parameters, signature analysis and classifications. Section 3.7 summarizes the salient findings of the study. In the following section we present a list of polarimetric parameters used in this chapter.

3.4 SAR polarimetric parameters

A fully polarimetric SAR (Radarsat-2) produces a complex scattering matrix S for every resolution element in an image by measuring its amplitude and absolute phase.

$$S = \begin{bmatrix} S_{hh} & S_{hv} \\ S_{vh} & S_{vv} \end{bmatrix} \tag{3.1}$$

The polarimetric parameters utilized here are computed from S and are presented below. The derivations and nomenclature generally follow Drinkwater et al. (1992).

- Co-polarized and co-to-cross-polarized ratios

$$R_{hh/vv} = \frac{\langle S_{hh} S_{hh}^{*} \rangle}{\langle S_{vv} S_{vv}^{*} \rangle} \tag{3.2}$$

$$R_{hh/hv} = \frac{\langle S_{hh} S_{hh}^{*} \rangle}{\langle S_{hv} S_{hv}^{*} \rangle} \tag{3.3}$$

- Total power

$$SPAN = \langle S_{hh} S_{hh}^{*} \rangle + \langle S_{vv} S_{vv}^{*} \rangle + 2\langle S_{hv} S_{hv}^{*} \rangle \tag{3.4}$$

- Co-polarized phase difference

$$\phi_{hh-vv} = tan^{-1}\left[\frac{Im\langle S_{hh} S_{vv}^{*} \rangle}{Re\langle S_{hh} S_{vv}^{*} \rangle}\right] \tag{3.5}$$

- Co-polarized correlation coefficient

$$r_{hhvv} = \left| \frac{\langle S_{hh} S_{vv}^* \rangle}{\sqrt{\langle S_{hh} S_{hh}^* \rangle \langle S_{vv} S_{vv}^* \rangle}} \right| \tag{3.6}$$

In the equations above, $\langle \blacksquare \rangle$ denotes the average over number of pixels and $|\blacksquare|$ denotes the modulus of complex number.

The transformation of the scattering matrix elements into Pauli target vector $k_P = \frac{1}{\sqrt{2}}[S_{hh} + S_{vv} \quad S_{hh} - S_{vv} \quad 2S_{hv}]^T$ allows the computation of coherency matrix $T = k_P k_P^{*T}$, where $[\blacksquare]^T$ denotes transpose of matrix and subscript "*" denotes complex conjugate. The eigenvalue decomposition of the T permits the derivation of four parameters i.e. entropy (H), anisotropy (A), alpha angle (α) and beta angle (β) (Cloude and Pottier, 1997). The complete derivation of the eigenvalue decomposition is presented in Cloude - Pottier (1997).

Similar to eigenvalue decomposition, the projection of the scattering matrix onto the Pauli basis using Kennaugh-Huynen con-diagonalization results in scattering vector model that allows the derivation of basis invariant target parameters (Touzi, 2007). The computed five parameters describe the magnitude (α_s) and the phase (ϕ_s) of scattering type and the orientation angle (ψ), helicity (τ_s) and the dominant eigenvalue (λ_s) of the maximum polarization response (Touzi, 2007).

Polarimetric parameters computed after Freeman-Durden (1998) decomposition are based on three component scattering model and yields three parameters that describe the power contributions due to rough surface scattering (P_s), double bounce scattering (P_d) and volume scattering (P_v). The full description of the algorithm is presented in Freeman-Durden (1998).

3.5 Methods and techniques

This study was part of the International Polar Year - Circumpolar Flaw Lead (IPY-CFL) experiment conducted between April and June, 2008.

3.5.1 Study area

The study area comprised of land-fast first year sea ice (FYI) and marginal sea ice located on the east and west coast of Parry Peninsula in Franklin Bay (70°N-125°W). Location of the study area with respect to Canada and the extent of overlap images showing sampling areas of ice types and open water are shown in Figure 3.1.

3.5.2 Data

A total of 9 Radarsat-2 SAR images acquired concomitant to field work were utilized in the study (Table 3.1). All images consisted of fine quad-pol products at spatial resolution ranging between 5.2 and 7.6 meters. The images also vary in incidence angle, with scene centers ranging between 22° and 37°.

Table 3.1. Details of Radarsat-2 images utilized in the study and the meteorological conditions at the time of image acquisition.

Date (yyyy-mm-dd)	Time (UTC)	Scan Direction	Incidence Angle (°)	No of Images	Air Temperature (°C)	Wind Speed (m/sec)	Wind Direction (° from North)
2008-05-04	01:41:16	Asc	35.49 - 37.04	1	- 5.09	10.27	70
2008-05-04	15:18:20	Desc	26.93 - 28.75	3	- 4.09	10.83	69
2008-05-11	01:37:02	Asc	31.38 - 33.05	2	- 2.18	8.61	260
2008-05-14	15:26:42	Desc	22.26 - 24.17	3	- 2.32	16.38	100

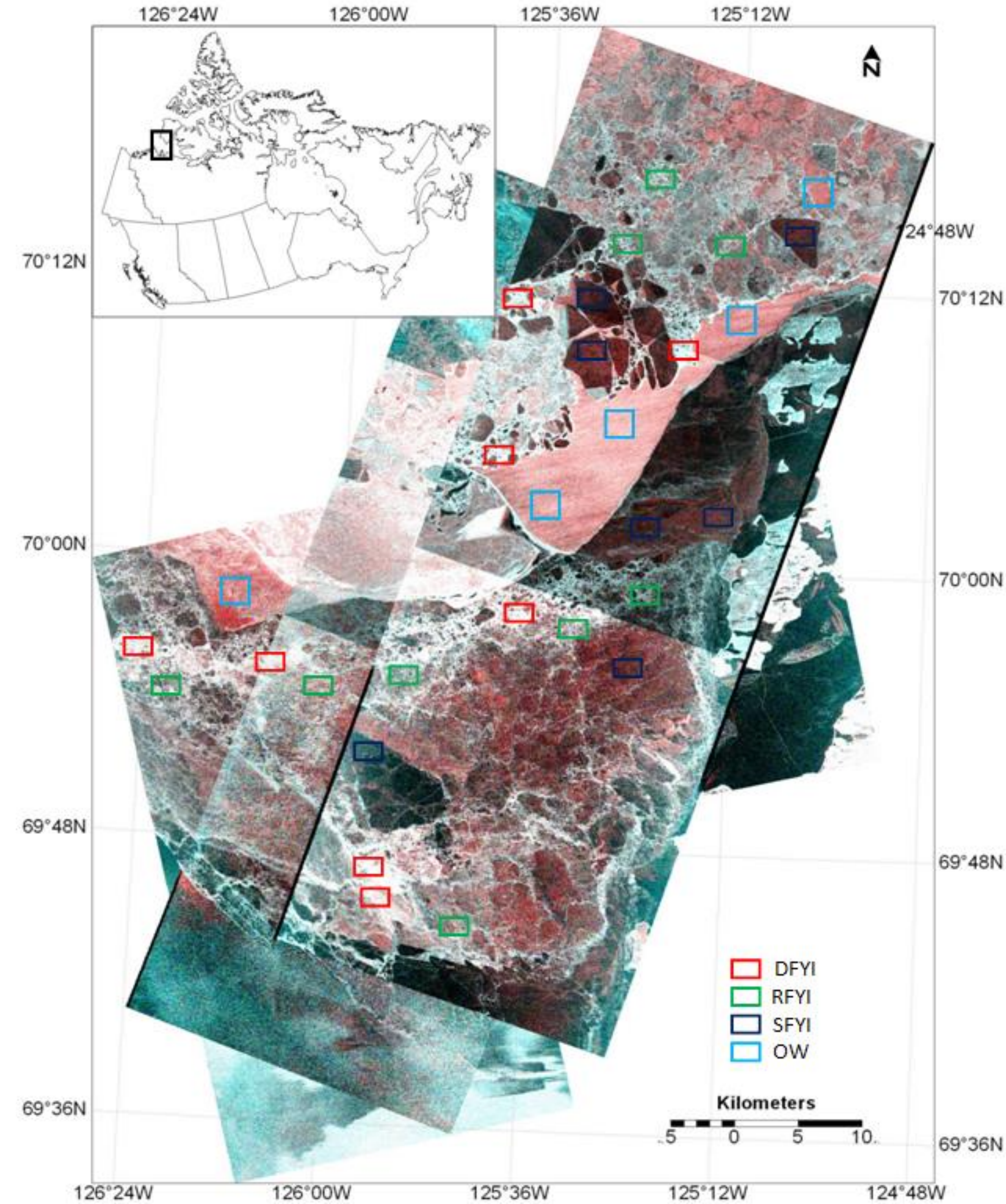

Figure 3.1. Map of Canada (top-left), overlaid with black rectangular box showing the study area (Amundsen Gulf) with respect to Canada. In the zoom is the mosaic of Radarsat-2 images used in the study, overlaid with windows of interest showing sampling areas of different ice types. Color combinations used in the images constitute red ($\boldsymbol{\sigma}^{\mathbf{0}}_{hh}$), blue ($\boldsymbol{\sigma}^{\mathbf{0}}_{hv}$) and green ($\boldsymbol{\sigma}^{\mathbf{0}}_{vh}$).

Ground truth data in the form of GPS coordinates and digital pictures were acquired for numerous ice types using helicopter flights. Three ice roughness classes were identified and characterized by overlaying the ground truth GPS coordinates on the satellite imagery: smooth first year ice (SFYI), rough first year ice (RFYI) and deformed first year ice (DFYI). SFYI was chosen as an ice form with no deformation. Small scale cracks or finger rafting is likely to be present on SFYI. RFYI consisted of a broken uneven surface with protruding ice blocks and floe edges, equivalent to the size of C-band wavelength. DFYI consisted of rubble ice, ridges and boulders with sizes greater than 1 meter. An open water (OW) class with its surface roughened by winds (speed 8.6 to 16.4 m/sec) is also included. For OW, GPS coordinates were not acquired as landing via helicopter was not possible. Therefore, OW was characterized using visual observation and the digital ice charts acquired from Canadian Ice Service.

Meteorological data consisting of daily mean atmospheric temperatures were averaged from 1 minute observations acquired at the meteorological station onboard the CCGS Amundsen. Wind speed, wind direction and precipitation data were acquired from Environment Canada, Paulatuk meteorological station located at 69.35°N, 124.08°W. The daily mean atmospheric temperatures ranged between -8°C to -1°C for the study period (May 4 - May 14, 2008). No significant precipitation events were observed during the period (Figure 3.2).

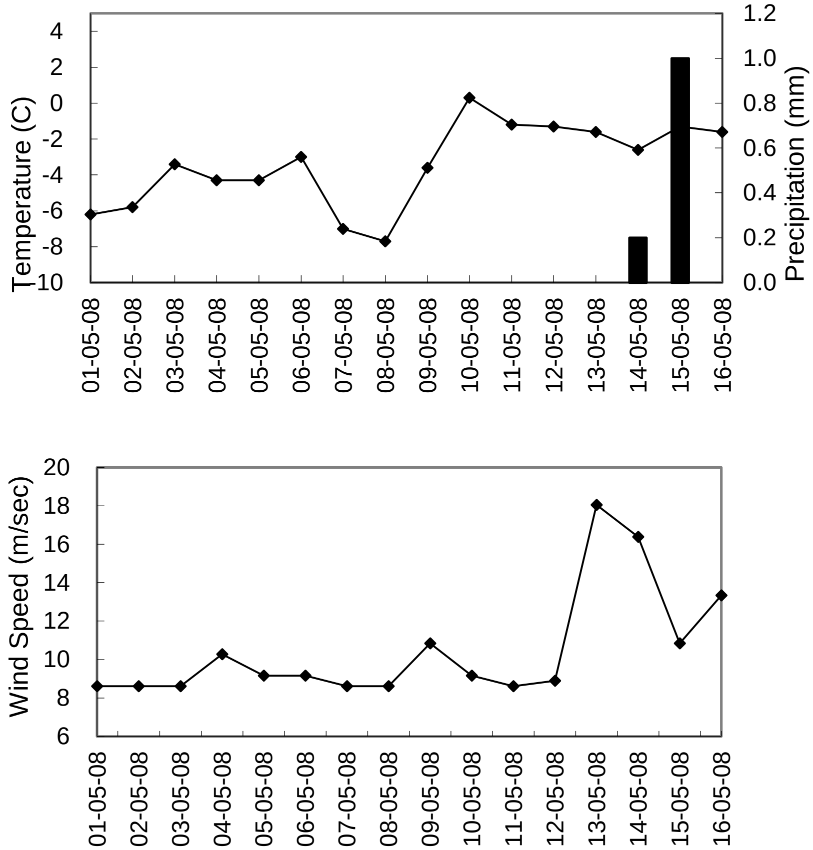

Figure 3.2. Meteorological conditions during the study period (4 May – 14 May, 2008). The top shows the mean diurnal temperature (connected line) and snowfall (solid bars). The bottom figure shows the mean diurnal wind speed in meters/second.

3.5.3 Signature sampling

Areas of interest (windows) for each ice type and open water were digitized on the overlapping images covering the entire study area in such a way that at least one digitized area of interest for every ice type and open water was found in all the images. Hereafter, open water is referred as an ice type in this chapter. Ice type samples were extracted from the delineated areas of interest. However, the same numbers of pixels were not sampled from all the images because of different image extents and ice type feature sizes.

3.5.4 Sea ice classification

Supervised classification was performed on parameters computed from an image acquired on 4 May, 2008 at an incidence angle of 27°. The K-means algorithm was used to produce classifications based on a single parameter and the maximum likelihood classifier (MLC) was used to produce classifications based on combinations of two and three parameters. K-means classifier calculates the mean vector of each training class and determines the Euclidean distance between each unknown pixel and the mean vector of each class (Lillesand and Kiefer, 2000). All pixels are then classified to the closest class. MLC assumes distribution of each class in each channel as Gaussian and then computes a probability density function for each unknown pixel. Each pixel is then assigned to the class associated with the maximum likelihood (Lillesand and Kiefer, 2000). Violation of the assumption of normality or Gaussian model misfit in the MLC can reduce the classification accuracy (Olson et al., 1989). In the current analysis, a preliminary comparison of the results of classifications performed on raw and normalized polarimetric data was made. The data normalized using logarithm and square root transformation did not exhibit any significant improvement over the raw data. All classification results and ice type signatures were computed from original SAR data without normalization performed.

A large number of surface validation points (SVP) for different ice classes, except open water, were collected during the field expedition. The SVPs were divided into two sets i.e. training samples and validation samples (Table 3.2) and subsequently utilized for classification and accuracy assessment. The training and the validation samples could not be split into a consistent and more commonly used ratio of 60-40 or 70-30. This was due to different ice type floe sizes. Confusion matrices were computed to assess the classification accuracy through three statistical parameters, i.e., overall accuracy, producer's accuracy and kappa coefficient. Overall accuracy was obtained by dividing the total number of accurately classified pixels (sum of major diagonal values in confusion matrix) by total number of pixels utilized in the training and validation of the classification process (Congalton, 1991). Producer's accuracy is a measure of the probability of a validation class that is correctly classified as that class. It is also a measure of the omission error and is computed by dividing the correctly classified pixels by the total number of pixels in that class obtained from validation data (i.e. column total) (Congalton, 1991). Kappa coefficient reflects a measure of the difference between actual agreement and chance agreement in the classification (Congalton, 1991). The kappa coefficient or KHAT statistic is computed after Congalton, 1991.

Table 3.2. Training and validation samples used in the classifications and accuracy assessment of polarimetric parameters.

Ice Class	Training Samples		Validation Samples	
	No. of Polygons	No. of Pixels	No. of Polygons	No. of Pixels
SFYI	23	356	15	235
RFYI	14	365	18	287
DFYI	13	320	19	117
OW	16	174	21	224

3.5.5 Parameter evaluation process

Radarsat-2 SAR images were processed to compute polarimetric parameters. Speckle (noise) was reduced using a 7x7 Refined Lee filter as it preserves the edge and point target information and yet suppresses the noise level sufficiently (Foucher and Lopez-Martinez, 2009). Means, standard deviations and probability density functions (PDFs) were computed for all polarimetric parameters and were employed to analyze the sensitivities of parameters to different ice types. PDFs were estimated with the Parzen method (Therrien, 1987) using a Gaussian Kernel function with a standard deviation of one. A window of one standard deviation achieved a good compromise between filtering out small scale fluctuations in the shape of the PDF and preserving large scale details.

$$P(x) = \frac{1}{n}\sum_{i=1}^{n}\frac{1}{\sqrt{2\pi}\sigma}\ exp\left(-\frac{(x_i - x)^2}{2\sigma^2}\right) \tag{3.7}$$

In the equation above, $P(x)$ denotes probability of x, n is the number of smaples, σ is the standard deviation and x_i denotes the sampled values.

Results from qualitative signature analysis and classifications were combined to determine the potential of polarimetric parameters for ice type classification. Parameters that classified any ice type with an accuracy greater than 60% were considered significant. This value was chosen heuristically as a cut-off limit to reduce the number of parameters in the evaluation process as the objective of the analysis was to determine parameters with higher classification accuracies. These parameters were further examined to assess if the information contained was highly correlated (non-complementary) or partially correlated (complementary). If the two parameters possessed similar discrimination properties (same ice classes) they were considered non-complementary, as their combination would not yield more number of classified ice types. Complementary parameters were further combined and utilized in the classification to determine if the group resulted in more classes and higher accuracy. All logical two and three parameter combinations were tested.

3.6 Results and discussion

3.6.1 Polarimetric ice type signatures

C-band polarimetric signatures of different ice types were analyzed at four radar incidence angles ranging from 22° to 37°. The means and standard deviations of polarimetric response are presented in Table 3.3. It must be noted that the images used for incidence angle dependence analysis were acquired over a period of ten days under variable meteorological conditions (Table 3.1). This may affect the ice type signatures due to change in geophysical and dielectric properties. The most prominent effects may be observed for signatures from open water as wind speed and wind direction relative to radar line of sight plays a significant role in defining the SAR backscatter (Fichaux and Ranchin, 2002). In general, higher wind speeds produce large backscatter and lower wind speeds produce low backscatter (Fichaux and Ranchin, 2002). Similarly, crosswind direction (perpendicular to range direction) produces low backscatter and upwind or downwind direction (parallel to range direction) produces higher backscatter (Fichaux and Ranchin, 2002). The polarization of received signal may also be affected due to differences in wind speed and wind direction. For the purpose of accessing the classification potential of polarimetric parameters, PDFs were computed for a single image acquired at an incidence angle (θ_i) of 27° and the results are presented in Figure 3.3 (a-t). Open water signatures observed within this single image represent only one wind speed (10.3 m/sec) and direction (70° from North).

3.6.1.1 Backscattering coefficients (σ^0_{hh}, σ^0_{vv} , σ^0_{hv})

Results show a general increase in mean $\sigma^0_{hh}, \sigma^0_{vv}$ and σ^0_{hv} with increase in surface roughness (Figure 3.3a-c). Smooth first year ice (SFYI) exhibits the lowest mean backscatter at all three polarizations, whereas DFYI and OW exhibit consistently close and high σ^0_{hh} and σ^0_{vv} at all radar incidence angles. The difference in σ^0_{hh} and σ^0_{vv} between DFYI and OW at is < 1dB. This makes the discrimination between the two very difficult for this wind speed (10.3 m/sec) and look direction (70° from north). At σ^0_{hv}, DFYI is easily separated from the OW but signatures of RFYI and OW are mixed. Low mean σ^0_{hh} and σ^0_{vv} in the range of -17 dB to -18 dB for SFYI are close to that reported by Geldsetzer and Yackel, 2009 and Askne and Dierking, 2008. In general $\sigma^0_{hh}, \sigma^0_{vv}$ and σ^0_{hv} for all ice types present a close match to those reported by Geldsetzer and Yackel, 2009 and Mäkynen and Hallikainen, 2004. Results of incidence angle dependence of polarimetric parameters (Table 3.3) show a general decrease in mean $\sigma^0_{hh}, \sigma^0_{vv}$ and σ^0_{hv} for all ice types with increase in θ_i. The decrease is more for SFYI when compared to other classes. The decrease is also more at σ^0_{hh} and σ^0_{vv} than σ^0_{hv}. This is because the θ_i dependence of σ^0 is higher at HH than at VH (Nghiem et al., 1997). A clear discrimination between DFYI and RFYI (difference at σ^0_{hv} $\approx$ 10dB), RFYI and SFYI (difference at σ^0_{hh}, σ^0_{vv} and σ^0_{hv} $\approx$ 5-7dB), SFYI and OW (difference at σ^0_{hh}, σ^0_{vv} and σ^0_{hv} $\approx$ 3-7dB) is observed from the mean σ^0 values (Table 3.3).

Similar results are also visible in the PDFs (Figure 3.3 a-c). It is not possible to discriminate between DFYI and RFYI using σ_{hh}^0 and σ_{vv}^0 and RFYI and OW using σ_{hv}^0.

3.6.1.2 Co-polarization and co-to-cross-polarization ratios ($\boldsymbol{R_{hh/vv}}$, $\boldsymbol{R_{hh/hv}}$)

Mean $R_{hh/vv}$ for all ice types at all incidence angles is within 0 and 1dB except for OW, where it is negative (Table 3.3). The negative mean $R_{hh/vv}$ for OW confirm what was reported by Geldsetzer and Yackel (2009), Drinkwater et al., (1992) and Scheuchl et al., (2001). $R_{hh/vv}$ shows very high variability in space and magnitude for all ice types but not for OW (Figure 3.3d). Low variability of OW is in accordance to that presented by Geldsetzer and Yackel (2009) and Drinkwater et al., (1992). High variability in $R_{hh/vv}$ for ice types hampers its use for unambiguous sea ice classification. However, $R_{hh/vv}$ differentiates OW from all other ice classes (Figure 3.3d).

The results show negative $R_{hh/hv}$ for all ice types. The lowest $R_{hh/hv}$ (between -7 to -23 dB) is observed for DFYI and highest for OW (between -1 to -15dB). DFYI and RFYI experience more multiple surface and volume scattering as compared to SFYI and therefore should have low $R_{hh/hv}$ (Lopez-Martinez et al., 2009). We find similar $R_{hh/hv}$ for RFYI and SFYI. $R_{hh/hv}$ for OW falls within the range exhibited by RFYI and SFYI (between -1 to -15dB) but with a higher mean centered around -7dB. The probable cause is the wind induced roughness. The wind speed was generally high (~11 m/sec on 4 May, 2008) during the time of image acquisition. Based on visual inspection of the PDF (Figure 3.4e) $R_{hh/hv}$ can only separate DFYI and OW to some degree.

3.6.1.3 Total power ($SPAN$)

The $SPAN$ increases with an increase in surface roughness at all radar incidence angles (Table 3.3). The values are lowest for SFYI (between -7 to -20 dB) and highest for OW (between -13 to -2 dB). From the PDF (Figure 3.3f) it is obvious that $SPAN$ is not suitable to discriminate between OW, RFYI and DFYI. However it can separate SFYI from other ice types. $SPAN$ is also sensitive to radar incidence angle and decreases with an increase in θ_i (Table 3.3).

3.6.1.4 Co-polarized phase difference (ϕ_{hh-vv})

The ϕ_{hh-vv} exhibit a slightly decreasing trend with an increase in θ_i. Ideally, single bounce scatterers exhibit ϕ_{hh-vv} of 180° and double bounce scatterers of 0°. Our results show ϕ_{hh-vv} for all ice types between -40° and +30° with means centered close to -3° at all incidence angles. PDFs (Figure 3.3g) demonstrate the incapacity of ϕ_{hh-vv} to discriminate between any ice types.

3.6.1.5 Co-polarized correlation coefficient (r_{hhvv})

The co-polarized correlation coefficient r_{hhvv} is found highest for OW (between 0.93 - 0.97), followed by SFYI and RFYI (between 0.80 - 0.94) and deformed ice (between 0.71 - 0.85). r_{hhvv} is inversely related to θ_i . PDFs of r_{hhvv} (Figure 3.3h) show a significant overlap of RFYI and SFYI, but a clear separation of DFYI and OW.

3.6.1.6 Entropy, anisotropy, alpha angle and beta Angle (H, A, α , β)

Results show high H for DFYI (between 0.38-0.58) followed by RFYI and SFYI (between 0.19-0.52) at θ_i ranging from 23°-37°. OW exhibits lowest H ranging between 0.05-0.20. High H values correspond to random scattering mechanisms and low H values signify single scattering mechanism (Cloude-Pottier, 1997). Observation of the PDFs of H (Figure 3.3i) demonstrates its capability to separate between DFYI and OW. However the signatures of RFYI and SFYI are mixed. H is sensitive to radar incidence angle as it increases with an increase in θ_i . Anisotropy (A) decreases with an increase in θ_i . A is nearly the same for OW and DFYI at all θ_i . PDFs of A (Figure 3.3j) show similar results where OW and DFYI are classified as one class whereas SFYI is clearly separable from other classes. Similar results are exhibited by alpha angle (α). Alpha angle combined with H (if $H \approx 0$) highlights the nature of a dominant scattering mechanism (surface, volume or double bounce) (Cloude-Pottier, 1997). For OW and SFYI, where $H \approx 0$, we observe low α (between 3° and 10°) showing dominance of surface scattering. DFYI exhibit high α (between 7° and 17°) indicating a mixture of surface and volume scattering. RFYI is however mixed with OW and SFYI. Analysis of PDFs of β (Figure 3.3l) demonstrates some potential for discrimination of OW from other ice types.

3.6.1.7 Freeman-Durden components (P_s, P_d, P_v)

Results show lowest contributions due to P_d (between 0 and 0.06) followed by P_v (between 0 and 0.14) and P_s (between 0 and 1) for all ice types. Within the ice classes, the three scattering components P_s, P_d and P_v (surface, double bounce and volume) are found lowest for SFYI (Figure 3.3m-o). P_s demonstrates the capability to separate between SFYI and OW. DFYI observes the highest P_d and P_v and is clearly separable from the other classes whereas its signatures are mixed with RFYI in P_s (Figure 3.3m). From the PDFs of P_v (Figure 3.3o), three separate ice classes are clearly discernable where OW and RFYI are mixed.

3.6.1.8 Touzi's parameters (ψ, ϕ_s, τ_s, α_s, λ_s)

The range of ψ, ϕ_s and τ_s for all ice types is found between -1.5 and 1.38 radians. The values of α_s are positive for all ice types and the λ_s ranges between 0.5 and 1. The PDFs of ψ show nearly similar curve for OW, RFYI and SFYI, with their peaks centered around zero (Figure 3.3p). However the variance is low and the probability is higher for OW. DFYI has a non- Gaussian curve with peak centered at 0.5 radian (Figure 3.3p). From ψ, it is possible to differentiate between OW and DFYI, whereas the other two classes are mixed. Similar PDFs are shown by τ_s with an exception that DFYI is now mixed with RFYI and SFYI (Figure 3.3t). The values of ϕ_s are lowest for OW and nearly similar for all other classes. Only OW can be classified unambiguously using ϕ_s (Figure 3.3s). Similar classification potential is shown by α_s (Figure 3.3r). The PDFs of λ_s demonstrate a clear separation of DFYI, OW and a mixed class of RFYI and SFYI (Figure 3.3q).

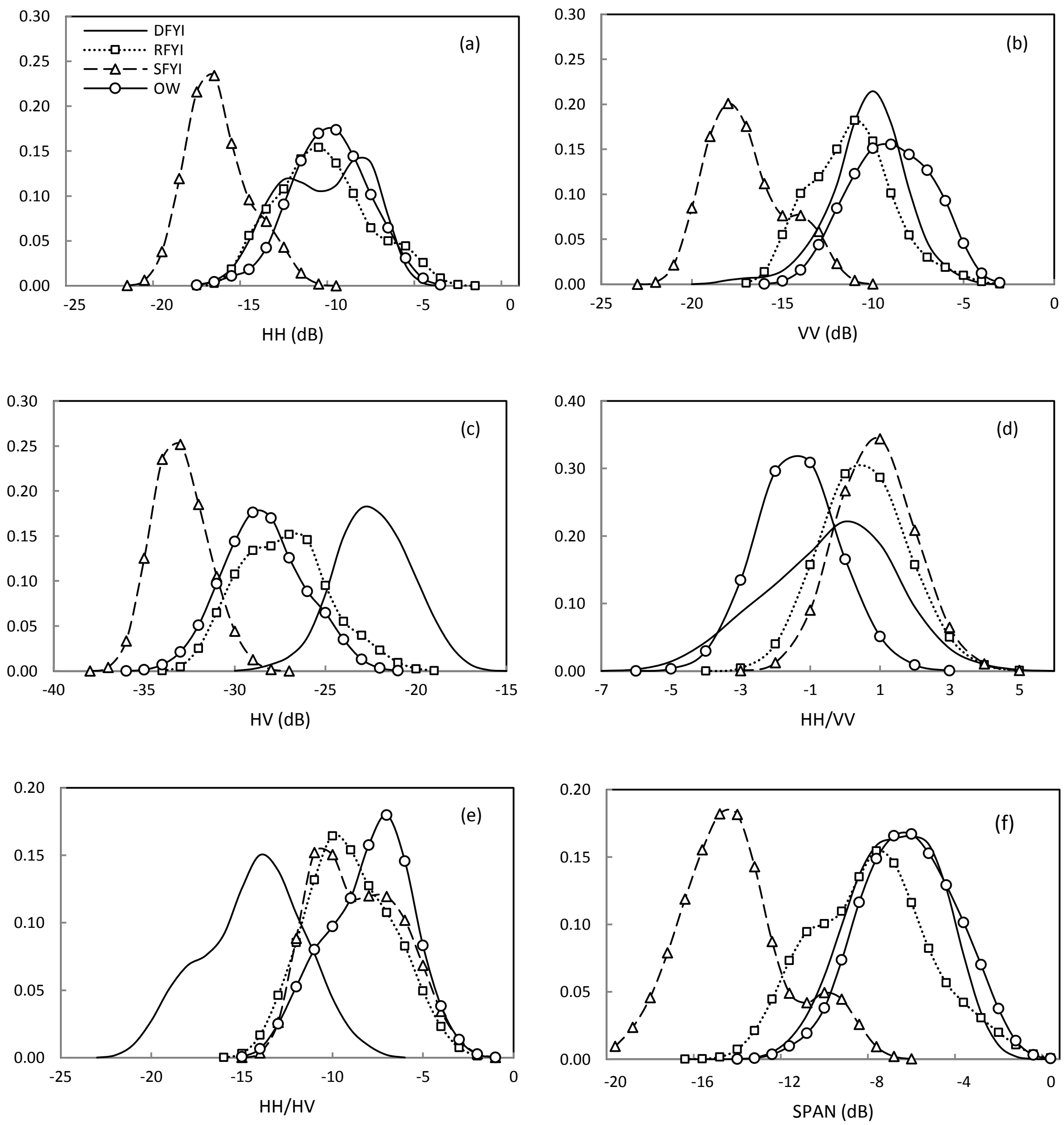

Figure 3.3. Probability density functions of polarimetric parameters computed from Radarsat-2 SAR data acquired on 4 May, 2008 at incidence angle of approx. 27 degrees. DFYI denotes deformed first year ice, RFYI denotes rough first year ice, SYFI denotes smooth first year ice and OW for open water.

(Continued on next page.)

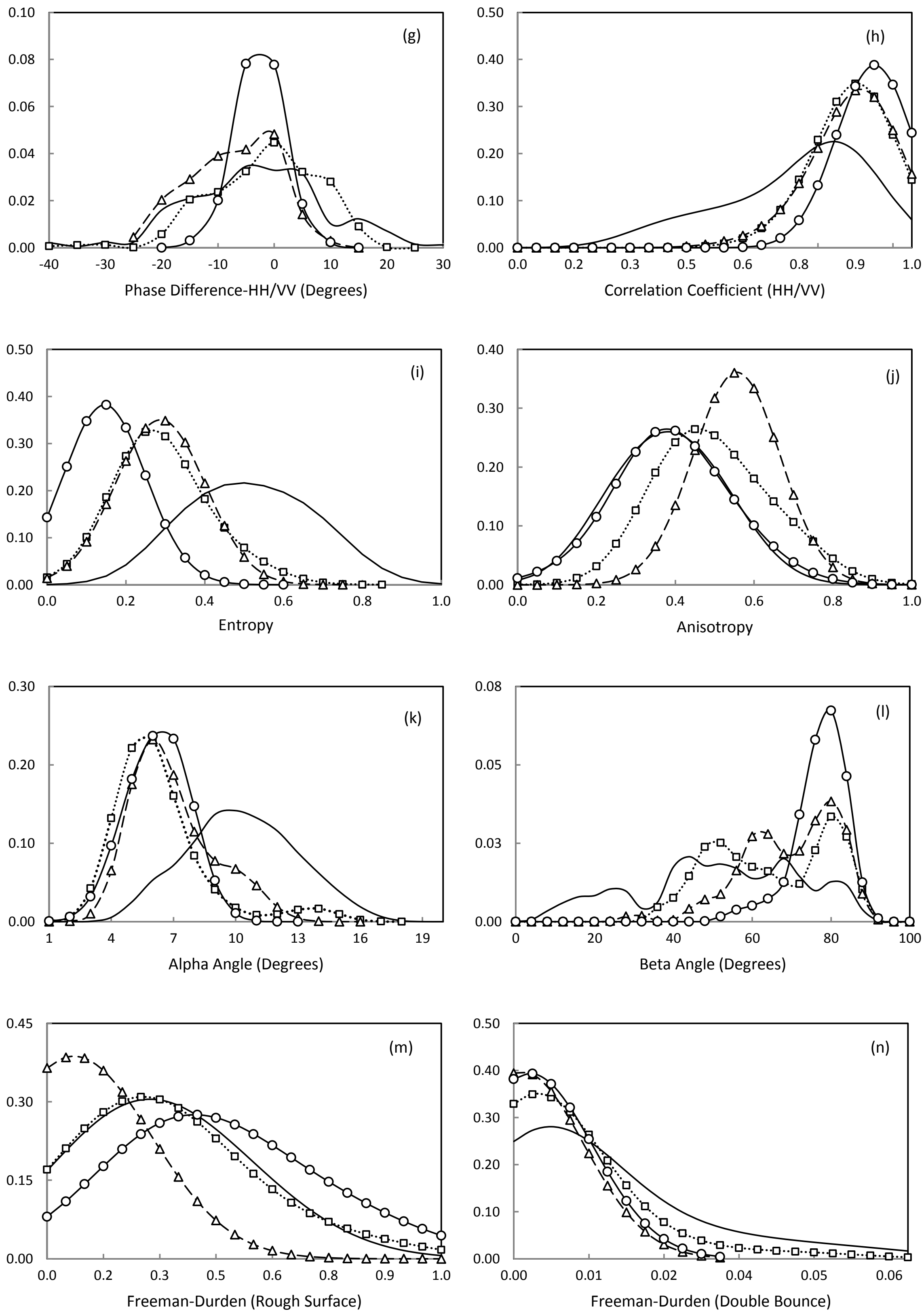
(g)
Phase Difference-HH/VV (Degrees)
(h)
Correlation Coefficient (HH/VV)
(i)
Entropy
(j)
Anisotropy
(k)
Alpha Angle (Degrees)
(l)
Beta Angle (Degrees)
(m)
Freeman-Durden (Rough Surface)
(n)
Freeman-Durden (Double Bounce)

(Continued on next page.)

Figure 3.3 (Concluded.)

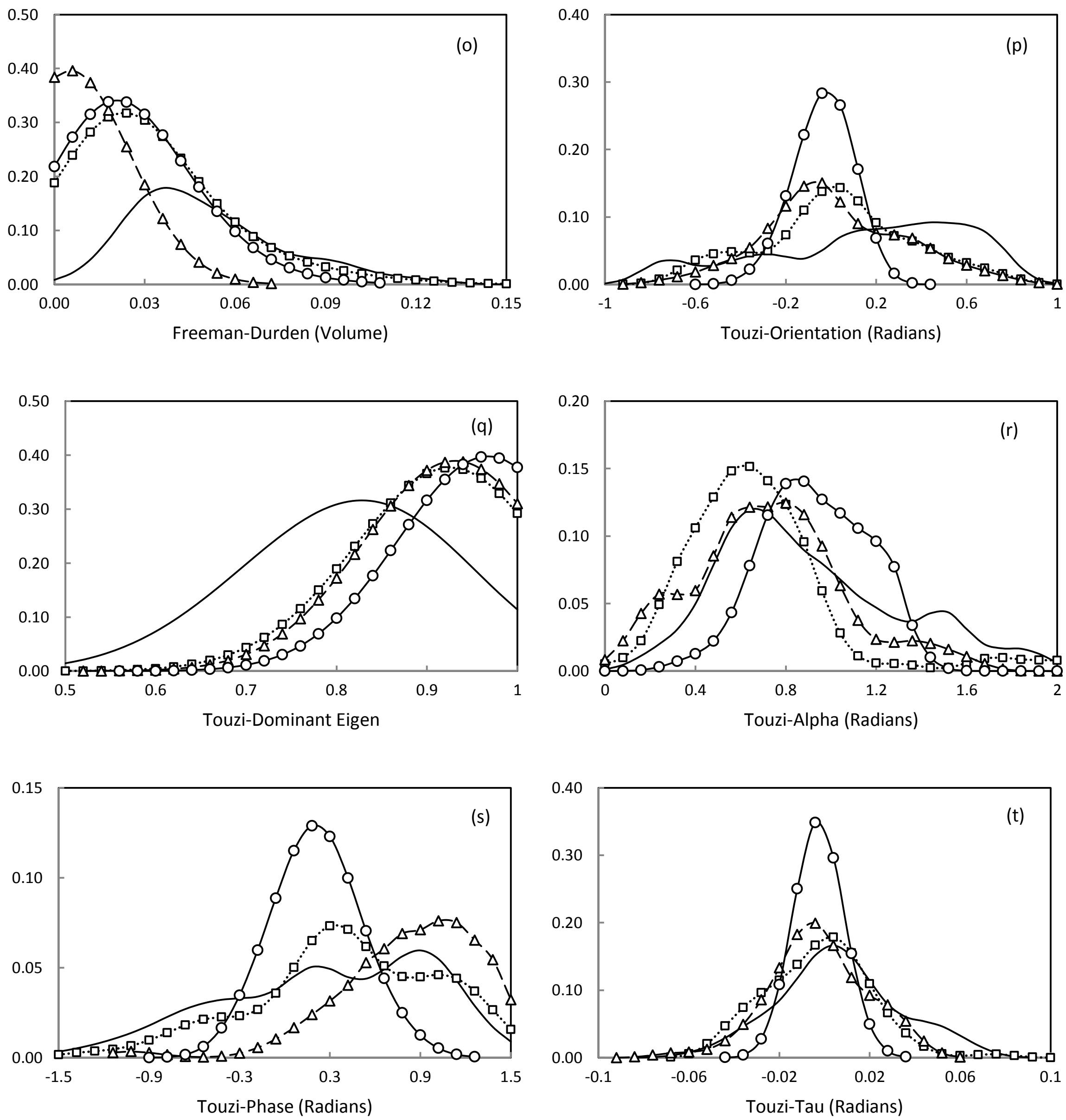

Figure 3.3. Probability density functions of polarimetric parameters computed from Radarsat-2 SAR data acquired on 4 May, 2008 at incidence angle of approx. 27 degrees. DFYI denotes deformed first year ice, RFYI denotes rough first year ice, SYFI denotes smooth first year ice and OW stands for open water.

Table 3.3. Results of polarimetric signatures of ice types at four different radar incidence angles computed from Radarsat-2 SAR data acquired on 4 May, 2008

Parameter	Ice Type	Signatures (Mean and Standard Deviations)							
		22˚- 24˚		26˚-28˚		31˚-33˚		35˚-37˚	
		mean	std.	mean	std.	mean	std.	mean	std.
σ^0_{hh} (dB)	SFYI	-17.61	1.24	-18.12	1.15	-20.45	1.34	-21.74	1.81
	RFYI	-10.69	1.10	-11.86	1.26	-11.73	1.42	-12.23	1.86
	DFYI	-7.93	1.85	-9.30	1.73	-9.66	1.75	-10.12	1.73
	OW	-7.85	1.05	-9.21	1.27	-9.09	0.95	-10.02	1.82
σ^0_{vv} (dB)	SFYI	-17.56	1.47	-18.29	1.02	-20.82	1.23	-21.01	1.87
	RFYI	-10.92	1.68	-11.24	1.75	-12.10	1.17	-12.55	1.84
	DFYI	-7.92	1.11	-9.04	1.56	-10.24	1.69	-10.83	1.59
	OW	-7.96	1.06	-8.94	1.19	-9.44	1.88	-10.01	0.41
σ^0_{hv} (dB)	SFYI	-31.08	1.26	-32.69	1.80	-33.05	1.31	-33.89	0.47
	RFYI	-25.26	1.40	-26.52	2.02	-26.43	1.57	-27.11	0.88
	DFYI	-21.99	1.79	-22.41	1.46	-23.49	1.74	-23.97	0.73
	OW	-27.54	1.30	-27.61	1.87	-29.28	0.93	-30.13	0.49
$R_{hh/vv}$	SFYI	0.86	0.82	0.95	0.92	0.90	0.91	0.99	0.85
	RFYI	0.20	0.94	0.28	0.67	0.30	0.58	0.32	0.18
	DFYI	0.12	0.42	0.16	0.61	0.18	0.17	0.21	0.15
	OW	-0.92	0.41	-1.27	0.60	-1.35	0.60	-1.61	0.63
$R_{hh/hv}$	SFYI	-8.46	1.50	-9.56	1.93	-9.60	1.05	-8.85	1.01
	RFYI	-9.56	1.66	-9.65	1.83	-8.70	1.88	-9.87	0.87
	DFYI	-14.07	1.96	-15.11	1.75	-13.82	2.90	-15.44	1.00
	OW	-6.69	1.92	-6.40	1.26	-7.37	2.23	-6.30	1.15
$SPAN$ (dB)	SFYI	-11.5	1.04	-12.2	1.02	-15.2	1.11	-17.0	1.21
	RFYI	-7.21	1.08	-7.96	1.07	-8.24	1.13	-8.54	1.01
	DFYI	-6.99	1.26	-7.21	1.13	-7.21	1.09	-7.45	1.12

	OW	-6.99	1.27	-7.21	1.11	-7.45	1.14	-7.70	1.08
ϕ_{hh-vv}	SFYI	-6.33	2.76	-7.45	2.55	-7.48	2.71	-8.15	2.81
	RFYI	-2.14	2.66	-2.55	2.44	-3.67	2.01	-3.12	2.58
	DFYI	-4.81	2.85	-6.11	2.41	-6.14	2.21	-7.05	2.10
	OW	-0.97	2.79	-2.59	2.12	-3.62	2.25	-4.38	2.52
r_{hhvv}	SFYI	0.93	0.03	0.93	0.03	0.92	0.04	0.89	0.02
	RFYI	0.91	0.07	0.92	0.05	0.91	0.08	0.89	0.02
	DFYI	0.84	0.07	0.83	0.09	0.80	0.09	0.79	0.07
	OW	0.98	0.01	0.97	0.02	0.97	0.01	0.96	0.01
H	SFYI	0.32	0.07	0.34	0.04	0.35	0.04	0.36	0.03
	RFYI	0.34	0.09	0.35	0.05	0.36	0.07	0.38	0.03
	DFYI	0.49	0.06	0.51	0.05	0.54	0.09	0.55	0.07
	OW	0.13	0.01	0.14	0.02	0.15	0.01	0.16	0.02
A	SFYI	0.62	0.13	0.62	0.07	0.58	0.09	0.54	0.10
	RFYI	0.46	0.07	0.45	0.14	0.43	0.06	0.42	0.15
	DFYI	0.39	0.10	0.38	0.13	0.37	0.08	0.36	0.18
	OW	0.39	0.09	0.39	0.13	0.38	0.09	0.37	0.13
α	SFYI	6.79	1.67	7.11	1.41	8.66	1.25	09.07	1.19
	RFYI	7.74	1.80	8.79	1.32	9.09	1.13	10.92	1.20
	DFYI	10.5	1.39	11.9	1.37	11.9	1.38	12.65	1.04
	OW	7.36	0.61	8.07	0.95	9.07	0.96	09.68	1.29
β	SFYI	72.27	9.61	70.12	6.22	73.67	7.51	74.12	6.11
	RFYI	71.48	6.35	68.66	5.61	64.02	5.04	66.34	5.25
	DFYI	50.04	8.45	50.30	4.41	49.60	4.89	51.22	5.01
	OW	81.89	1.07	79.40	1.55	76.32	1.25	78.56	1.45
P_s	SFYI	0.08	0.04	0.09	0.04	0.08	0.01	0.08	0.02
	RFYI	0.31	0.08	0.31	0.03	0.31	0.03	0.31	0.01
	DFYI	0.31	0.07	0.30	0.09	0.32	0.03	0.31	0.02
	OW	0.49	0.17	0.49	0.15	0.50	0.14	0.49	0.14
P_d	SFYI	0.006	0.001	0.005	0.001	0.005	0.001	0.004	0.001
	RFYI	0.008	0.003	0.009	0.001	0.008	0.003	0.007	0.003
	DFYI	0.010	0.006	0.011	0.009	0.012	0.005	0.011	0.004

	OW	0.004	0.001	0.004	0.003	0.005	0.001	0.005	0.001
P_v	SFYI	0.002	0.004	0.001	0.001	0.003	0.001	0.002	0.0001
	RFYI	0.028	0.015	0.027	0.020	0.028	0.010	0.029	0.011
	DFYI	0.049	0.022	0.051	0.021	0.054	0.011	0.052	0.012
	OW	0.023	0.001	0.024	0.005	0.024	0.001	0.024	0.001
ψ	SFYI	-0.027	0.10	-0.051	0.13	-0.015	0.12	-0.046	0.11
	RFYI	-0.004	0.13	-0.008	0.14	-0.006	0.13	-0.004	0.12
	DFYI	0.23	0.26	0.20	0.24	0.25	0.26	0.23	0.21
	OW	-0.034	0.04	-0.035	0.03	-0.021	0.02	-0.032	0.03
ϕ_s	SFYI	1.26	0.65	1.28	0.30	1.21	0.30	1.22	0.29
	RFYI	0.41	0.61	0.43	0.65	0.42	0.48	0.43	0.39
	DFYI	0.44	0.74	0.47	0.61	0.46	0.44	0.46	0.40
	OW	0.16	0.24	0.12	0.20	0.14	0.20	0.13	0.18
τ_s	SFYI	0.001	0.015	0.004	0.013	0.002	0.031	0.003	0.002
	RFYI	0.006	0.017	0.006	0.021	0.005	0.050	0.004	0.004
	DFYI	0.013	0.021	0.014	0.031	0.012	0.017	0.013	0.015
	OW	-0.002	0.003	-0.002	0.006	-0.004	0.005	-0.003	0.003
α_s	SFYI	0.67	0.03	0.68	0.05	0.67	0.02	0.68	0.03
	RFYI	0.61	0.03	0.60	0.03	0.62	0.04	0.63	0.04
	DFYI	0.76	0.02	0.75	0.02	0.76	0.04	0.75	0.03
	OW	0.96	0.01	0.98	0.01	0.97	0.02	0.96	0.02
λ_s	SFYI	0.92	0.02	0.91	0.01	0.92	0.01	9.91	0.02
	RFYI	0.88	0.03	0.89	0.02	0.88	0.03	0.88	0.03
	DFYI	0.81	0.02	0.80	0.02	0.81	0.04	0.82	0.02
	OW	0.99	0.03	0.97	0.06	0.97	0.04	0.98	0.04

3.6.2 Single polarimetric parameter ice type classifications

Single parameter supervised k-means classification is performed on 4 May, 2008 image acquired at an incidence angle of 27°. The classification accuracies of all individual parameters for all ice types are summarized in Table 3.4. The highest, single parameter overall classification accuracy is shown by P_v (73.74%) followed by σ^0_{hv} (68.56%), H (66.43%) λ_s (65.75%) and σ^0_{vv} (63.24%). Minimum overall classification accuracy is demonstrated by r_{hhhv} (22.14%) and ϕ_{hh-hv} (22.14%). It is noticeable, from Table 3.4, that none of the single parameters are able to classify all four individual ice types with accuracy greater than 60%. However, the classification accuracies of individual ice types show that most of the parameters can discriminate at least one ice class with accuracy greater than 60%, except $R_{hh/hv}$, A and τ_s. Thus, classification accuracies of individual ice types are of interest here, which complement the results from the PDF plots (Figure 3.3 a-t). From Table 3.4, it is observed that OW (at wind speed 10.3 m/sec) can significantly (accuracy >60%) be separated by twelve parameters whereas SFYI by nine parameters, DFYI by six parameters and RFYI can only be separated by two parameters. Further investigation of Table 3.4 indicates that only four parameters (σ^0_{hv}, H, P_v and λ_s) possess the capability to discriminate three classes significantly and only four parameters (σ^0_{hh}, σ^0_{vv}, P_s and P_d) can separate two classes each. The remaining parameters possess the capability to separate only one class. Therefore, parameters possessing different discrimination properties (different ice types) may be combined to achieve better classification results.

Table 3.4. Classification accuracies of single polarimetric parameters derived from k-means classification. Significant classification accuracies (>60%) are highlighted in bold.

Polarimetric Parameter	Ice Type Classification Accuracy (%)				Overall Accuracy (%)	Kappa Coefficient
	OW	SFYI	RFYI	DFYI		
σ_{hh}^{0}	**60.66**	**85.73**	36.51	20.65	52.28	0.35
σ_{vv}^{0}	**72.95**	**86.32**	40.70	46.02	**63.24**	0.50
σ_{hv}^{0}	36.89	**93.87**	**61.14**	**91.92**	**71.00**	0.61
$R_{hh/vv}$	**93.44**	41.88	16.28	13.27	43.83	0.24
$R_{hh/hv}$	56.56	29.91	33.72	48.67	42.92	0.24
$SPAN$	46.72	**92.31**	59.30	35.40	58.44	0.44
ϕ_{hh-vv}	**77.87**	08.55	17.44	09.73	29.90	0.05
r_{hhvv}	**88.52**	33.33	11.63	51.33	49.08	0.31
H	**89.34**	**63.25**	39.53	**65.49**	**66.43**	0.54
A	31.97	58.97	17.44	24.78	34.47	0.11
α	33.61	31.62	17.44	61.95	37.21	0.15
β	**69.67**	19.66	24.42	39.82	39.72	0.19
P_s	**63.93**	**88.89**	33.72	41.59	58.90	0.44
P_d	27.05	**90.60**	08.14	**66.37**	50.45	0.33
P_v	49.34	**90.00**	**62.79**	**92.04**	**73.74**	0.65
ψ	**60.66**	00.85	02.33	51.33	30.82	0.06
ϕ_s	**92.62**	11.11	18.60	14.16	36.07	0.14
τ_s	53.10	31.88	10.00	24.59	31.73	0.07
α_s	16.56	01.71	**65.58**	51.33	30.36	0.09
λ_s	**91.80**	**61.54**	36.05	**64.60**	**65.75**	0.54

3.6.3 *Ice type classification of two-parameter combinations*

Complimentary parameters derived from single parameter classification results are combined. A total of twenty-one paired combinations are produced. Parameter σ_{hv}^{0} possesses the capability to successfully discriminate between three ice types (SFYI, DFYI and RFYI) but fails to separate OW from RFYI. This is evident in the PDF plot (Figure 3.3c) and classification results (Table 3.4). A perfect combination of σ_{hv}^{0} would be the parameter that successfully separates OW from other ice types. We observe twelve parameters (Table 3.4) that are potential candidates and could result in classification of all ice types. Their combinations with σ_{hv}^{0} are tested here. A similar approach is followed to achieve all possible two-parameter combinations. MLC supervised classification is performed using pairs of complimentary parameters. Results in the form of producer's accuracy for all individual classes are presented in Table 3.4 along with overall accuracy and kappa coefficient. Two-dimensional feature spaces for all combinations are also examined and presented (Figure 3.4a-g). A 90% confidence ellipse is overlaid on all plots to show separation space.

3.6.3.1 *Combinations of $\boldsymbol{\sigma_{hv}^{0}}$*

The overall classification accuracy of single parameter σ_{hv}^{0} increases from 71% to 86.52%, 87.89%, 81.05%, 87.89% and 78.99% when combined with $R_{hh/vv}$, H, r_{hhvv}, λ_s and ϕ_s, respectively (Table 3.5). An improvement of 7%-17% is observed if complementary parameters are combined. The deficiency of σ_{hv}^{0} to separate OW from other classes has dramatically improved from 36.89% to 76.23% - 92.62%. In addition to improvement in discrimination of OW, an increase in classification accuracy for other ice classes except RFYI is also observed (Table 3.5). This is clearly visible from the two-dimensional scatter plots of σ_{hv}^0 and its combination parameters (Figure 3.4a-e). RFYI is usually mixed with OW and SFYI.

3.6.3.2 Combinations of H

Individually, H produces an overall classification accuracy of 66.43% (Table 3.4), possessing the capability to discriminate three ice classes (SFYI, DFYI and OW). RFYI cannot be discriminated using H. Therefore, H must be combined with a parameter that significantly separates RFYI from all other classes. Also, the classification accuracy of H for SFYI is lower than most other parameters (Table 3.4). Combining parameters that have higher classification accuracy for SFYI is also expected to increase the classification results. From Table 3.4 and Figure 3.3a-t, only σ_{hv}^0, α_s and P_v possess the capability to discriminate RFYI, significantly. Also, $SPAN$ can discriminate SFYI (92.31%) and RFYI (59.30%) to a greater extent. Four combinations (H-$SPAN$, H-P_v, H-P_s and H-σ_{hv}^0) are tested. The parameter combinations H-$SPAN$, H-P_v, H-P_s and H-σ_{hv}^0 increase the overall classification accuracy of H by approximately 18% to 21%. The lowest class accuracy is achieved for RFYI with maximum reaching 65.12% using a combination of H and σ_{hv}^0 .

3.6.3.3 Combinations of P_v and λ_s

Freeman-Durden's P_v component is highly correlated to σ_{hv}^0 and possesses similar classification properties to that of σ_{hv}^0 (Table 3.4). Similarly, Touzi's λ_s parameter is also highly correlated to Cloude-Pottier's H and has the same classification properties (Table 3.4). Therefore all possible parameter combinations achieved with σ_{hv}^0 are applied to P_v and all parameter combinations of H are applied to λ_s. The results of classifications are presented in Table 3.5. The ambiguities related to discrimination of RFYI remain persistent.

3.6.3.4 Combinations of $\boldsymbol{\sigma_{vv}^0}$

Single parameter σ_{vv}^0 possesses the capability to separate only two ice classes (OW and SFYI) but fails to discriminate RFYI and DFYI. Its complimentary parameters (σ_{hv}^0, H, α, P_d, P_v and λ_s can significantly separate RFYI and DFYI. This results in a total of five paired combinations of σ_{vv}^0. The paired classification accuracies are found to increase by 12-25%. The second highest classification accuracy among the two parameter combinations is achieved at 88.35% using σ_{vv}^0-H.

Results from the scatter plots (Figure 3.4) and two parameter classifications (Table 3.5) show that most parameter combinations discriminate between all ice types with an overall accuracy greater than 75%. The two highest classification accuracies are achieved using the combinations of H-P_v and σ_{vv}^0-H. The lowest class accuracy was found for RFYI in all the parameter combinations. This indicates that rough ice is the most difficult ice type to classify in the current scenario. This could be attributed to the fact that RFYI is essentially a spatially arranged random mixture of upturned ice fragments situated within a background of SFYI, both of which have varying proportions for all samples collected in this study.

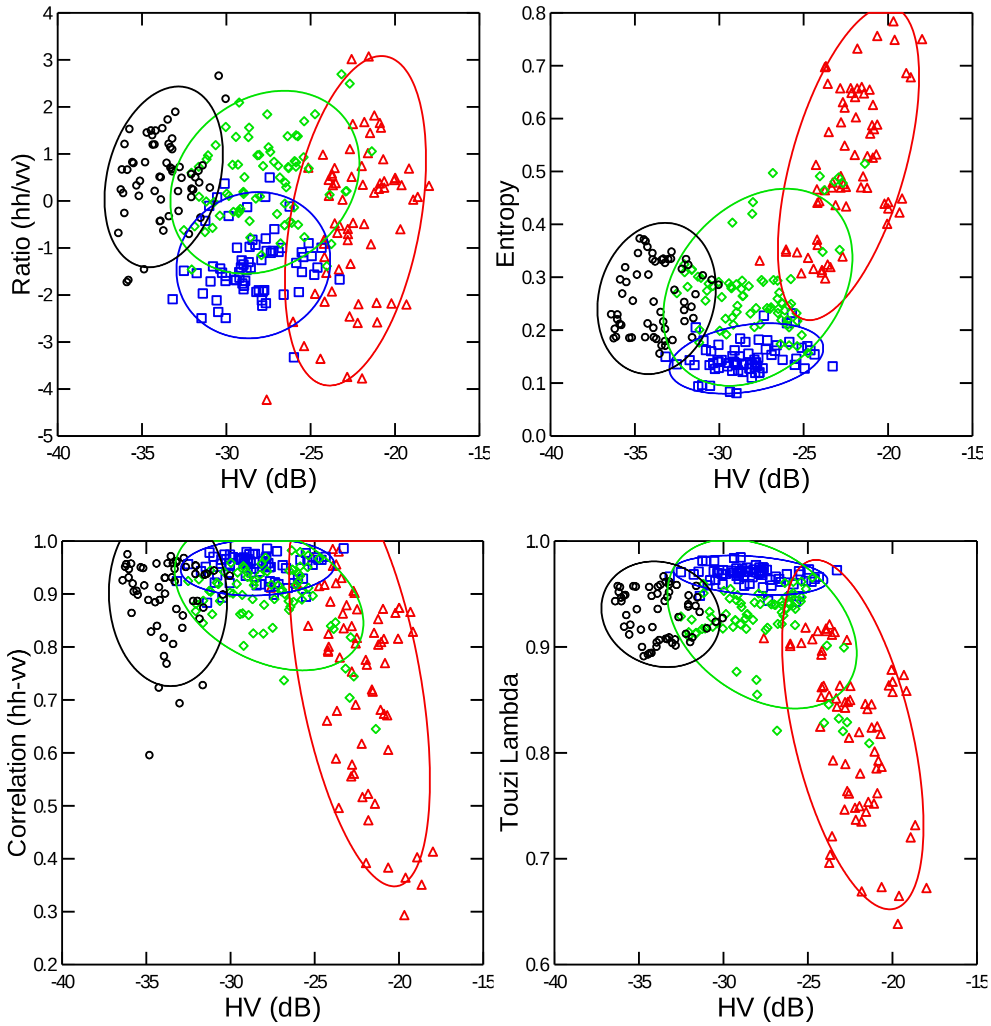

Figure 3.4. Two-dimensional scatter plots of paired polarimetric parameters overlaid with 90% confidence ellipse. Signatures in triangles (red) represent DFYI, squares (blue) represent OW, diamonds (green) and circles (black) represent RFYI and SFYI, respectively. The notation FD denotes Freeman-Durden.

(Continued on next page.)

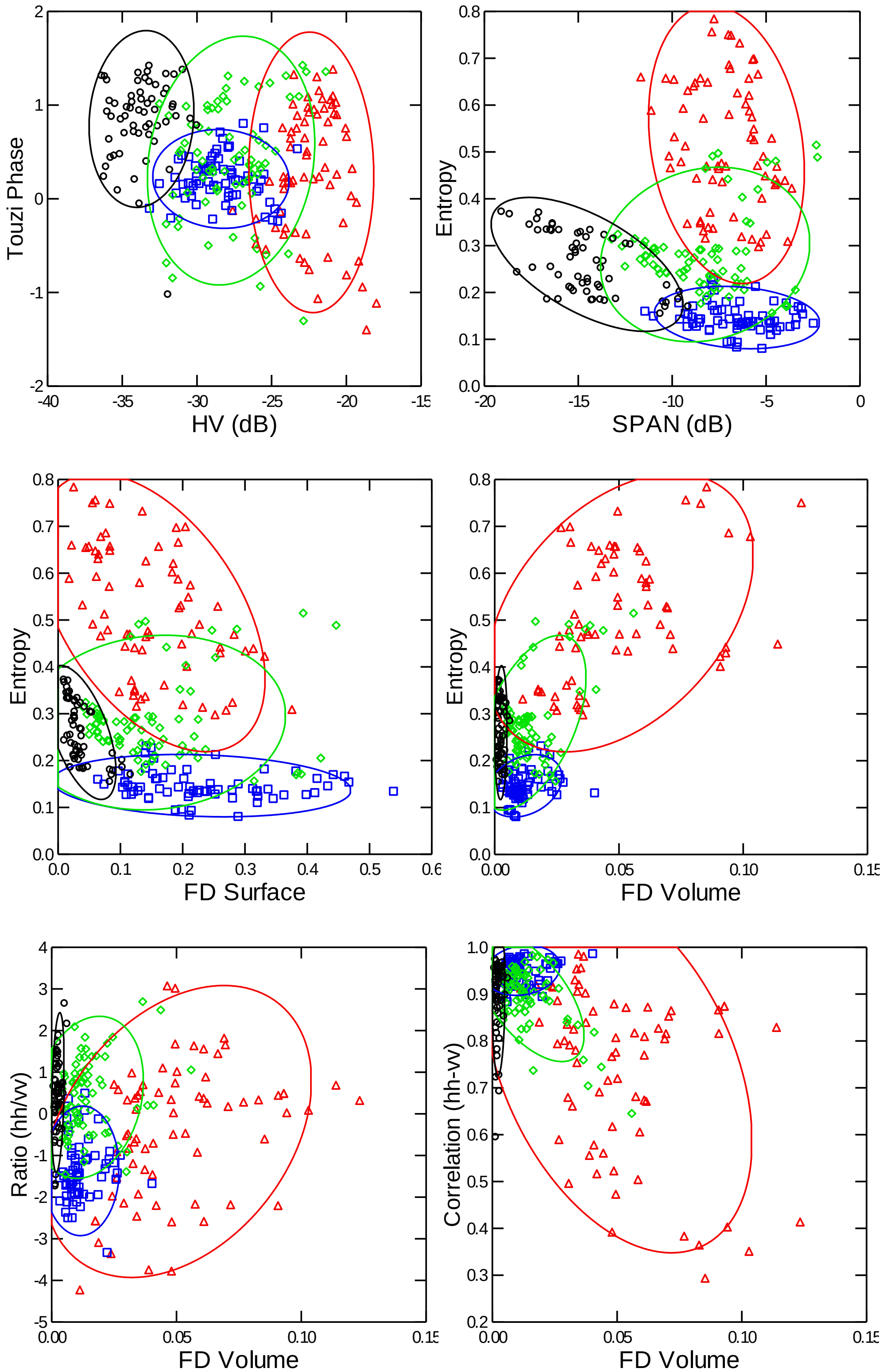

(Continued on next page.)

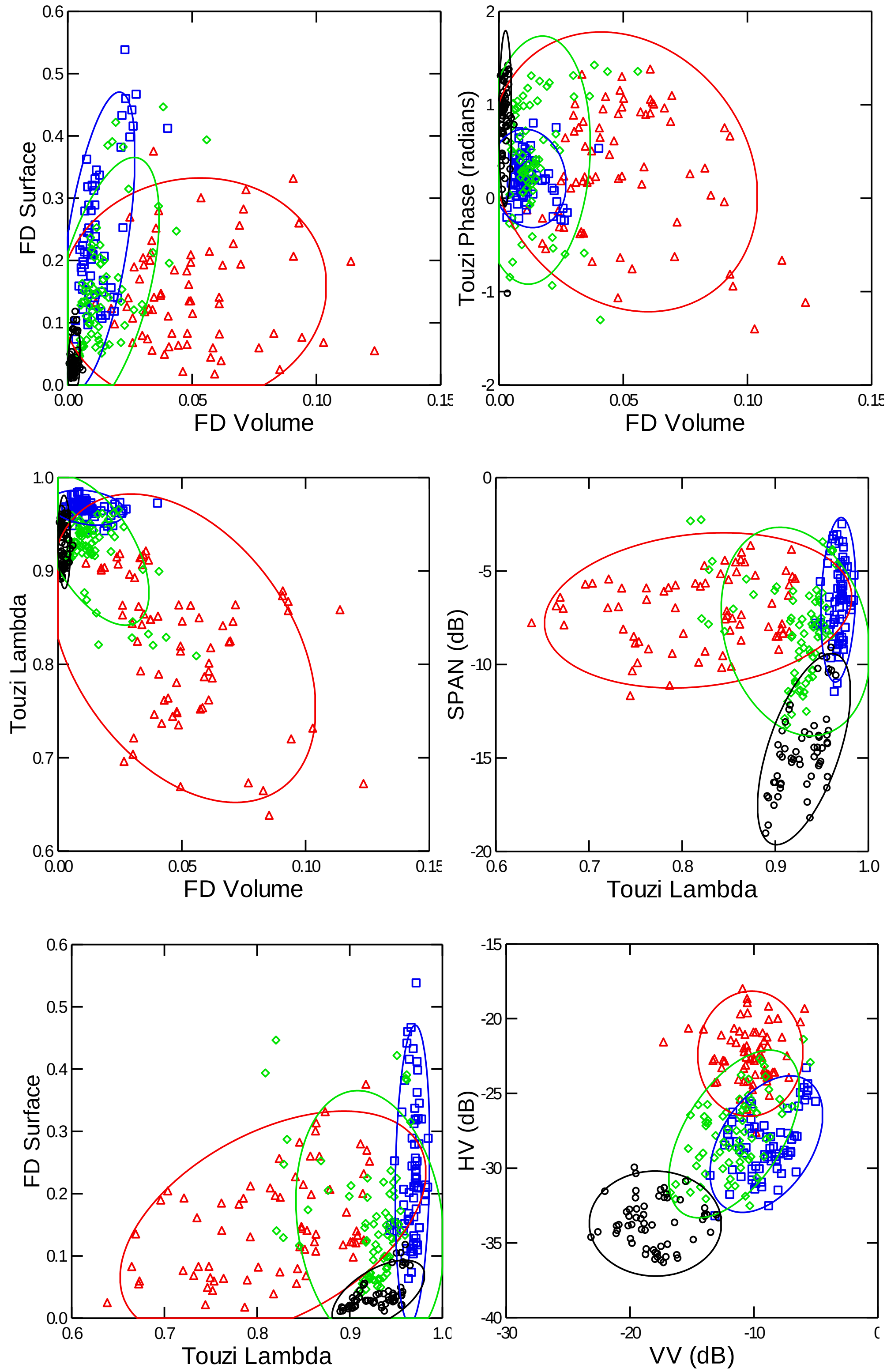

(Continued on next page.)

Figure 3.4 (Concluded.)

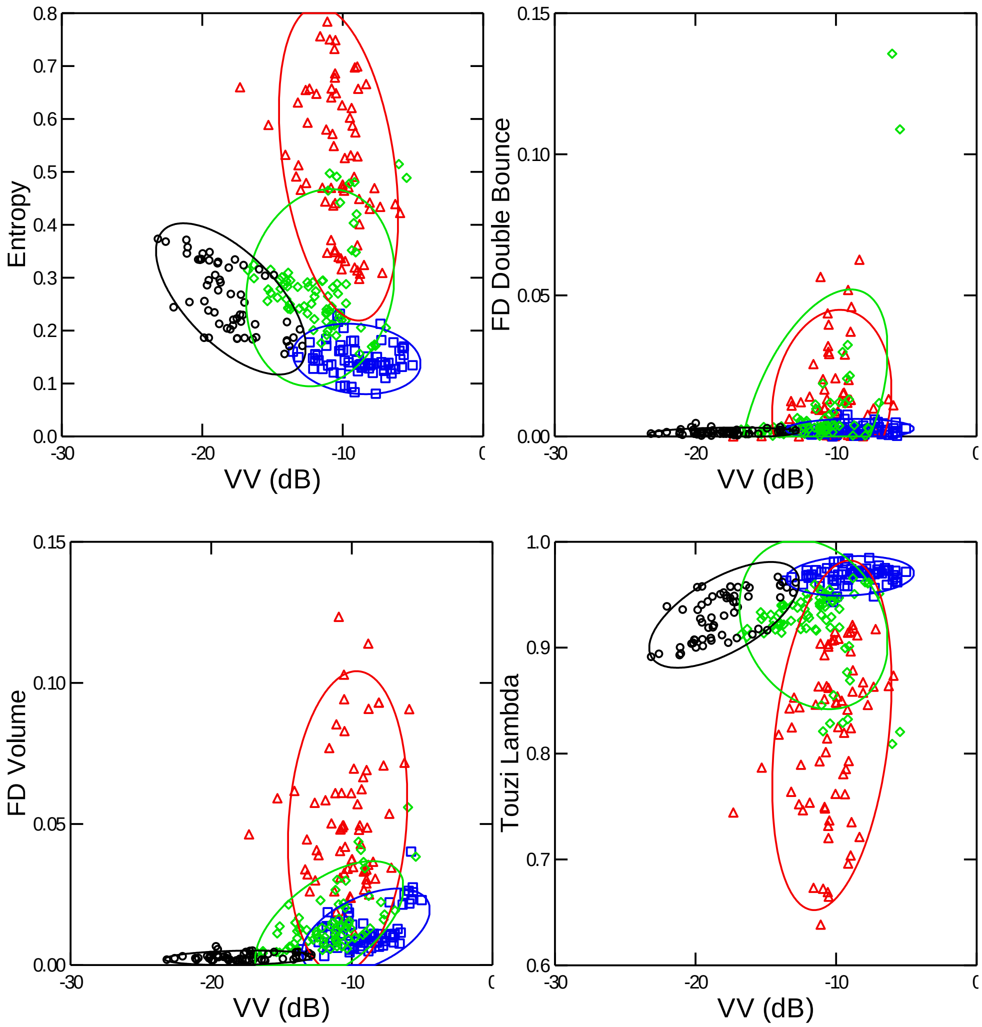

Figure 3.4. Two-dimensional scatter plots of paired polarimetric parameters overlaid with 90% confidence ellipse. Signatures in triangles (red) represent DFYI, squares (blue) represent OW, diamonds (green) and circles (black) represent RFYI and SFYI, respectively. The notation FD denotes Freeman-Durden.

Table 3.5. Classification accuracies of polarimetric parameters derived from Maximum Likelihood classifications of two parameter combinations.

Polarimetric Parameter	Ice Type Classification Accuracy (%)				Overall Accuracy (%)	Kappa Coeff.
	OW	SFYI	RFYI	DFYI		
σ_{hv}^{0}-$R_{hh/vv}$	90.16	94.87	59.30	94.69	86.52	0.81
σ_{hv}^{0}-H	92.62	94.02	65.12	93.81	87.89	0.83
σ_{hv}^{0}-r_{hhvv}	89.34	93.16	36.05	93.81	81.05	0.74
σ_{hv}^{0}-λ_s	92.62	94.02	65.12	93.81	87.89	0.83
σ_{hv}^{0}-ϕ_s	76.23	94.87	40.70	94.69	78.99	0.71
σ_{hv}^{0}-P_v	45.90	97.44	44.19	95.58	72.14	0.62
H -$SPAN$	92.62	97.44	56.98	93.81	87.21	0.82
H- P_s	90.98	94.87	53.49	88.50	84.01	0.78
H-P_v	95.08	94.02	63.95	95.58	88.81	0.84
P_v-$R_{hh/vv}$	81.97	98.29	55.81	95.58	84.70	0.79
P_v-r_{hhvv}	89.34	97.44	36.05	96.46	82.87	0.76
P_v-P_s	75.41	97.44	54.65	95.58	82.42	0.76
P_v-ϕ_s	73.77	95.73	24.42	96.46	75.79	0.67
P_v-λ_s	95.08	94.02	60.47	95.58	88.12	0.84
λ_s-$SPAN$	91.80	97.44	54.65	93.81	86.52	0.81
λ_s-P_s	91.80	94.02	50.00	89.38	83.56	0.77
σ_{vv}^{0}-σ_{hv}^{0}	92.62	94.02	58.14	93.81	86.52	0.81
σ_{vv}^{0}- H	95.90	98.29	65.12	87.61	88.35	0.84
σ_{vv}^{0}-P_d	89.34	89.74	53.49	61.95	75.34	0.66
σ_{vv}^{0}-P_v	90.98	96.58	51.16	96.46	86.07	0.81
σ_{vv}^{0}-λ_s	96.72	97.44	62.79	87.61	87.89	0.83

3.6.4 Ice type classification of three-parameter combinations

RFYI was most poorly classified class using the two-parameter combinations. In order to better classify RFYI, triplets of parameters were tested. Table 3.4 shows that only three (σ^0_{hv}, P_v and α_s) parameters can successfully discriminate RFYI from other classes. These parameters were alternatively combined with all two parameter combinations (from Table 3.4) in the classification process. The results are presented in Table 3.6. Interestingly, three-parameter combinations resulted in both a decrease and increase in classification accuracies. However, the best four classification accuracies were achieved using the three-parameter combinations of σ^0_{vv}- H-σ^0_{hv} (90.63%), σ^0_{vv}-λ_s-σ^0_{hv} (90.63%), H-$SPAN$-P_v(89.72%), H-P_s-P_v(89.49%) and σ^0_{vv}-λ_s-P_v (89.49%). This is an increase of approximately 2% over the pairs of the same parameters. The classified images of the best three triplets are shown in Figure 3.5.

Table 3.6. Classification accuracies of polarimetric parameters derived from Maximum Likelihood classification of three parameter combinations.

Polarimetric Parameter	Ice Type Classification Accuracy (%)				Overall Accuracy (%)	Kappa Coeff.
	OW	SFYI	RFYI	DFYI		
σ_{hv}^0-$R_{hh/vv}$-α_s	86.89	91.45	56.98	95.58	84.47	0.79
σ_{hv}^0-$R_{hh/vv}$-P_v	75.41	94.87	63.95	95.58	83.56	0.77
σ_{hv}^0-H-α_s	94.26	92.31	67.44	93.81	88.35	0.84
σ_{hv}^0-H-P_v	94.26	95.73	61.63	95.58	88.58	0.84
σ_{hv}^0-r_{hhvv}-α_s	83.61	92.31	38.37	95.58	80.13	0.73
σ_{hv}^0-r_{hhvv}-P_v	82.79	97.44	46.51	96.46	83.10	0.77
σ_{hv}^0-λ_s-α_s	94.26	92.31	70.93	93.81	89.04	0.85
σ_{hv}^0-λ_s-P_v	92.62	96.58	60.47	95.58	88.12	0.84
σ_{hv}^0-ϕ_s-α_s	74.59	93.16	39.53	94.69	77.85	0.70
σ_{hv}^0-ϕ_s-P_v	72.13	97.44	47.67	96.46	80.36	0.73
H-$SPAN$-α_s	93.44	94.87	58.14	93.81	86.98	0.82
H-$SPAN$-σ_{hv}^0	93.44	97.44	63.95	95.58	89.26	0.85
H-$SPAN$-P_v	95.90	98.29	61.63	95.58	89.72	0.86
H- P_s-α_s	93.44	92.31	51.16	87.61	83.33	0.77
H- P_s-σ_{hv}^0	94.26	97.44	63.95	93.81	89.04	0.85
H- P_s-P_v	95.08	98.29	61.63	95.58	89.49	0.85
H-P_v-α_s	72.13	76.92	46.51	76.11	69.40	0.58
H-P_v-σ_{hv}^0	90.98	100.0	61.63	96.46	89.04	0.85
P_v-$R_{hh/vv}$-σ_{hv}^0	75.41	94.87	63.95	95.58	83.56	0.77
P_v-$R_{hh/vv}$-α_s	79.51	96.58	52.33	96.46	83.10	0.77
P_v-r_{hhvv}-σ_{hv}^0	82.79	97.44	46.51	96.46	83.10	0.77
P_v-r_{hhvv}-α_s	83.61	96.58	40.70	97.35	82.19	0.75

P_v-P_s-σ_{hv}^0	80.33	98.29	55.81	95.58	84.24	0.78
P_v-P_s-α_s	77.05	96.58	52.33	96.46	82.42	0.76
P_v-ϕ_s-σ_{hv}^0	72.13	97.44	47.67	96.46	80.36	0.73
P_v-ϕ_s-α_s	72.13	94.87	33.72	96.46	76.94	0.68
P_v-λ_s-σ_{hv}^0	92.62	96.58	60.47	95.58	88.12	0.84
P_v-λ_s-α_s	95.08	92.31	61.63	96.46	88.12	0.84
λ_s-$SPAN$-σ_{hv}^0	93.44	96.58	61.63	95.58	88.58	0.84
λ_s-$SPAN$-α_s	93.44	93.16	56.98	93.81	86.30	0.81
λ_s-$SPAN$-P_v	93.44	95.73	60.47	95.58	88.12	0.84
λ_s-P_s-σ_{hv}^0	93.44	96.58	63.95	94.69	88.81	0.84
λ_s-P_s-α_s	93.44	92.31	51.16	89.38	83.79	0.78
λ_s-P_s-P_v	93.44	95.73	60.47	95.58	88.12	0.84
σ_{vv}^0-σ_{hv}^0-α_s	90.98	93.16	58.14	94.69	86.07	0.81
σ_{vv}^0-σ_{hv}^0-P_v	89.34	94.02	60.47	95.58	86.52	0.81
σ_{vv}^0- H-α_s	95.90	95.73	69.77	87.61	88.58	0.84
σ_{vv}^0- H-σ_{hv}^0	96.72	96.58	67.44	95.58	90.63	0.87
σ_{vv}^0- H-P_v	95.90	97.44	65.12	95.58	90.18	0.86
σ_{vv}^0-P_d-σ_{hv}^0	90.98	94.87	51.16	96.46	85.61	0.80
σ_{vv}^0-P_d-α_s	80.33	95.73	40.70	73.45	74.88	0.66
σ_{vv}^0-P_d-P_v	88.52	98.29	53.49	98.23	86.75	0.82
σ_{vv}^0-P_v-α_s	86.07	96.58	52.33	96.46	84.93	0.79
σ_{vv}^0-P_v-σ_{hv}^0	89.34	94.02	60.47	95.58	86.52	0.81
σ_{vv}^0-λ_s-α_s	96.72	95.73	63.95	87.61	87.67	0.83
σ_{vv}^0-λ_s-σ_{hv}^0	97.54	95.73	66.28	96.46	90.63	0.87
σ_{vv}^0-λ_s-P_v	95.08	97.44	62.79	95.58	89.49	0.85

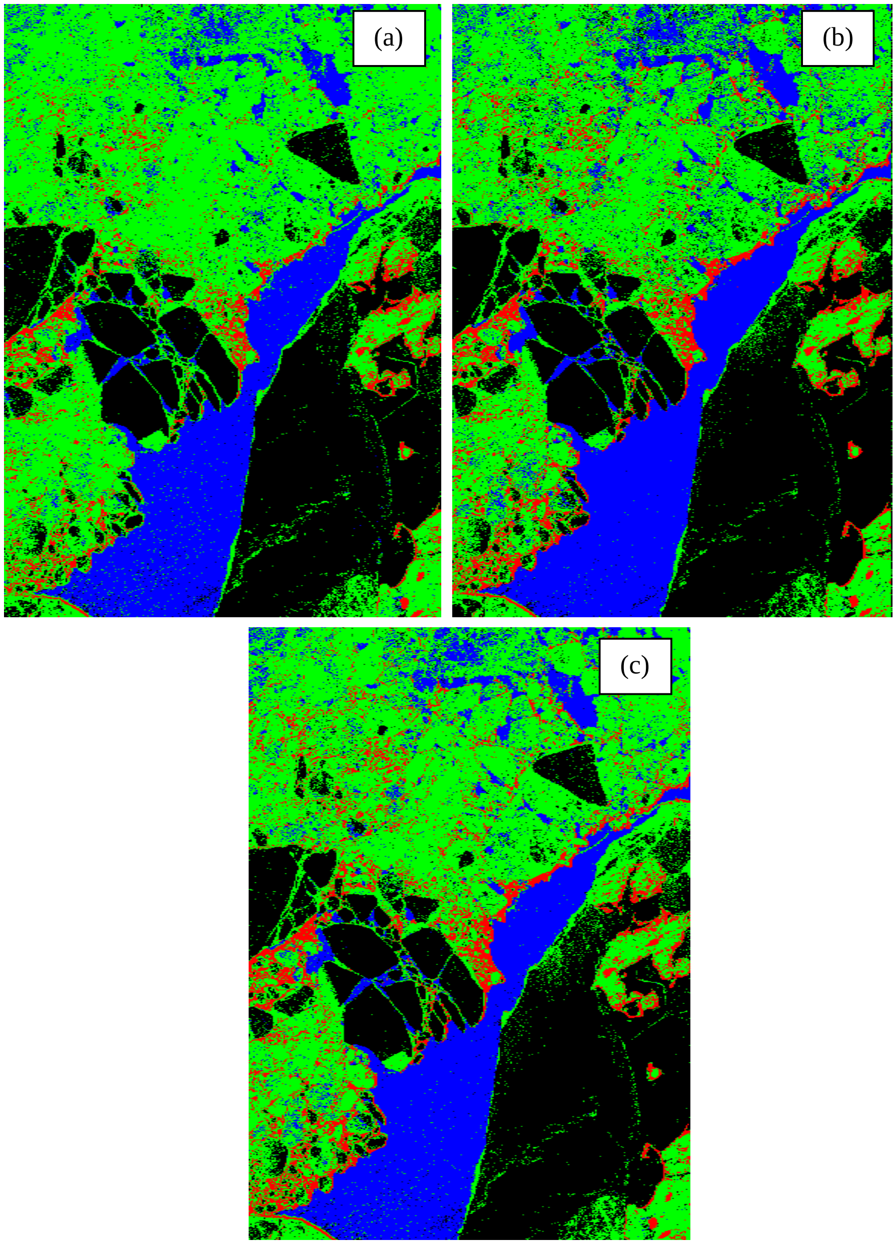

Figure 3.5. Image maps of the best three maximum likelihood classifications, achieved using a combination of polarimetric parameters $\boldsymbol{\sigma^0_{vv}}$*-* $\boldsymbol{H}$*-*$\boldsymbol{\sigma^0_{hv}}$ *(left),* $\boldsymbol{H\text{-}SPAN\text{-}P_v}$ *(middle) and* $\boldsymbol{\sigma^0_{vv}}$*-*$\boldsymbol{\lambda_s}$*-*$\boldsymbol{\sigma^0_{hv}}$ *(right). The overall classification accuracies for the three parameter combinations were achieved at 90.63% (a), 89.72 % (b) and 90.63% (c), respectively. The poorest classification accuracy was observed for RFYI at 67.44% (left), 61.63% (middle), 66.28% (right), respectively. The colors denote, Red = DFYI, Green = RFYI, Blue = OW and Black = SFYI.*

3.7 Conclusion

Polarimetric signatures of different ice types were analyzed at four radar incidence angles. The results were compared with previous studies to examine the variation of signatures with varying sea ice geophysical states and SAR parameters. The study was further extended to investigate the potential of polarimetric parameters for ice type discrimination. This was achieved by analyzing the polarimetric signatures in one and two-dimensional feature spaces and also through a combination of adopted classification algorithms.

Observations of the SAR polarimetric signatures of ice types (DFYI, RFYI and SFYI) showed an increase in mean σ_{hh}^0, σ_{vv}^0, σ_{hv}^0, , $SPAN$, H, α, P_d, P_v, ψ and τ_s with increase in surface roughness. Other parameters such as $R_{hh/vv}$, $R_{hh/hv}$, r_{hhvv}, A, β and λ_s decreased with the same increase in surface roughness. Polarimetric parameters P_s, ϕ_s and α_s demonstrated no direct relationship to sea ice roughness. The analysis also found that polarimetric parameters are sensitive to incidence angle and the strength of sensitivity varies by parameter and ice type. A decrease in mean σ_{hh}^0, σ_{vv}^0, σ_{hv}^0, $SPAN$, ϕ_{hh-vv} and A with increase in θ_i was observed for all ice types. Means of H and α on the other hand increased with the same variation in θ_i .

Results from evaluation of polarimetric parameters for sea ice classification at a single incidence angle of 27° showed that no single parameter possessed the capability to discriminate between all the ice types with individual class accuracies >60%. The best overall classification accuracies from single parameters were produced from H, σ_{hv}^0, P_v and λ_s. Pairing of two polarimetric parameters increased the classification accuracy by 10-22%. The best two-parameter classification accuracies were produced by using the combinations of H-P_v, σ_{vv}^0- H, P_v-λ_s and σ_{hv}^0-H. RFYI was found the least accurately classified ice type. Combining a third polarimetric parameter did not necessarily increase the classification accuracy. In nearly 50% of the three-parameter combinations the results were found to decrease by approximately 2-5%. However the best classification was achieved from three-parameter combinations of σ_{vv}^0- H-σ_{hv}^0 and σ_{vv}^0-λ_s-σ_{hv}^0 at an accuracy of 90.63%.

The results of the study are limited by the use of a small range of incidence angle images. The dependence of polarimetric SAR signatures on θ_i is carried out at only four incidence angles (between 22° and 37°), therefore the results are not valid outside this range. Additionally, the results may not be suitable for normalization of incidence angle variation in SAR images, primarily done for multi-image comparison. The parameter specific classification analysis is performed on a single image, thus the results are applicable only at θ_i = 27°.

CHAPTER FOUR:
ANALYSIS OF CONSISTENCY IN FIRST-YEAR SEA ICE CLASSIFICATION POTENTIAL OF C-BAND SAR POLARIMETRIC PARAMETERS DURING THE TRANSITION FROM COLD TO WARM ATMOSPHERIC CONDITIONS

4.1 Abstract

In this chapter, polarimetric microwave signatures of first-year sea ice (FYI) types and classification potential of C-band SAR polarimetric parameters is analyzed by comparing the results of two studies conducted for the same ice types under different geophysical settings during the transition from early melt to melt onset. Probability density functions, grey level parameter images and classification statistics derived using k-means classifier are used in the comparative analysis.

4.2 Introduction

Numerous active Synthetic Aperture Radar (SAR) based sea ice classification studies have been conducted using a variety of approaches (Dierking et al., 2003; Geldsetzer and Yackel, 2009; Scheuchl et al., 2003a; Nghiem and Bertoia, 2001; Carlström and Ulander, 1995). Most studies have demonstrated the potential of SAR for ice type discrimination (Dierking and Askne, 1998, Scheuchl et al., 2003b). However, the results of these studies are confined to their specific conditions and are mostly not applicable to other environmental settings. This is primarily due to the difference in the use of the radar parameters and the site specific geophysical conditions. To further investigate the causes of variability in the results, multiple additional studies have been carried out. The objective of these studies has been to identify appropriate radar incidence angle (Geldsetzer and Yackel, 2009; Mäkynen et al, 2002), frequency (Rignot and Drinkwater, 1992; Scheuchl et al, 2002) and polarization (Scheuchl et. al, 2005; Gill and Yackel, 2012) for sea ice classification purposes. Results reveal that backscatter response from sea ice varies as a function of radar parameters (frequency, incidence angle and polarization), sea ice dielectric properties and sea ice geophysical properties (roughness, size and shape; Ulaby et al., 1986). This has led to a general understanding that active SAR remote sensing of sea ice is data and condition specific. However, the identification of suitable and widely applicable radar parameters for sea ice classification over a range of environmental settings remains elusive. In this respect, the use of polarimetric information for sea ice classification is an active field of research. One approach towards the development of a generalized sea ice classification scheme is to identify polarimetric parameters that retain their classification capability under a variety of environmental settings for the same ice types while keeping the radar parameters nearly constant.

FYI type classification potential of twenty C-band SAR polarimetric parameters were evaluated by Gill and Yackel, 2012 (chapter 3 of this thesis). The study was carried out at one specific environmental setting. The results of the study highlighted that certain parameters were better classifiers than others. In this study we perform the same analysis for a different environmental setting and compare the results. The intention is to investigate the consistency in classification potential of twenty polarimetric parameters under the two different environmental conditions.

The two studies are conducted ten days apart, for the same study area but different environmental conditions, exhibiting a difference in air temperature of approximately 7.5°C. A warm period with temperatures rising up above 0°C in-between the two studies is important with respect to alteration in the electro-thermo-physical properties of the snow covered sea ice. Ideally, scattering from a snow covered sea ice is largely a function of brine volume (brine inclusions and brine pockets), snow grain size (which can subsequently act as large scattering centers once they become brine coated at warmer temperatures), and roughness at the snow-ice interface (Barber and Nghiem, 1999). Under cold dry conditions (<-20° C), scattering at C-band is mainly due to the sea ice roughness as snow is transparent to electromagnetic waves. With an increase in temperature, brine volume near the snow-ice interface increases due to a vapour pressure gradient which acts to wick brine from upper layer of the sea ice into the basal layer of the snow. As a result, the backscatter also increases. This increase is attributed to several factors, such as (1) enhanced dielectric contrast (effective permittivities) between snow basal layers and ice surface, (2) larger brine scatterers and (3) overall higher brine volume in snow basal layers (Barber and Nghiem, 1999). This increase in backscatter is less for thick snow covers and rougher ice surfaces (Barber and Nghiem, 1999). Other factors such as wind speed, wind direction and movement of the marginal ice zone with respect to radar line of sight also play a significant role in defining the SAR polarimetric response of water (Fichaux and Ranchin, 2002; Vachon and Wolfe, 2011). With an increase in wind speed both the co-polarized and the cross-polarized backscatter increases. (Vachon and Wolfe, 2011). Similarly, co-polarized backscatter is sensitive to wind direction and cross-polarized backscatter is insensitive (Vachon and Wolfe, 2011). The ratio of the co-polarized backscatter coefficients is also independent of wind speed and wind direction (Vachon and Wolfe, 2011).

Radarsat-2 images utilized in the two studies are acquired at similar incidence angles though not exactly the same (image centers ~23° and ~27°). Implication of this can be expected in the slight differences in ice type polarimetric backscatter signatures between the two studies. For smooth snow covered FYI, at smaller incidence angles, linear and cross polarized backscattering coefficients exhibit higher backscatter when compared to larger incidence angle (Geldsetzer et al., 2007). However, not all polarimetric parameters demonstrate the same relationship with radar incidence angle. Co-polarized ratio and co-polarized phase differences for smooth snow covered FYI show no relationship with radar incidence angle (Geldsetzer et al., 2007; Mäkynen et al, 2002). Similarly, co-polarized correlation coefficient demonstrates negligible incidence angle dependence at low angles (<30°), but negative relationship at large angles (> 30°) (Geldsetzer et al., 2007). The reverse is true for depolarization ratio (Geldsetzer et al., 2007). The incidence angle dependence of polarimetric SAR signatures is also a function of sea ice surface roughness and snow cover properties (Geldsetzer et al., 2007; Mäkynen et al., 2002). For deformed sea ice surfaces, the incidence angle dependence of horizontal co-polarized backscatter is low whereas for a smooth FYI surface it is higher (Mäkynen et al., 2002). Similarly, for wet snow covers, the slope between the incidence angle and SAR backscatter is steeper when compared to dry snow covers (Mäkynen et al., 2002). The effect of the difference in incidence angle of 3°-4° between the two studies is inherent in the polarimetric backscatter response but may not be substantial enough to surpass the effect of the differences in geophysical and thermodynamically driven effects on dielectric property changes towards microwave backscatter.

The polarimetric parameters included in this study (Table 4.1) are derived after Cloude-Pottier (1997) decomposition, Touzi (2007) decomposition, Freeman-Durden (1998) decomposition, normalized radar cross section (NRCS) measurements, phase differences and statistical SAR correlation measures (Drinkwater et al. 1992). A detailed description of the polarimetric parameters is provided in Gill and Yackel, 2012 and the references therein. Analysis is performed for four pre-identified sea ice types namely deformed first-year ice (DFYI), rough first-year ice (RFYI), smooth first-year ice (SFYI) and open water (OW). For definition of ice types, see Gill and Yackel, 2012.

Table 4.1. Nomenclature, symbols and the references of the SAR polarimetric parameters used in the study.

Polarimetric Parameter	**Symbol**	**Reference**
Backscattering coefficient (co-polarized horizontal)	σ_{hh}^0	Drinkwater et al., 1992
Backscattering coefficient (co-polarized vertical)	σ_{vv}^0	Drinkwater et al., 1992
Backscattering coefficient (cross-polarized)	σ_{hv}^0	Drinkwater et al., 1992
Co-polarized Ratio	$R_{hh/vv}$	Drinkwater et al., 1992
Cross-polarized ratio	$R_{hh/hv}$	Drinkwater et al., 1992
Total Power	$SPAN$	Drinkwater et al., 1992
Phase difference (co-polarized)	ϕ_{hh-vv}	Drinkwater et al., 1992
Correlation coefficient (co-polarized)	ρ_{hhvv}	Drinkwater et al., 1992
Entropy	H	Cloude and Pottier, 1997
Anisotropy	A	Cloude and Pottier, 1997
Alpha angle	α	Cloude and Pottier, 1997
Beta angle	β	Cloude and Pottier, 1997
Dominant scattering component (surface)	P_s	Freeman and Durden, 1998
Dominant scattering component (double bounce)	P_d	Freeman and Durden, 1998
Dominant scattering component (volume)	P_v	Freeman and Durden, 1998
Orientation angle	ψ	Touzi, 2007
Alpha angle	α_s	Touzi, 2007
Phase	ϕ_s	Touzi, 2007
Hellicity	τ_s	Touzi, 2007
Dominant eigenvalue	λ_s	Touzi, 2007

4.3 Methods

This study is a part of the International Polar Year - Circumpolar Flaw Lead (IPY-CFL) experiment conducted between April and June, 2008.

4.3.1 Study area

The study area is comprised of landfast FYI and marginal ice located on the west coast of Parry Peninsula in Franklin Bay (70°N, 125°W). Location of the study area with respect to Canada and images showing sampling areas of ice types are shown in Figure 4.1.

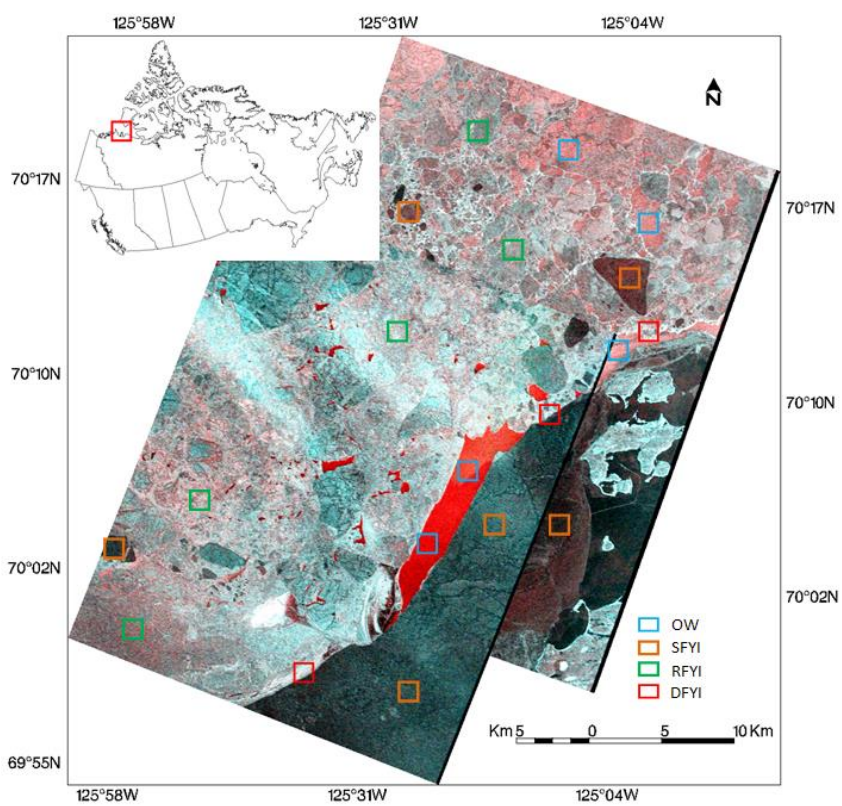

Figure 4.1. Map of Canada (top-left), overlaid with red box showing the study area (Amundsen Gulf). In the main window are the Radarsat-2 SAR images used (14 May, 2008), overlaid with windows of interest showing sampling areas of different ice types. Color combinations used in the images are HH (red), HV (blue) and VH (green).

4.3.2 Dataset

Two Radarsat-2 SAR fine quad-pol images at a spatial resolution ranging from 5.2 to 7.6 meters were utilized in the study. The incidence angles at the center of the images were approximately 27° and 23° (Table 4.2).

Table 4.2. Technical specifications of the Radarsat-2 SAR images utilized in the two studies and meteorological conditions during the hour of image acquisitions. Wind direction is relative to the radar line of sight.

Date	**Time (UTC)**	**Scan Direction**	**Incidence Angle (°)**	**Air Temperature (°C)**	**Wind Speed (m/sec)**	**Wind Direction (°)**
2008-05-04	15:18:20	Desc	26.93 - 28.75	-7.9	18.06	140
2008-05-14	15:26:42	Desc	22.26 - 24.17	-0.4	11.39	170

Ground truth data in the form of GPS coordinates and digital pictures were acquired for numerous ice types using helicopter flights. Three ice roughness classes (DFYI, RFYI and SFYI) and an open water class (OW) were identified and characterized by overlaying the ground truth GPS coordinates on the satellite imagery. For OW, no GPS coordinates were acquired. OW was characterized using visual observation and the digital ice charts acquired from the Canadian Ice Service. SFYI was chosen as an ice form with no deformation. Small scale cracks or finger rafting is likely to be present on SFYI. RFYI consisted of broken uneven surface with protruding ice blocks and floe edges, equivalent to the size of C-band wavelength. DFYI consisted of rubble ice, ridges and boulders with sizes greater than 1 meter.

Meteorological data consisting of hourly mean air temperatures, wind velocities and precipitation were acquired from Environment Canada, Cape Parry meteorological station located at 70.16°N, 124.71°W (Figure 4.2). Meteorological conditions during the same hour of image acquisitions are presented in Table 4.2. A temperature difference of ~7.5°C existed between the two image acquisitions. Wind speeds were generally high at 18.06 m/sec and 11.39 m/sec, during the same hour of image acquisitions. Wind direction was 140° and 170° with respect to radar line of sight during the same hour of image acquisitions (Table 4.2).

Snow properties were measured by excavating snow pits of ~0.5 m^2 (Figure 4.3). All measurements were carried out on the non-illuminated face of the snow pit. Snow temperatures were measured using a digital thermometer (accuracy ±0.2°C) at 2 cm vertical intervals in the snowpack. Snow samples at each interval were extracted using a rectangular snow sampler (66 cm^3) and snow densities were calculated using the gravimetric method (±0.04g/cm^3, Drobot and Barber, 1998). Snow salinity was determined for each interval using a digital conductivity meter (±0.5%) from melted snow density samples. The brine volume fraction, dielectric constant and dielectric loss of snow were modeled from measured snow properties after Geldsetzer et al., 2009a.

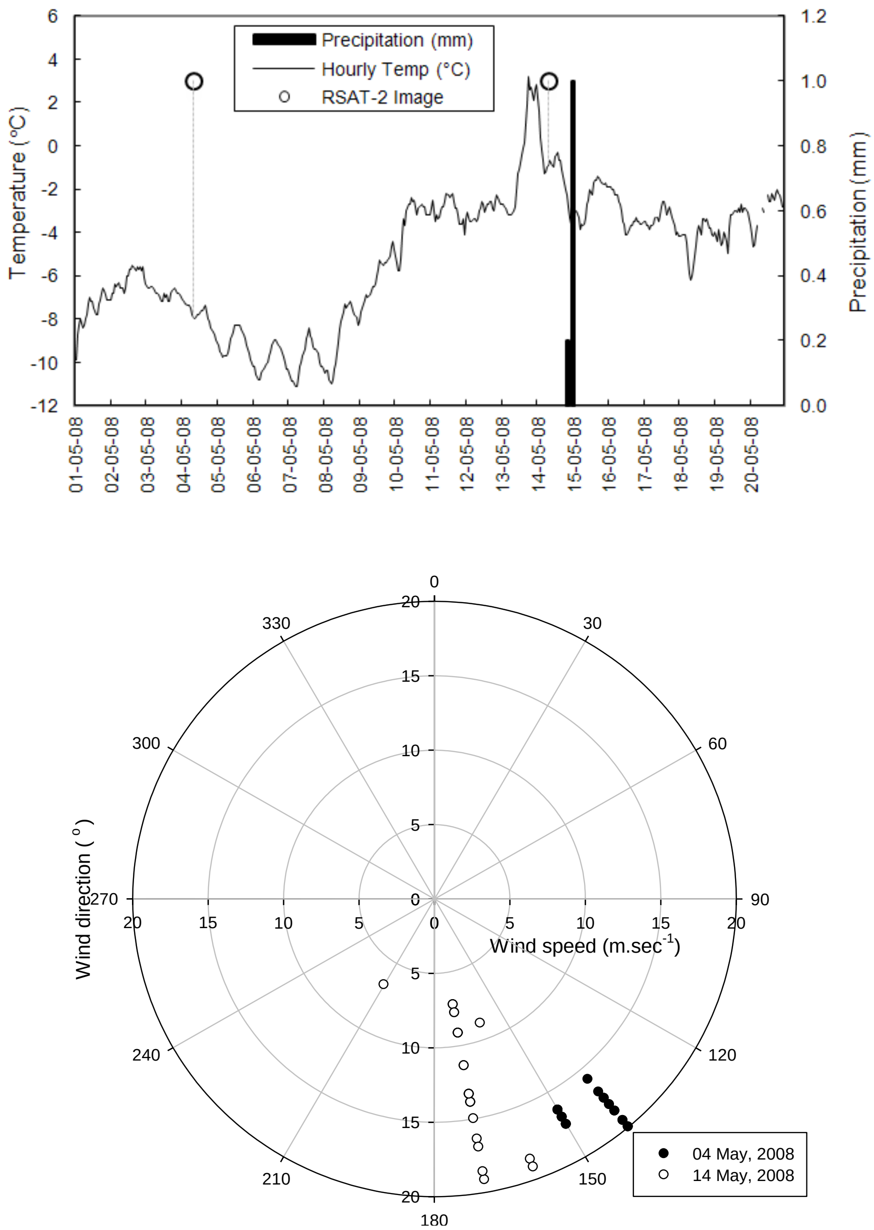

Figure 4.2. Meteorological conditions during the study period (4 May – 20 May, 2008). Connected line denotes hourly air temperatures and solid bars denote precipitation. Hourly wind speed and wind direction with respect to radar line of sight for 4 May, 2008 and 14 May, 2008 are shown in the bottom figure. Data was acquired from Environment Canada Cape Parry and Paulatuk weather stations.

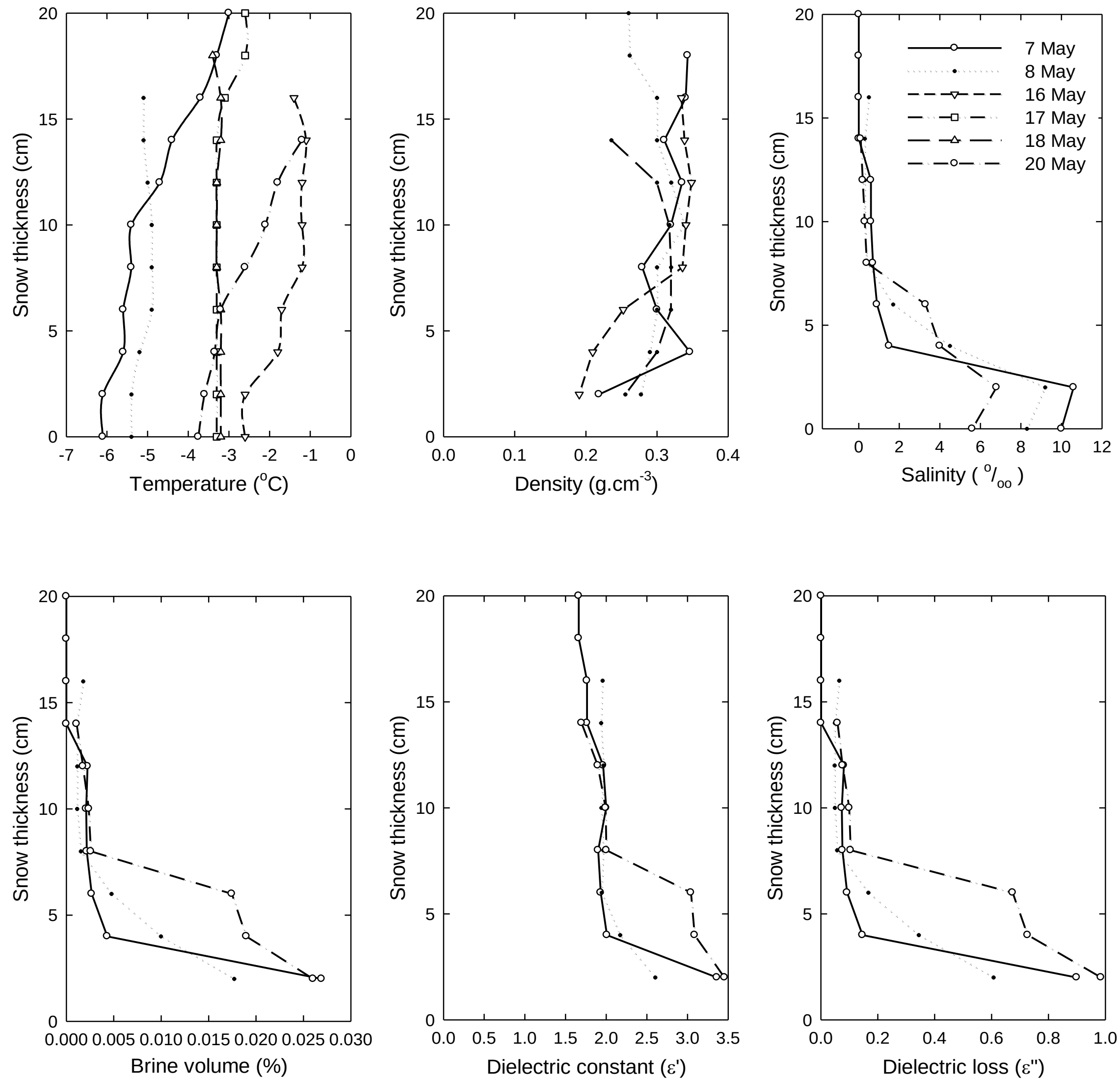

Figure 4.3. Discrete measured and modelled properties of snow over SFYI. Only temperatures are available for 16, 17 and 18 of May, 2008.

4.3.3 Sea ice classification

Classification was performed on Radarsat-2 SAR images acquired on 14 May, 2008 and 4 May, 2008 following Gill and Yackel, (2012). A K-means algorithm was used to classify single parameter images. The K-means classifier calculates the mean vector of each training class and determines the Euclidean distance between each unknown pixel and the mean vector of each class (Lillesand and Kiefer, 2000). All pixels are then classified to the closest class.

A large number of surface validation points (SVP) for different ice classes except open water were collected. The SVP's were divided into two sets i.e. training samples and validation samples (Table 4.3) and subsequently utilized for classification and accuracy assessment. Confusion matrices were computed to assess the classification accuracy through three statistical parameters i.e overall accuracy, producer's accuracy and kappa coefficient. A detailed description of the classification accuracy measures is presented in Gill and Yackel, (2012).

Table 4.3. Training and validation samples used in the classifications and accuracy assessment of polarimetric parameters of the study-2.

Ice Class	**Training Samples**		**Validation Samples**	
	No. of Polygons	**No. of Pixels**	**No. of Polygons**	**No. of Pixels**
SFYI	18	102	21	147
RFYI	19	183	15	138
DFYI	11	79	12	76
OW	17	122	21	121

4.3.4 Parameter consistency analysis

Radarsat-2 images were processed to compute polarimetric parameters. Speckle noise was reduced using a 7x7 Refined Lee filter (Lee et al., 1997) as it preserves the edges and point target information and yet suppresses the sufficient noise level (Foucher and Lopez-Martinez, 2009). Probability density functions (PDFs) were computed for all polarimetric parameters and were employed to analyze the sensitivities of parameters to different ice types. PDFs were estimated with the Parzen method (Therrien, 1987) using a Gaussian Kernel function with a standard deviation of one. Mathematical formulation is described in Gill and Yackel, 2012. Results from PDFs and classifications are compared and assessed.

4.4 Results and discussion

4.4.1 Comparison of meteorological and geophysical conditions

A difference of approximately 7.5°C in air temperatures existed between the two studies at the time of image acquisitions. The air temperatures increased from -7.9°C on 4 May to -0.4°C on 14 May, 2008. Wind speeds were generally high at 18.06 m/sec and 11.39 m/sec at the time of image acquisition on 4 May, 2008 and 14 May, 2008, respectively (Table 4.2). Wind direction relative to radar line of sight changed by 30° between the two studies, becoming relatively parallel to look direction on 14 May, 2008 (Table 4.2). Temperatures within the snow pack over SFYI also increased by approximately 3-5°C between 7 May and 16 May (Figure 4.3). Salinities decreased by approximately 4ppt in the first 2-3cm of snow basal layers but increased in the 4-6 cm of snow pack between 7 May and 20 May (Figure 4.3). As a consequence, brine volume, dielectric constant and dielectric loss also increased in the 4-6 cm of snow pack between 7 May and 20 May (Figure 4.3). Densities showed no significant change.

4.4.2 Classification consistency analysis

The results of the Radarsat-2 SAR dataset acquired on 4 May, 2008 represent cold atmospheric conditions and are hereafter referred as study-1. The results of the Radarsat-2 dataset acquired on 14 May, 2008 represent warm atmospheric conditions and are hereafter referred as study-2. Grey color polarimetric parameter images of study-2 and that of study-1 are displayed in Figure 4.4 through Figure 4.7. The best classified images for both the studies are presented in Figure 4.8. PDFs of the polarimetric parameters of the two studies are displayed in Figures 4.9 through 4.11. Results of the classifications of the study-2 are shown in table 4 and that of study-1 are shown in table 4.5.

Comparative analysis of the classification results of the polarimetric parameters show an overall decrease in classification accuracies of study-2 when compared to study-1. A decrease in overall accuracy was observed in 75% of the parameters. Considering the class specific accuracies, 75% of the parameters showed a decrease in classification accuracy for DFYI, 50% of parameters for RFYI and 55% of parameters for OW and SFYI (Table 4.4). Among the five parameters (σ_{vv}^0, σ_{hv}^0, H, P_v and λ_s) that showed significant overall classification accuracy (>60%) in study-1, only two (σ_{hv}^0 and P_v) entered the significant accuracy group in the study-2. The value of significance (>60%) was chosen heuristically as a cut-off limit to analyze better classifiers in the comparative process. If the threshold of significance is lowered from 60% to 50% for both the studies, nine parameters fall under the significant classifier group in study-1 and six parameters out of those nine qualify as significant classifiers in the study-2. This shows that among all the polarimetric parameters that exhibited high classification accuracy under one set of environmental conditions (study-1), nearly two third showed high accuracy under different set of environmental conditions (study-2). The question is whether these parameters always classify the same ice types with similar accuracies under different environmental settings. This is analyzed below for each of the parameters considered in the study.

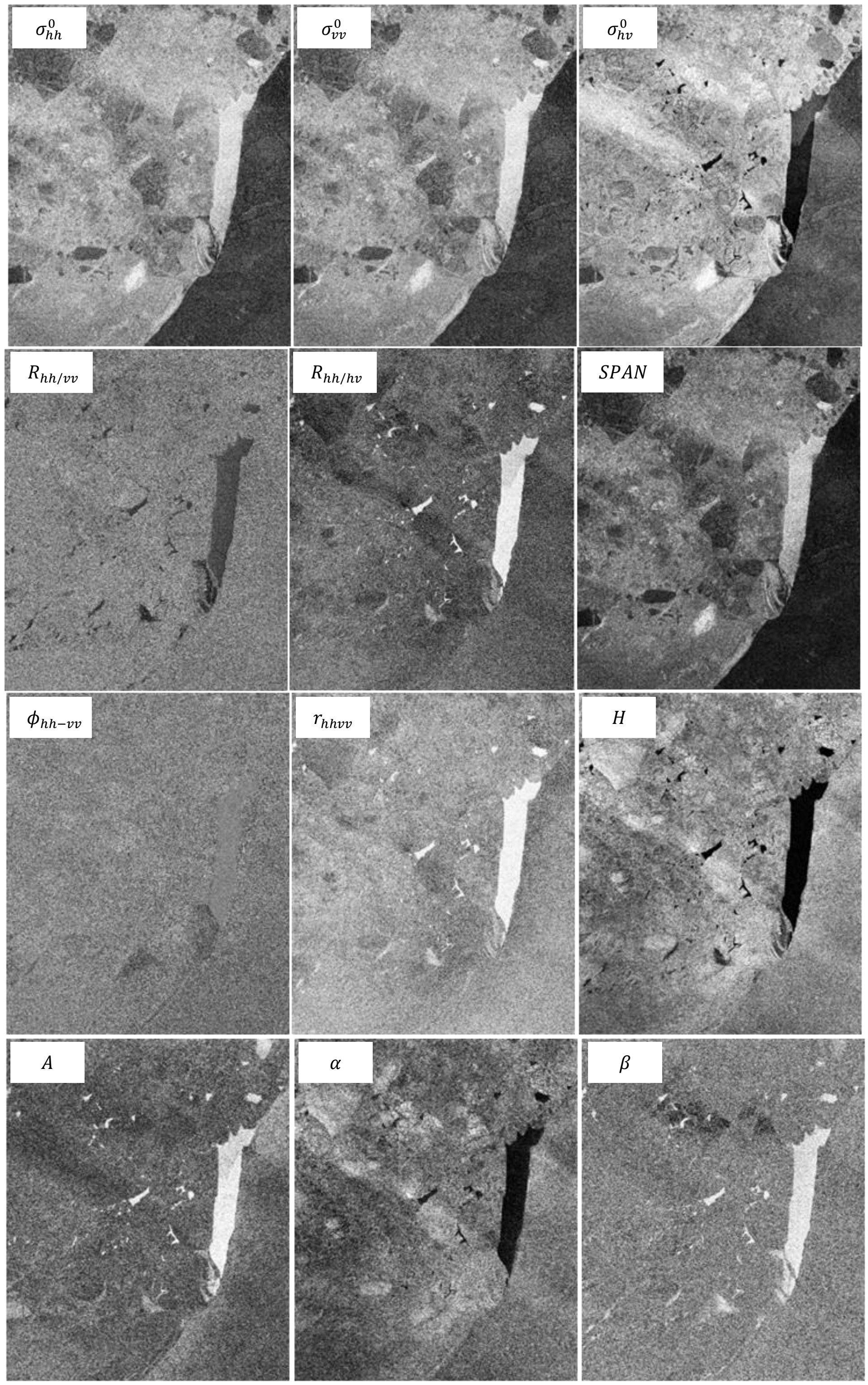

Figure 4.4. Polarimetric parameter images of sea ice types and open water from Radarsat-2 SAR data acquired on 14 May, 2008. Darker tone in the grey level images correspond to low parameter values and brighter tone to high parameter values.

Table 4.4. Classification accuracies of polarimetric parameters derived from k-means classification. Classification is performed on Radarsat-2 SAR image acquired on 14 May, 2008 at approximately 23° incidence angle. Significant classification accuracies (>60%) are highlighted in bold. The arrows denote increase or decrease in classification accuracy when compared to results of the study-1.

Polarimetric Parameter	**Ice Type Classification Accuracy (%)** OW		**SFYI**		**RFYI**		**DFYI**		**Overall Accuracy (%)**		**Kappa Coeff.**
σ^0_{hh}	58.17	▼	**90.68**	▲	44.14	▲	26.49	▲	54.92	▲	0.39
σ^0_{vv}	55.28	▼	**92.23**	▲	33.30	▼	30.40	▼	52.69	▼	0.37
σ^0_{hv}	59.33	▲	49.71	▼	**65.01**	▲	**84.67**	▼	**62.43**	▼	0.50
$R_{hh/vv}$	**75.24**	▼	16.87	▼	25.35	▲	17.51	▲	35.99	▼	0.12
$R_{hh/hv}$	**90.98**	▲	37.87	▲	36.32	▲	28.44	▼	51.77	▲	0.35
$SPAN$	17.33	▼	**98.34**	▲	38.84	▼	53.66	▲	52.87	▼	0.37
ϕ_{hh-vv}	5.77	▼	29.66	▲	23.74	▲	35.62	▲	22.74	▼	0.01
ρ_{hhvv}	**91.76**	▲	49.71	▲	11.11	▼	27.39	▼	47.31	▼	0.28
H	**100.0**	▲	31.87	▼	29.93	▼	21.76	▼	47.56	▼	0.30
A	**89.34**	▲	30.98	▼	42.08	▲	19.63	▼	46.42	▲	0.28
α	**86.05**	▲	29.36	▼	27.05	▲	17.25	▼	42.74	▲	0.22
β	**97.11**	▲	35.29	▼	24.39	▼	27.96	▼	49.20	▲	0.31
P_s	**61.68**	▼	**82.66**	▼	25.95	▼	27.44	▼	50.18	▼	0.33
P_d	06.51	▼	56.57	▼	06.57	▼	34.31	▼	37.80	▼	0.04
P_v	**69.99**	▲	56.43	▼	**61.61**	▼	**74.77**	▼	**64.08**	▼	0.52
ψ	43.97	▼	24.41	▲	17.78	▲	21.89	▼	27.06	▼	0.03
ϕ_s	42.18	▼	16.48	▲	20.98	▲	13.26	▼	22.07	▼	0.02
τ_s	47.18	▼	03.62	▼	20.42	▲	14.48	▼	21.41	▼	0.03
α_s	15.51	▼	19.05	▲	23.74	▼	19.70	▼	21.10	▼	0.08
λ_s	**100.0**	▲	25.43	▼	27.16	▼	30.25	▼	47.63	▼	0.30
% of parameter increased accuracy	45		45		50		20		25		

4.4.2.1 Backscattering coefficients ($\boldsymbol{\sigma^0_{hh}}$, $\boldsymbol{\sigma^0_{vv}}$, $\boldsymbol{\sigma^0_{hv}}$)

By comparison of the grey level tone for each of the sea ice classes in the backscatter images of the two studies (Figure 4.4 and 4.6), it is observed that σ^0_{hh} and σ^0_{vv} do not show any significant differences. Analyses of the PDFs of the ice types (Figure 4.9a and 9b) show a slight positive shift in σ^0_{hh} and σ^0_{vv} for the study-2 when compared to study-1. The positive shift in PDF curves can be attributed to the combined effect of the difference in incidence angle and the geophysical properties. The effect of 4° change in incidence angle produces an increase in mean σ^0_{hh} and σ^0_{vv} by approx. 2.5dB for SFYI and approx. 1.75dB for DFYI (Geldsetzer et al., 2009; Mäkynen, 2002). Our results demonstrate slightly higher increase at $\Delta\sigma^0_{hh}$= 3.01dB and $\Delta\sigma^0_{vv}$ = 2.76dB for SFYI and slightly lower increase at $\Delta\sigma^0_{hh}$= 1.58dB and $\Delta\sigma^0_{vv}$ = 1.33dB for DFYI. The additional increase in σ^0_{hh} and σ^0_{vv} for SFYI can be attributed to the increase in brine volume in the snow basal layers. Higher brine volume in snow leads to higher co-polarized backscatter (Barber and Nghiem, 1999). A slightly lower increase in σ^0_{hh} and σ^0_{vv} for DFYI can be due to the masking effect of the snow pack. The presence of liquid water and brine volume in snow reduce the microwave penetration depth and subsequently reduced surface and multiple scattering from DFYI (Barber et. al., 1995). In case of OW, an increase in mean σ^0_{hh} and σ^0_{vv} is observed at 1.33dB and 1.93dB, respectively. Geldsetzer et al., 2009 showed the effect of incidence angle on radar backscatter for wind roughened (10m/sec) melt ponds on FYI at 10.4° wind direction relative to radar line of sight. For 4° increase in incidence angle (23°-27°), σ^0_{hh} and σ^0_{vv} increased by approx. 2.5dB (Geldsetzer et al., 2009). Our results show a slightly smaller increase in σ^0_{hh} and σ^0_{vv} for the same difference in incidence angle (4° from 23°-

27°). This can be due to the difference in wind speed, wind direction and OW versus melt pond conditions. We used CMOD5n model to estimate σ_{vv}^0 (after Hersbach et al., 2007; Hersbach, 2008) and σ_{hh}^0 (after Vachon and Wolfe, 2011). The modeled σ_{hh}^0 and σ_{vv}^0 for the study-1 (4 May) and the study-2 (14 May) as a function of their wind speeds, wind directions and incidence angles showed an increase of 0.99dB and 0.47dB, respectively. Our results confirm the presence of the effects of incidence angle and geophysical properties on σ_{hh}^0 and σ_{vv}^0, but are difficult to quantify separately. However, the separation between the ice types appears similar for both the studies. Low backscatter is observed for SFYI and higher but mixed backscatter for DFYI, RFYI and OW. Comparing the results of the classification from table 4.3 for the study-2 and table 4.4 for study-1, it is evident that SFYI is clearly discriminated in both the studies. Minor differences exist in separation of OW, wherein study-1, σ_{hh}^0 and σ_{vv}^0 show higher accuracies (60.66% and 72.95%) when compared to study-2 accuracies of 58.17% and 55.28%, respectively. Overall accuracies of σ_{hh}^0 and σ_{vv}^0 also show slight differences, where σ_{hh}^0 demonstrate an increase of 2.64 % and σ_{vv}^0 demonstrate a decrease of 11.55%.

With respect to σ_{hv}^0, a positive shift in PDFs is observed for SFYI, RFYI and DFYI but a negative shift is observed for OW. The positive shift in PDF is due to the combined effect of the difference in incidence angle and the geophysical properties between the two studies. Geldsetzer et al., 2009 showed an increase in mean σ_{hv}^0 of 1.5dB for 4° decrease in incidence angle over snow covered SFYI. Our results show similar but slightly higher increase in σ_{hv}^0 at 1.87dB for the same decrease in incidence angle. The additional increase can be attributed to the differences in geophysical properties between the two studies. The negative shift in the PDF (mean $\Delta\sigma_{hv}^{0}$ = -3.81dB) for OW is due to the effect of wind speed. This is verified through modeling σ_{hv}^{0} after Vachon and Wolfe, (2011). The modeled results show σ_{hv}^{0} at -24.90dB for study-1 (4 May) against Radarsat-2 derived mean σ_{hv}^{0} of -27.61dB for the same study (4 May) and -28.85dB for study-2 (14 May) against Radarsat-2 mean σ_{hv}^{0} of -31.42dB. Although there are minor differences in modeled and Radarsat-2 derived σ_{hv}^{0}, the negative shift in σ_{hv}^{0} between the study-1 and the study-2 is validated. The observed difference in σ_{hv}^{0} is -3.81dB against modeled difference of -3.95dB. Inspection of the grey level image of σ_{hv}^{0} (Figure 4.4) and PDF curve (Figure 4.9c), show two separate clusters of two classes each, where OW and SFYI are mixed to form one cluster and RFYI and DFYI as another cluster. This is different from the results of study-1 where three separate clusters were evident (Figure 4.6 and Figure 4.9c). The obvious reason for the difference is the dramatic change in signatures of OW. The OW curve in PDF plot (Figure 4.9c) has shifted to the left and now overlaps with SFYI. This was not the case in study-1, where OW signatures were drastically different from SFYI, rather resembling RFYI. The implications of this are that SFYI can no longer be significantly (accuracy > 60%) discriminated from other classes, although the classification accuracy of OW has increased dramatically by 22.44% between study-1 and the current.

Overall, the classification potential of all three parameters (σ_{hh}^{0}, σ_{vv}^{0} and σ_{hv}^{0}) has decreased. Two classes were significantly separated by σ_{hh}^{0} and σ_{vv}^{0} and three classes by σ_{hv}^{0} in study-1. The number of separable classes has reduced by one for each of the backscattering coefficients. However, σ_{hh}^{0} and σ_{vv}^{0} does show a consistency in signature patterns between the two studies while σ_{hv}^0 does not. Yet, σ_{hv}^0 retains its high classification (overall accuracy = 62.43%) ranking among the parameters considered (Table 4.4).

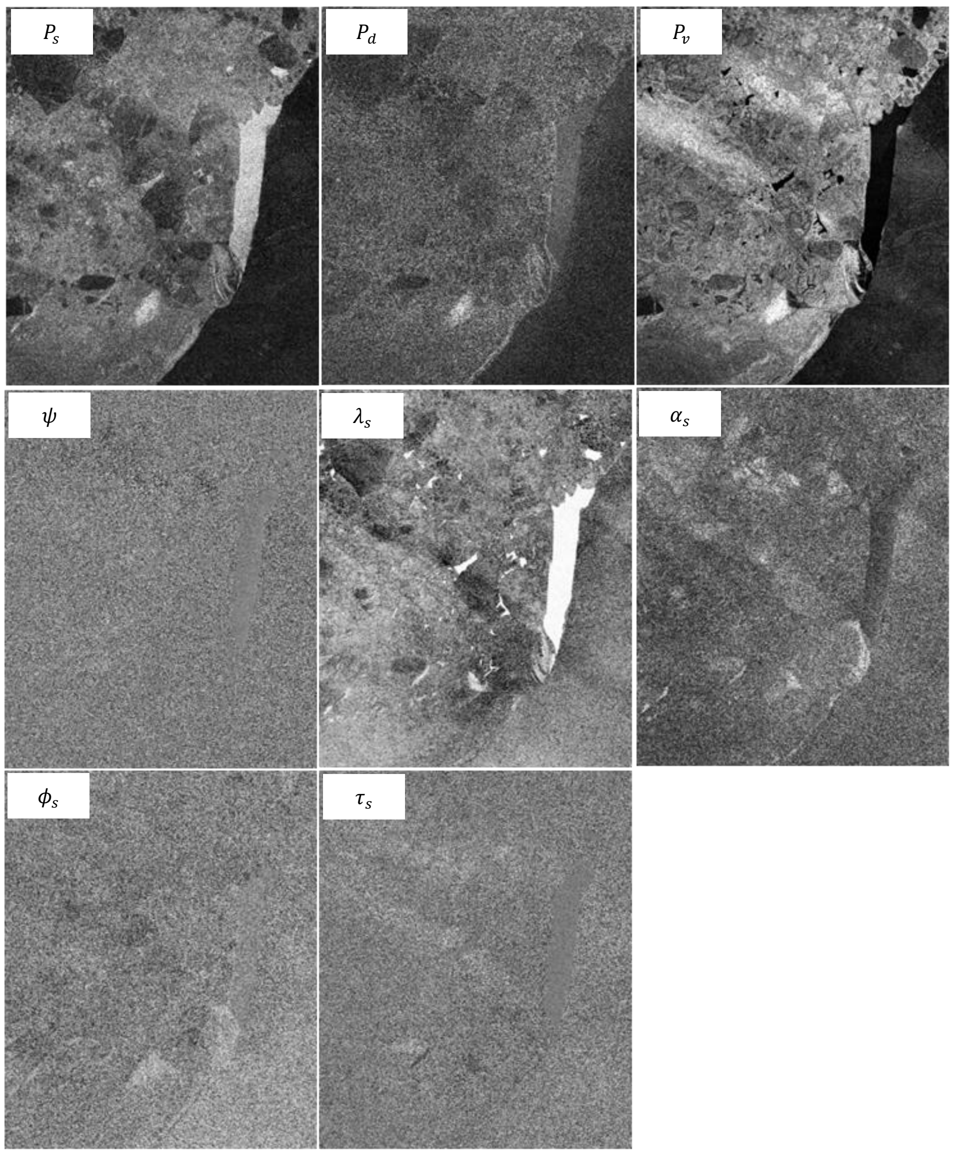

Figure 4.5. Polarimetric parameter images of sea ice types and open water from Radarsat-2 SAR data acquired on 14 May, 2008. Darker tone in the grey level images correspond to low parameter values and brighter tone to high parameter values.

Table 4.5. Classification accuracies of polarimetric parameters derived from k-means classification. Classification is performed on Radarsat-2 SAR image acquired on 4 May, 2008 at approximately 27° incidence angle. Significant classification accuracies (>60%) are highlighted in bold.

Polarimetric	**Ice Type Classification Accuracy (%)**				**Overall**	**Kappa**
Parameter	**OW**	**SFYI**	**RFYI**	**DFYI**	**Accuracy (%)**	**Coeff**
σ_{hh}^0	**60.66**	**85.73**	36.51	20.65	52.28	0.35
σ_{vv}^0	**72.95**	**86.32**	40.70	46.02	**63.24**	0.50
σ_{hv}^0	36.89	**93.87**	**61.14**	**91.92**	**71.00**	0.61
$R_{hh/vv}$	**93.44**	41.88	16.28	13.27	43.83	0.24
$R_{hh/hv}$	56.56	29.91	33.72	48.67	42.92	0.24
$SPAN$	46.72	**92.31**	59.30	35.40	58.44	0.44
ϕ_{hh-vv}	**77.87**	08.55	17.44	09.73	29.90	0.05
ρ_{hhvv}	**88.52**	33.33	11.63	51.33	49.08	0.31
H	**89.34**	**63.25**	39.53	**65.49**	**66.43**	0.54
A	31.97	58.97	17.44	24.78	34.47	0.11
α	33.61	31.62	17.44	61.95	37.21	0.15
β	**69.67**	19.66	24.42	39.82	39.72	0.19
P_s	**63.93**	**88.89**	33.72	41.59	58.90	0.44
P_d	27.05	**90.60**	08.14	**66.37**	50.45	0.33
P_v	49.34	**90.00**	**62.79**	**92.04**	**73.74**	0.65
ψ	**60.66**	00.85	02.33	51.33	30.82	0.06
ϕ_s	**92.62**	11.11	18.60	14.16	36.07	0.14
τ_s	53.10	31.88	10.00	24.59	31.73	0.07
α_s	16.56	01.71	**65.58**	51.33	30.36	0.09
λ_s	**91.80**	**61.54**	36.05	**64.60**	**65.75**	0.54

4.4.2.2 Co-polarization and co-to-cross-polarization ratios ($R_{hh/vv}$, $R_{hh/hv}$)

Through the visual analysis of grey level images (Figure 4.4 and Figure 4.6), PDF plots (Figure 4.9d) and classification accuracy statistics (Table 4.4 and Table 4.5) it is clear that the response of $R_{hh/vv}$ remained consistent between the two studies. Although a slight positive shift in PDFs of DFYI and OW, and a slight negative shift in PDFs of RFYI and SFYI is observed in the study-2 when compared to study-1, the relative separation of the ice classes remains unchanged. As expected, the effect of incidence angle is negligible on $R_{hh/vv}$. Similar results have been shown for SFYI and hummock ice by Geldsetzer et al., 2009. A slight positive relationship exists between $R_{hh/vv}$ and incidence angle for wind roughened melt ponds on FYI (Geldsetzer et al., 2009) and our results confirm this. An insignificant difference in $R_{hh/vv}$ for all ice types is found between the two studies. Only OW could be separated in either of the studies. By comparison, of the classification results of $R_{hh/vv}$ between the two studies, the overall and OW accuracy decreased by 7.84%and 18.2%, respectively in the study-2. With respect to the separation capability of $R_{hh/hv}$, none of the ice classes could be classified significantly in study-1 whereas in the study-2 OW is classified with accuracy of 90.98%. This is due to the negative shift in PDFs of SFYI, RFYI and DFYI, likely because of the combined effect of the change in incidence angle and snow properties between the two studies. In the polarimetric grey level image of $R_{hh/hv}$ (Figure 4.4) OW can be clearly distinguished through bright signature in the dark background representing all other classes. As a conclusion it can be inferred that $R_{hh/vv}$ was highly stable in its signature response and classification potential between the two studies, whereas $R_{hh/hv}$ was not.

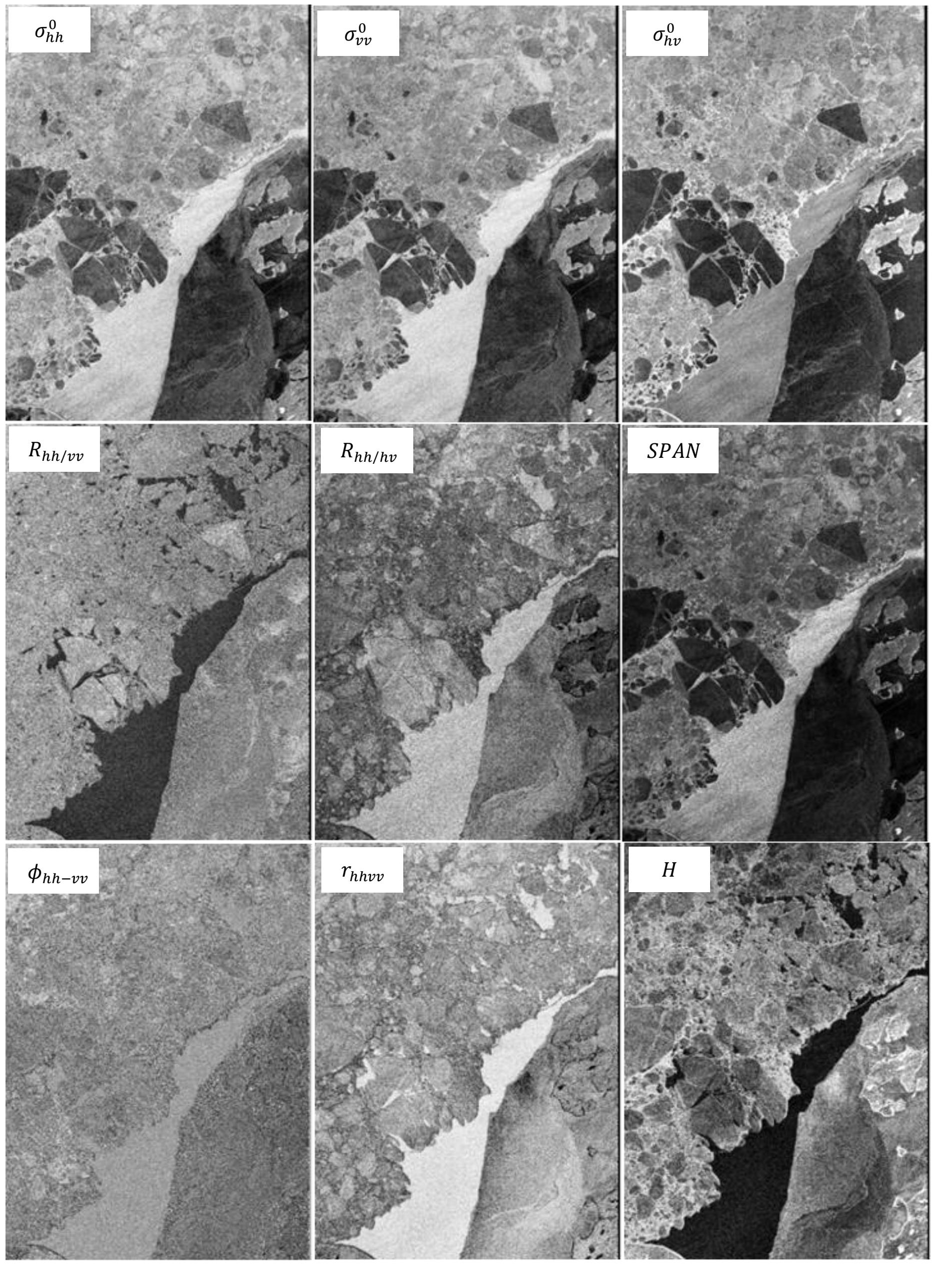

Figure 4.6. Polarimetric parameter images of sea ice types and open water from Radarsat-2 SAR data acquired on 4 May, 2008. Darker tone in the grey level images correspond to low parameter values and brighter tone to high parameter values.

(Continued on next page.)

Figure 4.6 (Concluded.)

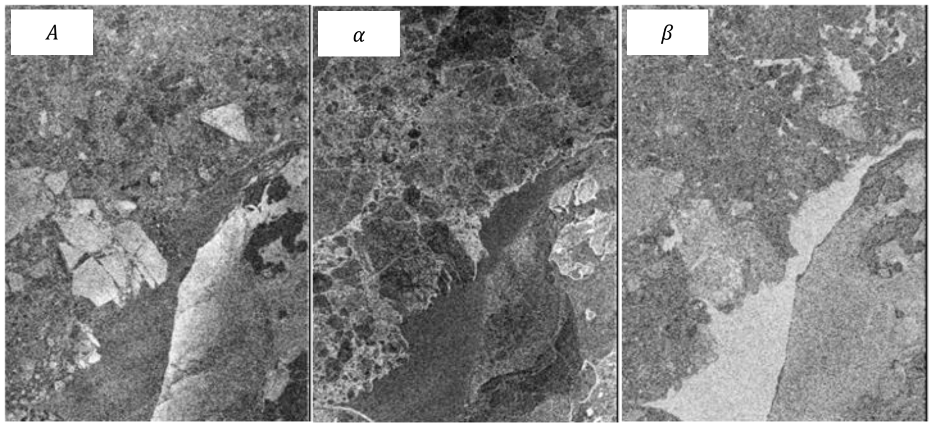

Figure 4.6. Polarimetric parameter images of sea ice types and open water from Radarsat-2 SAR data acquired on 4 May, 2008. Darker tone in the grey level images correspond to low parameter values and brighter tone to high parameter values.

4.4.2.3 Total power ($SPAN$)

A positive shift in PDFs of all ice classes is observed in the study-2 when compared to study-1 (Figure 4.9f). The shift in PDFs is similar to σ^0_{hh} and σ^0_{vv} and are likely due to the same effects of incidence angle and geophysical properties. No significant difference in terms of ice type discrimination potential of $SPAN$ exists between the two studies. Only SFYI could be separated using $SPAN$ in either of the studies. Signatures of all other classes are mixed. Although there is a decrease in overall classification accuracy of $SPAN$ in the study-2 by 5.57%, the classification accuracy of SFYI has increased by 6.03%.

4.4.2.4 Co-polarized phase difference (ϕ_{hh-vv})

Comparison of ϕ_{hh-vv} grey level images (Figure 4.4 vs Figure 4.6), PDF plots (Figure 4.10g) and classification results (Table 4.4 vs Table 4.5) shows that ϕ_{hh-vv} is highly consistent between the two studies but at the same time it is one of the least useful parameters for classification of FYI.

4.4.2.5 Co-polarized correlation coefficient (ρ_{hhvv})

The lowest ρ_{hhvv} response is observed for DFYI and highest for OW in study-1 (Figure 4.6 and Figure 4.10h). This is not the case in study-2 where DFYI exhibits similar response to RFYI and SFYI (Figure 4.4 and Figure 4.10h). This indicates the masking effect of brine wetted snow on DFYI. By reducing the microwave penetration depth at C-band, snow decreases the multiple and surface scattering component, thus increasing the ρ_{hhvv} and making it appear similar to RFYI and SFYI. OW shows highest response in both studies. Classification results from both the studies indicate that only OW could be separated from other ice classes (Table 4.4 vs Table 4.5). There is some consistency shown by ρ_{hhvv} in classification of sea ice types when compared between the two studies, although the overall accuracy in the study-2 decreased by 1.67% and OW accuracy increased by 3.24%.

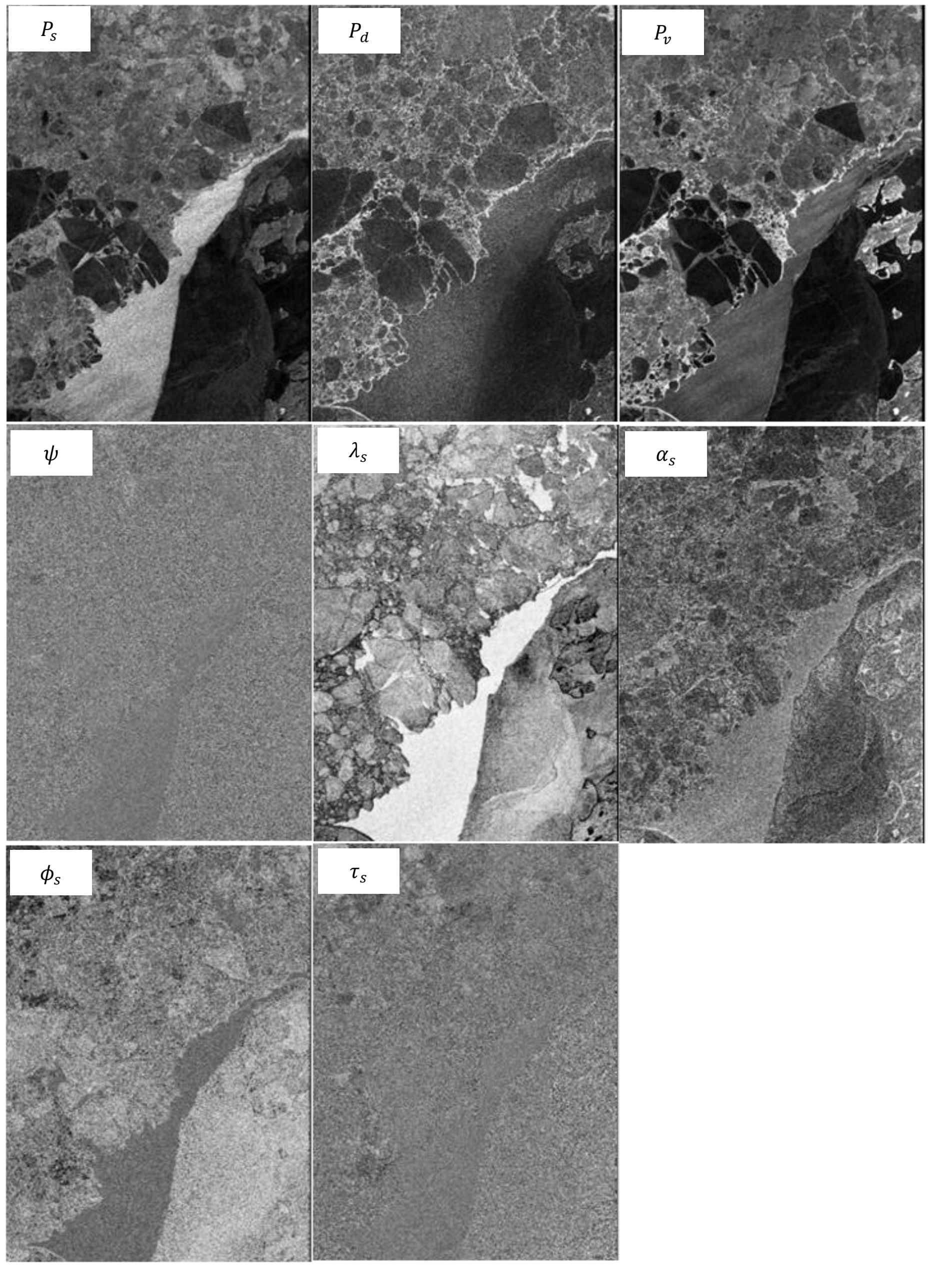

Figure 4.7. Polarimetric parameter images of sea ice types and open water from Radarsat-2 SAR data acquired on 4 May, 2008. Darker tone in the grey level images correspond to low parameter values and brighter tone to high parameter values.

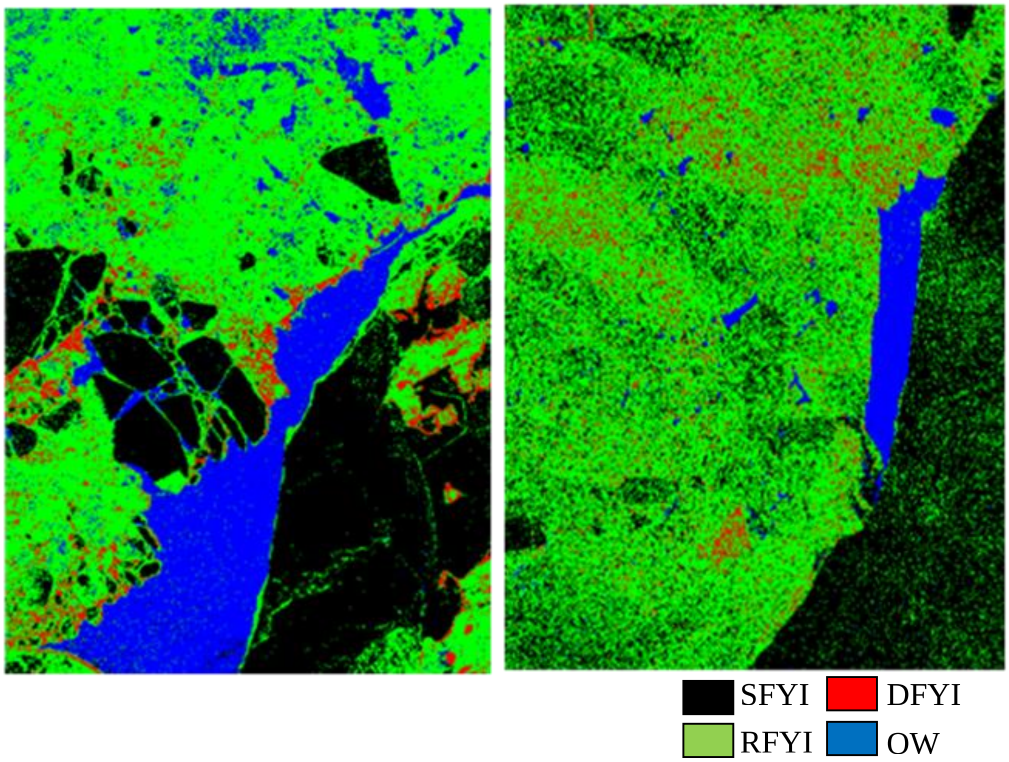

*Figure 4.8. Classified polarimetric images of sea ice types and open water from Radarsat-2 SAR data acquired on 4 May (left) and 14 May, 2008 (right). On the left image, a three-parameter classification is shown ($\boldsymbol{\sigma^0_{vv}}$- $\boldsymbol{H}$-$\boldsymbol{\sigma^0_{hv}}$); with an accuracy of 90.63% (with permission from Gill and Yackel, 2012). On the right image, a two-parameter classification is shown ($\boldsymbol{H}$-$\boldsymbol{\sigma^0_{hv}}$); with an accuracy of 83.77***%.***

4.4.2.6 Entropy, anisotropy, alpha angle and beta angle (H, A, α , β)107

The signature response of H for DFYI and OW has decreased whereas for SFYI and RFYI it increased in the study-2 when compared to study-1 (Figure 4.10i). No consistent trend in signature response of H is visible as a function of change in incidence angle or geophysical conditions between the two studies. At least three classes i.e. OW, DFYI and a group of SFYI and RFYI were discriminated successfully in study-1. This is also evident in the classification results (Table 4.5) and grey level image of H (Figure 4.6), where DFYI exhibits a brighter tone, OW as dark black tone and SFYI and RFYI as grey tone. The signature trend remains nearly the same in the study-2 except for DFYI which is now confused with SFYI and RFYI (Figure 4.10i). Only OW and a group of all other ice classes could now be discriminated. DFYI, SFYI and RFYI represent a single class in the study-2. The classification results of the study-2 (Table 4.4) show an increase in accuracy of OW by 10.66% whereas the overall classification accuracy and all other class specific accuracies have decreased.

The signature response of A in the study-2 as compared to study-1 exhibits a significant difference. None of the ice classes were significantly classified in study-1 (Figure 4.10j), whereas one class i.e. OW could be separated in the study-2. Visual inspection of grey level images of both the studies shows this difference, where bright signatures of OW are visible in Figure 4.4 and not in Figure 4.6. The overall classification accuracy of A increased by 11.95%. Thus, A becomes a useful parameter for the OW discrimination in the study-2 but with inconsistency in signature response.

Large signature differences are also observed in α, especially with respect to DFYI and OW. The signatures of both the classes (OW and DFYI) have decreased. DFYI exhibited distinctively higher response in study-1, which is evident in PDFs (Figure 4.10k) and grey level image (Figure 4.6). This is not the case in the study-2 where signatures of DFYI are now confused with SFYI and RFYI. On the other hand, the signatures of OW that were mixed with SFYI and RFYI in study-1 are now distinctively lower and separate (Figure 4.10k). OW is classified with significance (86.05%) in the study-2 whereas DFYI was classified significantly (61.95%) in study-1 (Table 4.4 and Table 4.5). Beta angle (β) is highly consistent in terms of signature response and classification potential. In both the studies, β demonstrates the capability to separate OW from other classes. Although the overall classification accuracy and OW accuracy has increased by 9.48% and 27.44%, respectively, β remains a poor classifier for the ice classes considered in both the studies.

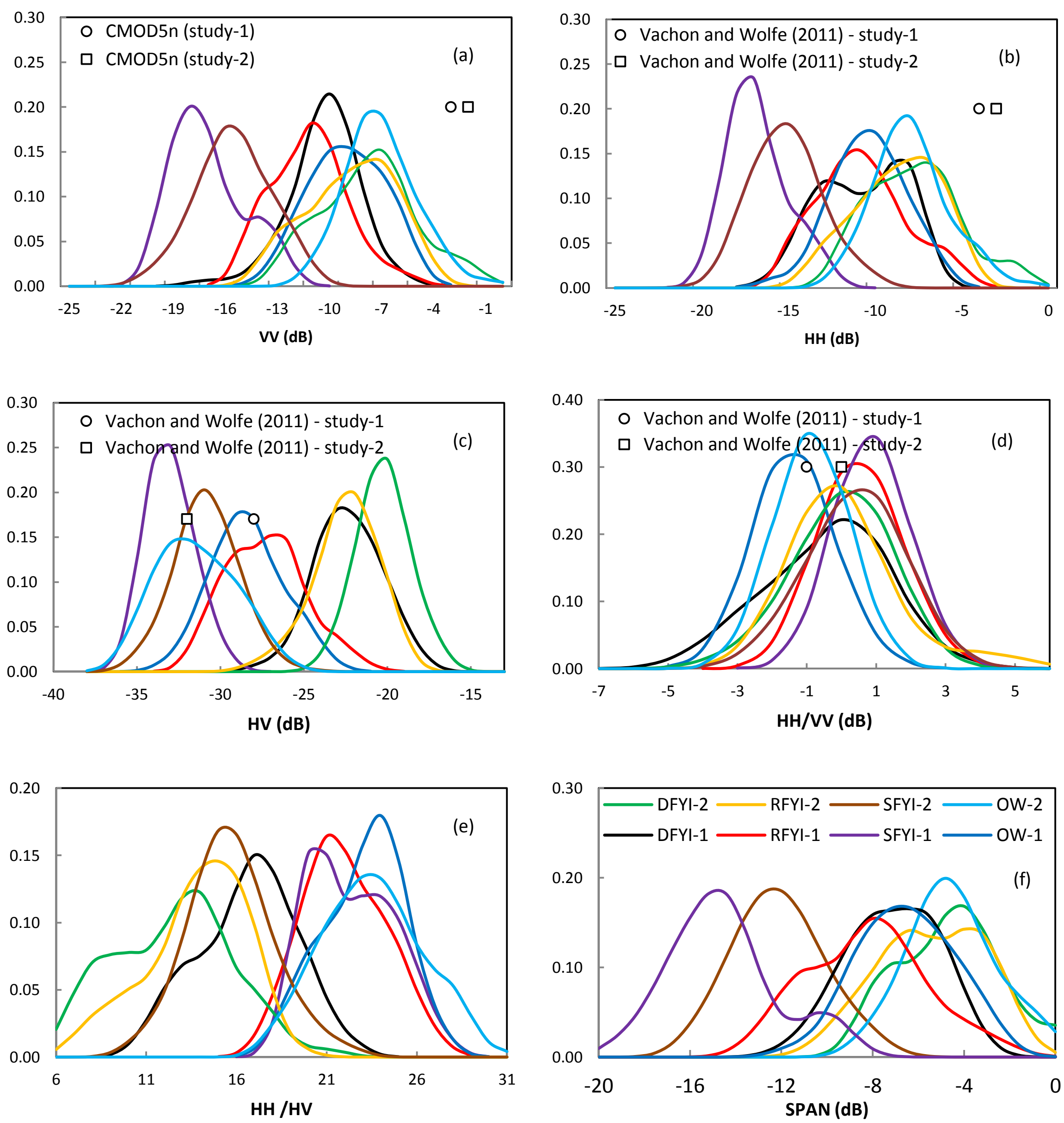

Figure 4.9. Probability density functions of polarimetric parameters computed from Radarsat-2 SAR data for study-1 (4 May, 2008) and study-2 (14 May, 2008) at incidence angles of approximately 27° and 23°, respectively. Markers represent modeled values using CMOD5n (Hersbach et al., 2007; Hersbach, 2008) and Vachon and Wolfe, 2011 as a function of wind speed and wind direction for OW.

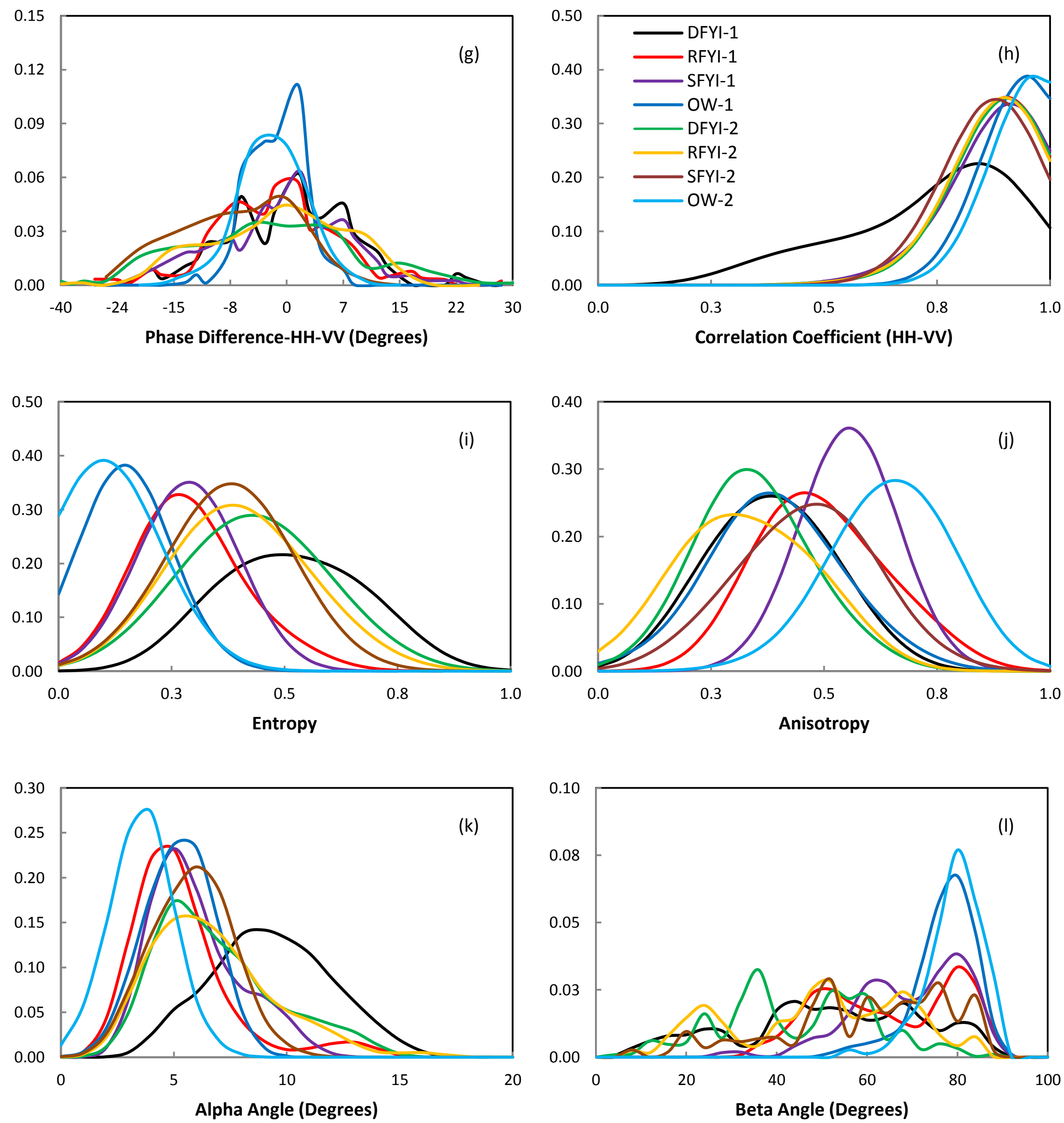

Figure 4.10. Probability density functions of polarimetric parameters computed from Radarsat-2 SAR data for study-1 (4 May, 2008) and study-2 (14 May, 2008) at incidence angles of approximately 27° and 23°, respectively.

(Continued on next page.)

Figure 4.10 (Concluded.)

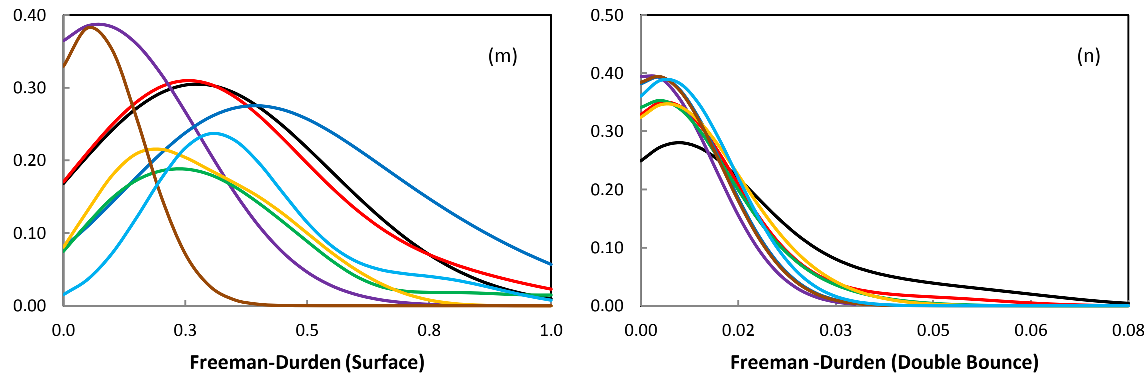

Figure 4.10. Probability density functions of polarimetric parameters computed from Radarsat-2 SAR data for study-1 (4 May, 2008) and study-2 (14 May, 2008) at incidence angles of approximately 27° and 23°, respectively.

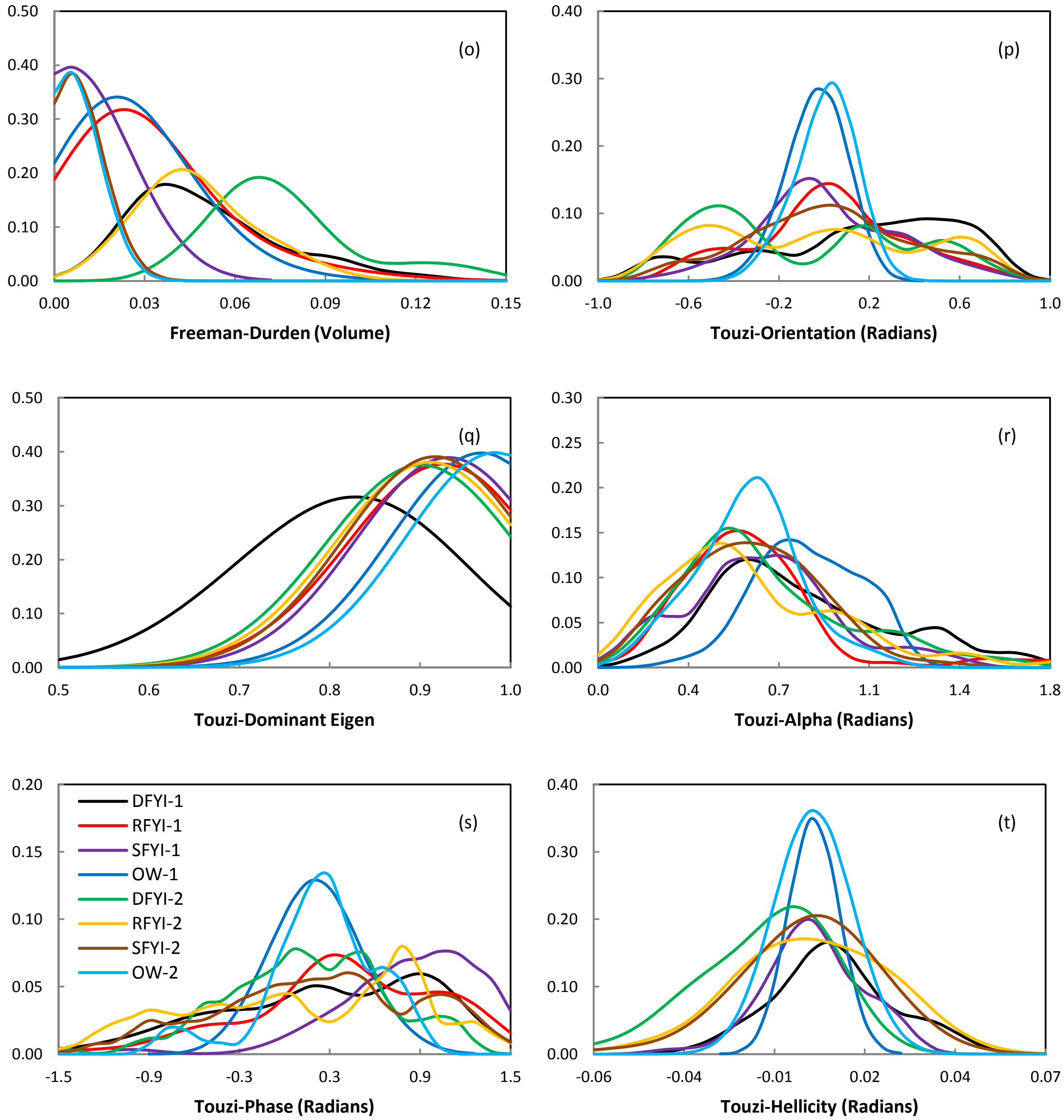

Figure 4.11. Probability density functions of polarimetric parameters computed from Radarsat-2 SAR data for study-1 (4 May, 2008) and study-2 (14 May, 2008) at incidence angles of approximately 27° and 23°, respectively.

4.4.2.7 Freeman-Durden's components (P_s, P_d, P_v)

No significant signature differences or classification potential of P_s are observed between the two studies. OW exhibits highest values, SFYI exhibits the lowest values and RFYI and DFYI exhibit overlapping intermediate values. In both studies, OW and SFYI are classified with significant (>60%) accuracies. P_s is highly consistent between the two studies.

The signature response of P_d for all ice classes, except DFYI, is similar between the studies. In study-1, P_d demonstrates the capability to separate SFYI and DFYI from other classes with significant accuracy. In the study-2, similar separation capabilities are observed however the accuracies are significantly lower than study-1, thus, rendering P_d a poor classifier for study-2 conditions.

The response of P_v for DFYI and RFYI has increased, whereas that of SFYI has decreased in the study-2 when compared to study-1 (Figure 4.11o). The similar backscatter response is also visible in the grey level images of the two studies (Figure 4.5 vs Figure 4.7). The major difference is found in the signatures of OW. In study-1, the signatures of OW overlapped with that of RFYI, whereas in the study-2, OW overlaps SFYI. This results in the change in classification potential of P_v. Three classes; SFYI, RFYI and DFYI were significantly classified in study-1, whereas in study-2, a different set of three classes (OW, RFYI and DFYI) are classified significantly. Although the overall classification accuracy of the study-2 dropped by 9.66%, the parameter still possesses the potential to accurately discriminate between three of the four ice types.

4.4.2.8 Touzi's parameters (ψ, ϕ_s, τ_s, α_s, λ_s)

Orientation angle (ψ), Alpha angle (α_s), Phase (ϕ_s) and Hellicity (τ_s) show no significant differences in terms of signatures or classification potential when compared between the two studies. ψ and ϕ_s demonstrated the potential to discriminate OW, and α_s to discriminate RFYI from all other ice types in study-1, similar results are visible here although the accuracies are significantly lower (Table 4.4 and Table 4.5). The signatures of the dominant eigenvalue (λ_s) for all ice types, except DFYI, remain mostly consistent between the two studies. DFYI is visually separable in grey level image (Figure 4.4) and a PDF plot (Figure 4.11q) for study-1 but not in the case of study-2 (Figure 4.11q). OW is discernible in both the studies. As a result, only OW is significantly classified in the study-2 and three classes i.e. OW, SFYI and DFYI are classified in study-1. Also, the overall classification accuracy of λ_s decreased by 22.12%.

4.5 Summary and conclusion

The consistency in FYI classification potential of C-band polarimetric parameters was analyzed by comparing the results of two studies conducted ten days apart. A warm period with temperatures rising above 0°C in between the two studies is believed to have changed the geophysical properties of the sea ice. This change in geophysical properties must be implicitly visible in the polarimetric response. The question is whether all polarimetric parameters were affected by these geophysical changes or some of the parameters were insensitive to these changes. Was the classification potential of all the polarimetric parameters altered with change in these geophysical conditions or are there parameters that exhibit consistent classification behavior at variable environmental settings? The intention was to identify parameters that may be applicable for generalized sea ice classification scheme.

Analyses of the results suggest that the polarimetric parameters could be grouped into six categories based on their environmental sensitivity and classification potential (Table 4.6).

Table 4.6. List of polarimetric parameters categorized on the basis of their backscatter consistency and overall classification accuracy between the two studies.

Category	Parameters	Consistency	Classification Accuracy
1	σ^0_{hh}, σ^0_{vv}, $SPAN$, P_s	High	Medium
2	$R_{hh/vv}$, ϕ_{hh-vv} , β, P_d, ψ, α_s, ϕ_s, τ_s	High	Low
3	A, α	Low	Low
4	σ^0_{hv}, P_v	Low	High
5	H, λ_s	Medium	High
6	$R_{hh/hv}$, ρ_{hhvv}	Medium	Low

Category 1: These are the parameters that were found consistent in terms of their ice type signature response between the two studies and also demonstrated medium to high classification potential. The four parameters that qualify for this category include σ^0_{hh}, σ^0_{vv}, $SPAN$ and P_s. These parameters discriminated the same ice types in both the studies, although at slightly lower accuracies in the study-2. These parameters may be applicable for sea ice classification at a wider range of environmental conditions.

Category 2: These are the parameters that were also found to be consistent in terms of their ice type signature response between the two studies, but they maintained low classification potential. Eight parameters that come under this category are $R_{hh/vv}$, ϕ_{hh-vv}, β, P_d, ψ, α_s, ϕ_s and τ_s. These parameters were found to be either noisy or showed overlapping signatures of ice types. Although these parameters showed a consistent behavior between the two studies, their use for sea ice classification is limited due to their low ice type separation capability.

Category 3: These are the parameters that were found to be highly inconsistent in terms of their ice type signature response between the two studies and also showed low classification potential. Only two parameters that entered this category are A and α. The ice type signatures of these parameters were significantly different when compared between the two studies. These parameters may not be applicable for a generalized sea ice classification scheme.

Category 4: These are the parameters that were highly inconsistent in terms of their ice type signature response between the two studies but showed high classification potential. These parameters are σ_{hv}^0 and P_v. When comparing the two studies, these parameters exhibited significant differences in at least one of the ice classes. These are possibly two of the best parameters for sea ice classification but their use in generalized sea ice classification scheme is doubtful.

Category 5: These are the parameters that were found to be somewhat consistent in terms of their ice type signature response between the two studies and also showed high classification potential. The only two parameters that came under this category are H and

λ_s. The signatures of these parameters differ only for one of the ice types when compared between the two studies. The polarimetric response for all other ice types is fairly consistent. These parameters possess the potential use for sea ice classification over wider environmental conditions.

Category 6: These are the parameters that were found to be somewhat consistent in terms of their ice type signature response between the two studies but showed low classification potential. These parameters are $R_{hh/hv}$ and ρ_{hhvv}. The signatures of these parameters differ only for one of the ice types when compared between the two studies. The polarimetric response of all other ice types is fairly consistent. Use of these parameters is limited for sea ice classification due their low classification potential.

4.6 Limitations

The analysis in the study has been performed from one perspective, where the focus was to identify parameters that exhibited consistency in signature behavior and classification potential over different environmental conditions. The other perspective could be to identify parameters that would pick up any minor changes in geophysical properties which otherwise would not be visible in many other parameters. The parameters that were found to be highly inconsistent in the study-2 may be sensitive to small property changes which are not being picked up in highly consistent parameters.

The selection of a different set of samples for classification and signature analysis for the two studies can result in different outcomes. Every attempt was made in both the studies to select accurate and pure ice type samples. This was achieved given the near match of the PDF curves of some of the polarimetric parameters.

CHAPTER FIVE:
SENSITIVITY OF C-BAND SAR POARIMETRIC PARAMETERS TO SNOW THICKNESS ON FIRST-YEAR SEA ICE

5.1 Abstract

In this chapter, C-band linear and polarimetric parameters derived from synthesis and decomposition of Radarsat-2 SAR data are analyzed and evaluated with respect to snow covers of variable thickness on smooth first year sea ice (SFYI). The study is conducted for two selected temperature conditions: 1) cold (-7.9°C) and 2) warm (-0.4°C). First, the polarimetric SAR response from the snow cover at cold conditions is analyzed with an objective to investigate the sensitivity of linear and polarimetric backscatter to snow thickness. Second, the changes in these sensitivities are examined as a function of change in surface air temperature (from -7.9°C to -0.4°C) through the changes manifested in snow geophysical and dielectric properties. The dependence of linear and polarimetric backscatter response on radar incidence angle for different snow thicknesses is also evaluated.

5.2 Introduction

Snow cover thickness on Arctic sea ice has generated increasing scientific interest in recent years. This is attributed to the increasingly important role that snow geophysical and thermodynamic processes play within the ocean-sea ice-atmosphere (OSA) system (Barber et al., 1998). These controls range from micro- to meso-scale, affecting the local habitats to the global climate system. At the micro-scale, the absorption properties of snow for photosynthetic active radiation determines the life cycle of epontic algal communities. Too thick or too thin of a snow cover hinders the algal growth by either starvation or overabundance of light (Cota and Horne, 1989). At local to regional scales, snow cover controls the life cycle of arctic seals and polar bears. At regional to hemispherical scales, snow cover governs the conductive, radiative and turbulent energy exchanges between the atmosphere and the underlying ocean, thus acting as a barrier and impeding the energy transfer and regulating the accretion and ablation of sea ice (Maykut, 1978). At a global scale, the OSA is expected to show signs of global climate change much earlier and at higher magnitudes than temperate or tropical regions. This is due to snow-sea ice albedo feedback mechanisms (Curry et. al., 1994). Snow cover thus plays a significant role in the energy balance of the OSA due to its low thermal diffusivity, low transmissivity and high albedo and is considered one of the most important variables in climate change scenarios (Williams, 1975).

Numerous fields of scientific and operational inquiry require estimates of snow thickness distribution on sea ice. As a result, a number of snow studies have been undertaken using an array of *in-situ* based (Barber et al., 1994a & 1994b & 1995; Iacozza and Barber, 2010; Sturm et al., 2002), laboratory based (Fung et al., 1994; Lytle et al., 1993; Bredow and Gogineni, 1990) and satellite imagery based techniques (Barber and Nghiem, 1999; Markus et al., 2006; Yackel and Barber, 2007; Kwok et al., 2011). *In-situ* and laboratory methods are useful for micro-scale snow analysis but are practically unviable when snow thickness information at large spatial scales is required. Therefore, current snow thickness estimates must rely on remote sensing methods. In this respect, active microwave Synthetic Aperture Radar (SAR) sensors can be useful due to their cloud penetrating and day/night data acquisition capabilities.

Snow thickness estimation using active microwave backscatter inversion (Beaven et al., 1995) and using the thermal dependence of Synthetic Aperture Radar (SAR) backscatter (Barber and Nghiem, 1999) has been attempted. The active microwave techniques exploiting the geophysical and thermodynamic properties of snow covered sea ice have demonstrated linear co-polarized backscatter to increase with snow thickness on FYI for a given increase in air temperature (Barber and Nghiem, 1999; Yackel and Barber, 2007). However, no direct empirical models have been successfully established to estimate snow thickness. Most snow studies to date have explored single or dual polarized SAR data. The use of full polarimetric SAR for snow cover studies is either missing or limited. This is partly due to the relative newness of polarimetric sensors, with Radarsat-2 operational only since 2007, ALOS PALSAR since 2006 to 2011 and polarimetric experimental modes on TerraSAR-X since 2008. However, polarimetric SAR investigations of sea ice have been performed (Wakabayashi et al., 2004; Scheuchl et al., 2005; Gill and Yackel, 2012 and Gill et al., 2013). These studies have highlighted the additional information contained in polarimetric SAR for sea ice classification. Similarly, the polarimetric SAR investigations of snow cover may provide additional information to help in the development of snow thickness estimation algorithms. Investigation of the polarimetric SAR signatures of snow cover also supports the new polarimetric and hybrid-polarimetry satellites that will provide additional SAR data (e.g. ALOS PALSAR-2, Radarsat Constellation Mission, RISAT-1 and Sentinel-1).

In the current study, we investigate the effect of snow thickness on C-band SAR polarimetric parameters derived using synthesis and decomposition techniques. More specifically the objectives are: 1) to analyze the sensitivities of SAR polarimetric parameters to snow thickness over land-fast smooth SFYI at cold (-7.9°C) and warm (-0.4°C) conditions; and 2) to analyze the changes in these parameter sensitivities with increase in the air temperature (from -7.9°C to -0.4°C). The overall intention is to identify if any of the SAR polarimetric parameters included in the study exhibit any relationship to snow thickness. If yes, then of what kind and under what environmental conditions?

5.3 C-band microwave scattering as a function of snow thickness

C-band polarimetric microwave backscatter from winter snow-covered SFYI is largely described by a combination of: a) surface scattering from the air-snow interface, the dry snow brine-wetted snow interface, and the snow-sea ice interface; and, b) volume scattering from the dry snow, the brine-wetted snow, and the upper layers of sea ice (Figure 5.1). During cold conditions, backscatter is generally low from snow-free SFYI. It increases with the presence of snow on sea ice. Small scale roughness and dielectric contrast at snow-ice interface are the primary factors contributing to backscatter increase when snow thickness increases from 0 to 12 cm (Beaven et al. 1995). With further increases in snow thickness, snow thermodynamics play a role in contributing to the total backscatter (Barber and Nghiem, 1999). Thick snow, due to its low thermal conductivity, results in relatively higher temperature at the snow-ice interface. In contrast, for the same winter air temperature, thin snow exhibits lower temperatures at the snow ice interface. The increased snow-ice interface temperature in thick snow induces an increase in brine volume in the basal snow and the adjacent sea ice layer (Barber and Nghiem, 1999). Brine acts as an effective scatterer and as a consequence radar backscatter increases.

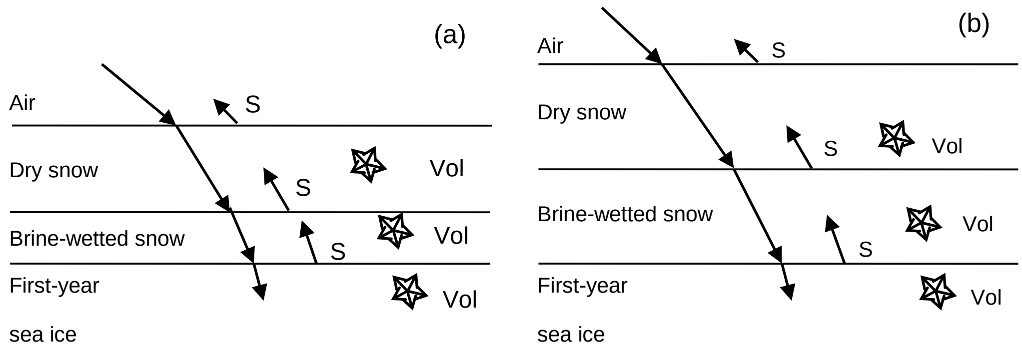

Figure 5.1. Conceptual schematic of C-band microwave interaction with snow-covered SFYI demonstrating: surface (S), and volume (Vol) scattering mechanisms, for a) thin snow and b) thick snow during cold conditions. Thicker brine-wetted snow layer for thick snow covers (figure b) is associated with an increase in volume scattering component to the total scattering.

5.4 C-band microwave scattering as a function of temperature change

For a given snow thickness on SFYI, an increase in air temperature (from -18°C to -11°C) results in an increase in brine volume at the snow-ice interface, following the eutectic phase distribution curve (Barber and Nghiem, 1999; Cox and Weeks, 1983) (Figure 5.2). Consequently, backscatter at C-band also increases (Barber and Nghiem, 1999). The increase in backscatter is attributed to several factors: (1) strengthening of the scattering effects due to enhanced contrast between the brine and the background (Barber and Nghiem, 1999); (2) stronger backscatter effects due to enlargement of brine scatterers at higher temperatures leading to large scattering cross-sections (Barber and Nghiem, 1999) ; (3) an overall higher brine volume in the snow and sea ice layers at higher temperatures (Barber and Nghiem, 1999); and (4) an enhanced contrast (effective permittivity) across the snow-sea ice interface (Barber and Nghiem, 1999). For thicker snow covers and rougher ice surfaces, the increase in C-band backscatter is less (Barber and Nghiem, 1999; Yackel and

Barber, 2007). With further increase in air temperature (approaching ~ 0ºC) snow surface layers experience water in liquid phase, which absorbs C-band microwaves and reduces the penetration depth (Barber et al., 1994b). In the case of thick snow, the scattering from basal snow layers or the sea ice surface can be highly attenuated or completely absorbed, thus reducing the total backscatter (Mäkynen and Hallikainen, 2004).

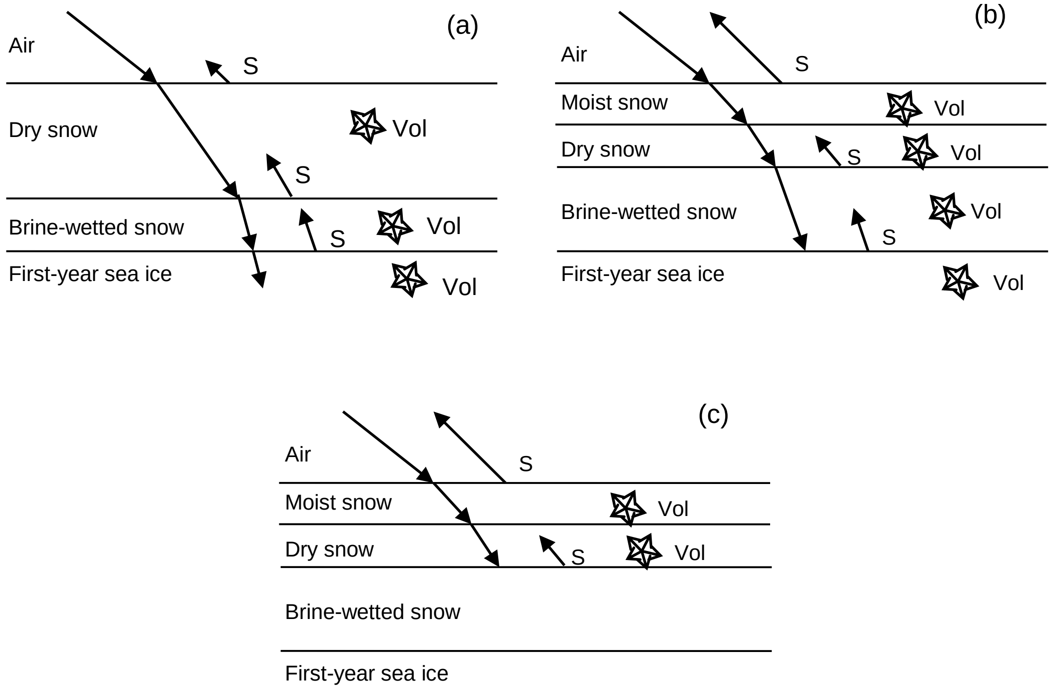

Figure 5.2. Conceptual schematic of C-band microwave interaction with snow-covered SFYI demonstrating: surface (S), and volume (Vol) scattering mechanisms for snow, under: a) cold conditions, b) warm/moist conditions c) very moist conditions.

5.5 Methods

5.5.1 Study area

This study was conducted as part of the International Polar Year - Circumpolar Flaw Lead (IPY-CFL) campaign conducted from 1 May - 20 May, 2008. The study area comprised of snow covered land-fast SFYI ice located on the west coast of Parry Peninsula in Franklin Bay (70˚N-125˚W). The location of the study area with respect to Canada and the extent of Radarsat-2 images overlaid with snow sites are shown in figure 5.3.

5.5.2 Polarimetric SAR data

Nine polarimetric Radarsat-2 SAR images acquired concomitant to the field work were utilized in the study (Table 5.1). All images were fine quad-pol products at spatial resolutions ranging from 5.2 to 7.6 meters. The images varied in incidence angle, with scene centers ranging between 22.3° and 37.0°. The images were pre-processed using a 7×7 refined Lee filter (Lee et al., 1981) to increase the effective number of looks and to reduce speckle. The linear and polarimetric parameters used in the analysis were, the horizontal transmit-receive intensity (σ_{hh}^0), vertical transmit-receive intensity (σ_{vv}^0), horizontal transmit-vertical receive intensity (σ_{hv}^0), co-polarized ratio (R_{co}), co-polarized phase difference (ϕ_{hh-vv}), co-polarized correlation coefficient (ρ_{co}), decomposition parameters i.e. entropy (H), anisotropy (A), alpha angle (α) and beta angle (β) after (Cloude and Pottier, 1997), decomposition parameters i.e. alpha (α_s), phase (ϕ_s), orientation angle (ψ), dominant eigenvalue (λ_s) and helicity (τ_s) after (Touzi, 2007), decomposition parameters indicating power contributions due to surface scattering (P_s), double bounce scattering (P_d) and volume scattering (P_v) after (Freeman-Durden, 1998) and synthesized parameters i.e.

maximum of the degree of polarization (P_{max}), minimum of the degree of polarization (P_{min}), fractional polarization (f_p) and coefficient of variation (γ_{var}) after (Touzi et al., 1992, Van Zyl et al., 1987, Zebker et al., 1987). A detailed description of the polarimetric parameters is presented in Table 5.2.

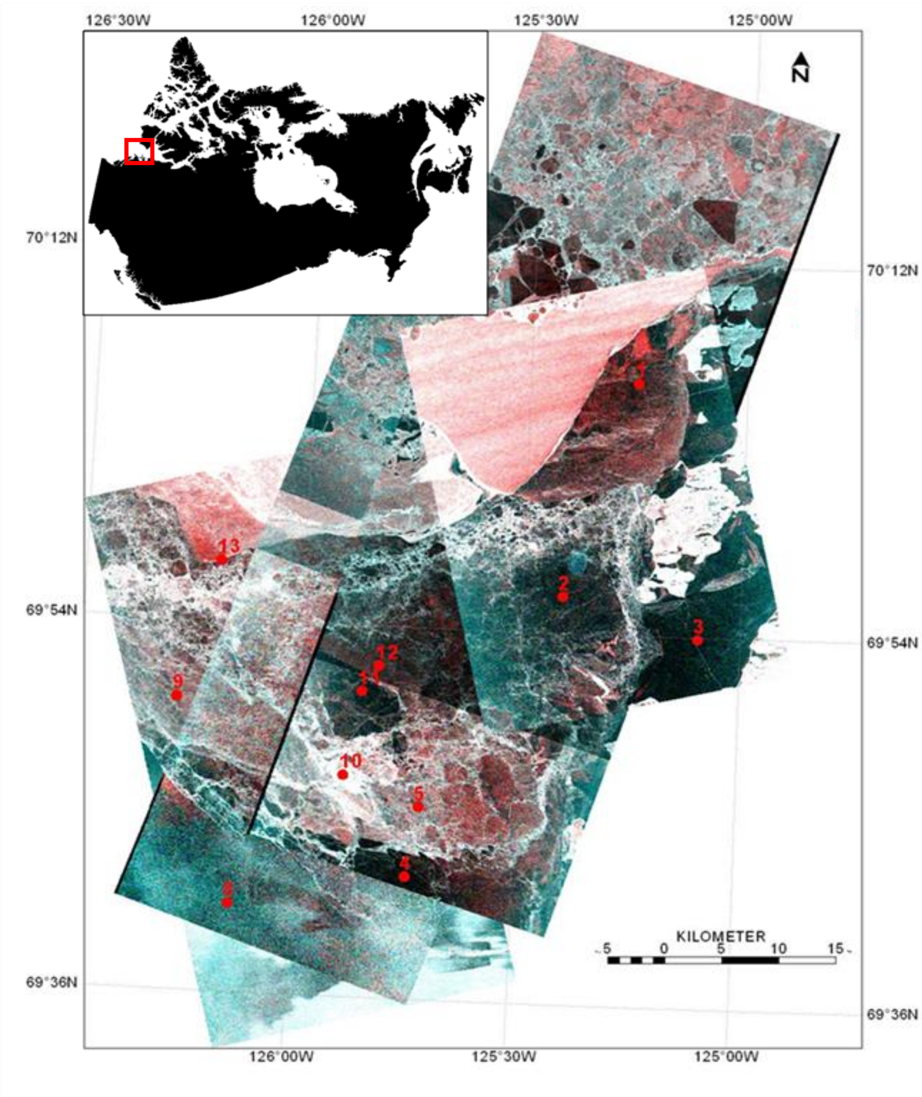

Figure 5.3. Study area in Franklin Bay, Northwest Territories, Canada. Color composite mosaic (Red: HH, Green: HV, Blue: HV) of the Radarsat-2 images acquired during the study period (1 May - 20 May, 2008). Snow sampling sites are shown by red dots.

Table 5.1. Details of the polarimetric Radarsat-2 imagery utilized in the study and the surface air temperature conditions at the time of image acquisition.

Date	Time (UTC)	Orbit	Incidence angle (°)	No of images	Temperature °C
2008-05-04	01:41:16	Asc	35.49 - 37.04	1	-7.9
2008-05-04	15:18:20	Desc	26.93 - 28.75	3	-8.0
2008-05-11	01:37:02	Asc	31.38 - 33.05	2	-3.5
2008-05-14	15:26:42	Desc	22.26 - 24.17	3	-0.4

Table 5.2. Details of the polarimetric parameters computed from filtered Radarsat-2 data. For complete derivation and explanation of the parameters, see the respective references.

Symbol	**Nomenclature**	**Reference**	**Derivation**	**Sensitivity / Indicator of**
σ_{hh}^0	Linear power (horizontal)	Drinkwater et. al., 1992	$\sigma_{pq}^0(\theta_0) = \frac{4\pi r^2 \langle \lvert E_p^s \rvert^2 \rangle}{a \lvert E_q^i \rvert^2}$	Surface roughness, dielectric properties.
σ_{vv}^0	Linear power (vertical)	Drinkwater et. al., 1992	θ_0 = incidence angle p = received polarization q = transmitted polarization	Surface roughness, dielectric properties.
σ_{hv}^0	Cross-polarized power	Drinkwater et. al., 1992	E_p^s = scattered wave electric field E_q^i = incident wave electric field a = area illuminated by radar r = distance between target and antenna	Surface roughness, dielectric properties.
$R_{hh/vv}$	Co-polarized ratio	Drinkwater et. al., 1992	$R_{hh/vv} = \frac{\sigma_{hh}^0}{\sigma_{vv}^0} = \frac{\langle S_{hh} S_{hh}^* \rangle}{\langle S_{vv} S_{vv}^* \rangle}$ S= scattering matrix	Surface roughness, dielectric properties.
$SPAN$	Total power	Drinkwater et. al., 1992	$SPAN = \langle S_{hh} S_{hh}^* \rangle + \langle S_{vv} S_{vv}^* \rangle + 2\langle S_{hv} S_{hv}^* \rangle$	Surface roughness, dielectric properties.
ϕ_{hh-vv}	Co-polarized phase difference	Drinkwater et. al., 1992	$\phi_{hh-vv} = tan^{-1}\left[\frac{Im\langle S_{hh} S_{vv}^* \rangle}{Re\langle S_{hh} S_{vv}^* \rangle}\right]$	Surface roughness, dielectric properties.
ρ_{hhvv}	Co-polarized correlation coefficient	Drinkwater et. al., 1992	$r_{hhvv} = \left\lvert \frac{\langle S_{hh} S_{vv}^* \rangle}{\sqrt{\langle S_{hh} S_{hh}^* \rangle \langle S_{vv} S_{vv}^* \rangle}} \right\rvert$	
H	Entropy	Coude-Pottier, 1997	$\mathrm{H} = \sum_{i=1}^{3} -P_i \, log_n(P_i)$ $P_i = \frac{\lambda_i}{\sum_{i=1}^{3} \lambda_i}$ λ_i= eigenvalues of coherency matrix	Degree of randomness. Range = 0-1 H=0, One dominant scattering (pure single or double bounce). H=1, Mixed scattering.
A	Anisotropy	Coude-Pottier, 1997	$\mathrm{A} = \frac{\lambda_2 - \lambda_3}{\lambda_2 + \lambda_3} = \frac{P_2 - P_3}{P_2 - P_3}$	Scatterer shape, size, roughness. Range = 0-1 $A = 1$, spherical scatterers or smooth surface. $A < 1$, needle like scatterers or rough surface.
α	Alpha angle	Coude-Pottier, 1997	$\alpha = P_1\alpha_1 + P_2\alpha_2 + P_3\alpha_3$	Dominant scattering. Range = 0°-90° α = 0°, trihedral isotropic /

				surface scattering; α = 45°, dipole / volume scattering; $\alpha = 90°$, isotropic dihedral / double bounce scattering.
β	Beta angle	Coude-Pottier, 1997	$\beta = P_1\beta_1 + P_2\beta_2 + P_3\beta_3$ α_i and β_i = target scattering mechanism and orientation angle	Scattering orientation. Range = 0°-180°
P_s	Surface scattering power	Freeman-Durden, 1998	$P_s = f_s(1 + \|\beta\|^2)$ $\beta = \langle S_{hh}S_{vv}^*\rangle$	Surface / Bragg scattering. Range = 0-1 (power), 0-100(%)
P_d	Double-bounce scattering power	Freeman-Durden, 1998	$P_d = f_d(1 + \|\alpha\|^2)$ $\alpha = \langle S_{hh}S_{vv}^*\rangle$	Anisotropic dihedral scattering. Range = 0-1 (power), 0-100(%)
P_v	Volume scattering power	Freeman-Durden, 1998	$P_v = 8f_v/3$ f_s, f_d, f_v = VV power contribution from surface, double bounce and volume scattering.	Randomly oriented dipole volume scattering. Range = 0-1 (power), 0-100(%)
ψ	Orientation	Touzi, 2007	$\vec{V}^{orient-inv} = \lambda_s.\left[\cos\alpha_s \cos 2\tau_s, \sin\alpha_s e^{j\phi_{\alpha_s}}, -j\cos\alpha_s \sin 2\tau_s\right]^T$	Measure of target tilt angle.
ϕ_s	Phase	Touzi, 2007	-	Absolute phase of target.
τ_s	Helicity	Touzi, 2007	-	Degree of target scattering symmetry.
α_s	Alpha	Touzi, 2007	-	
λ_s	Dominant eigenvalue	Touzi, 2007	-	Maximum target amplitude.
P_{max}	Maxima of degree of polarization	Touzi et. al., 1992	$P = \frac{\lambda_1 - \lambda_2}{\lambda_1 + \lambda_2} = \frac{\sqrt{\langle s_1^2\rangle + \langle s_2^2\rangle + \langle s_3^2\rangle}}{\langle s_0\rangle}$	Scattering mechanism, complexity, spatial heterogeneity.
P_{min}	Minima of degree of polarization	Touzi et. al., 1992	λ_1, λ_2 = real positive eigenvalues of coherency matrix. $\langle s_0\rangle, \langle s_1\rangle, \langle s_2\rangle, \langle s_3\rangle$ = elements of stokes vector.	
γ_{var}	Coefficient of variation	Van Zyl et. al., 1987	$\gamma_{var} = \frac{P_r^{min}}{P_r^{max}}$ P_r^{max} = maxima of received power. P_r^{max} = minima of received power.	Variation in scattering. Due to different scatterers or diffuse multiple scattering / noise.
f_p	Fractional polarization	Zebker et. al., 1987	$f_p = \frac{P_r^{max} - P_r^{min}}{P_r^{max} + P_r^{min}}$	Purity of polarization. Single vs. multiple scattering.

5.5.3 Meteorological data

Hourly mean surface air temperature (SAT, ±0.1°C) was acquired from the Environment Canada Cape Parry meteorological station (70.16°N, 124.71°W), and the closest available precipitation data (±0.1mm) were obtained from the Environment Canada Paulatuk meteorological station (69.21°N, 124.04°W) (Figure 5.4). Air temperatures at the time of image acquisitions are presented in Table 5.1. No significant precipitation events were observed between the first and last image acquisitions (4 May-14 May, 2008).

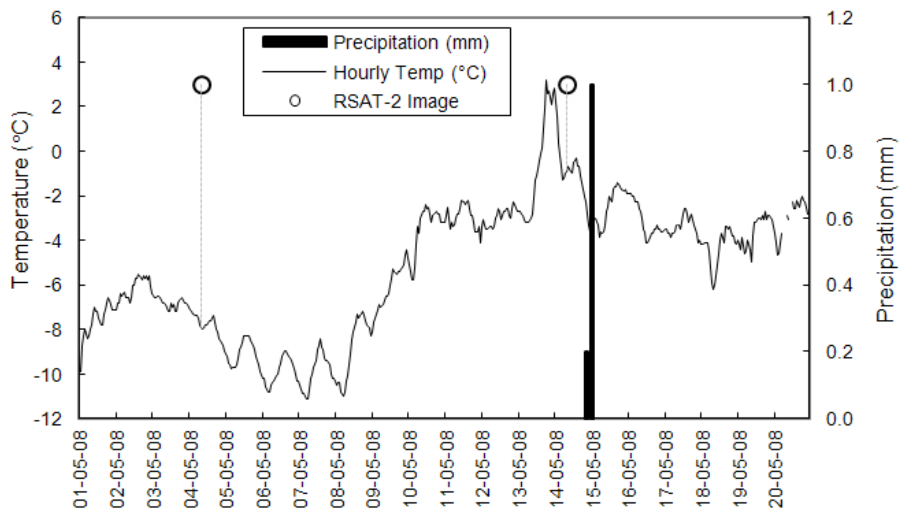

Figure 5.4. Meteorological conditions during the study period (4 May - 20 May, 2008). Data was acquired from Environment Canada Cape Parry meteorological station.

5.5.4 Snow thickness data

Snow thickness for 13 sites were measured *in-situ* over pre-identified sufficiently large (~500 m²) and homogeneous SFYI patches using intersecting transects of 100-200 meters in length, each running parallel and orthogonal to the predominant snow drift patterns. Measurements were acquired at one meter intervals using a meter stick, read to the nearest centimeter. The mean snow thickness for the thinnest and thickest snow site ranged between 6.3±5.9 cm and 37.6±12.7 cm, respectively (Figure 5.5). Standard deviations from the thin snow sites were always lower compared to the thick snow sites, indicating the effect of increasing variability for thicker snow (Sturm et al., 2002).

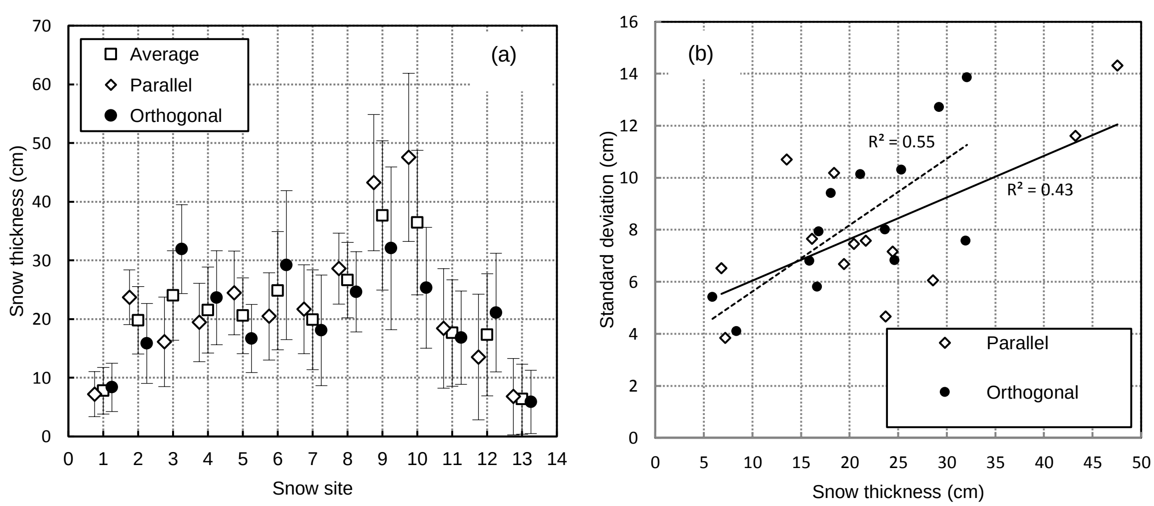

Figure 5.5. Measured snow thickness distribution for the 13 snow sites. Diamonds denote means of the snow thickness measurements acquired parallel to the snow drift and circles denote means of the snow thickness measurements acquired orthogonal to the snow drift pattern. a) Squares represent the averages of the parallel and orthogonal measurements with error bars as standard deviations. b) The relationship between snow thickness and standard deviation for orthogonal and parallel measurements.

5.5.5 Snow property data

Snow properties were measured *in-situ* by excavating snow pits of ~0.5 m^2 in size (Figure 5.6). All measurements were carried out on the non-illuminated face of the snow pit. Snow temperatures were measured using a digital thermometer (accuracy ±0.2 °C) at 2cm vertical intervals in the snowpack. Snow samples at each interval were extracted using a rectangular snow sampler (volume = 66 cm^3) and snow densities were calculated using the gravimetric method (±0.04 g cm^{-3}) after Drobot and Barber, 1998. Snow salinity was determined for each interval using a digital conductivity meter (±0.05%) from melted snow density samples. The brine volume fraction, dielectric constant and dielectric loss of snow were modeled from measured snow properties after Geldsetzer et al. (2009a). Snow properties on the day of image acquisitions were not always measured. To aid in the analysis, snow-ice interface temperatures were modeled using a simple 1-D thermodynamic model after (Nakawo and Sinha, 1981) (Table 5.3). The following data were used: 1) SAT; 2) mean snow thickness per field site; 3) a mean snow density for all field sites (0.35 g/cm^3); 4) the melting / freezing point of sea ice (-1.8°C); 5) the thermal conductivities of snow (Mellor, 1977) and ice (Schwerdtfeger, 1963); and 6) sea ice thickness (1.5 meters).

Table 5.3. Modeled snow-ice interface temperature for thin, medium and thick snow classes, for Radarsat-2 SAR acquisition date/times of May 4 (SAT = -7.9°C), May 11(SAT = -3.5°C) and May 14, 2008 (SAT = -0.9°C).

Snow class	Snow thickness (cm) mean (std. dev)	Temperature (°C) 4 May, 2008	Temperature (°C) 11 May, 2008	Temperature (°C) 14 May, 2008
Thin	7.78 (3.96)	-5.4	-2.8	-1.3
Medium	20.56 (6.47)	-3.9	-2.4	-1.5
Thick	36.44 (12.30)	-3.3	-2.2	-1.6

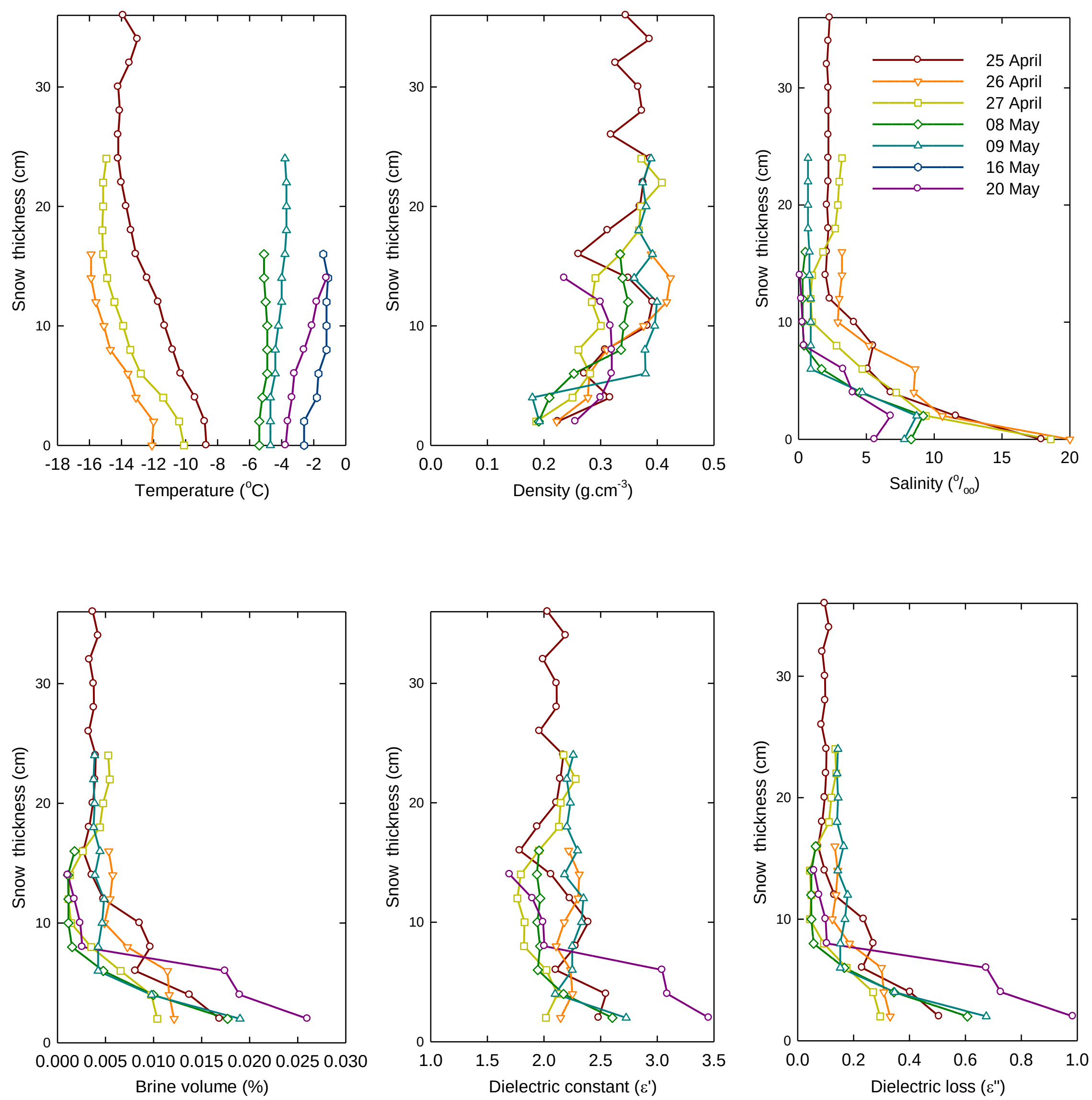

Figure 5.6. Measured and modelled properties of snow over SFYI. Brine volume and dielectric properties are modelled. Bottom represents the snow-ice interface at 0 cm.

5.6 Results and discussion

5.6.1 Incidence angle dependence

The dependence of linear and polarimetric backscatter response on radar incidence angle (θ_i) was investigated for snow sites 1, 5 and 10 (Figure 5.3) exhibiting mean snow thicknesses of 7.7±3.9 cm (thin), 20.5±6.4 cm (medium) and 36.4±12.3 cm (thick), respectively. These sites were selected to encompass the range of snow thicknesses commonly encountered over SFYI in the Canadian Arctic and to facilitate maximum snow site coverage in the acquired Radarsat-2 images. Circular buffers with a radius of 200 meters from the intersection of snow measurement transects were used to extract samples from the imagery. Approximately 5000 pixels for each site were extracted and utilized in the analysis. Four Radarsat-2 images acquired on 4 May ($\theta_i \approx 36°$ and $\theta_i \approx 27°$) and two Radarsat-2 images acquired on 11 May, 2008 ($\theta_i \approx 32°$) were used. The small number of Radarsat-2 images precluded a detailed analysis; thus the results provided are only first estimates. It must be noted that there a difference in SAT by ~4.4°C between 4 May (-7.9°C) and 11 May, 2008 (-3.5°C). The difference in SAT is expected to affect the snow-ice geophysical properties through increase in brine volume fraction in the basal snow, which in turn may affect the incidence angle dependence analysis. The change in snow covered sea ice backscatter (European Remote Sensing Satellite, ERS-1) caused by the change in air temperature from -18ºC to -11ºC was on the order of 1-3 dB (Barber and Nghiem, 1999). This is small in comparison to the current study incidence angle dependence estimates.

Our results demonstrate both positive and negative correlations to θ_i (Table 5.4). Positive correlations were observed for polarimetric parameters ϕ_{hh-vv}, H, α, P_v, ψ, τ_s, α_s

and γ_{var}, whereas a negative correlations existed for all other parameters except β, where the relationship was ambiguous (Table 5.4). The relationship between backscattering coefficient (σ^0) and θ_i from 19° to 46° has been described by a linear fit (Mäkynen et al., 2002). We modeled the relationship between polarimetric parameters and θ_i using simple linear regression (Table 5.4). As expected, the slope of σ_{vv}^0 and σ_{hh}^0 versus θ_i was steeper (more negative) than σ_{hv}^0 for all snow thickness classes. This is because the θ_i dependence of σ^0 is higher at co-polarization than at cross-polarization (Mäkynen et al., 2002). With respect to polarimetric parameter relationships to θ_i , the decrease in P_{max} and P_{min} with an increase in θ_i (Table 5.4) for all snow thicknesses was observed. This indicates that snow covered SFYI is less polarized at high θ_i , signifying dominance of multiple / volume scattering at oblique angles. γ_{var} also showed an increase with θ_i whereas f_p showed the reverse, indicating that the purity of polarization and heterogeneity in scattering elements that compose the signature also decreases with θ_i . In other words, the lower the f_p , the greater is the multiple scattering (un-polarized component) and less is the purity of the signature (Zebker et al., 1987). These results were consistent with the decomposition parameters derived after (Cloude-Pottier, 1997), where H increased and A decreased with an increase in θ_i . H is an indicator of degree of randomness and A is sensitive to the scatterer's shape, size and surface roughness. An increase in H signifies an increase in mixed scattering, whereas a decrease in A corresponds to scattering from heterogeneous material. This was confirmed by the three component scattering parameters derived after (Freeman-Durden, 1998), showing a decrease in surface and double bounce scattering and an increase in volume scattering with an increase in θ_i .

Table 5.4. Polarimetric signatures of thin (7.7±3.9 cm), medium (20.5±6.4) and thick (36.4±12.3 cm) snow covers over SFYI for different radar incidence angles and simple linear regression model parameters.

Polarimetric Parameter	**Snow Thickness (cm)**	**Signature (Mean and Standard Deviations)**						**Slope**	**Intercept**
		26°- 28°		**31°-33°**		**35°-37°**			
		mean	**std.**	**mean**	**std.**	**mean**	**std.**		
σ^0_{hh}	Thin	-20.92	1.96	-21.30	1.90	-23.47	1.84	-0.27	-13.18
	Medium	-19.89	2.14	-20.24	2.01	-22.24	1.95	-0.25	-12.75
	Thick	-13.98	2.21	-15.32	2.12	-17.01	2.04	-0.33	-4.85
σ^0_{vv}	Thin	-20.93	1.99	-21.50	2.53	-23.82	2.04	-0.31	-12.20
	Medium	-20.10	2.17	-21.11	2.01	-22.71	1.94	-0.28	-12.26
	Thick	-14.25	2.16	-16.02	2.06	-18.01	2.09	-0.41	-2.96
σ^0_{hv}	Thin	-35.71	1.69	-36.89	2.53	-37.95	1.55	-0.24	-28.99
	Medium	-34.39	1.86	-35.09	1.72	-36.72	1.56	-0.25	-27.35
	Thick	-26.83	2.12	-27.29	1.95	-29.18	1.59	-0.25	-19.74
$R_{hh/vv}$	Thin	-0.018	1.05	-0.205	1.31	-0.350	1.26	-0.036	0.97
	Medium	-0.222	1.15	-0.869	1.40	-0.864	1.21	-0.073	1.67
	Thick	-0.277	1.50	-0.704	1.33	-1.000	1.43	-0.080	1.88
$SPAN$	Thin	-17.34	0.98	-17.82	1.26	-18.90	1.69	-0.16	-12.65
	Medium	-16.08	1.28	-16.13	1.66	-17.27	1.50	-0.12	-12.46
	Thick	-11.26	1.35	-12.03	1.18	-13.91	1.40	-0.28	-3.29
ϕ_{hh-vv}	Thin	7.65	8.25	9.21	11.58	9.92	11.44	0.25	-0.84
	Medium	10.89	8.196	8.19	12.07	12.73	12.27	0.17	-5.10
	Thick	9.57	11.05	9.59	11.50	12.89	12.38	0.35	0.51
ρ_{hhvv}	Thin	0.88	0.06	0.84	0.09	0.82	0.09	-0.006	1.06
	Medium	0.89	0.07	0.80	0.09	0.81	0.09	-0.009	1.14
	Thick	0.83	0.09	0.83	0.10	0.80	0.11	-0.004	0.95
H	Thin	0.27	0.05	0.37	0.09	0.40	0.06	0.014	-0.10
	Medium	0.28	0.07	0.40	0.08	0.41	0.07	0.015	-0.10
	Thick	0.33	0.09	0.41	0.09	0.43	0.08	0.010	0.05
A	Thin	0.48	0.12	0.36	0.12	0.37	0.11	-0.012	0.80
	Medium	0.36	0.11	0.27	0.10	0.30	0.11	-0.006	0.52
	Thick	0.28	0.28	0.29	0.10	0.26	0.10	-0.001	0.33
α	Thin	6.61	2.00	9.37	2.95	9.81	2.63	0.36	-2.91
	Medium	8.47	2.25	11.87	2.73	11.72	2.89	0.37	-1.15
	Thick	10.84	3.14	11.63	3.04	12.02	3.00	0.13	7.32

β	Thin	65.93	14.44	63.71	15.87	66.33	14.97	0.02	64.53
	Medium	69.21	14.52	65.44	16.02	65.64	14.39	-0.49	79.04
	Thick	60.33	16.21	60.56	17.19	62.66	12.20	0.24	53.28
P_s	Thin	-16.93	0.96	-16.97	1.24	-19.04	1.67	-0.22	-10.51
	Medium	-16.49	1.12	-17.03	1.06	-18.57	1.49	-0.22	-10.19
	Thick	-12.60	1.34	-14.41	1.17	-14.88	1.38	-0.25	-5.82
P_d	Thin	-31.00	1.51	-30.39	1.80	-31.55	1.51	-0.05	-29.29
	Medium	-32.55	1.57	-32.50	1.47	-33.00	1.42	-0.04	-31.20
	Thick	-27.27	1.19	-30.73	1.10	-29.22	1.36	-0.23	-21.63
P_v	Thin	-27.18	1.74	-23.14	1.33	-22.73	1.93	0.50	-40.44
	Medium	-26.54	1.17	-22.86	1.15	-21.70	1.10	0.54	-41.01
	Thick	-18.53	1.87	-18.35	1.54	-16.44	1.78	0.22	-24.91
ψ	Thin	-0.005	0.38	0.014	0.37	0.020	0.37	0.002	-0.08
	Medium	-0.012	0.41	-0.047	0.42	0.029	0.42	0.004	-0.14
	Thick	0.008	0.39	0.004	0.41	0.031	0.40	0.002	-0.05
ϕ_s	Thin	0.75	0.53	0.67	0.57	0.70	0.57	-0.005	0.86
	Medium	0.73	0.57	0.51	0.63	0.65	0.56	-0.009	0.95
	Thick	0.61	0.55	0.62	0.60	0.52	0.50	-0.009	0.90
τ_s	Thin	0.0029	0.02	0.0037	0.03	0.0042	0.03	0.0001	-0.0006
	Medium	0.0037	0.03	0.0042	0.04	0.0047	0.04	0.0001	0.0005
	Thick	0.0049	0.03	0.0051	0.03	0.0062	0.04	0.0001	0.0012
α_s	Thin	0.070	0.03	0.096	0.04	0.098	0.04	0.0032	-0.012
	Medium	0.089	0.03	0.103	0.04	0.105	0.04	0.0018	0.041
	Thick	0.102	0.04	0.098	0.04	0.121	0.06	0.002	0.043
λ_s	Thin	0.92	0.01	0.90	0.03	0.87	0.03	-0.005	1.07
	Medium	0.92	0.02	0.88	0.03	0.85	0.03	-0.007	1.12
	Thick	0.86	0.04	0.84	0.04	0.84	0.04	-0.002	0.94
P_{max}	Thin	0.95	0.02	0.93	0.03	0.91	0.03	-0.004	1.08
	Medium	0.94	0.02	0.89	0.04	0.88	0.05	-0.006	1.12
	Thick	0.92	0.04	0.88	0.04	0.87	0.06	-0.006	1.08
P_{min}	Thin	0.80	0.09	0.71	0.14	0.68	0.13	-0.014	1.18
	Medium	0.79	0.10	0.69	0.15	0.66	0.14	-0.014	1.18
	Thick	0.75	0.16	0.66	0.15	0.63	0.17	-0.013	1.10
γ_{var}	Thin	0.019	0.01	0.030	0.01	0.039	0.01	0.0022	-0.04
	Medium	0.020	0.01	0.037	0.02	0.042	0.02	0.0025	-0.04
	Thick	0.034	0.02	0.048	0.02	0.055	0.03	0.0023	-0.02
f_p	Thin	0.94	0.02	0.92	0.03	0.90	0.03	-0.004	1.05
	Medium	0.93	0.02	0.88	0.04	0.87	0.04	-0.006	1.11
	Thick	0.91	0.03	0.87	0.04	0.86	0.05	-0.005	1.04

We compared the linear modeled results for a selected set of polarimetric parameters with that of Geldsetzer et al., 2007 and Mäkynen et al., 2002 (Figure 5.7). Polarimetric backscatter incidence angle dependence analysis of homogeneous pure samples of snow cover (41cm) on SFYI was carried out using a surface based C-band scatterometer (Geldsetzer et al., 2007). Detailed analysis of the horizontal linear backscatter on radar incidence angle for SFYI was performed using a Radarsat-1 ScanSAR narrow product (Mäkynen et al., 2002). The results between the three studies show similar polarimetric backscatter relationship with θ_i, although the slopes differ. The differences in slopes may be attributable to the difference in sampled spatial resolutions, sampled snow cover thicknesses over sea ice and / or the specific geophysical conditions. We conclude that all the polarimetric parameters included in the study, except β, demonstrated some dependence on θ_i , at least for the current set of snow geophysical and thermodynamic conditions.

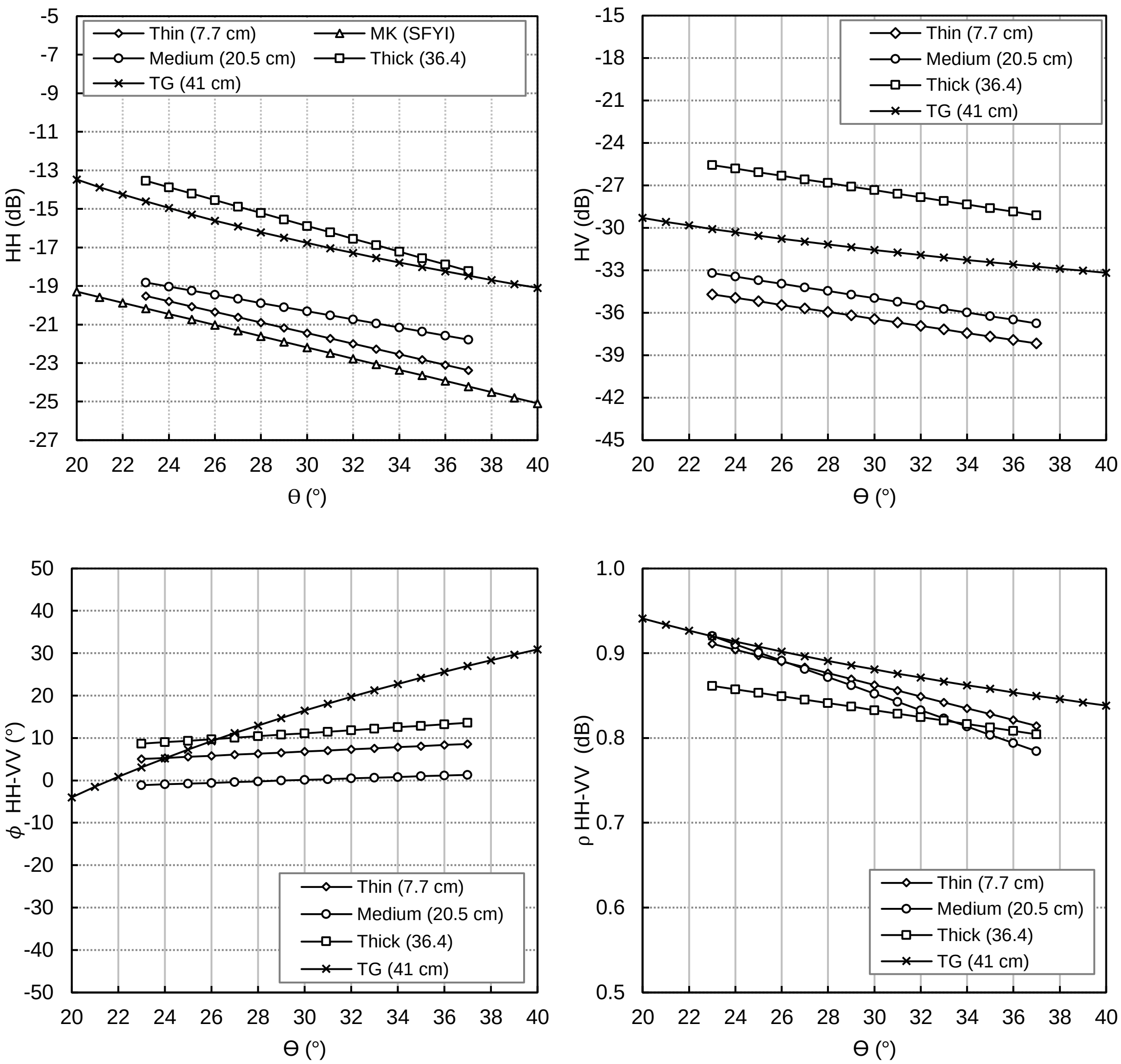

Figure 5.7. Comparison of linear-modeled incidence angle dependence of C-band polarimetric backscatter response for thin, medium and thick snow vs. linear-modeled (MK) results for SFYI after Mäkynen et al., 2002 and polynomial-modeled (TG) results for snow (41cm) over SFYI after Geldsetzer et al., 2007.

5.6.2 Polarimetric parameter relationship to snow thickness

The correlation and sensitivity analysis of the polarimetric parameters to increasing snow thickness (from 6.3cm - 36.4cm) was carried out for cold conditions at three radar incidence angle ranges (at 26.93°-28.75°, 31.38°-33.05°, 35.49°-37.04°). The images utilized in the analysis were acquired on 4 May and 11 May, 2008 (Table 5.1).

5.6.2.1 Electro-thermo-physical properties of snow (cold)

Snow properties measured during the cold and warm periods of the study are presented in Figure 5.6. During the very cold period (25-27 April) the temperatures were low (-16°C to -14°C) at the snow surface and higher (-12°C to -9°C) at the snow-ice interface. These snow-ice interface temperatures were higher (-9°C vs. -12°C) for the thicker snow covers than for the thinner snow covers, for similar SAT. This is in accordance with the modeled snow-ice interface temperatures estimated after Nakawo and Sinha, 1981 (Table 5.3). During the relatively warmer, but cold conditions (-5°C on 8-9 May) the temperatures within the snowpack were constant at all depths (Figure 5.6). Measured salinities were found higher in the snow basal layers, reaching a maximum of 20 ppt at the snow-ice interface and gradually decreasing towards the snow-air interface (Figure 5.6). The high salinities at the snow base are consistent with the occurrence of brine wicking phenomenon that operates at the snow-sea ice interface (Barber et al., 1994). Lower salinities in the top layers are due to the decreasing power of the capillary suction with distance from the saline source (Barber and Nghiem, 1999). Brine volume followed a trend similar to salinity. Brine volume at the snow basal layers was higher for thick snow than for thin snow. This was primarily due to the higher temperature at snow-ice interface for thick snow. Measurements of density exhibit inverse trends to that of salinity and brine volume. Densities at the snow basal layers were between 0.2 g/cm³ and 0.3 g/cm³ and increased gradually to 0.4 g/cm³ at the snow-air interface. Low snow densities at the base indicate the presence of depth hoar. The dielectric constant (ε') and loss (ε'') of snow also followed the trends similar to that of brine volume and salinity. This is because the complex dielectric constant of snow is largely a function of brine volume and temperature (Barber et al., 1995b).

5.6.2.2 Effect of snow thickness

The observed backscatter at σ_{vv}^0 for all snow thicknesses incorporated in the current study ranged between -25 dB and -14.25 dB (Figure 5.8). This is well within the upper limit of σ_{vv}^0 for SFYI, presented by Partington and Hanna (1994), Hallikainen and Toikka (1992), Johannessen et al., (1992), Gogineni et al., (1986), Cunningham et al., (1992), Hallikainen and Toikka (1992) and Fetterer and Gineris (1992). This supports field observations that all snow sites are SFYI and any polarimetric backscatter differences between them is primarily due to snow thickness.

Among the polarimetric parameters analyzed, 14 demonstrated a positive correlation with increasing snow thickness whereas 9 showed a negative correlation with the same increase in snow thickness (Figure 5.8). The strength (R^2) of the relationship of the parameters to snow thickness varied with θ_i , snow geophysical conditions and the number of snow samples utilized in the analysis. Therefore, it is difficult to ascertain conclusively which parameters were highly correlated to snow thickness.

As expected, we observed an increase in σ_{hh}^0, σ_{vv}^0, σ_{hv}^0, $SPAN$and ϕ_{hh-vv} with an increase in snow thickness. This is consistent with the results presented by Barber and

Nghiem, 1999 and Geldsetzer, 2009b. The increase is likely due to the elevated brine volume in the basal snow layers as a function of increase in snow thickness. Brine volume adds an additional volume scattering component to the total scattering (Bredow and Gogineni, 1990). This is supported by the Freeman-Durden volume scattering parameter (P_v), which also increased with snow thickness. It is interesting to note that Freeman-Durden surface scattering parameter (P_s) also increased with snow thickness. The increase in P_s can be attributed to scattering from a dry snow brine-wetted snow interface. Such additional interfaces have been identified during *in-situ* snow pit wall observations but unpublished (Geldsetzer, 2009b). These interfaces are primarily found in cases of thick snow when brine is wicked upwards uniformly, throughout the snow profile, forming a very distinct layer (Geldsetzer, 2009b). In contrast to the above, we observed a negative relationship for $R_{hh/vv}$ and ρ_{hhvv} with snow thickness. This indicates that as snow thickness increases, scattering heterogeneity in snow properties also increases.

Decomposition parameter entropy (H), anisotropy (A) and dominant eigenvalue (λ_s) showed similar response. With an increase in snow thickness H increased whereas A decreased. An increase in H suggests an increase in mixed scattering (Cloude and Pottier, 1997). A decrease in A suggests an increase in surface roughness or elongation of scatterers as opposed to spherical scatterers (Cloude and Pottier, 1997). Interestingly, double bounce parameter (P_d) also demonstrated a positive relationship to snow thickness, although with a lower slope. This increase in double bounce scattering could result from the elongation of snow grains as a consequence of brine wicking. The synthesized parameters P_{max}, P_{min} and f_p showed a negative relationship to snow thickness. Decreases in P_{max} and P_{min} indicate an increase in scattering complexity or target heterogeneity (Touzi et al., 1992). Similarly, a decrease in f_p indicates a loss of purity of polarization, or an increase in multiple scattering with an increase in snow thickness. Coefficient of variation (γ_{var}) further supports this by exhibiting a positive relationship with snow thickness. The mean co-pol phase difference (ϕ_{hh-vv}) was > 0° for all snow thicknesses, and displayed a weak increasing trend with snow thickness (Figure 5.8). The co-pol correlation coefficient (ρ) was high for all snow thickness classes, providing support for dominant surface scattering. However, it decreased with increasing snow thickness indicating an increasing component of volume scattering for thicker snow.

In summary, the polarimetric response from variable snow thicknesses indicates that scattering from cold snow-covered SFYI is dominated by surface scattering, most likely from the snow-ice interface, with likely contributions from the dry snow-brine-wetted snow interface. The increasing importance of volume, mixed, or multiple scattering with increasing snow thickness was also evident in the polarimetric response. The dominance of mixed scattering increased for thicker snow. The increasing volume / mixed scattering component with increasing snow thickness may stem from interaction with a greater number of dry snow grains, and/or from more interaction with greater brine volumes in the brine-wetted snow or upper sea ice layer due to warmer snow-ice interface temperatures associated with thicker snow covers.

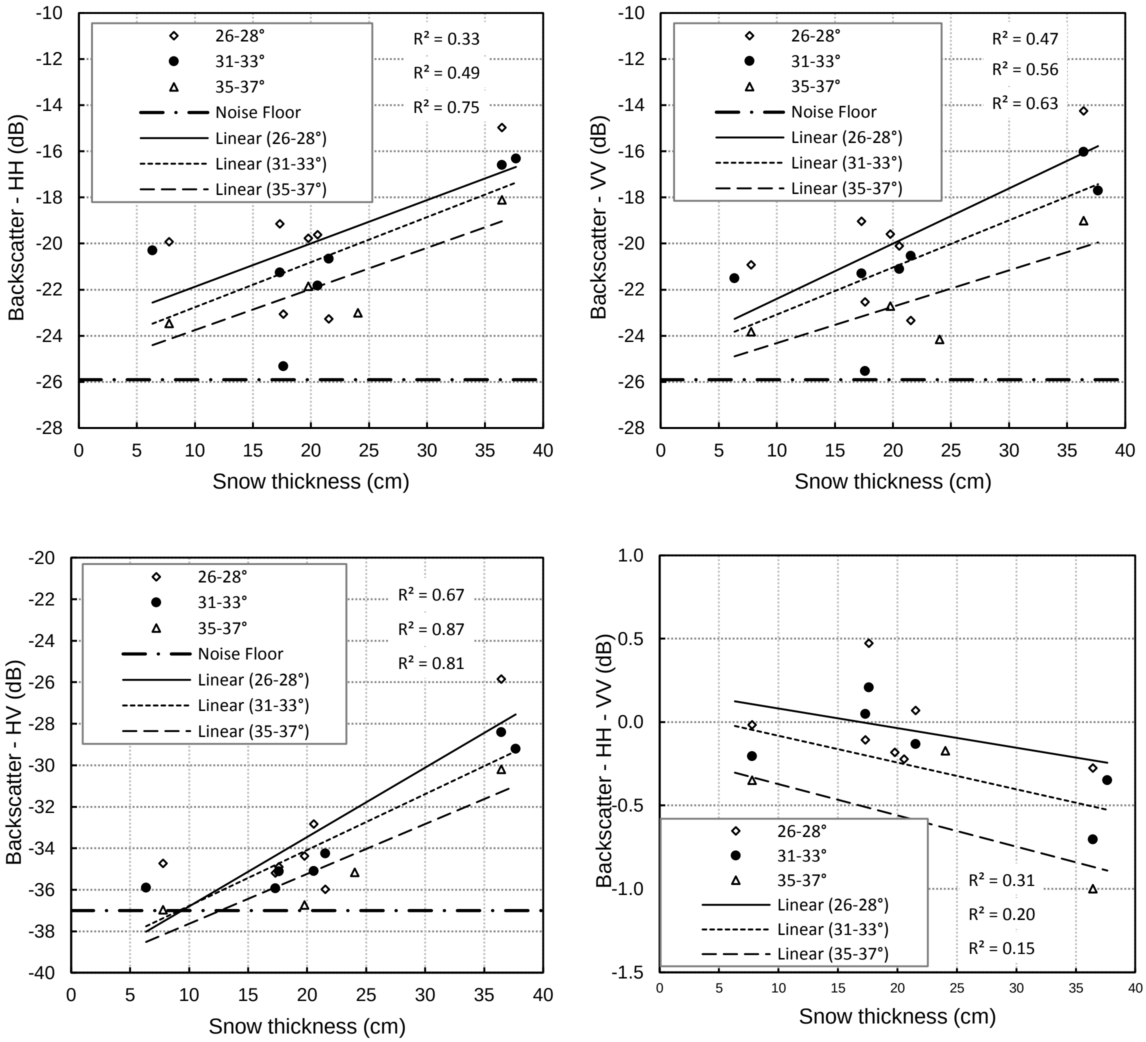

Figure 5.8. Polarimetric backscatter response with respect to snow thickness at three radar incidence angles (26°-28°, 31°-33° and 35°-37°). R² is in order of increasing incidence angle. The trend lines are simple linear fits to the data points.

(Continued on next page.)

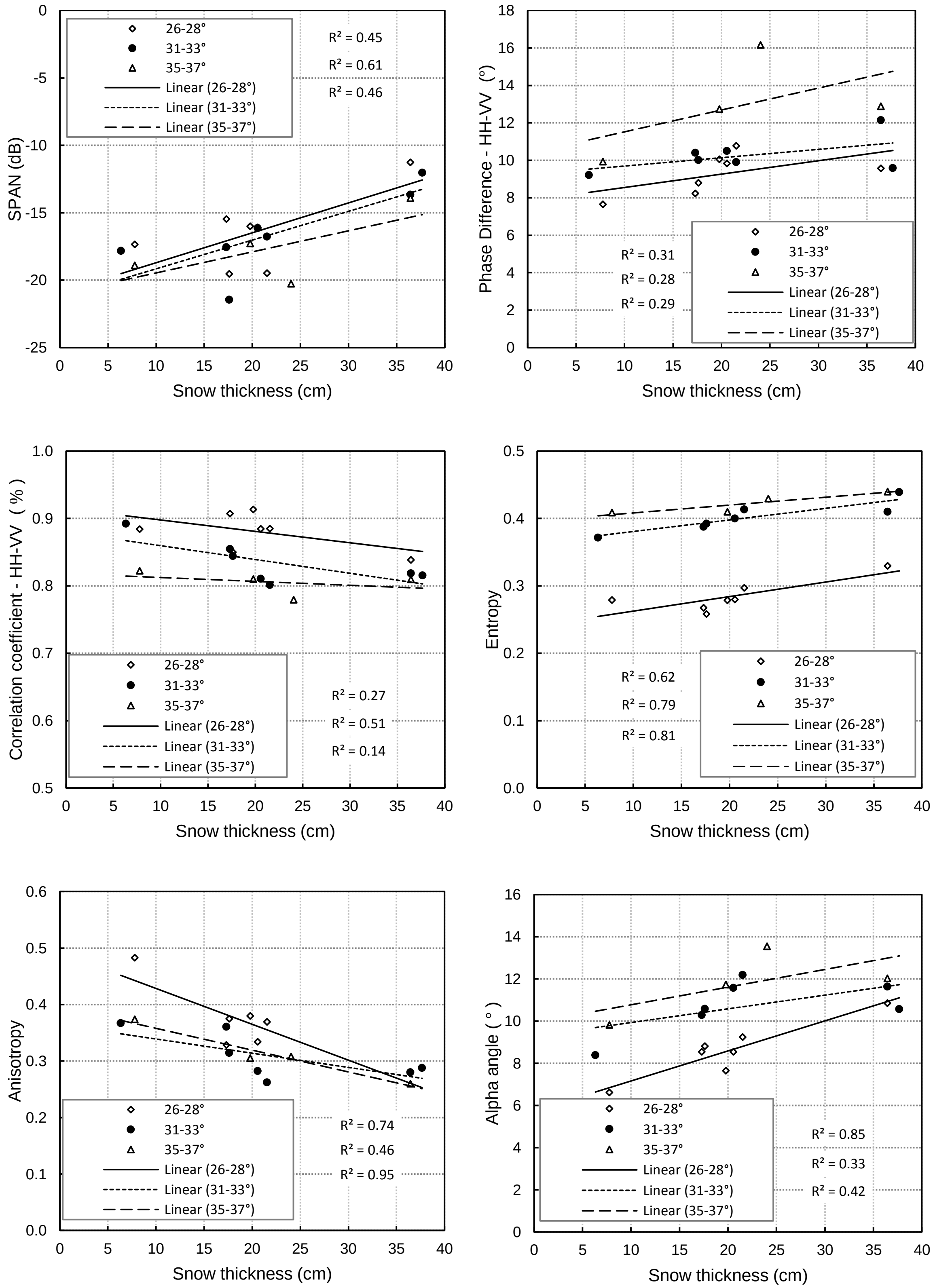

(Continued on next page.)

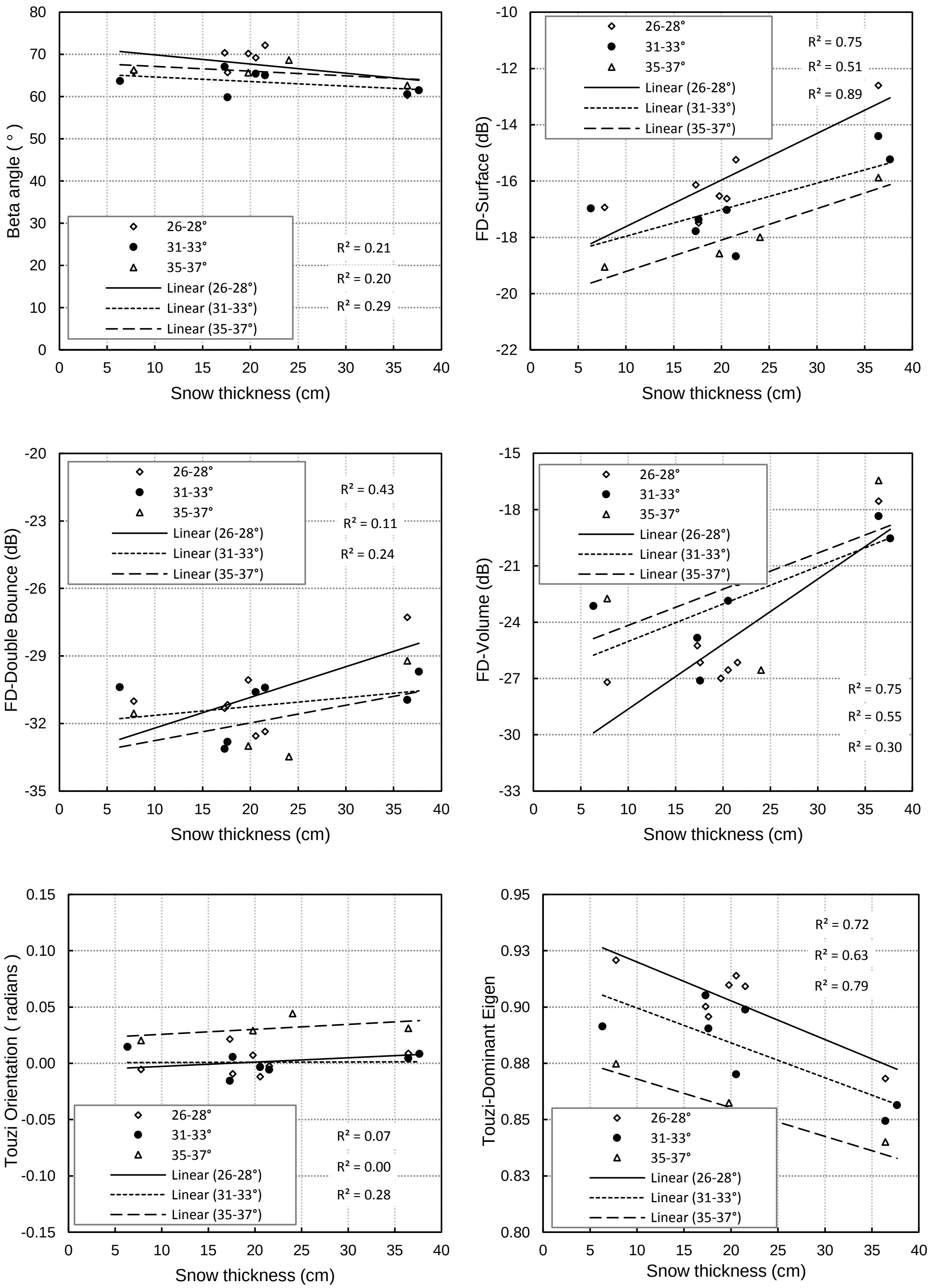

(Continued on next page.)

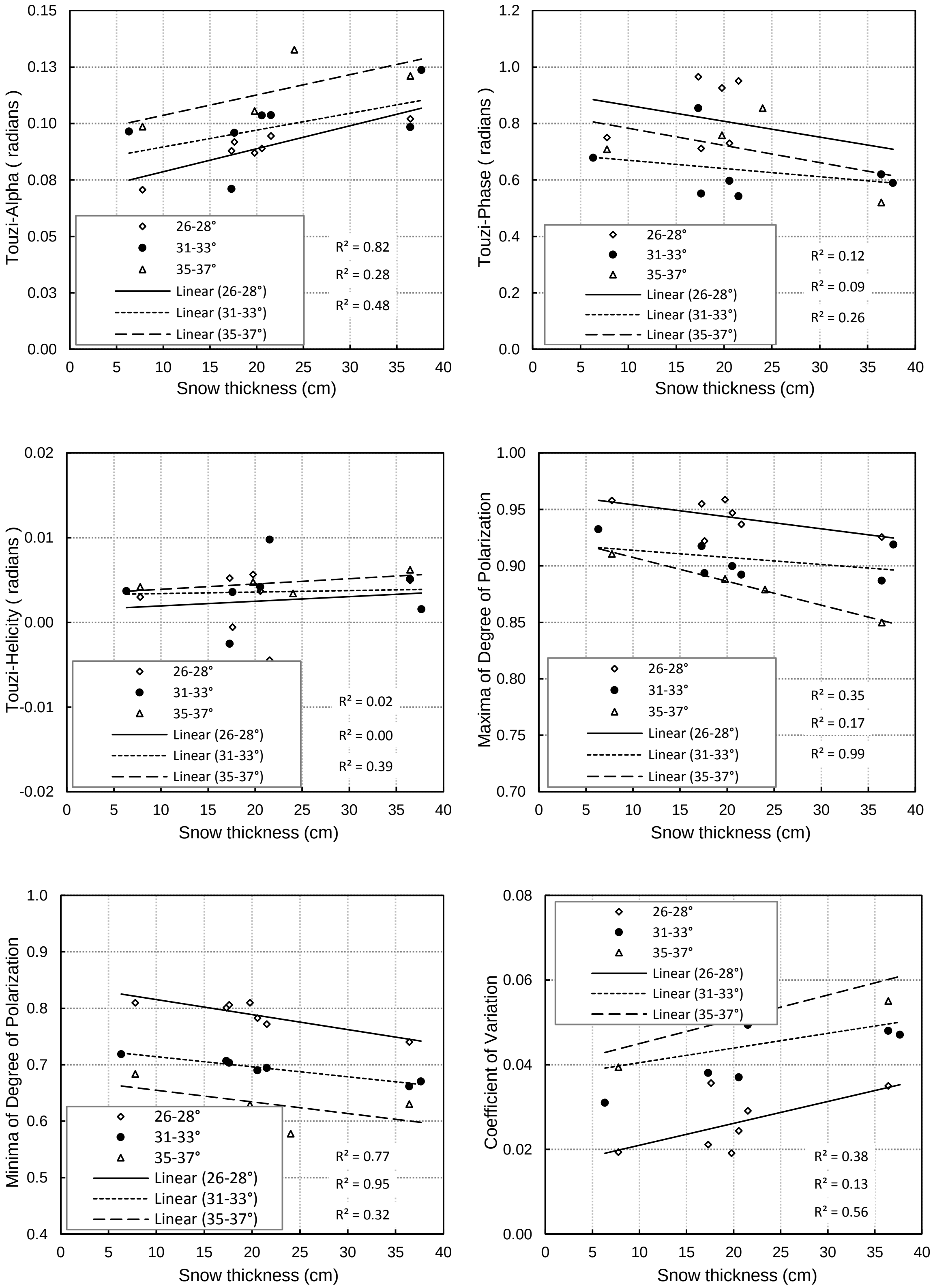

(Continued on next page.)

Figure 5.8 (Concluded).

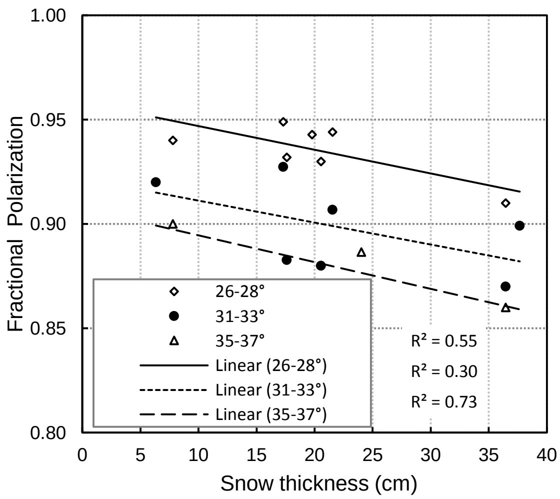

Figure 5.8. Polarimetric backscatter response with respect to snow thickness at three radar incidence angles (26°-28°, 31°-33° and 35°-37°). R^2 is in order of increasing incidence angle. The trend lines are simple linear fits to the data points.

5.6.3 Polarimetric parameter sensitivity to temperature change

A comparison of the sensitivities of polarimetric backscatter response from thick (Site 10, thickness = 36.4±12.3 cm), medium (Site 5, thickness = 20.5±6.4 cm) and thin (Site 1, thickness = 7.7±3.9 cm) snow covers was carried out at cold (SAT = -7.9°C) and warm (SAT = -0.4°C) conditions. The Radarsat-2 images utilized were acquired on 4 May and 14 May, 2008 at θ_i= ~27° and ~23°, respectively (Table 5.1). The image at θ_i= ~27° was normalized to θ_i= ~23° using the linear models presented in Table 5.4. All subsequent analyses were conducted at the same radar incidence angle of 23°. Probability density functions (PDFs) were estimated after the Parzen method (Therrien, 1987) using a Gaussian Kernel function with a standard deviation of 1. A window of one standard deviation achieved a good compromise between filtering out small scale fluctuations in the shape of the PDF and preserving large scale details.

5.6.3.1 Electro-thermo-physical properties of snow (cold vs. warm)

Snow properties measured during the cold and warm periods of the study are presented in Figure 5.6. During the cold period (25-27 April), air temperatures were low (hourly observations ranged between -14°C to -15.5°C) at the snow surface and higher (-12°C to -9°C) at the base of the snow. In contrast, during the warm period (16 and 20 May) the temperatures were high (-2°C) at the snow surface and slightly lower (-2.8°C to -3.9°C) at the base. This temperature gradient corresponds well with the snow-ice interface temperatures modeled after Nakawo and Sinha, 1981 (Table 5.3). The brine volume, dielectric permittivity (ε') and the dielectric loss (ε'') were higher in the snow basal layers for the warm conditions when compared to cold conditions for the similar snow thickness (Figure 5.6). No significant differences in snow density and salinity were observed between the cold and warm conditions. Moreover, the SAT varied considerably in the 24 hours preceding the warm case image acquisition: the SAT exceeded 0°C for 11 hours, and was only slightly below freezing for the 5 hours preceding the image acquisition. This indicates the likely presence of small quantities of liquid water in snow (at least in the upper snow layers).

5.6.3.2 Effect of temperature change

A positive shift in PDFs of σ_{hh}^{0}, σ_{vv}^{0}, σ_{hv}^{0} and $SPAN$ was observed for thin and medium snow covers when compared between the cold and warm conditions (Figure 5.9a-c, e). This positive shift can likely be attributed to the moderating effect of a moist snow cover. The increases in backscatter are caused by an increase in surface scattering at the air-snow interface and an increase in volume scattering from moist snow grains near in the upper portion of the snow. Underlying variations in brine volume and scattering from the snow-ice interface are masked by a reduction in microwave penetration depth. Such seasonal variations in snow cover signatures have been widely reported (e.g. Livingstone and Drinkwater, 1991; Barber et al., 1995a). Should microwaves penetrate through the moist snow layers, additional backscatter may be related to the increased scattering from brine-wetted snow, which is increasingly wicked up into the snow as a consequence of an increase in basal snow temperatures and an increase in the vapour pressure gradient (Barber and Nghiem, 1999). In contrast, a negative shift in PDFs of σ_{hh}^{0}, σ_{vv}^{0}, σ_{hv}^{0} and $SPAN$ was observed for the thick snow cover. This can also be attributed to the moderating effect of a moist snow cover. In this case, the higher backscatter from within the snow cover is masked by surface scattering from the moist snow layer near the air-snow interface. This backscatter decrease is also consistent with the reported observations. No significant differences in the cold-to-warm signatures of ϕ_{hh-vv}, $R_{hh/vv}$ and ρ_{hhvv} were evident for any of the snow thicknesses (Figure 5.9d, f-g), except a slight increase in ρ_{hhvv} for thick snow at warm conditions. The moderating effect of moist snow was observed in the Freeman-Durden parameters as well (Figure 5.9l-n), where P_s, P_d and P_v increased for thin and medium snow covers and decreased for thick snow. Although moderated, the decomposition parameters derived after Freeman-Durden, 1998 showed surface scattering as the dominant scattering mechanism for both the cold and warm conditions. Parameters derived after (Cloude and Pottier, 1997) also demonstrated significant sensitivity to temperature change, although not all parameters exhibited similar response. Entropy H increased for thin and medium snow covers and decreased for thick snow (Figure 5.9h); consistent with Freeman-Durden parameters and linear backscatter responses. In physical terms, this indicates that multiple/mixed scattering increased for thin and medium snow covers when SAT increased. Anisotropy A decreased for all snow thicknesses (Figure 5.9k). This decrease was most pronounced for thin snow and nearly insignificant for medium and thick snow. The response of A indicates that the greatest changes within the snow covers (grain size, shape and surface roughness) occurred for thin snow when SAT increased from -7.9°C to -0.9°C. The geophysical changes in the thicker snow cover produced an insignificant effect on A. Alpha angle α increased for thin snow cover and decreased for medium and thick snow covers (Figure 5.9j). The absolute values of α for all the snow thicknesses ranged between 0°-20°, indicating dominance of surface scattering. The relative change in α between cold-warm conditions indicates an increase in the volume scattering component for thin snow. For medium and thick snow covers, the reverse is true, with a decreasing importance of volume scattering. Among the decomposition parameters derived after (Touzi, 2007) only λ_s and α_s were affected by the change in SAT. Alpha parameter α_s demonstrated a response similar to alpha α. Dominant-eigen value λ_s showed a decrease for thin snow and an increase for thick snow (Figure 5.9p). No significant change was observed for medium snow. With respect to synthesized parameters, the response of P_{max}, P_{min} and f_p was found similar and highly correlated to each other and with other parameters previously analyzed. All three parameter signatures decreased for thin and medium snow covers and increased for thick snow (Figure 5.9u-w). The largest changes were observed for P_{min}. This indicates that the purity of polarization and the complexity of scattering mechanisms / target heterogeneity decreased for thin and medium snow cover as the SAT increased from -7.9°C to -0.4°C. The response of γ_{var} verifies this through its opposite response. It increased for thin and medium snow cover and decreased for thick snow cover, indicating an increase in diffuse / multiple scattering for thin and medium snow covers and decrease for thick snow cover (Figure 5.9t).

The comparison of the polarimetric parameter responses from cold and warm snow conditions showed a general increase in linear co- and cross-pol backscatter for thin and medium snow covers and a decrease in linear co- and cross-pol backscatter for thick snow cover. This is likely caused by reduced penetration depth resulting in increasingly dominant surface scattering from the air-moist snow interface, and/or the dry snow brine-wetted snow interface - as opposed to the snow-ice interface. The increasing importance of mixed or multiple scattering with increasing SAT was also evident in the polarimetric response. The dominance of mixed / multiple scattering increased for thin and medium snow covers, likely due to increased volume scattering from moist snow grains and higher brine volumes in the brine-wetted snow. The consequences of this were visible in the sensitivity of polarimetric parameters to snow thickness. None of the parameters demonstrated a significant relationship to snow thickness for the warm conditions. This suggests that snow thickness estimation through the effect of snow thermodynamics on SAR during moist snow / warm conditions is not possible.

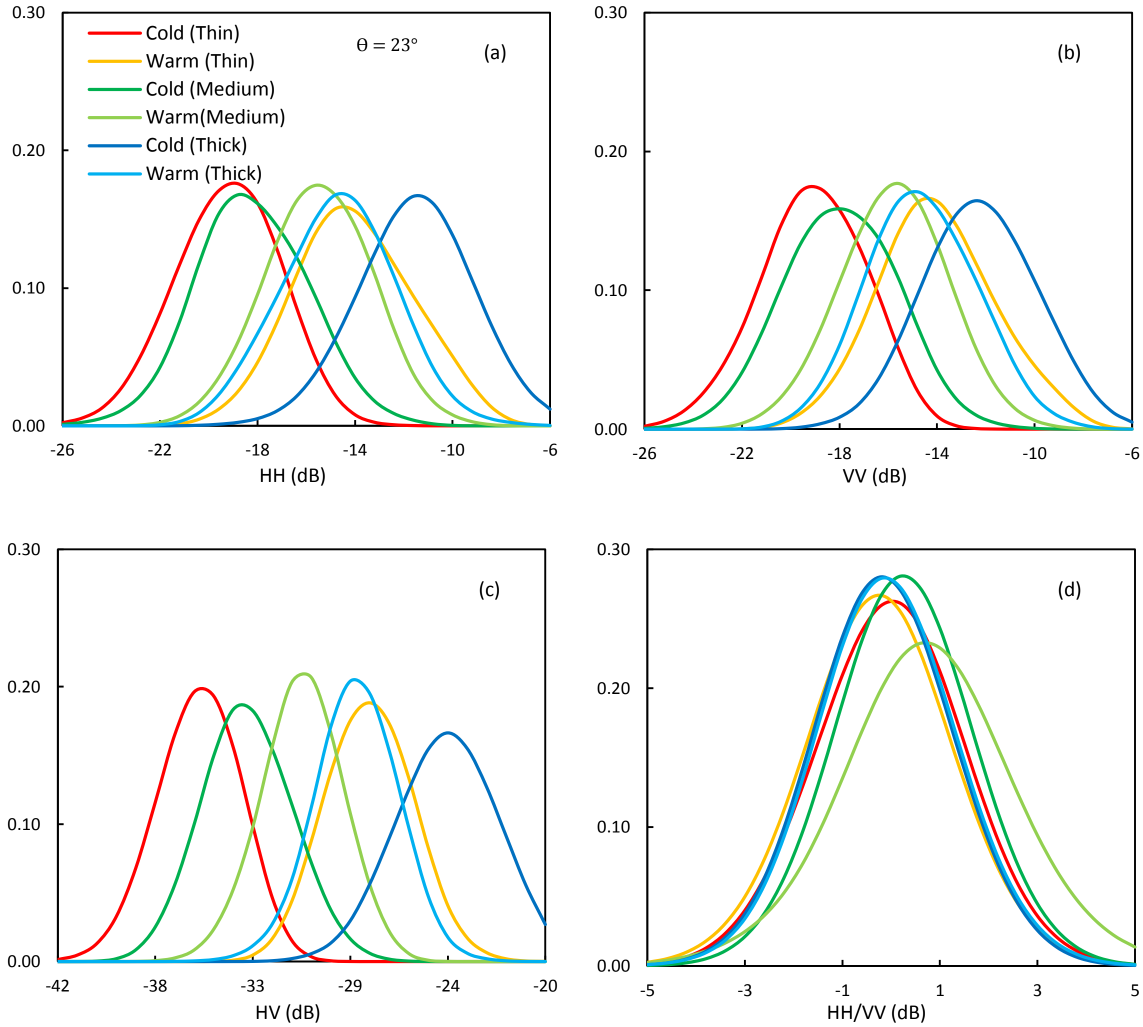

Figure 5.9. Comparison of PDF's for polarimetric backscatter responses from thick (36.44±12.30 cm), medium (20.56±6.47 cm) and thin (7.78±3.96 cm) snow covers at cold (-7.9°C) and warm (-0.4°C) conditions. All results are at ~23°. The Radarsat-2 SAR images utilized were acquired on 4 May and 14 May, 2008 at $\boldsymbol{\theta_i}$ *= ~27° and ~23°, respectively. The image at* $\boldsymbol{\theta_i}$ *= ~27° was normalized to ~23°. Y-axis denotes probability.*

(Continued on next page.)

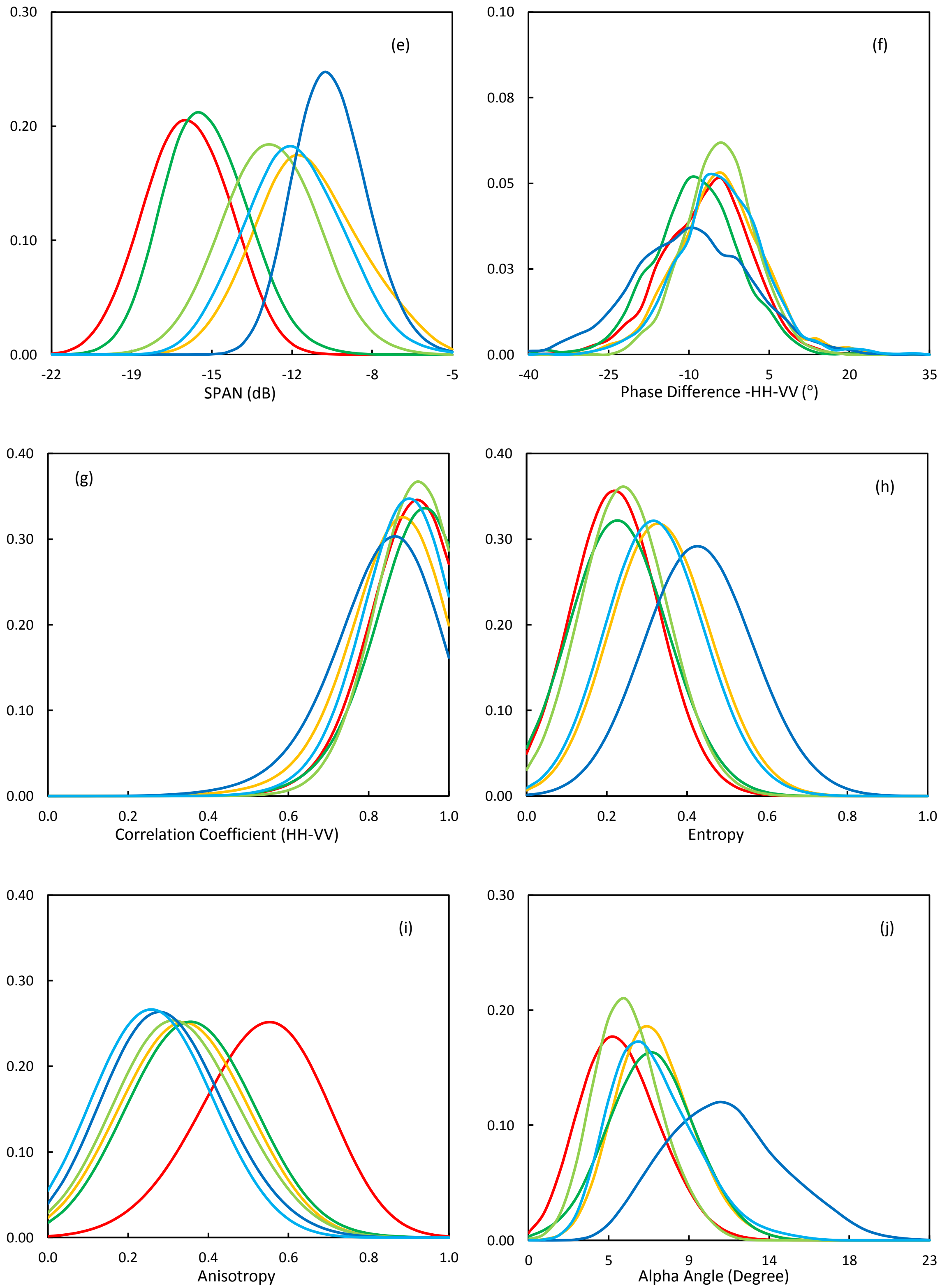

(Continued on next page.)

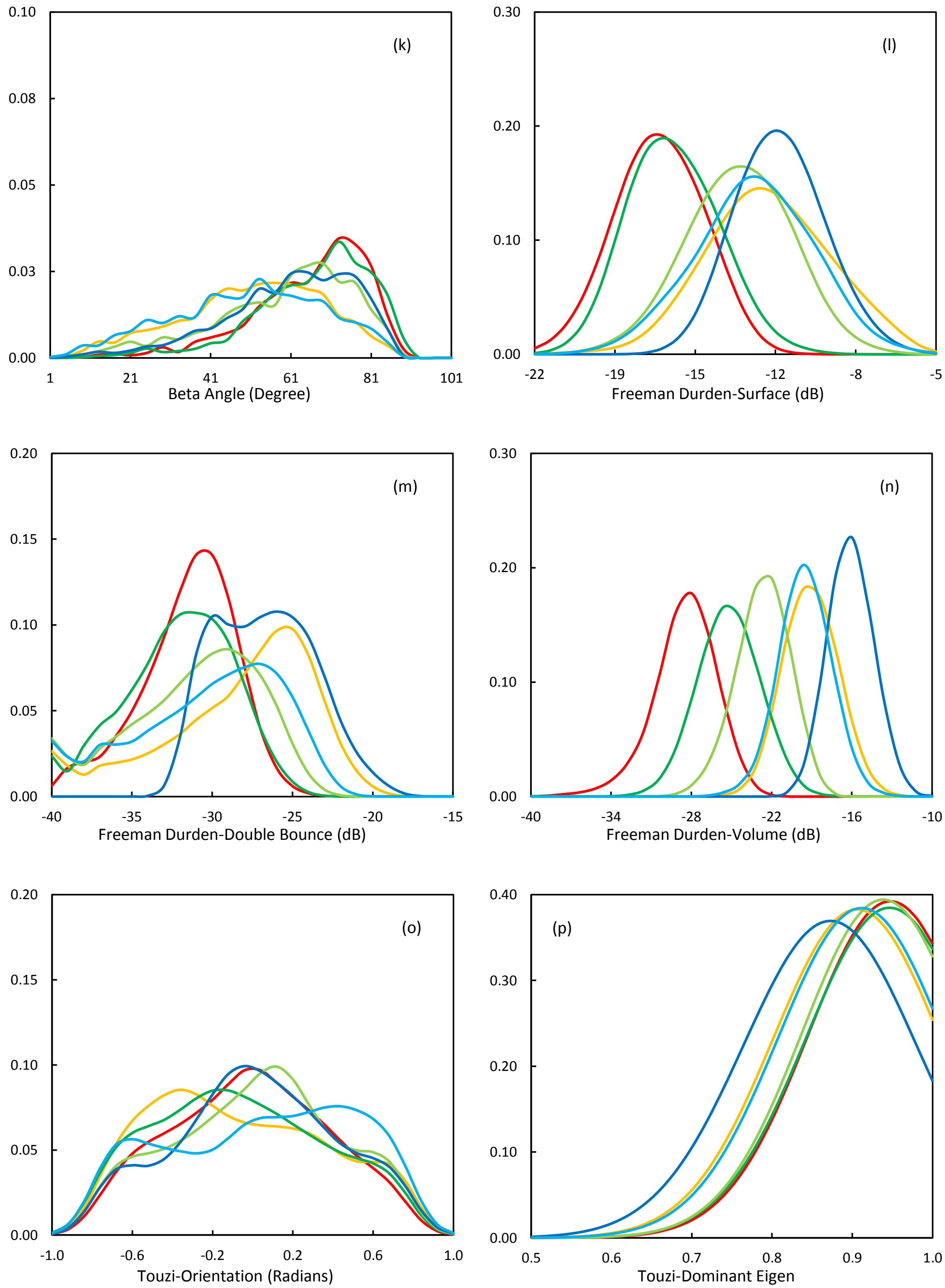

(Continued on next page.)

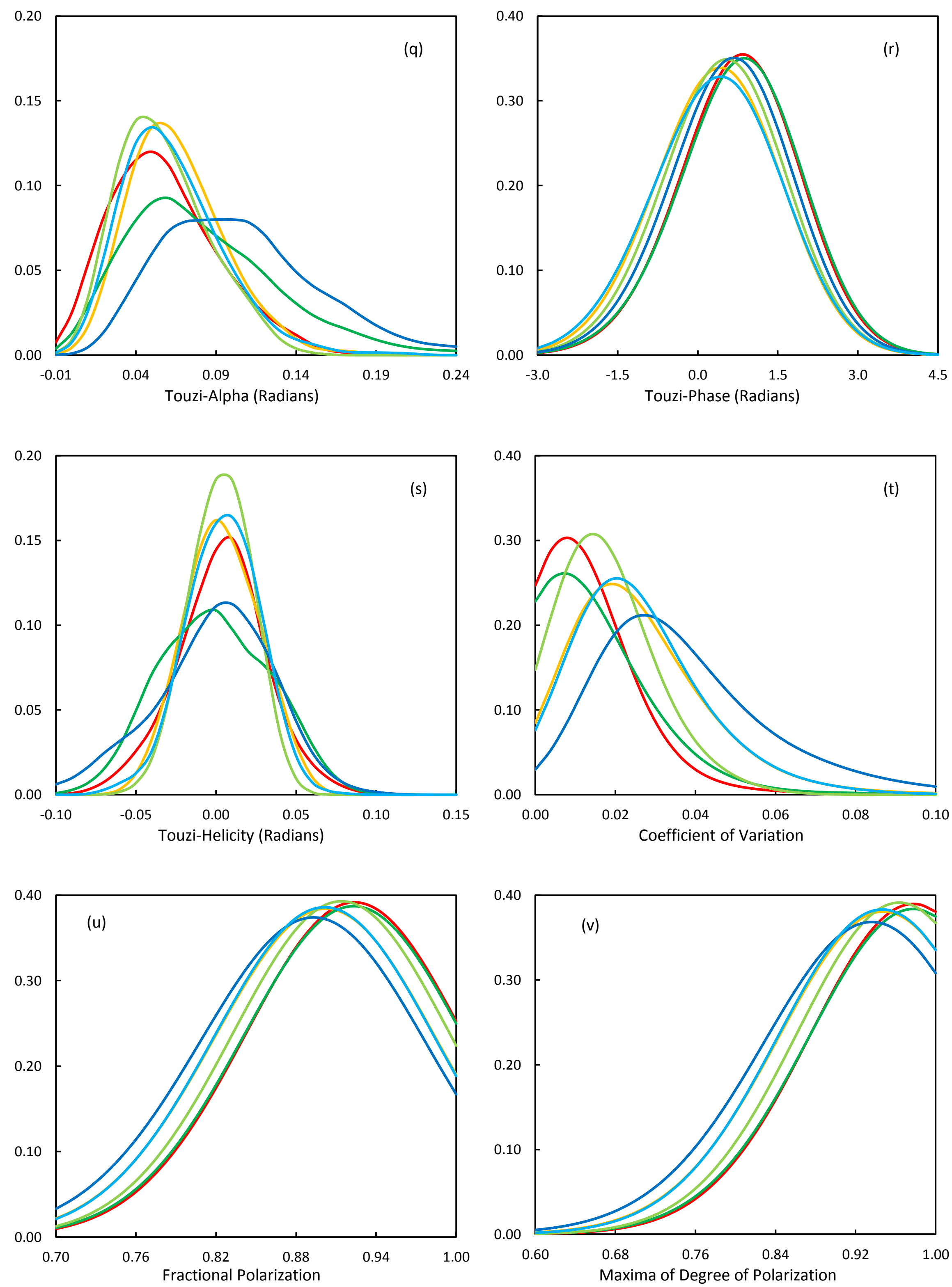

(Continued on next page.)

Figure 5.9 (Concluded.)

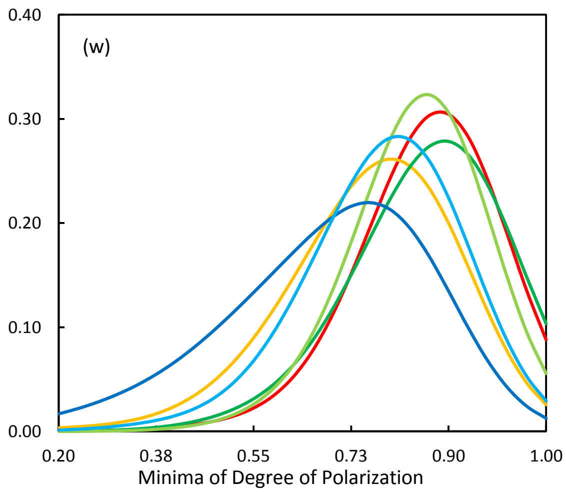

Figure 5.9. Comparison of PDF's for polarimetric backscatter responses from thick (36.44±12.30 cm), medium (20.56±6.47 cm) and thin (7.78±3.96 cm) snow covers at cold (-7.9°C) and warm (-0.4°C) conditions. All results are at ~23°. The Radarsat-2 SAR images utilized were acquired on 4 May and 14 May, 2008 at $\boldsymbol{\theta_i}$ *= ~27° and ~23°, respectively. The image at* $\boldsymbol{\theta_i}$ *= ~27° was normalized to ~23°.*

5.7 Conclusion

Linear and polarimetric SAR backscatter response from variable snow thicknesses over SFYI were examined under cold (SAT = -7.9°C) and warm (SAT = -0.4°C) conditions. The objectives were to investigate the sensitivity of the linear and polarimetric response with respect to snow thickness and the variation in this response with an increase in surface air temperature, through the changes manifested in snow geophysical properties.

Measurements were made from 4 May to 14 May 2008 in the Franklin Bay region of the Canadian Arctic on landfast smooth FYI. Field sites with snow thicknesses ranging between 6.3 ± 5.9 cm and 37.6 ± 12.7 cm on SFYI were evaluated. RADARSAT-2 SAR Fine-quad data at incidence angles ranging between 22.3° and 37.0° were used to derive linear and polarimetric parameters.

During the cold conditions, low to high correlations of linear and polarimetric parameters to snow thickness were observed. The strength and the direction of the correlations varied with parameter type, radar incidence angle, snow geophysical properties and number of snow samples utilized in the analysis. Among the polarimetric parameters analyzed, 14 demonstrated a positive relationship with snow thickness whereas 9 showed a negative relationship with the same increase in snow thickness. The analysis showed that scattering from snow-covered SFYI at SAT (-7.9°C) was dominated by surface scattering occurring from the snow-ice interface with likely contributions from the dry snow but brine-wetted (basal snow layer). The increasing importance of volume, mixed or multiple scattering with increasing snow thickness was also evident in the polarimetric response. The dominance of mixed scattering increased for thicker snow cover. The increasing volume / mixed scattering component with increasing snow thickness was likely from interaction with a greater number of dry snow grains, and/or from more interaction with greater brine volumes in the brine-wetted snow or upper sea ice layer due to warmer snow-ice interface temperatures associated with thicker snow covers.

During warm conditions, a general increase in linear co- and cross-pol backscatter for thin and medium snow covers and a decrease for thick snow was observed. This increase was greater for thin snow than medium snow, likely due to the masking effect of moist snow surface layers. Additional causes may be the insulating effect of the medium snow cover, resulting in lower amounts of brine wicking and consequently lower volume scattering. The decrease in linear co- and cross-pol backscatter for the thick snow cover was also associated with the masking effect of moist snow layers. The increasing importance of mixed or multiple scattering with increasing SAT was clearly evident in the polarimetric response. Parameters P_s, P_d, P_v, H and γ_{var} increased for thin and medium snow covers and decreased for thick snow cover. In contrast, parameters P_{max}, P_{min} and f_p were found to decrease for thin and medium snow covers and increase for thick snow. This indicates that the amount of mixed / multiple scattering increases for thin and medium snow covers at warm conditions, likely due to increased volume scattering from the moist snow layers and higher brine volumes in the brine-wetted snow.

The comparison of the results from cold and warm conditions revealed that none of the parameters demonstrated any relationship to snow thickness during the warm conditions, whereas significant relationships existed during cold temperatures. This suggests that snow thickness estimation through the effect of snow thermodynamics on SAR at warm conditions is practically not possible.

CHAPTER SIX:
POLARIMETRIC C-BAND MICROWAVE SIGNATURES OF SNOW COVER ON SMOOTH FIRST-YEAR SEA ICE FROM EARLY MELT TO MELT ONSET

6.1 Abstract

In this chapter**,** the observations of the diurnal and time series coincident geophysical and dielectric properties of thick and thin snow cover over smooth first-year sea ice (SFYI) and the corresponding polarimetric backscatter response at C-band are presented. First, an analysis of the diurnal observations of snow properties and the microwave backscatter is carried out for two temperature regimes: 1) early melt and 2) melt onset period. Second, observations of C-band microwave signatures of thick and thin snow cover over SFYI, coincident *in-situ* measured snow properties from early melt to melt onset are presented. A scattering model is used for identification of scattering contributions and geophysical interpretation of observed backscatter.

6.2 Introduction

Snow covered FYI is a multi-layered media. Snow on sea ice can consist of fresh snow, low and high density layers of wind slab and highly saline brine-wetted depth hoar (Barber et al., 1995) and air. Sea ice can also have several layers: frazil consisting of randomly oriented grains and columnar ice. All the snow and sea ice layers have different physical and electrical properties. Moreover, these properties change over time beginning from freeze-up through advanced melt. The biggest changes in these properties are observed during freeze-up and from early melt to advanced melt. More complexity is added by the change of these properties over diurnal time scales during the transition from early melt to melt onset.

The complexity demonstrated by the layers in snow covered FYI awkward and the variation in the physical and electrical properties of the media over seasonal and temporal scales add ambiguity in interpreting C-band microwave backscatter signatures. In general, the upper dry snow layers are found to contribute both surface scattering from air/snow interface and volume scattering from snow grains (Ulaby et al., 1984). Brine-wetted snow is mainly a contributor of volume scattering. The degree of volume scattering from the brine wetted basal snow layer is a function of brine volume fraction which further depends on salinity, temperature and density. Sea ice contributes both surface and volume scattering. Surface scattering occurs at the snow/ice interface and volume scattering within the first few centimeters of uppermost ice layer.

A large number of quantitative physical models have been developed to estimate backscatter from snow covered FYI (Ulaby et al., 1984; Kim et al., 1984; Drinkwater, 1989; Winebrenner et al., 1992; Nghiem et al., 1995a; Kendra et al., 1998; Fung and Chen, 2004). These models require reliable input parameters in the form of snow and sea ice geophysical properties for accurate computation of backscatter. The modeled backscatter further requires validation and cannot be compared to satellite or airborne data, due to scale differences. Although, a large number of snow covered sea ice studies have utilized C-band SAR imagery acquired coincident to field geophysical measurements for interpretation of received backscatter (Gill et al., 2012; Gill et al., 2013; Geldsetzer et al., 2007; Scharien et al., 2005), the results are not representative of pure and homogeneous snow and sea ice conditions. To reduce these ambiguities, surface-based scatterometer measurements acquired coincident *in-situ* snow and sea ice geophysical measurements have been used (Onstott, 1992). Such experiments have allowed continuous time-series measurements of homogenous snow and sea ice areas. The spatially and temporally pure samples of snow-covered sea ice and associated backscatter provide for better model parameterization and backscatter validation.

This chapter investigates the following research questions.

1. How do snow covered smooth FYI geophysical properties and associated polarimetric C-band microwave backscatter change over a diurnal period?
2. How do snow covered smooth FYI geophysical properties and associated polarimetric C-band microwave backscatter change from early melt to melt onset period?
3. What are the scattering mechanisms in snow covered smooth FYI and how they change with changing snow and sea ice properties over diurnal and seasonal time scales?
4. What are the differences in snow covered smooth FYI geophysical properties and associated polarimetric C-band microwave backscatter between thick and thin snow cover from early melt to melt onset period?

To investigate these questions, the analysis is segmented into two sections.

In study-1, high frequency diurnal measurements of snow covered smooth FYI physical and electrical properties coincident polarimetric C-band surface-based scatterometer measurements are presented for the early melt and melt onset period. The polarimetric scatterometer results are further compared to Radarsat-2 SAR backscatter for validation.

In study-2, the physical and electrical properties of snow covered smooth FYI coincident with polarimetric C-band surface-based scatterometer measurements are presented from the early melt to melt onset period. The analysis is performed for two snow thicknesses (6 cm and 16 cm). Scattering contributions from the snow covered FYI are modeled. Snow and sea ice properties acquired over homogeneous areas are used to parameterize the scattering model. Geophysical interpretation is made from the modeled results.

6.3 Methods

6.3.1 Study area

The study area consisted of a single site, located on a pan of very smooth FYI (74.70435°N, 95.63381°W) in Resolute Passage, ~4 km southwest of Sheringham Point, Cornwallis Island, Nunavut (Figure 6.1). The field site was accessed using snowmobiles from the Polar Continental Shelf Program (PCSP) in Resolute Bay, NU. The study was conducted from 15 May to 30 May, 2012.

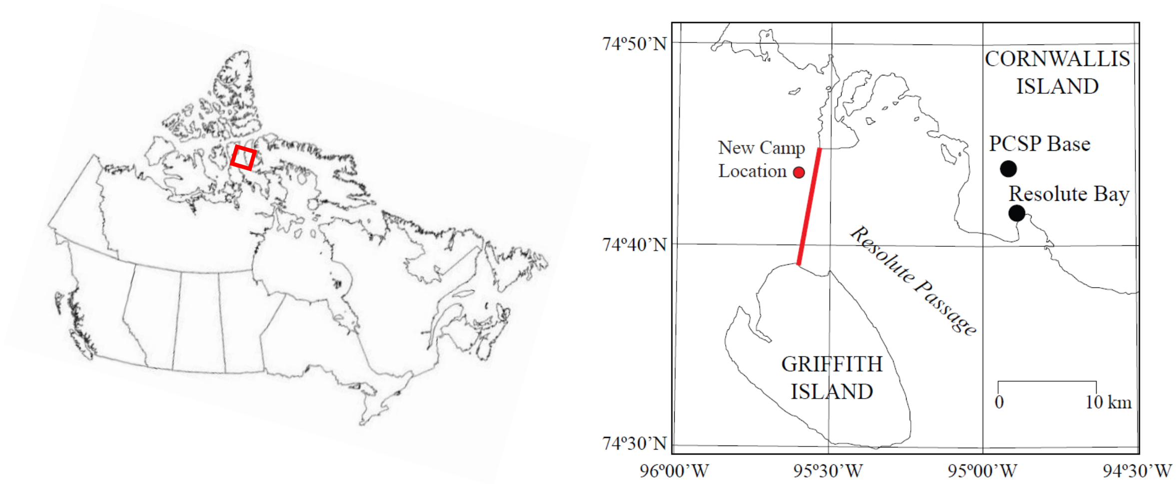

Figure 6.1. Map showing the location of the study area with respect to Canada (left) and the zoom in on Resolute Bay (right) showing the location of field site (red dot).

6.3.2 Meteorological data

Hourly meteorological data of air temperature, wind speed, wind direction and precipitation (snow and rain) was measured using a self-installed weather station on smooth FYI in close proximity to the field site A second set of meteorological data (Figure 6.2) was acquired from the Environment Canada, Resolute Bay meteorological station located on land, 68 meters above sea level, 2km south east of Allen Bay on Cornwallis Island and approximately 20km south east of the study site.

During the study period, the temperature at the Resolute Bay meteorological station ranged from -19°C to -3°C (Figure 6.2). On-ice air temperatures reached a maximum of 2.6° C on 29 May. Strong winds occurred on 24 May, which caused significant snow redistribution, resulting in changes to the *in-situ* snow sampling site.

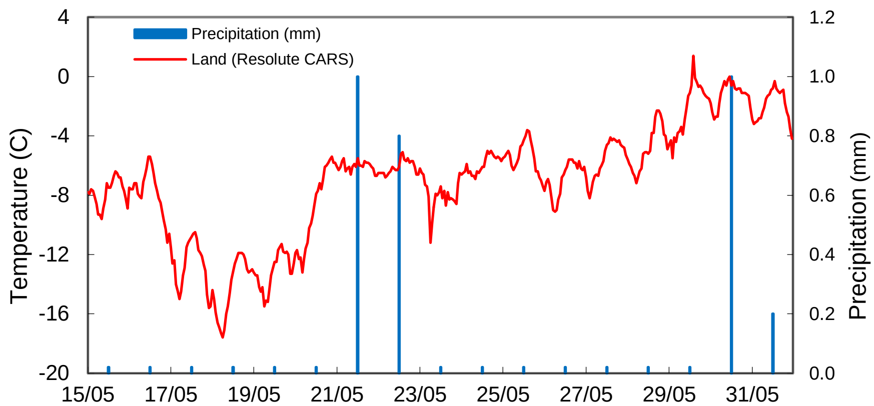

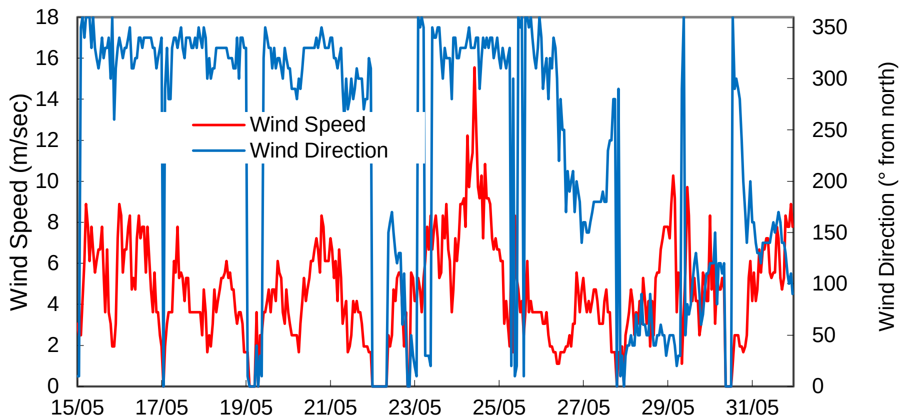

Figure 6.2. Air temperature, precipitation, wind speed and wind direction for the study period. Data is acquired from Environment Canada Resolute Bay Canada Aviation Regulations (CARS) meteorological station.

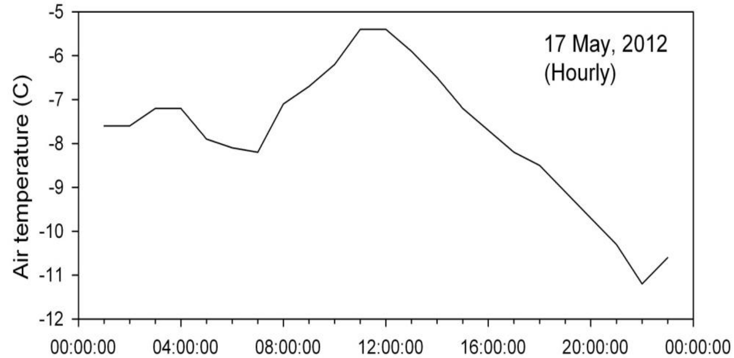

Figure 6.3. Hourly observations air temperature for 17 May, 2012 for a period of 24 hours. Data acquired from Environment Canada Resolute Bay meteorological station.

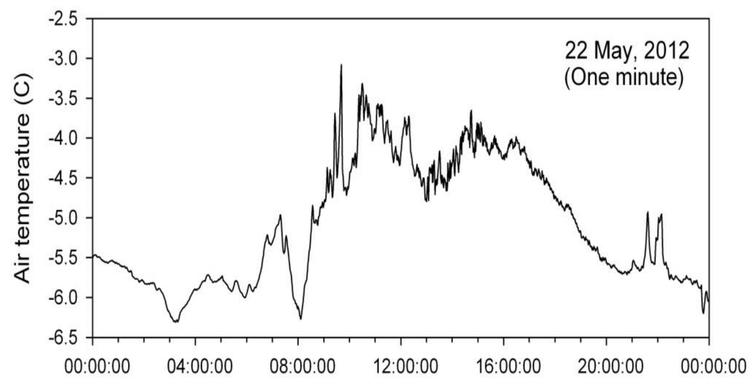

Figure 6.4. One minute observations of air temperature for 22 May, 2012 for a period of 24 hours. Data acquired from self-installed meteorological station on smooth FYI.

6.3.3 Snow property data

A variety of time series snow property data was collected during the study period.

Snow profile measurements were made by excavating snow pits. The snowpack was shaded for measurements within 30cm of the surface. Snow temperature measurements were acquired vertically at 2cm intervals using a Digi-Sense RTD thermometer probe. The probe measured at a resolution of 0.1°C with an accuracy ±0.2°C. Measurement range of the probe was -200°C to 850°C.

Snow permittivity was measured vertically every 2cm in the snowpack using a HydroProbe dielectric moisture meter with flat capacitance sensor (Denoth, 1989). The instrument operated at a frequency of 50 MHz with an effective measuring area of 3×5.7 cm. The measuring permittivity accuracy of the sensor is 0.6% and that for loss is 0.7%.

Snow density was sampled every 2 cm vertically in the snowpack using a 66.35 cm3 sampler (1.95 cm high) and Gram Precision GX-230 scale, with an accuracy of 0.01 g. The snow samples were collected and transported in Whirlpak™ plastic bags. The samples were weighed in the whirlpaks with the tear tab removed. The average weight of the "large" bags without the tear tab was 3.43 ±0.06 g and the "long" bags were 3.16 ±0.18g.

Snow salinity was measured every 2 cm vertically in the snowpack. The salinity was measured using a WTW Cond 330i conductivity meter with an accuracy of ±0.5%. Snow salinities were measured in the laboratory once the snow density samples had melted and reached room temperature.

Snow grain size and shape measurements were computed from photographs of disaggregated grains on a millimeter-grid crystal plate (Figure 6.5). Snow grains were characterized based on Colbeck et al. (1990) and Canadian Avalanche Association (1995). Three types of snow grains were identified. They are described in Table 6.1. Snow-pit wall photos were occasionally taken, when conditions were conducive (Figure 6.6).

Snow depth was measured at the snow pits and in the study area through snow surveys using meter stick to the nearest 0.5cm. Snow depth and variability over larger areas were measured following Iacozza and Barber (2001) using a statistical variogram technique.

Table 6.1. Description of snow identified in the field. Classification after Colbeck et al., 1990.

Classification	**Description**	**Physical processes**
2bk	Rounded fragments of precipitation particles or packed shards	Fragmentation and degree of packing increases with wind speed
4mx	Faceted particles of recent rounding facets	Faceted grains are rounded due to decrease in temperature gradient
6mf	Individual crystals frozen in a solid polycrystalline grains	Melt-freeze cycles form poly crystals when water in voids freezes

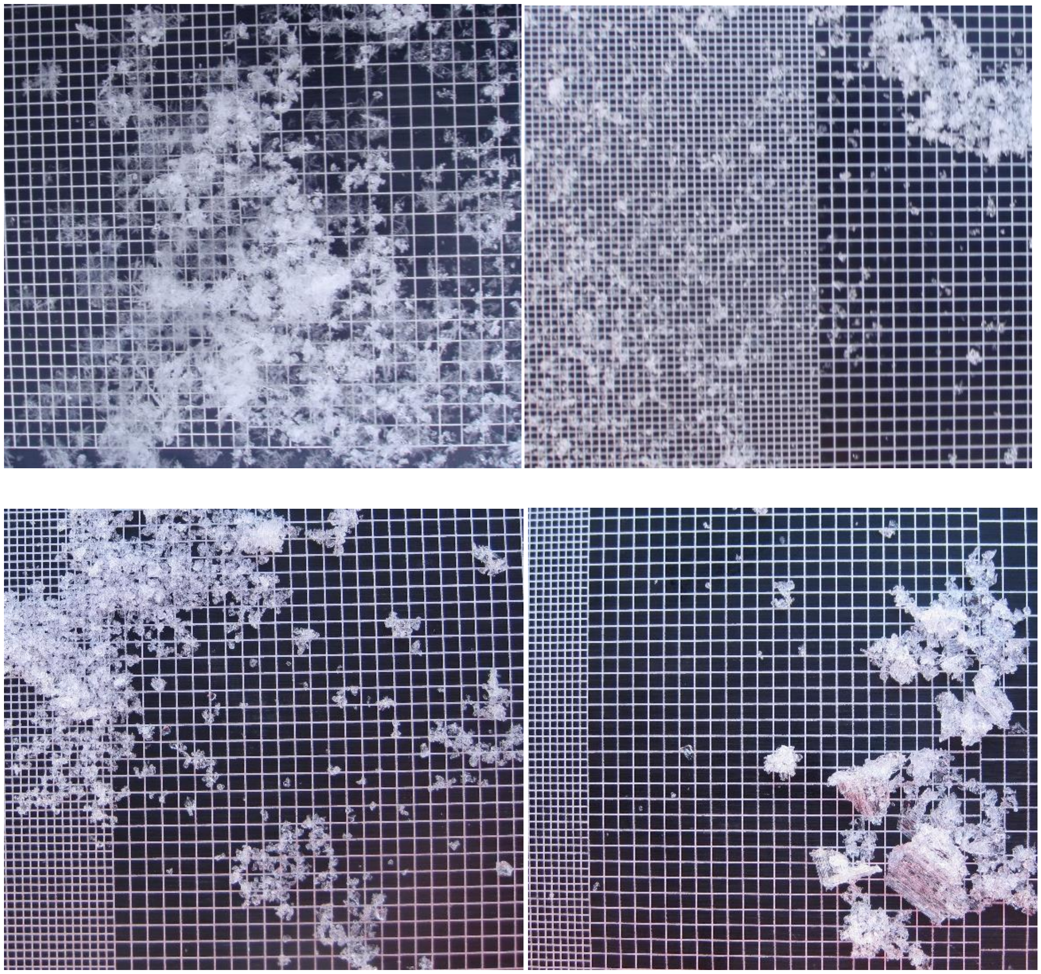

Figure 6.5. Photographs of the snow grains on a millimeter-grid crystal plate. The first photograph (top-left) shows the faceted fresh snow grains (fine powder) found in the uppermost 1 cm of the snowpack, the second photograph (top-right) shows the very small, rounded, closely packed grains found in the top-middle layers just below the fresh snow, third photograph (bottom-left) shows the rounded, closely packed grains found in the lower middle layers and the fourth photograph (bottom-right) shows the large ice crystals and poly-aggregates of depth hoar found in the bottommost 2-4 cm of the snowpack. The pictures were acquired on 16 May, 2012.

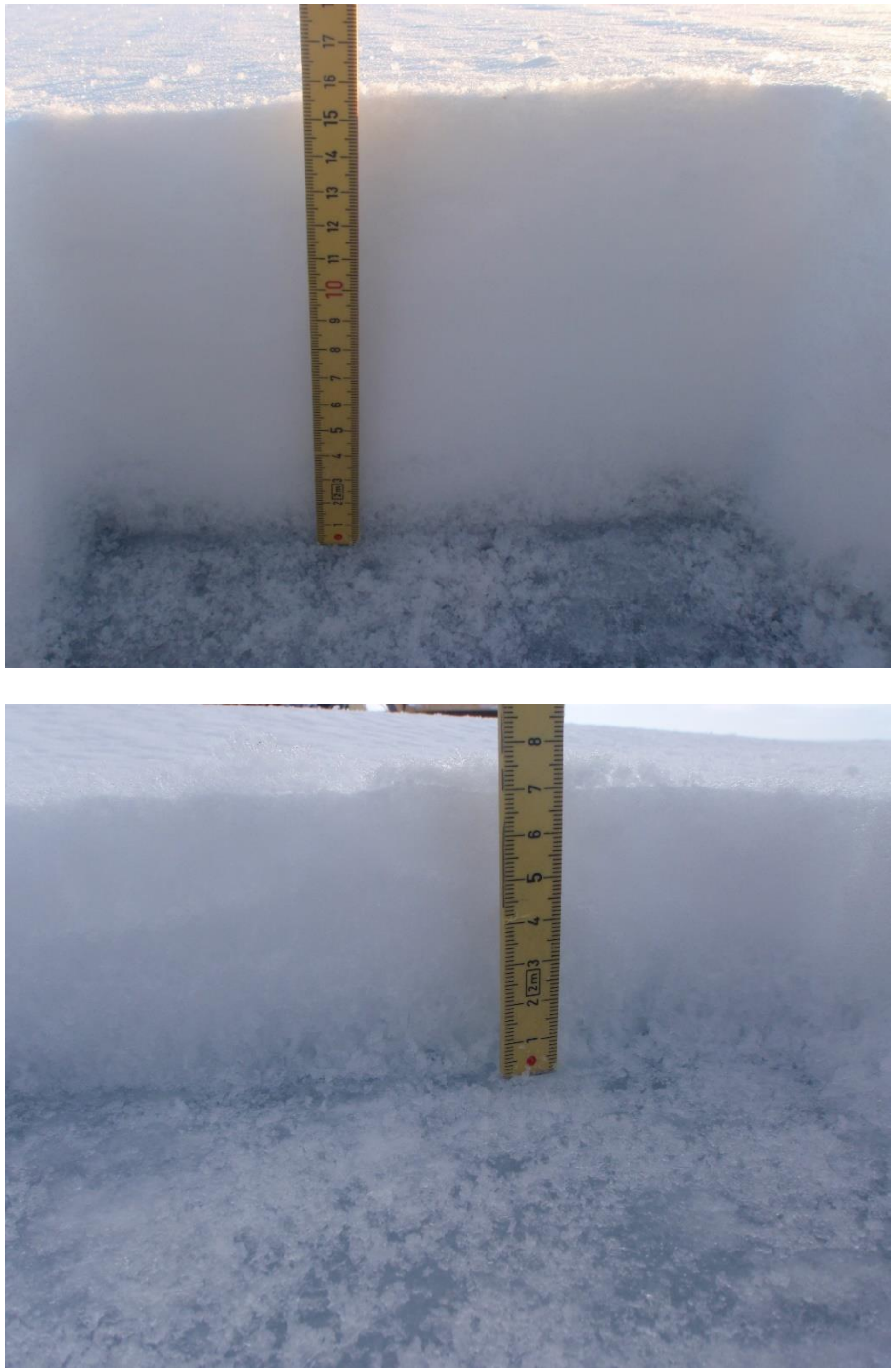

Figure 6.6. Photograph of the snow wall (16 cm and 6 cm) showing the tightly packed wind slab in the middle and depth hoar in the bottom-most 2-3 cm of the snowpack. The photographs were acquired on 15 and 16 May, 2012.

6.3.4 Sea ice property data

Ice thickness was measured using a 9 cm diameter ice core obtained from FYI at the field site on 10 May, 2012. The total ice thickness was 130 cm. Cores were cut into 2.0 or 2.5 cm thick slices. The slices were weighed for density, then melted for salinity measurements. Ice salinity from melted ice cores was acquired using a WTW Cond 330i conductivity meter with an accuracy of ±0.5%.

6.3.5 Surface-based microwave scatterometer data

C-band microwave data using a fully polarimetric scatterometer (Figure 6.3) was acquired for selected thin, medium and thick snow sites. For multi-temporal study purposes, a minimum of three measurements per day were acquired for each of the three snow sites from 15 May - 30 May, 2012. For the *diurnal* study, ~10 measurements per day over a 48-hour period were acquired for the thin and thick snow sites.

Details of the C-band scatterometer, its signal processing, and near-field correction are provided in Geldsetzer et al. (2007). Only a brief description is presented here. The C-band polarimetric scatterometer operates at a central frequency of 5.5 GHz with a bandwidth of 1 GHz. The scatterometer has an antenna diameter of 0.61m, an antenna beam-width of 5.4° and a range resolution of 0.30 m. The scatterometer possesses the capability to obtain pure samples at high spatial and temporal resolutions. The co-pol noise floor of the sensor is ~ -36 dB and that of cross-pol is ~ -42 dB.

External calibration was carried out by placing a trihedral corner reflector with a radar cross-section of 2.26 m^2 in the far-field of the antenna (>14m). The scans were made at 2° increments from 15° to 75° incidence angle. The azimuth range was 60°. Replicate scans were made for each measurement, to obtain multiple (usually 3) “looks” of the same area. To reduce the amount of near-field correction during processing, the scatterometer was elevated during sampling; using a platform on a komatiq thereby providing an axis height 2.6 m.

The acquired scatterometer data was further processed and quality checked. The processing included calibration, an adjustment of incidence angles, and identification and deletion of bad data lines. After processing, the program resulted in normalized radar cross-section values for co- and cross-polarized backscatter and various polarimetric measures derived from the covariance matrix.

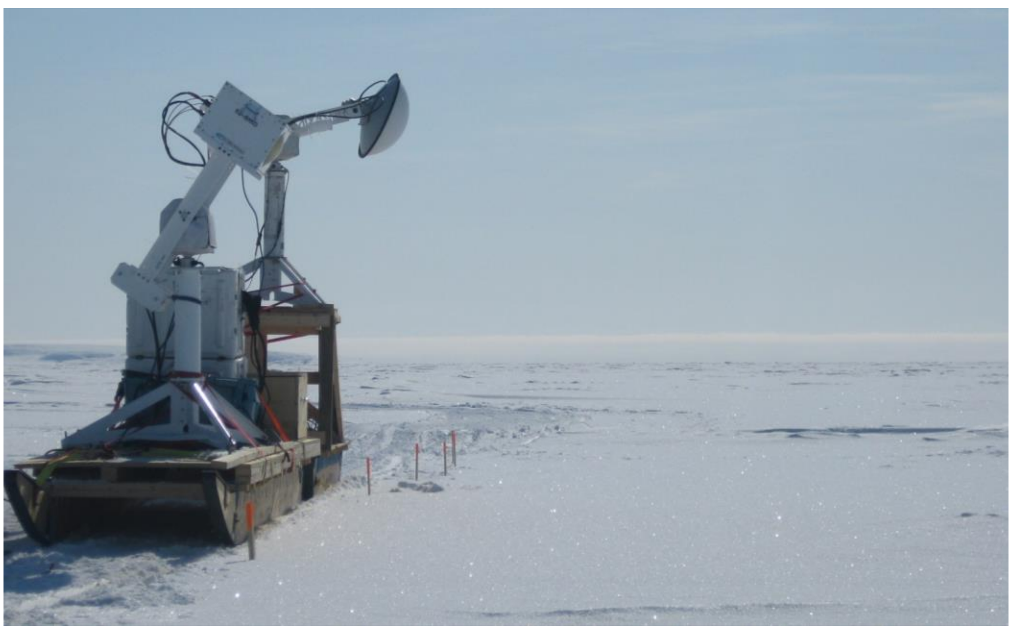

Figure 6.7. C-band polarimetric microwave scatterometer over smooth FYI, in Resolute Bay, in May, 2012.

6.3.6 SAR data

Polarimetric Radarsat-2 SAR data were collected over the field site during the study period. Acquisitions are summarized in Table 6.1. Co- and cross-polarized polarimetric parameters, co-polarized ratio, total power and co-polarized correlation coefficient were computed for analysis.

Table 6.2. Specifications of the Radarsat-2 SAR imagery utilized in the study and the temperature conditions at the time of image acquisition.

Date (yyyy-mm-dd)	Time (UTC)	Scan Direction	Incidence Angle (°)	Temperature (°C)
2012-05-17	23:41	Asc	40	-11.9
2012-05-17	13:16	Desc	38	-13.4
2012-05-22	23:53	Asc	35	-5.8
2012-05-22	13:28	Desc	33	-6.4

6.3.7 Photographic data

The photographic data included the pictures of different ice and snow cover surfaces to validate and provide record of surficial conditions.

Figure 6.8. Photographs showing snow and sea ice surface conditions. The snow (top) and the sea ice (bottom) after removing the snow cover, show the smooth surface. The destructive snow sampling site was within 100 meters from the non-destructive sites.

6.3.8 *Modelling*

The brine volume fraction was calculated from the measured snow physical properties. The refraction, reflection, loss factors and penetration depth of the microwaves at C-band frequency were calculated using measured snow dielectric properties. Snow physical and dielectric properties were used in combination to model the surface and volume scattering from snow covered smooth FYI.

6.3.8.1 Brine volume fraction

The brine volume fraction of snow (φ_{bs}) was calculated after Drinkwater and Crocker (1988), using equation 6.1.

$$\varphi_{bs} = \left[\frac{\varphi_{bsi}\rho_b}{(1-\varphi_{bsi})\rho_i + \varphi_{bsi}\rho_b}\right]\left[\frac{\rho_s}{\rho_b}\right] \tag{6.1}$$

where ρ_s is the density of snow (g cm^{-3}), ρ_i is the temperature-dependent density of pure ice (g cm^{-3}), ρ_b is the density of brine (g cm^{-3}) as a function of salinity and temperature, φ_{bsi} is the temperature-dependent brine volume fraction in sea ice.

The temperature-dependent density of pure ice was computed after Pounder (1965), equation 6.2.

$$\rho_i = 0.917 - 0.0001403T_S \tag{6.2}$$

where T_s is the temperature of snow (°C).

The salinity dependent density of brine ρ_b was derived using equation 6.3 (Cox and Weeks, 1975)

$$\rho_b = 1 + 0.0008S_b \tag{6.3}$$

where S_b is the temperature dependent brine salinity computed using equations 6.4, after Assur (1960) and Poe et al., (1972).

$$\begin{aligned} S_b &= 0.02515 - 17.787T_S^2 && ,T_S > -2°C \\ S_b &= 1.725 - 18.75T_S - 0.3964T_S^2 && ,-2°C \geq T_S \geq -8.2°C \\ S_b &= 57.041 - 9.929T_S - 0.1604T_S^2 - 0.002396\, T_S^3 && ,-8.2°C \geq T_S \geq -22.9°C \end{aligned} \tag{6.4}$$

The temperature dependent brine volume fraction of sea ice was calculated after Assur, (1960), Frankenstein and Garner (1967), Poe et al., (1972), equation 6.5.

$$\begin{aligned} \varphi_{bsi} &= 10^{-3}S_S 500.9 && ,T_S = -0.1°C \\ \varphi_{bsi} &= 10^{-3}S_S 250.5 && ,T_S = -0.2°C \\ \varphi_{bsi} &= 10^{-3}S_S 167.1 && ,T_S = -0.3°C \\ \varphi_{bsi} &= 10^{-3}S_S 125.4 && ,T_S = -0.4°C \\ \varphi_{bsi} &= 10^{-3}S_S\left(-\frac{52.56}{T_S} - 2.28\right) && ,-0.5°C \geq T_S \geq -2.06°C \\ \varphi_{bsi} &= 10^{-3}S_S\left(-\frac{45.917}{T_S} + 0.93\right) && ,-0.26°C \geq T_S \geq -8.2°C \\ \varphi_{bsi} &= 10^{-3}S_S\left(-\frac{43.795}{T_S} + 1.189\right) && ,-8.2°C \geq T_S \geq -22.9°C \end{aligned} \tag{6.5}$$

where S_S is the snow salinity (‰).

6.3.8.2 Penetration depth and loss factor

The microwave penetration depth in a single medium ignoring the losses was computed by equation 6.6 (Ulaby et al., 1984)

$$\delta_p(\theta) = \frac{\lambda_0}{4\pi}\left\{\frac{\varepsilon'}{2}\left[\left(1+\left(\frac{\varepsilon''}{\varepsilon'}\right)^2\right)^{1/2} - 1\right]\right\}^{-1/2} \tag{6.6}$$

where λ_0 is the wavelength in free space. The vertical penetration depth was computed using equation 6.7.

$$\delta_p = cos\theta\delta_p(\theta) \tag{6.7}$$

To account for the losses, the extinction coefficient was computed using equation 6.8, two-way loss in the snow layer using equation 6.9 (Winebrenner et al., 1992) and one-way loss factor using equation 6.10.

$$Ke = \frac{1}{\delta_p(\theta)} \tag{6.8}$$

$$L = exp\left(\frac{-2Ke\tau}{cos\theta'}\right) \tag{6.9}$$

$$l = exp\left(\frac{-Ke\tau}{cos\theta'}\right) \tag{6.10}$$

where τ is the thickness of snow layer (m). The penetration depth was found to have reached when equation 6.11 (Hallikainen and Winebrenner, 1992) was satisfied.

$$\frac{P(d)}{P(0_+)} = \frac{1}{e} \tag{6.11}$$

where $P(d)$ is the power at depth d, and $P(0_+)$ is the original power entering the medium.

6.3.8.3 Surface scattering

Surface scattering from snow covered sea ice depends on surface roughness, dielectric mismatches within the snowpack, microwave frequency and radar incidence angle. Surface scattering can therefore occur at: 1) snow surface, 2) at the interface between dry snow/brine-wetted snow, and 3) at the snow/sea ice interface.

Surface scattering in the current study was modeled using a scalar approximation of Kirchoff's Gaussian scattering model after Rees (2006), equation 6.12.

$$\sigma_p^{\circ}(\theta) = \frac{4\pi^2 Lc^2}{\lambda^2} cos^2\theta R_p(\theta) exp\left(-\frac{16RMS^2 cos^2\theta}{\lambda^2}\right)$$

$$\times \sum_{n=1}^{\infty} \left[\frac{(16RMS^2 - cos^2\theta)/\lambda^2}{n!\,n}\right]^n exp\left(-\frac{4\pi^2 Lc^2 sin^2\theta}{n\lambda^2}\right) \tag{6.12}$$

where R_p is the polarization-dependent reflection coefficient in power. The estimates of vertical surface roughness in the form of root mean square error (RMS) and the horizontal homogeneity measure of roughness represented by correlation length (L_C) were obtained from Carlström and Ulander (1995). The RMS and the L_C values used for snow surface and snow/sea ice interface were 0.002 m and 0.03 m, respectively. The RMS and the L_C values used for internal snow interfaces were 0.005 m and 0.03 m, respectively.

6.3.8.4 Volume scattering

Volume scattering from snow covered FYI depends on the size, number and dielectric properties of snow grains, brine inclusions in snow and the brine inclusions in sea ice. The size of snow grains was obtained from digital analysis of the field photographs of snow. The number density of snow grains was estimated after Drinkwater (1989) using equation 6.13. The number density of brine inclusions was set to equal the number density of snow grains.

$$N_s = \frac{3\rho d_s}{4\pi r_s^3} \tag{6.13}$$

where ρd_s is the dry snow density measured in field, r_s is the mean radius of snow grains measured from grain photographs taken in the field.

The number density of brine inclusions in snow N_b was set to equal N_s. The number density of brine inclusions in sea ice was acquired from Light et al., (2003). It was 1×10^{10}. The radius of brine inclusions in snow r_b was estimated using equation 6.14.

$$r_b = \left(\frac{3\varphi_{bs}/N_b}{4\pi}\right)^{1/3} \tag{6.14}$$

where φ_{bs} is the snow brine volume fraction. The radii of brine inclusions in sea ice r_{bsi} were assumed as 0.0005m (Barber and LeDrew, 1994).

The scattering coefficients for a snow volume σ_{vol} and a sea ice volume $\sigma_{vol\,si}$ were modeled after Drinkwater (1989) using the equations 6.15 and 6.16, respectively.

$$\sigma_{vol} = N_s.\sigma_{grain} + N_b.\sigma_{brine} \tag{6.15}$$

$$\sigma_{vol\,si} = N_{sb\,si}.\sigma_{brine\,si} \tag{6.16}$$

where σ_{grain}, σ_{brine} and $\sigma_{brine\,si}$ are the individual backscatter cross-sections of snow grains, brine in snow and brine in sea ice, respectively. These were computed following Drinkwater (1989), using equation 6.17.

$$\sigma_{grain} = \frac{64\pi^5 r_s^6}{\lambda^4}\left|\frac{\varepsilon_i^* - \varepsilon_a^*}{\varepsilon_i^* + 2\varepsilon_a^*}\right|^2 \tag{6.17}$$

$$\sigma_{brine} = \frac{64\pi^5 r_b^6}{\lambda^4}\left|\frac{\varepsilon_b^* - \varepsilon_a^*}{\varepsilon_b^* + 2\varepsilon_a^*}\right|^2$$

$$\sigma_{brine\,si} = \frac{64\pi^5 r_{bsi}^6}{\lambda^4}\left|\frac{\varepsilon_b^* - \varepsilon_i^*}{\varepsilon_b^* + 2\varepsilon_i^*}\right|^2$$

where ε_a^* and ε_i^* are the complex dielectric constants of air and pure ice, respectively.

The normalized radar cross-section for the volume scattering component of the snow layer and sea ice layer were modeled after Kendra et al., (1998) by applying a two-way loss factor, equation 6.18.

$$\sigma^{\circ}_{vol} = \frac{1-L}{2Ke/cos\theta'}\sigma_{vol} \tag{6.18}$$

$$\sigma^{\circ}_{vol\,si} = \frac{1-L}{2Ke/cos\theta'}\sigma_{vol\,si}$$

6.3.8.5 Total scattering

Similar to Kim et al. (1984) and Ulaby et al. (1984), total scattering contributions from all snow and sea ice layers was computed following a multi-layer approach, equation 6.19.

$$\sigma^{\circ}_{total}\theta_{pp} = \sigma^{\circ}_{as} + \Psi^2_{as}(\theta)\sigma^{\circ}_{svu} + \sum_{k=1}^{m}\sigma^{\circ}_{k} \tag{6.19}$$

where σ°_{as} is the surface scattering component for the air-snow interface, $\Psi^2_{as}(\theta)$ is the polarization-dependent power transmission coefficient at the air-snow interface, $\sigma^{\circ}_{svu}$is the volume scattering component of the topmost snow layer, σ°_{k} is the scattering component for each snow layer k.

$$\sigma_k^\circ = \prod_{j=1}^{m} L_j(\theta') \, . \left(\prod_{j=1}^{m} \Psi_{\mathrm{j}}^2\,(\theta') . \,\sigma_{ss\,k}^\circ + \prod_{j=1}^{m} \Psi_j^2(\theta') . \,\Psi_k^2(\theta') \,. \,\sigma_{sv\,k}^\circ \right) \tag{6.10}$$

where $\sigma_{ss\,k}^\circ$ is the surface scattering component of individual snow or ice layer, $\sigma_{sv\,k}^\circ$ is the volume scattering component of snow or ice layer, j is the snow or ice layer immediately above k, m is the number of snow or ice layers above the layer k, L is the two-way loss factor, θ^i is the refracted incidence angle and $\Psi\left(\theta^i\right)$ is the power transmission coefficient at the upper surface of each layer.

6.4 Results and Discussion

The results are presented for two studies comprising two temporal periods: Study-1) Diurnal; and Study-2) Time-series from early melt to melt onset.

In Study-1, coincident electrical, thermal, physical and C-band microwave backscatter observations acquired over a 24-hour period for thick (16cm) snow covered smooth FYI are presented. Two cases of the diurnal observations are presented: Case-1) Early-melt period; Case-2) Melt onset period. All measurements were taken every 2-3 hours, resulting in at least 10-12 samples per day for both the cases.

In Study-2, continuous and coincident electrical, thermal, physical and C-band microwave backscatter observations acquired for thick (16cm) and thin (6cm) snow covered smooth FYI are presented. At least 5-6 measurements per day for both thick and thin snow sites were acquired.

6.4.1 Diurnal observations (Study-1)

6.4.1.1 Snow properties (Case-1)

All snow properties were typical of late winter or early melt period.

Snow temperatures displayed significant variability over time and depth, following the diurnal air temperature cycle during the transition from late winter to early melt. Snow temperatures were higher in the basal snow as compared to the upper snow layers during the night and the early hours of the morning. A temperature difference of ~5°C was observed between the uppermost snow layer and the snow-ice interface (Figure 6.9). During the late afternoon hours the snow temperature within the entire snowpack became isothermal.

Snow density remained mostly unchanged during the diurnal period. A small change in the basal snow temperature was observed as a consequence of penetration of surface heat. Overall, the density was found to be lower in the basal snow layers where the snow grains in the form of depth hoar are loosely packed.

Salinity was consistent over the diurnal cycle. It showed a peak (~20‰) at the 0-2 cm layer, immediately above the sea ice surface.

Brine volume fraction increased towards the sea ice. It was observed highest at the snow-ice interface and lowest at the uppermost layers of the snow. It showed a slight variation with the diurnal temperature cycle, increasing with temperature throughout the snowpack.

Dielectric constant and dielectric loss followed the trend similar to brine volume fraction. Both dielectric constant and dielectric loss were higher in the basal snow layers and showed a slight positive relationship with the diurnal air temperature cycle.

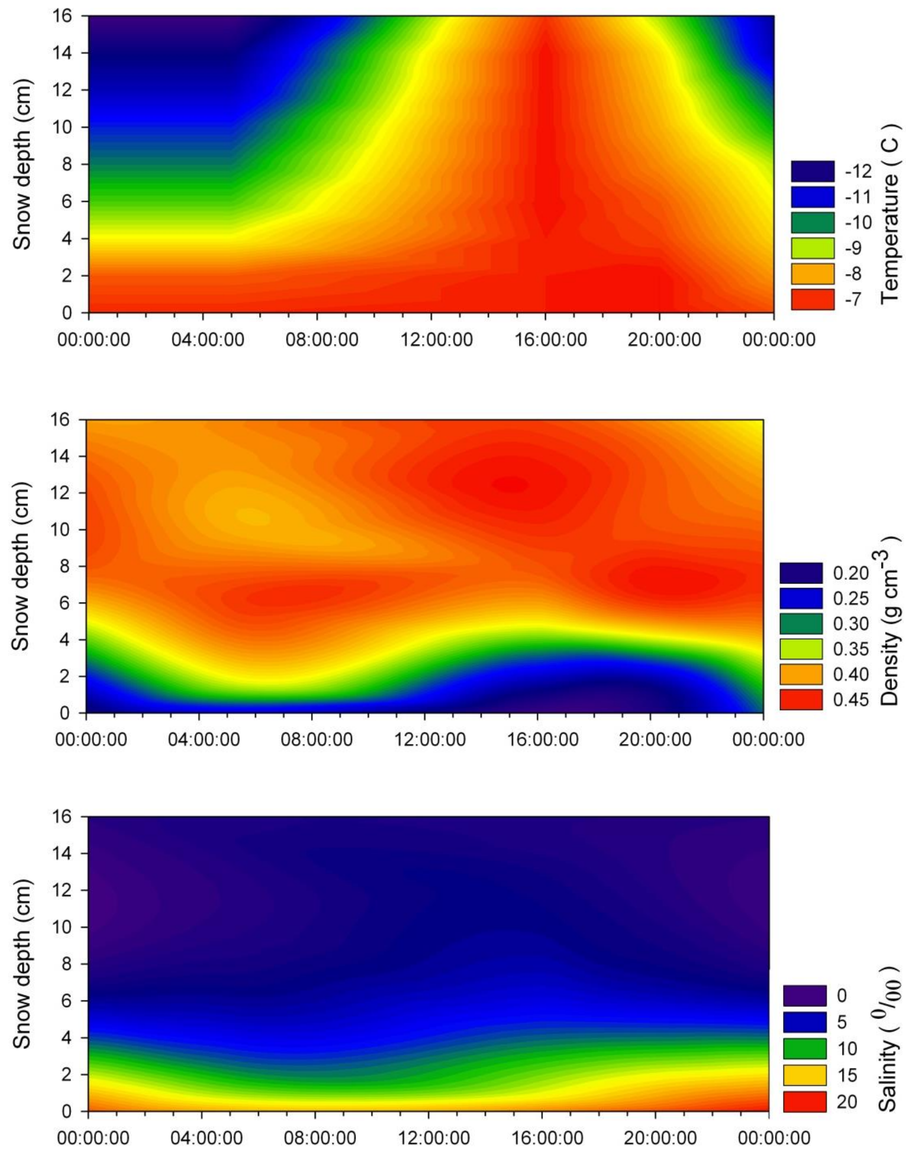

Figure 6.9. The measured and modeled diurnal snow properties of 16 cm snowpack for 17 May, 2012.

(Continued on next page)

Figure 6.6 (Concluded.)

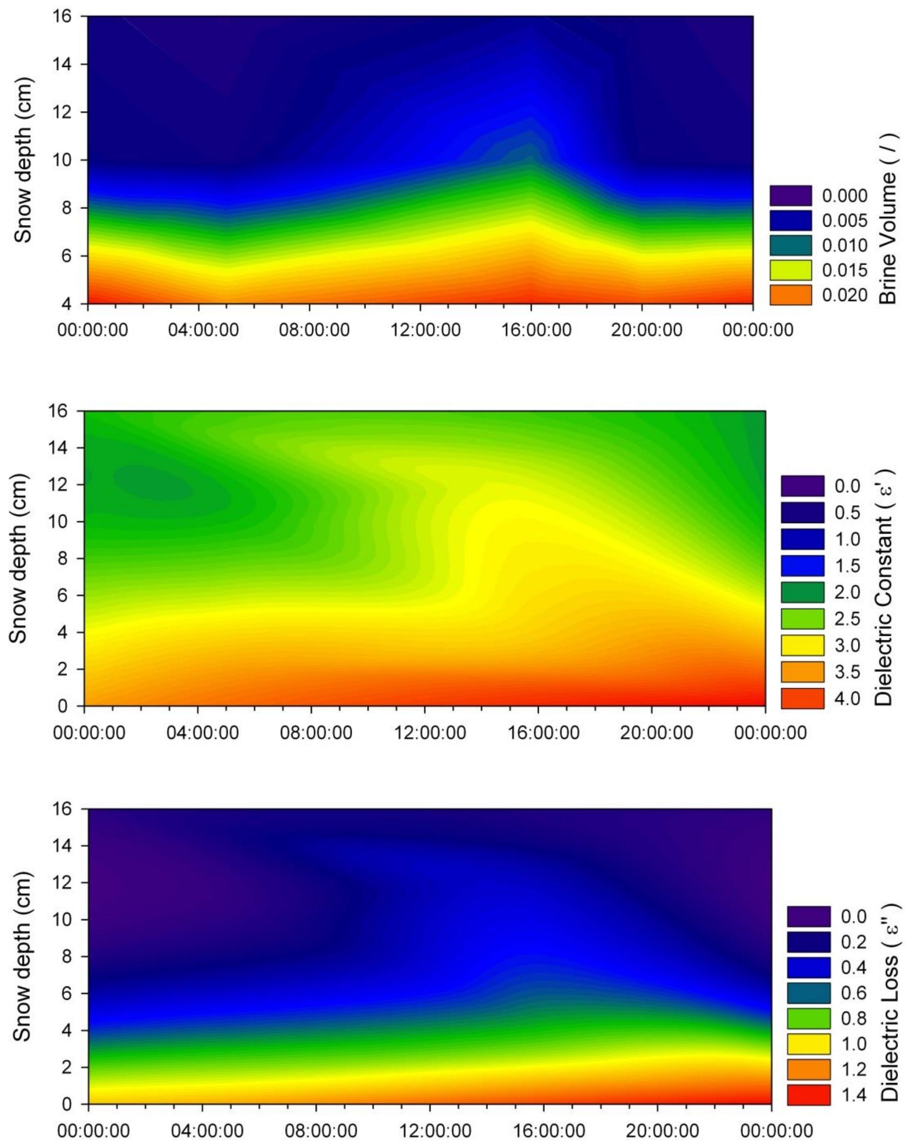

Figure 6.9. The measured and modeled diurnal snow properties of 16 cm snowpack for 17 May, 2012.

6.4.1.2 Snow properties (Case-2)

Case-2 exhibited snow properties typical of the melt onset period (Figure 6.10).

Snow temperatures within the volume did not exhibit any vertical gradient during the night and early hours of the day. A vertical temperature gradient began to appear only after the sun had warmed up the upper snow layers during the late morning to early afternoon hours. No significant variations in snow temperature as a consequence of diurnal temperature cycle were observed in the basal snow basal layer. However, the upper snow layers did demonstrate a positive relationship with diurnal air temperature.

Snow density was found to be higher in the middle layers of the snow pack throughout the day. Snow upper and basal layers demonstrated lower snow densities. The low basal snow densities can be attributed to less closely-packed depth hoar grains, whereas the low densities in the upper snow layers are due to increased incoming solar radiation resulting in snow warming and melting.

Salinities within the snowpack remained unchanged throughout the diurnal cycle. The salinities were higher in the basal layers and were concentrated between 0 and 6 cm of the snowpack.

Brine volume fraction, dielectric constant and dielectric loss followed the trend similar to that exhibited by salinity. Neither of these snow properties showed any variation as a consequence of diurnal temperature cycle.

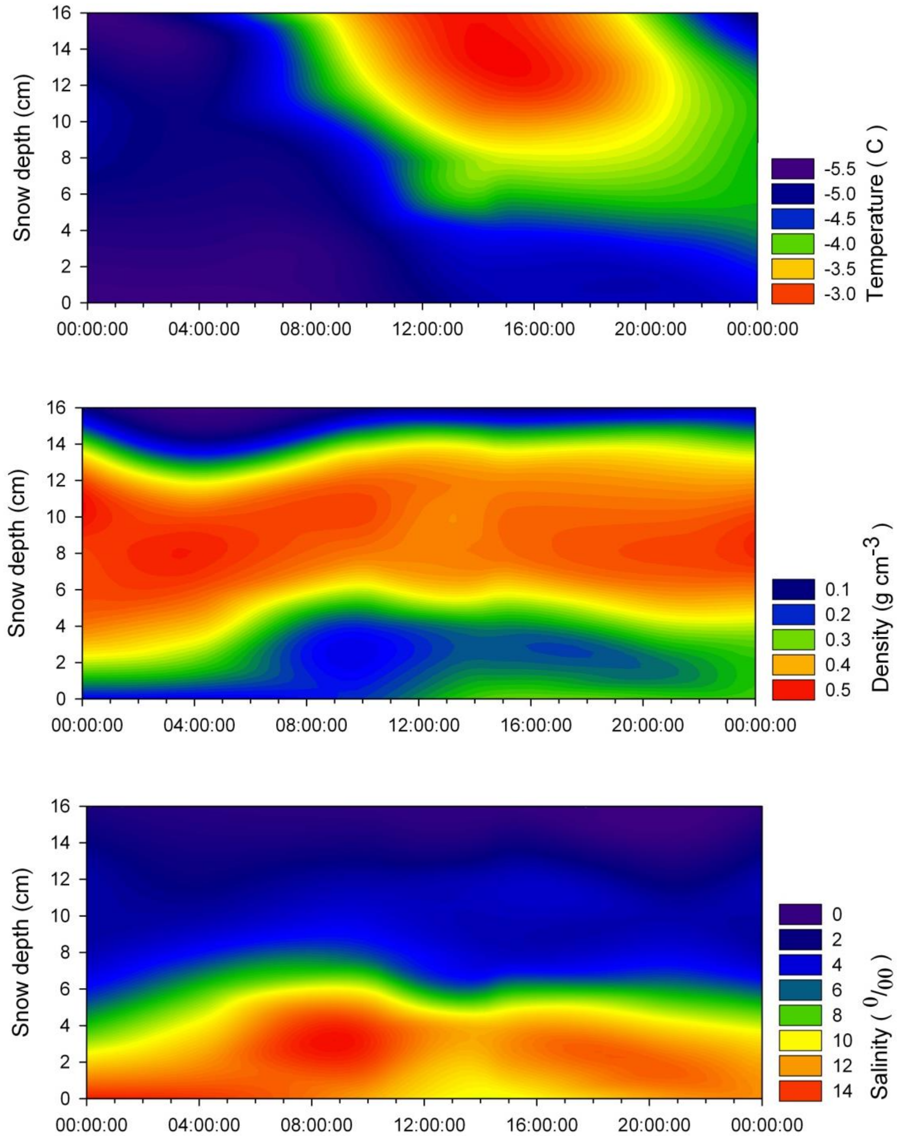

Figure 6.10. The measured and modeled diurnal snow properties of 16 cm snowpack for 22 May, 2012.

(Continued on next page.)

Figure 6.7 (Concluded.)

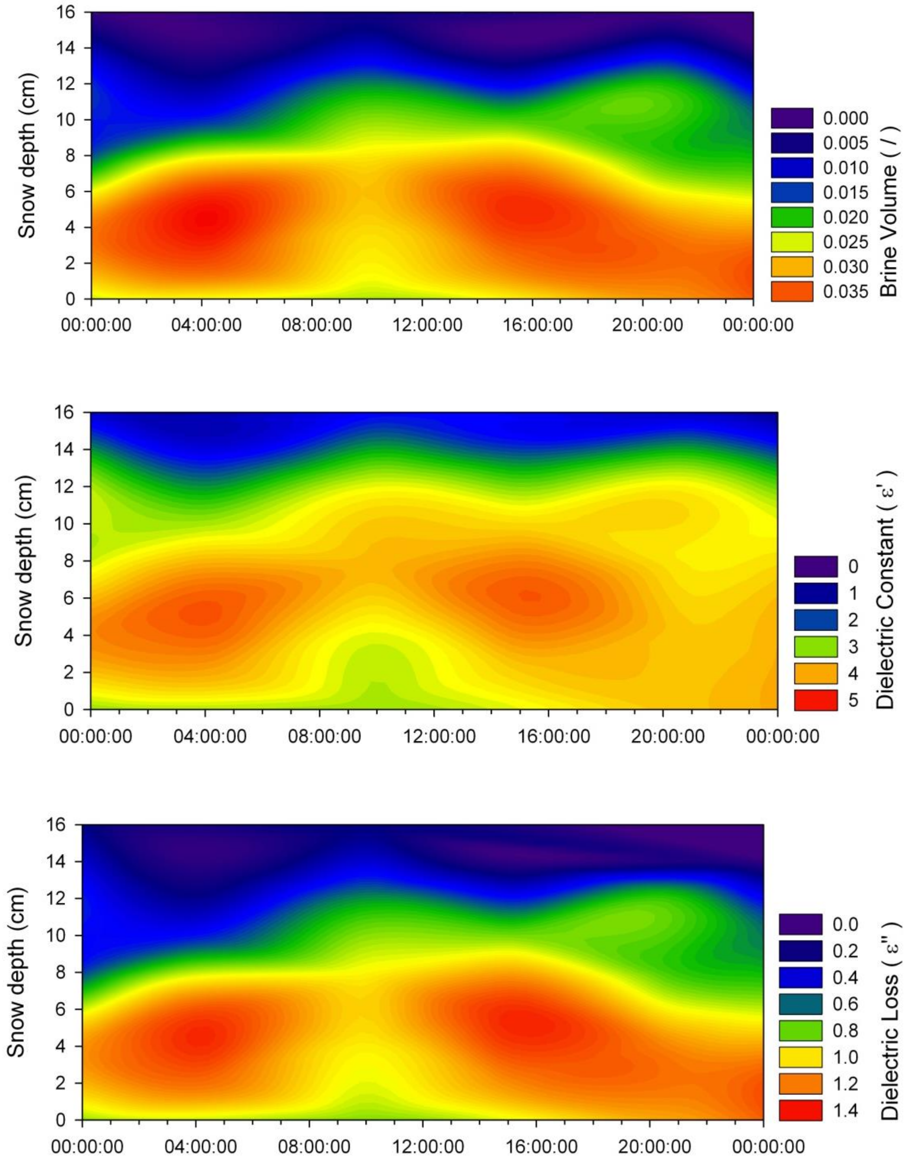

Figure 6.10. The measured and modelled diurnal snow properties of 16 cm snowpack for 22 May, 2012.

6.4.1.3 C-band scatterometer backscatter (Case-1)

Three polarimetric backscatter parameters were analyzed: vertical and horizontal co-polarized backscatter, and cross-polarized backscatter. Co and cross-polarized ratios, total power, phase differences did not present any useful information and were excluded.

The horizontal polarization noise floor was ~-34dB, the vertical polarization noise floor was ~ -36dB and the cross-polarization noise floor was at ~ -44dB.

The co-polarized horizontal backscatter (σ_{hh}^{o}) was higher at 20° incidence angle and gradually decreased with an increase in incidence angle (Figure 6.11). The decrease in $\sigma_{hh}^{o}$with incidence angle was greater from 20°-28° (10-12dB) and then gradual after 30°. This indicates the dominance of surface scattering at low incidence angles and the dominance of volume scattering at high incidence angles. The surface scattering may occur at the air/snow interface, snow/sea-ice interface or at the internal snow interfaces. The volume scattering may occur within in the snow or in few millimeters of upper sea ice layers. Between 50°-60° of incidence angle, noise floor was reached depending upon the hour of the diurnal period. Although no clear relationship could be established between the snow properties and σ_{hh}^{o}, the influence of the variations in snow properties over the diurnal cycle on σ_{hh}^{o} was evident. At an incidence angle of 20°, σ_{hh}^{o} gradually increased in the second half of the diurnal period (1200 to 2400 hours). This is primarily because the penetration depth at low incidence angles is higher. C-band microwaves that are able to penetrate deeper are more likely to be influenced by the basal snow properties or the properties of the uppermost layers of sea ice. In this context, brine volume in the basal snow or in the upper layers of sea ice is important. According to Barber and Nghiem, 1999 and Cox and Weeks, 1983, an increase in brine volume results in increased backscatter.

From 30°-40° incidence angle, no significant variation in σ_{hh}^{o} was observed during the 24 hour period. From 40°-60°, σ_{hh}^{o} changed in resonance with the snow properties.

The co-polarized vertical backscatter (σ_{vv}^{o}) showed similar response to σ_{hh}^{o}. The cross-polarized backscatter (σ_{hv}^{o}) did not present any useful information (Figure 6.11).

6.4.1.4 C-band scatterometer backscatter (Case-2)

In contrast to Case-1, σ_{hh}^{o}, σ_{vv}^{o} and σ_{hv}^{o} did not exhibit any variation over the 24 hour period (Figure 6.12). This can be attributed to two reasons: 1) Due to surficial warming, the snow was already too wet to allow any penetration of microwaves into the lower layers of the snowpack; 2) the snow properties did not change much over the 24 hour period to exert any influence on the microwave backscatter

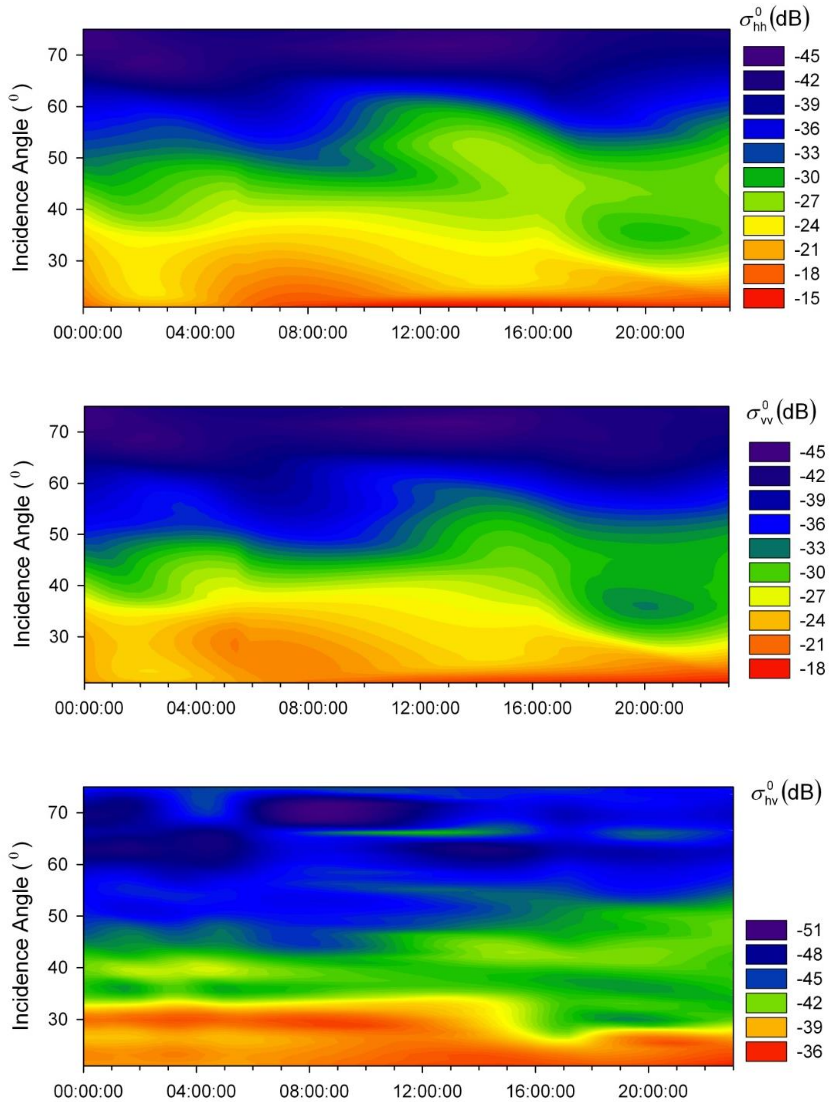

Figure 6.11. Diurnal polarimetric C-band microwave scattering properties of snow covered (16cm) smooth FYI for 17 May, 2012. Properties were measured using surface-based C-band scatterometer.

.

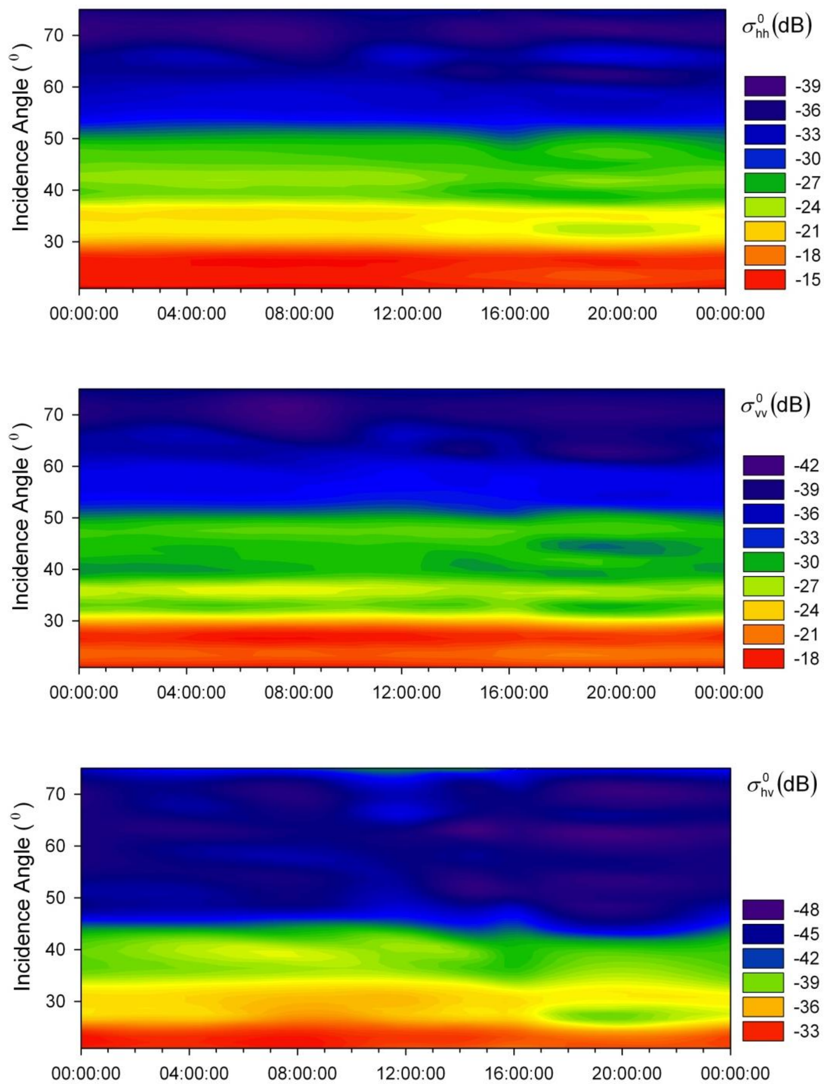

Figure 6.12. Diurnal polarimetric C-band microwave scattering properties of snow covered (16cm) smooth FYI for 22 May, 2012. Properties were measured using surface-based C-band scatterometer.

6.4.1.5 SAR backscatter (Case-1)

To validate the results, backscatter from Radarsat-2 SAR images acquired on 17 May, 2012 are analyzed for the same snow site. Results showed a difference of ~4 dB for σ^{o}_{hh} and σ^{o}_{vv} between the ascending and descending images (Figure 6.13). For σ^{o}_{hv}, the difference between the Radarsat-2 SAR image pair was ~2.5dB (Figure 6.13). Moreover, the two images analyzed were acquired at a difference of only 2° incidence angle. The backscatter difference due to incidence angle could possibly have further minimized the effect of diurnal variations in snow covered FYI ice properties on SAR backscatter.

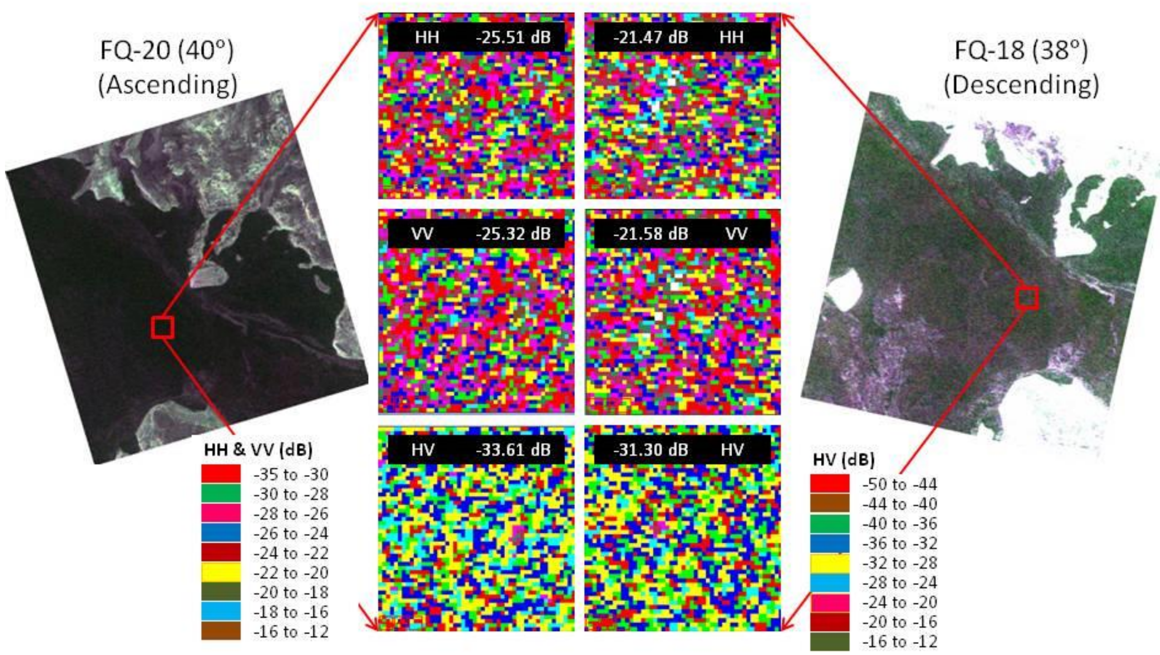

Figure 6.13. Polarimetric C-band microwave scattering from snow covered (16cm) smooth FYI for 17 May, 2012. Statistics are calculated from diurnally acquired Radarsat-2 SAR data.

6.4.1.6 SAR backscatter (Case-2)

Similar to Case-1, the backscatter from Radarsat-2 SAR images acquired on 22 May, 2012 are analyzed for the same snow site. Results show a difference of <1 dB for σ_{hh}^{o} and σ_{vv}^{o} between the ascending and descending imagery (Figure 6.14). For σ_{hv}^{o} the difference between the morning and evening passes of Radarsat-2 imagery was 1.26dB (Figure 6.14). These differences in backscatter could be the consequence of the radar incidence angle as the two images were acquired at a difference to 2° incidence angle.

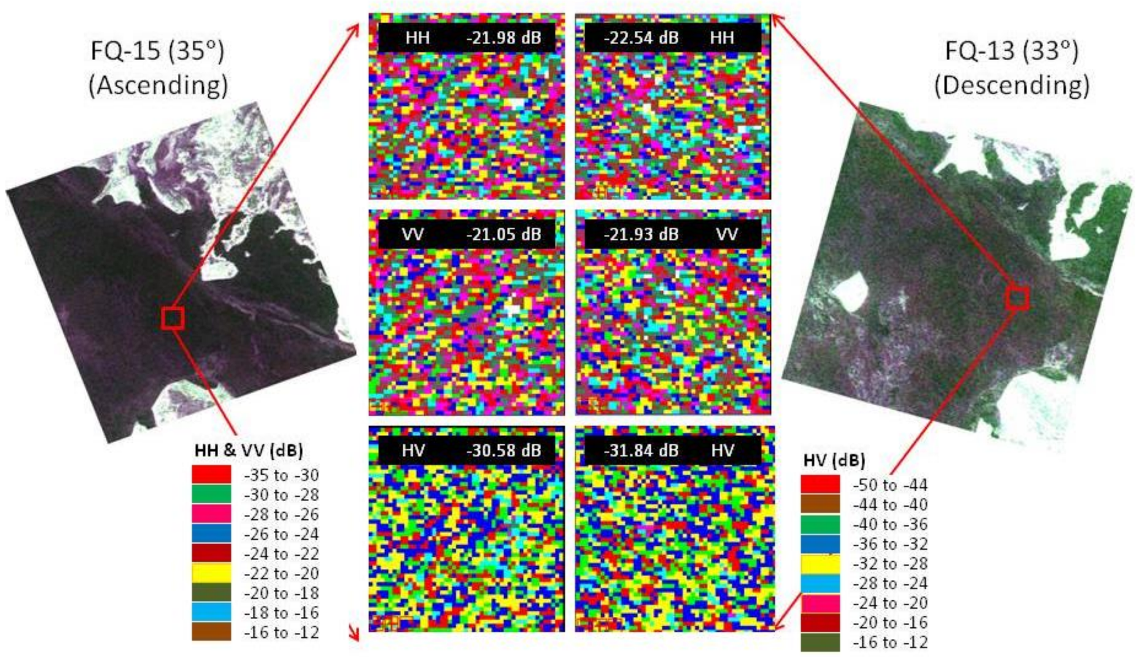

Figure 6.14. Polarimetric C-band microwave scattering properties of snow covered (16cm) smooth FYI for 22 May, 2012. Properties are acquired from Radarsat-2 data.

6.4.2 Time-series observations (Study-2)

Coincident electrical, thermal, physical and C-band microwave properties of thick (16cm) and thin (6 cm) snow covered smooth FYI are presented from early melt period to melt onset (acquired from 15 May to 30 May, 2012). To investigate the effect of snow thickness on polarimetric microwave backscatter at C-band frequency, six polarimetric parameters were evaluated: vertical and horizontal co-polarized backscatter, cross-polarized backscatter, co-polarized ratio, total power and co-polarized correlation coefficient.

6.4.2.1 Snow properties (Thick snow)

Temperatures in the snow pack (Figure 6.15) showed a close association with the air temperatures as shown in Figure 6.2. The overall trend was an increase in snow temperatures from 15 May to 25 May, 2012. Based on the snow temperatures, the entire study period could be split into two stages: 1) the early melt period until 20 May, 2012; and 2) the melt onset period from 21 May to 25 May, 2012. During the early melt period, the snow temperatures were higher in basal snow compared to the upper portion of the snow volume. The effects of diurnal temperature cycles were visible through striations representing intermittent periods of colder and warmer temperatures. After 20 May, a reversal in snow temperatures was observed. The temperatures in the basal snow were lower than the upper snow layers. The effect of diurnal temperature cycles was reduced and the snow volume temperature tended toward isothermal.

Snow densities from 15 May to 20 May, 2012 were typical of late winter to early melt period. The densities were higher in the upper and middle snow layers and low in the basal snow. This is due to the presence of less closely-packed depth hoar in the basal snow and the presence of compact wind slab in the middle snow layers. After 20 May, 2012 snow densities in the uppermost snow layers decreased as a consequence of surficial heating and melting of snow.

The salinities in the snowpack remained unchanged throughout the study period. The brine volume fraction remained concentrated at the snow-ice interface and in the first 3 cm of adjacent snow layers during the early melt period. After 20 May, 2012, brine volume fraction was observed reaching up-to 10 cm in the snow. This is due to the upward migration of brine through capillary action under the influence of increase in snowpack temperature (Barber and Nghiem, 1999; Cox and Weeks, 1983). The dielectric constant and the dielectric loss followed the trends similar to brine volume fraction.

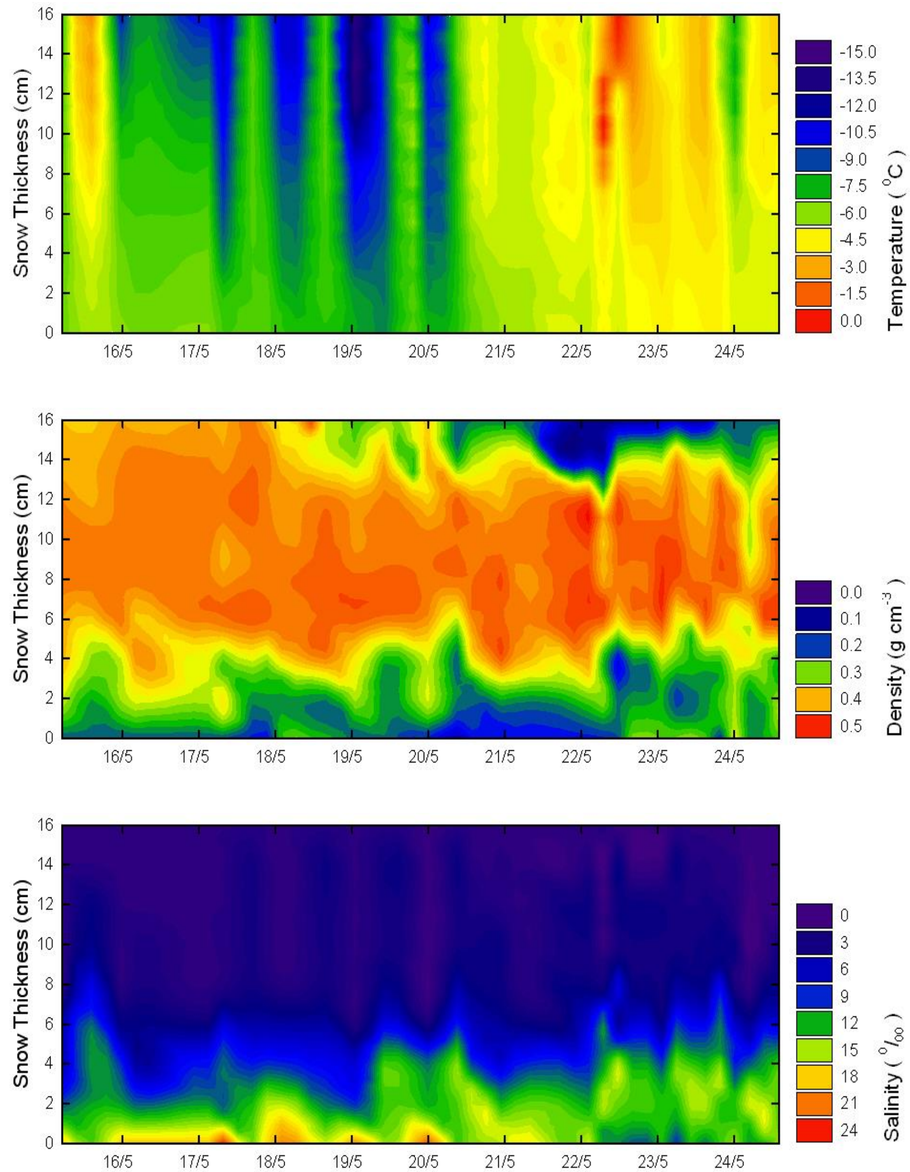

Figure 6.15. Measured and modelled time series physical, thermal and electrical properties of thick snow (16cm) from 15 May - 25 May, 2012. Measurements acquired were every ~4 hours.

(Continued on next page.)

Figure 6.15 (Concluded.)

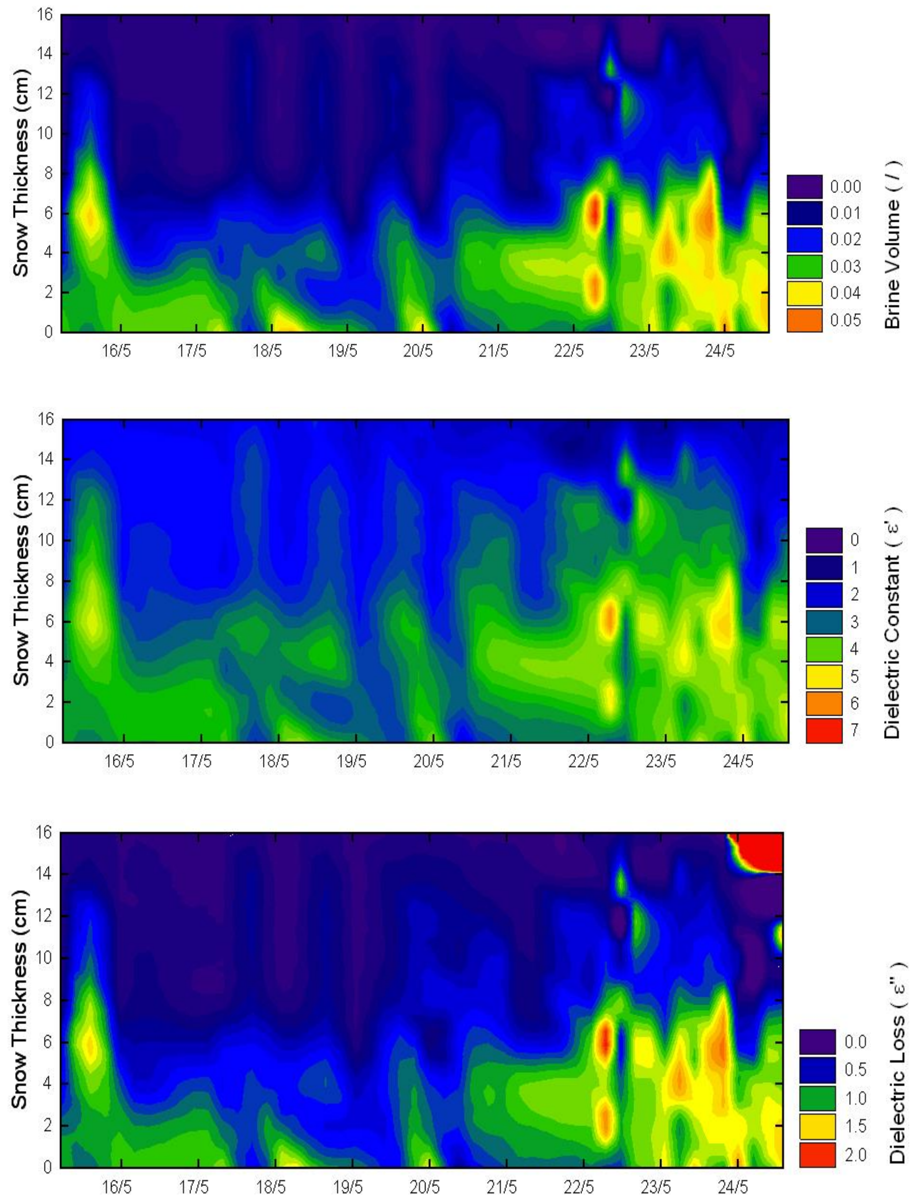

Figure 6.15. Measured and modelled time series physical, thermal and electrical properties of thick snow (16cm) from 15 May - 25 May, 2012. Measurements were acquired every ~4 hours.

6.4.2.2 Snow properties (Thin snow)

The physical and dielectric properties of thin snow (6cm) are presented from 15 May to 20 May, 2012 and from 25 May to 30 May, 2012 (Figure 6.16). The properties between 21 May and 25 May were not measured.

Thin snow temperatures during the early melt period were similar to thick snow temperatures demonstrating slightly higher values in the basal snow layer and the effect of diurnal temperature cycles through intermittent cold and warm periods. During the melt onset period (25 May-30 May, 2012) the entire snowpack observed higher temperatures (between -2°C and -6°C) as compared to early melt period. No differences in temperature with depth were evident.

Snow densities during the early melt and the melt onset periods were found to be randomly distributed within the snowpack. This is in contrast with the thick snow densities which showed a trend associated with changing air and snow temperatures. Salinities during the early melt period were higher as compared to melt onset period. In contrast to thick snow salinities, the salinities in thin snow were observed distributed throughout the snow pack, even reaching the snow surface, although slightly higher concentration was observed in the basal snow. Brine volume fraction was also distributed throughout the snow pack with slightly higher values in the basal snow. This is because in thin snow covers the vertical temperature gradient is strong and depth hoar develops more readily. The shape of depth hoar and a surplus of brine at the sea ice surface make the thin snow cover completely brine-wetted. Brine wicking under the influence of strong temperature gradient is another common phenomenon of thin snow covers. Interestingly, brine volume fraction increased during the melt onset period whereas salinities were found to decrease.

The dielectric constant and dielectric loss followed trends similar to brine volume fraction throughout the study period.

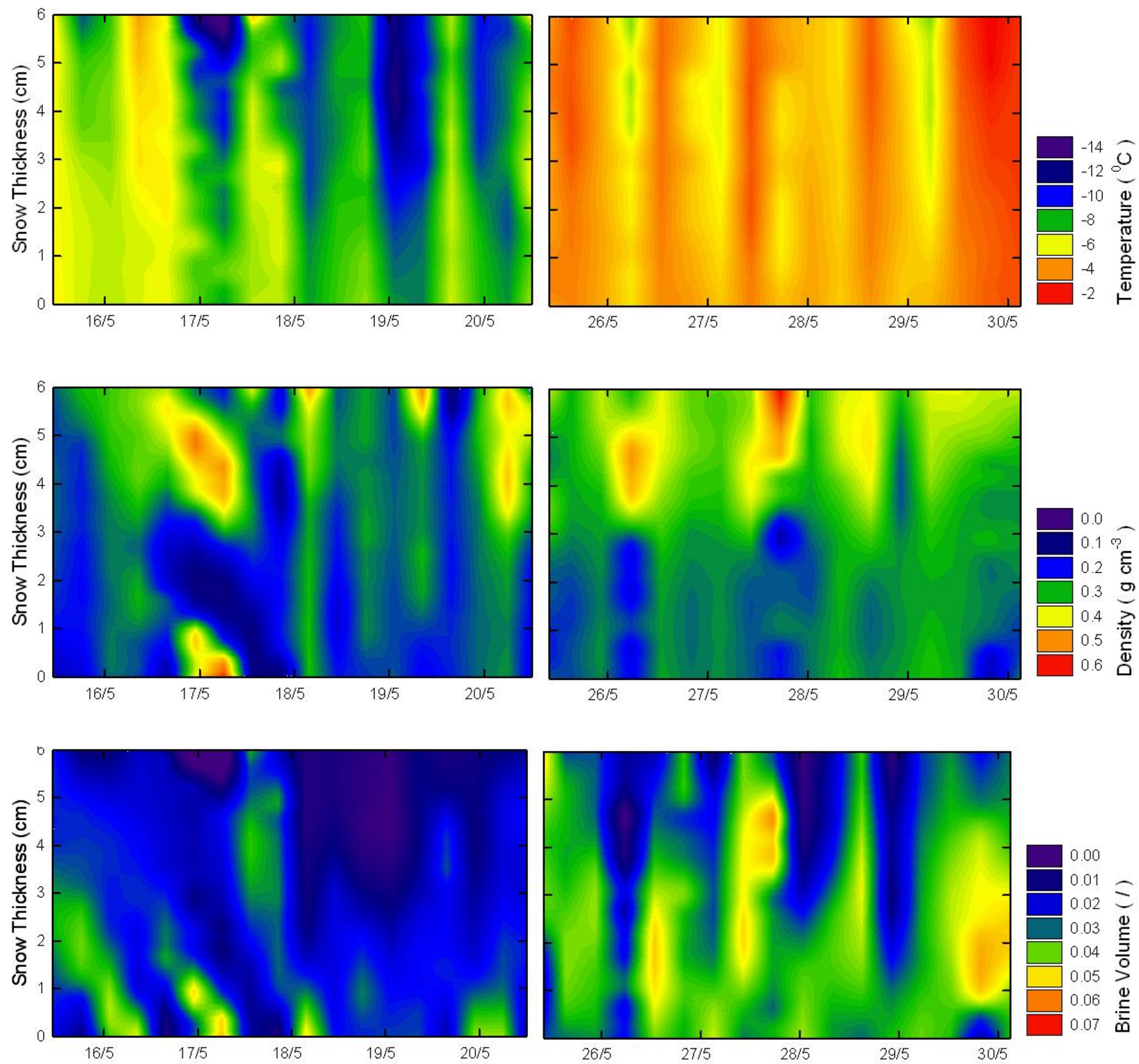

Figure 6.16. Measured and modelled time series physical, thermal and electrical properties of thin snow (6cm) from 15 May - 30 May, 2012. Measurements were acquired every ~4 hours.

(Continued on next page.)

Figure 6.16 (Concluded.)

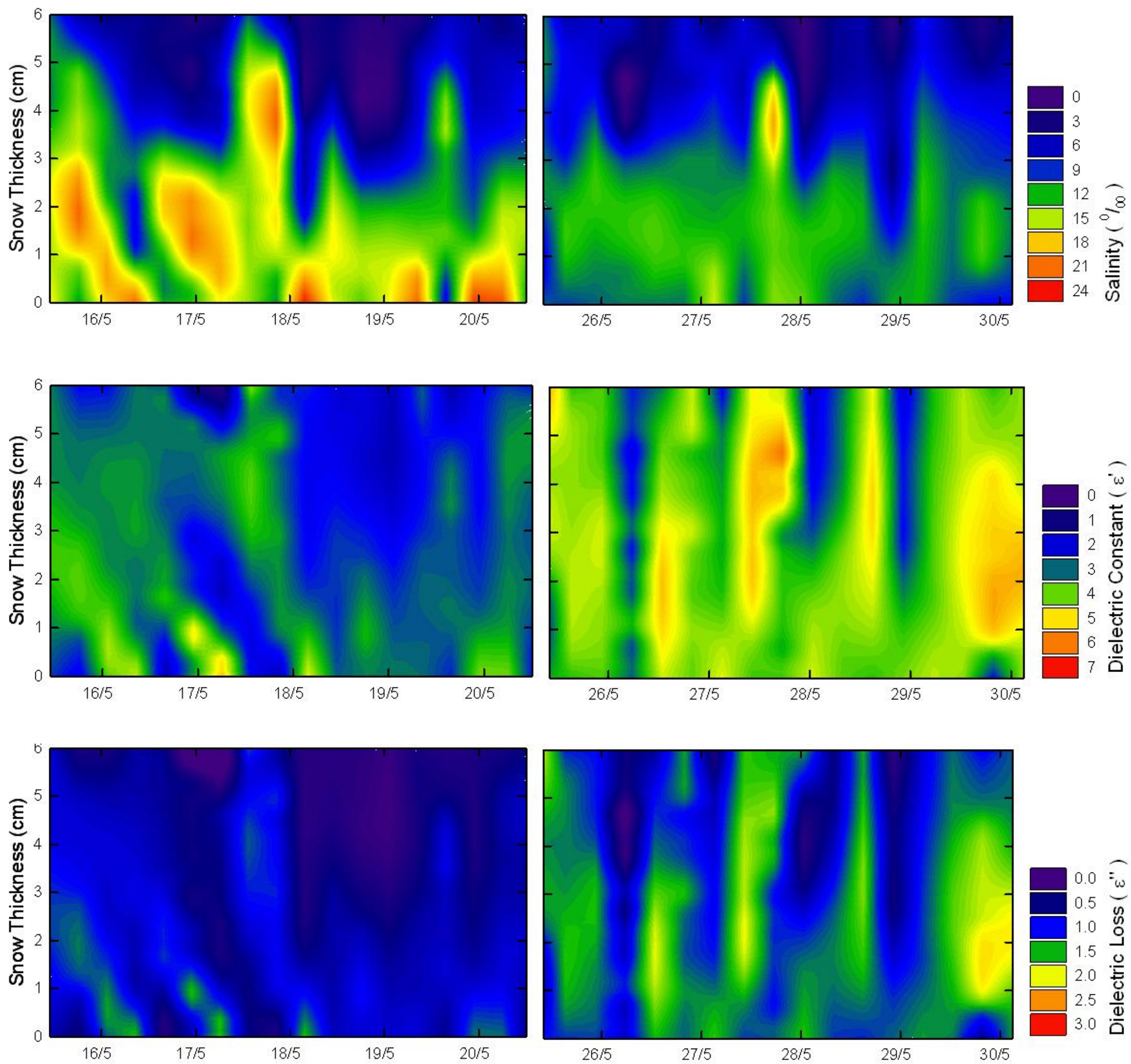

Figure 6.16. Measured and modelled time series physical, thermal and electrical properties of thin snow (6cm) from 15 May - 30 May, 2012. Measurements were acquired every ~4 hours.

6.4.2.3 Time series C-band scatterometer backscatter for thick snow

The response of six polarimetric parameters is analyzed in time series from measurements acquired from 15 May to 30 May, 2012 (Figure 6.17). The results are supplemented by modeled results of penetration depth (Figure 6.18), surface and volume scattering (Figure 6.16 – Figure 6.18) to help diagnose the scattering mechanisms from snow covered smooth FYI.

Co- and cross-polarized backscatter σ^o_{hh}, σ^o_{vv} and σ^o_{hv} demonstrated a correlated response over the study period (Figure 6.17). As expected, the backscatter was higher at low incidence angles. From 15 May to 21 May, the co- and cross-polarized backscatter at all incidence angles remained consistent and showed response to diurnal temperature cycles. It is interesting to note that on 16 May, σ^o_{hh}, σ^o_{vv} and σ^o_{hv} showed a rise at incidence angle below 50°. Above 50°, σ^o_{hh}, σ^o_{vv} and σ^o_{hv} showed a dip. The rise in σ^o_{hh}, σ^o_{vv} and σ^o_{hv} could be due to a warming event that occurred on 15 May. The lag of one day requires further investigation but given the thicker snow cover and low thermal conductivity of snow it stands to reason that the increase in backscatter due to increasing dielectrics from the warming event on 15 May may not be reflected in the snow cover until the following day. Similarly, σ^o_{hh}, σ^o_{vv} and σ^o_{hv} increased after 21 May at low incidence angles (between 20°-30°) and decreased above 30° incidence angle. This increase in σ^o_{hh}, σ^o_{vv} and σ^o_{hv} can be attributed to the rise in air and snow temperatures after 20 May. Once again, the lag of one day between the rise in snow temperatures and their effect on microwave backscatter necessitates further investigation.

The penetration depth at C-band for thick snow was computed for the study period (Figure 6.18). The highest penetration depth reached was 7 cm during cold phases on 17-19

May. For the most part of the study period the penetration depth was 3 cm at all incidence angles. This suggests that the backscatter was largely from the top few layers of snowpack. The influence of basal snow properties was negligible.

The surface and volume scattering contributions from the thick snow cover were modeled at three incidence angles: 20°, 40° and 60° (Figure 6.19 - Figure 6.21). Since the highest penetration depth was 7 cm, the results of surface and volume scattering are presented for the top 8 cm of the snowpack. At steep incidence angle of 20°, the total scattering was dominated by surface scattering (Figure 6.19). Surface scattering was low during the early melt period and gradually increased during melt onset period. Surface scattering usually occurs at the air/snow interface, at the dielectrically-mismatched media within snow, and at the snow/ice interface. Since the scattering was largely from the top few centimeters of snow and a little possibility of the presence of dielectrically-mismatched media in top snow layers, it can be concluded that surface scattering occurred at the air/snow interface. At 40° and 60° incidence angle, the scattering was largely volume (Figure 6.20 and Figure 6.21). Opposite to the trends of surface scattering, volume scattering was high during the early melt period and low during the melt onset period.

With respect to other polarimetric parameters, total power (Span) demonstrated response similar to co- and cross-polarized backscatter. Span is a sum of intensities at all polarizations. The co-polarized ratio r_{co} was mostly negative at all incidence angles throughout the study period. Negative r_{co} suggests second-order scattering effects. The co-polarized correlation coefficient ρ_{co} was close to one at steep incidence angles (20°-30°). It was >0.7 for the entire study at incidence angles below 60°. High ρ_{co} suggests highly polarized backscatter. At incidence angle >60°, ρ_{co} suggests depolarization.

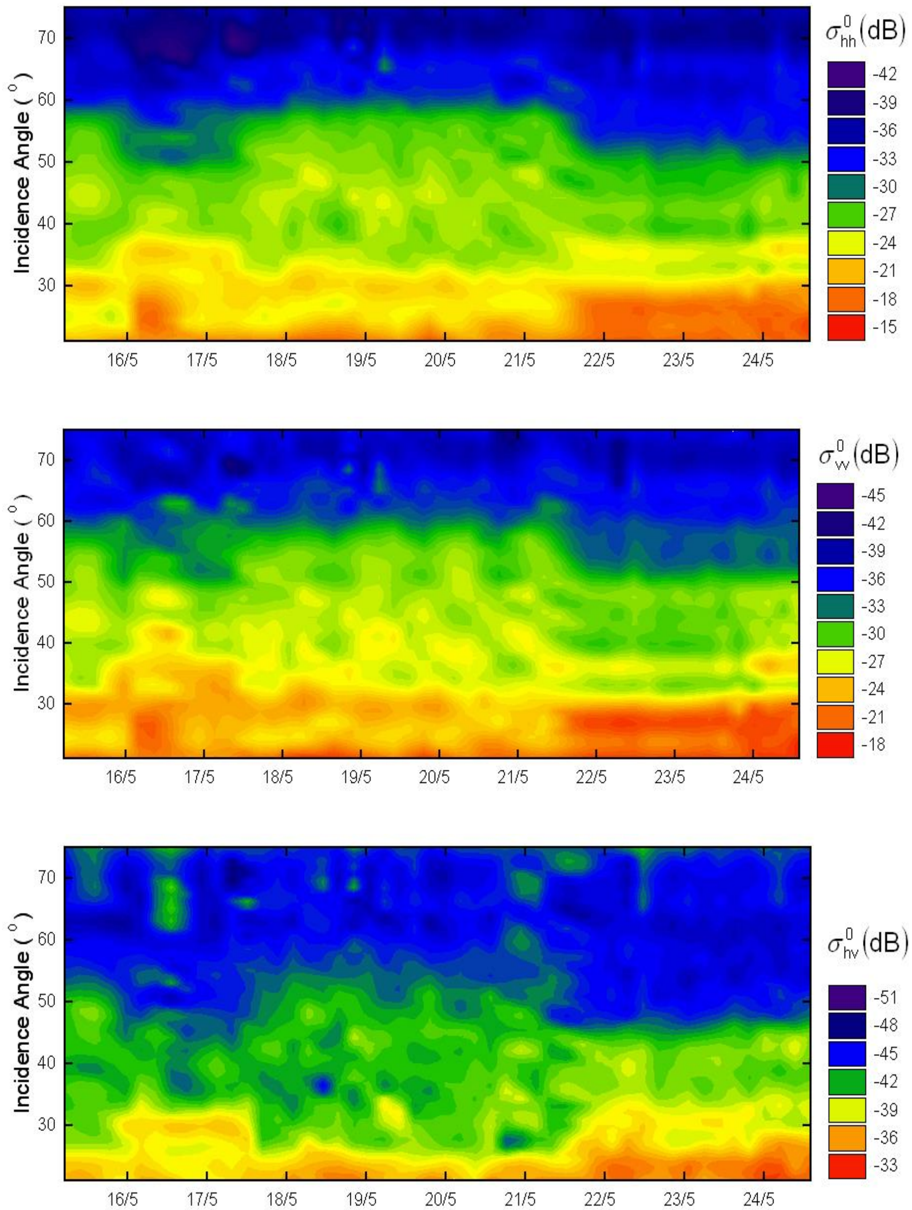

Figure 6.17. Time series polarimetric C-band microwave scattering properties of snow covered (thick, 16cm) smooth FYI from 15 May - 25 May, 2012. Properties were measured using surface-based C-band scatterometer.

(Continued on next page.)

Figure 6.17 (Concluded.)

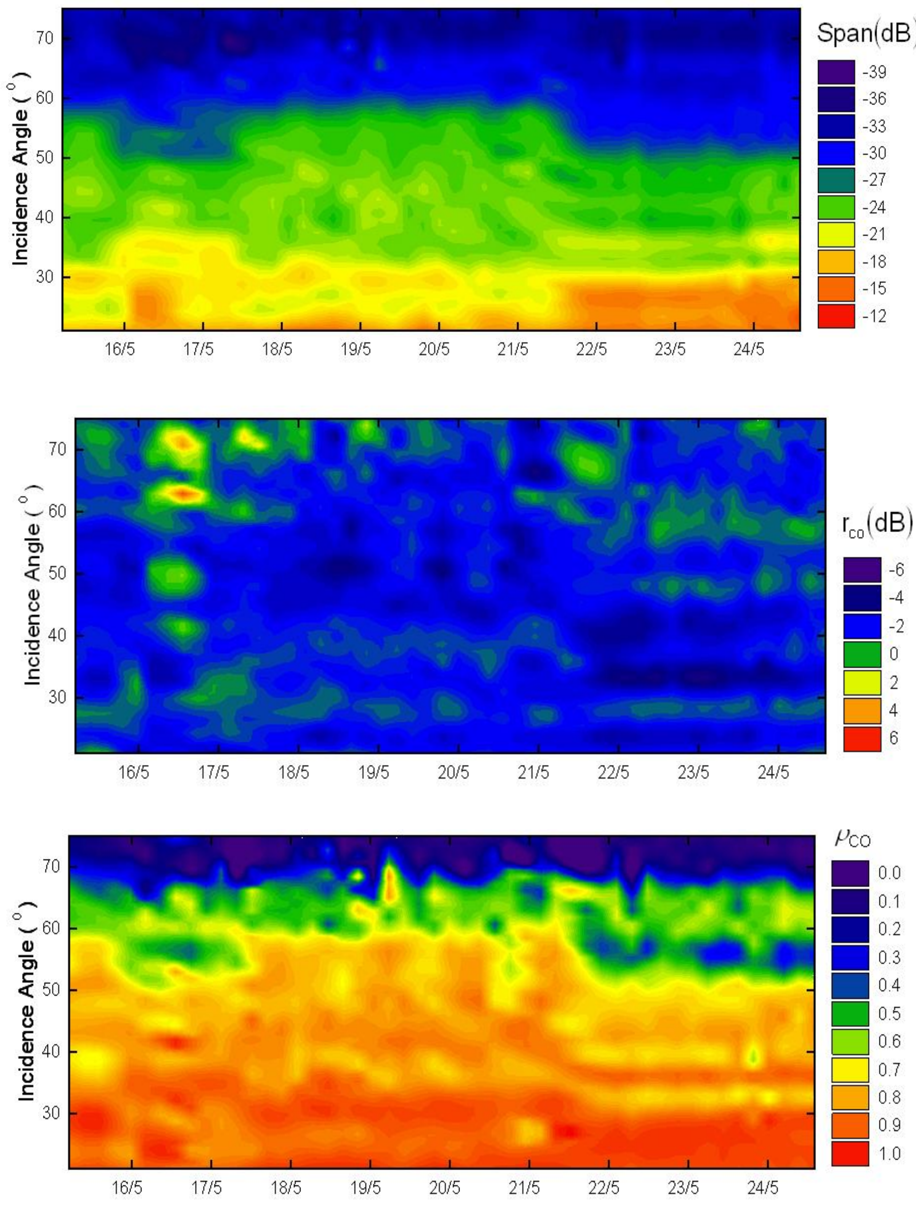

Figure 6.17. Time series polarimetric C-band microwave scattering properties of snow covered (thick, 16cm) smooth FYI from 15 May - 25 May, 2012. Properties were measured using surface-based C-band scatterometer.

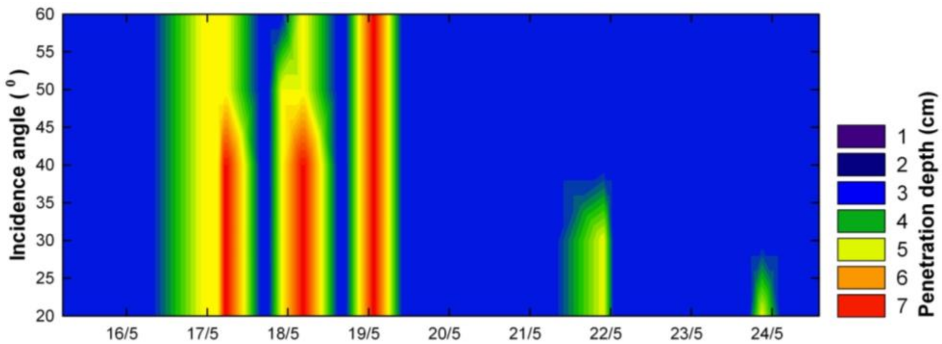

Figure 6.18. Time series penetration depth of polarimetric C-band microwave for thick snow covered (16cm) smooth FYI from 15 May - 25 May, 2012.

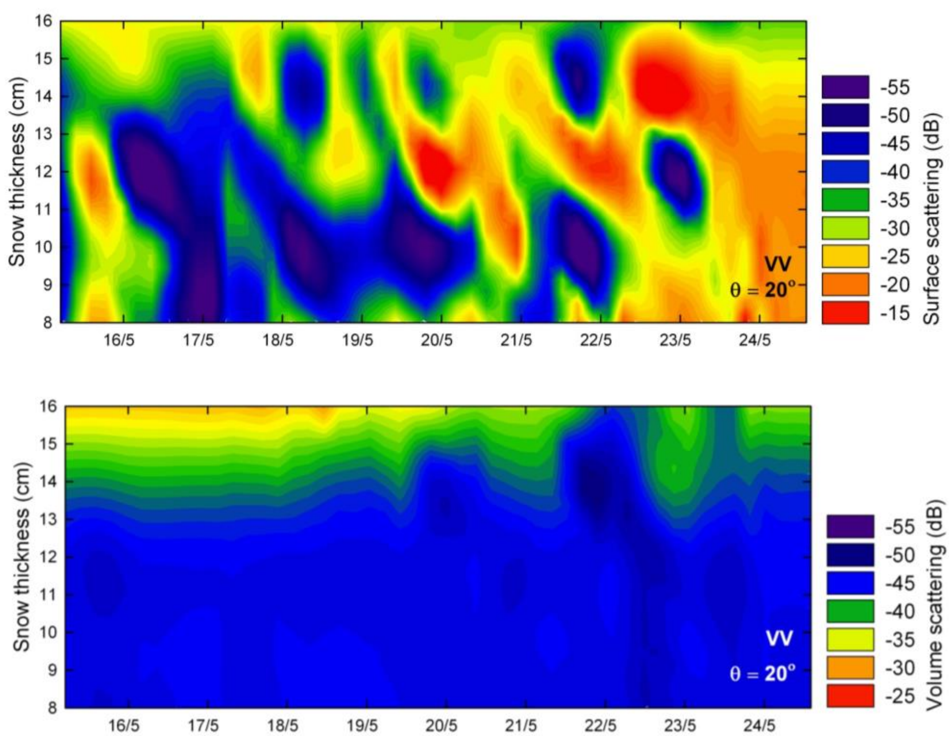

Figure 6.19. Time series modeled potential surface and potential volume scattering for C-band microwave at 20° incidence angle for thick snow covered (16cm) smooth FYI from 15 May - 25 May, 2012. (Note: Potential here means scattering from snow layer considering absence of any layer above it and also not taking scattering losses into account).

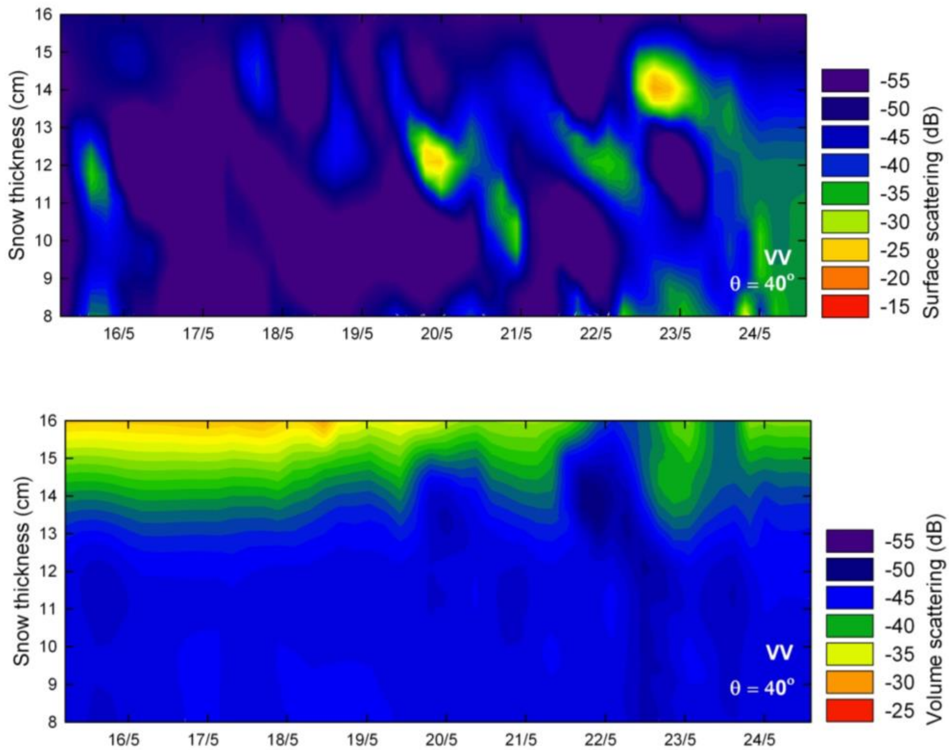

Figure 6.20. Time series modeled potential surface and potential volume scattering for C-band microwave at 40° incidence angle for thick snow covered (16cm) smooth FYI from 15 May - 25 May, 2012. (Note: Potential here means scattering from snow layer considering absence of any layer above it and also not taking scattering losses into account).

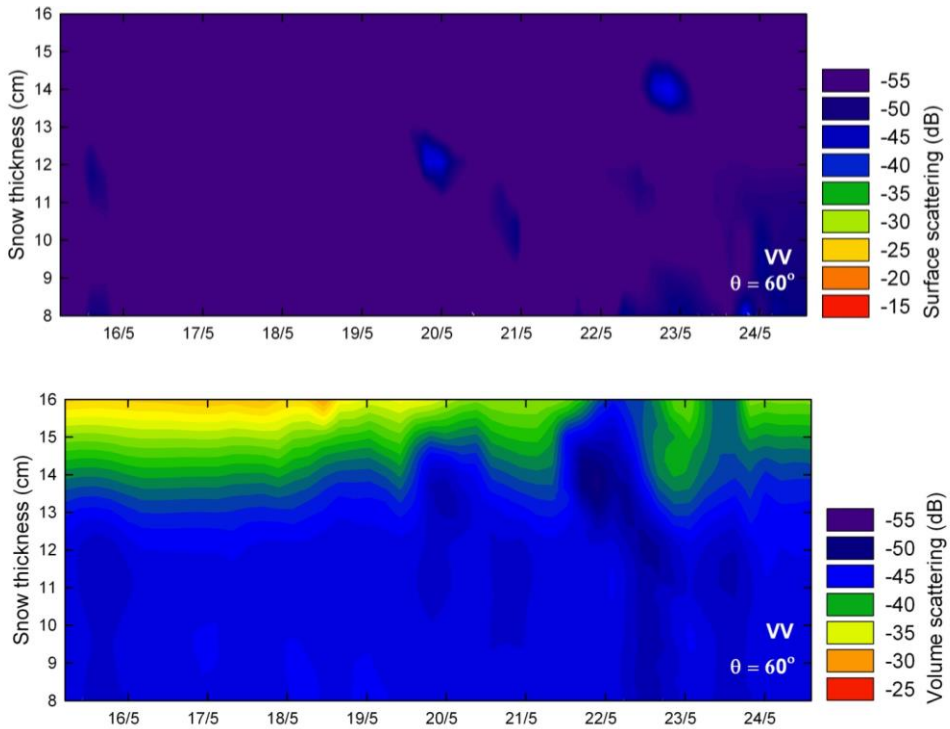

Figure 6.21. Time series modeled potential surface and potential volume scattering for C-band microwave at 60° incidence angle for thick snow covered (16cm) smooth FYI from 15 May - 25 May, 2012. (Note: Potential here means scattering from snow layer considering absence of any layer above it and also not taking scattering losses into account).

6.4.2.4 C-band scatterometer backscatter for thin snow

C-band polarimetric parameters computed from scatterometer measurement are evaluated for thin snow (6cm) over smooth FYI for the early melt (15 May – 20 May 2012) and melt onset period (25 May to 30 May, 2012). The results are explained using modeled time series penetration depth and modeled surface and volume scattering contributions from the snow pack.

Co- and cross-polarized backscatter parameters σ_{hh}^{o}, σ_{vv}^{o} and σ_{hv}^{o} demonstrated signatures slightly higher than thick snow by ~3dB at incidence angles < 60°, during the early melt period (Figure 6.22). This is opposite to commonly presented scattering theories.

According to Nakawo and Sinha, 1981 and Barber and Nghiem, 1999, thick snow results in a small vertical temperature gradient in the snow pack and relatively higher temperature at the snow ice interface at temperatures below 10°C. On the contrary, thin snow exhibits higher vertical temperature gradient in snow pack and lower temperature at the snow ice interface. The increased snow ice interface temperature in thick snow induces an increase in brine volume in the basal snow and adjacent sea ice layer. As a consequence radar backscatter is higher from thick snow cover for early melt period. The higher backscatter from thin snow could be attributed to low penetration depth. The penetration depth for both thick and thin snow is 3cm for most part of the study period (Figure 6.18 and Figure 6.22). Therefore the scattering in both cases is from the top 3cm of the snow pack. In the case of thin snow, due to higher temperature gradient, brine volume is wicked up to the topmost snow layer, which therefore allows microwave interaction with brine resulting in higher backscatter. In case of thick snow, microwaves are unable to reach the brine layers and consequently produce lower backscatter. Similar to thick snow, co- and cross-polarized backscatter from thin snow also exhibit cyclic fluctuations, following the diurnal temperature cycle. During the melt onset period, σ_{hh}^{o}, σ_{vv}^{o} and σ_{hv}^{o} from thin snow was 5-7dB lower than the thick snow. This is because thin snow melts earlier than thick snow. By 25 May, thin snow is already saturated and has become a highly absorptive media.

Other polarimetric parameters such as total power (Span) demonstrate a response similar to co- and cross-polarized backscatter. The co-polarized ratio r_{co} was a mix of negative and positive values at all incidence angles throughout the study period. This suggests no second-order scattering was present. The co-polarized correlation coefficient

ρ_{co} was ~1 at steep incidence angles (20°-40°) and was >0.7 below 65°, for the entire study period (Figure 6.22). High ρ_{co} indicates polarized backscatter.

Analysis of the modeled scattering contributions at vertical co-polarization for the thin site shows the dominance of surface scattering at 20° incidence angle and the dominance of volume scattering at 40° and 60° incidence angle. Surface scattering usually occurs at the dielectrically-mismatched interfaces. Considering the penetration depth of 3cm, surface scattering mainly occurred at the air/snow interface. Volume scattering contributions were mainly low and did not change with incidence angle.

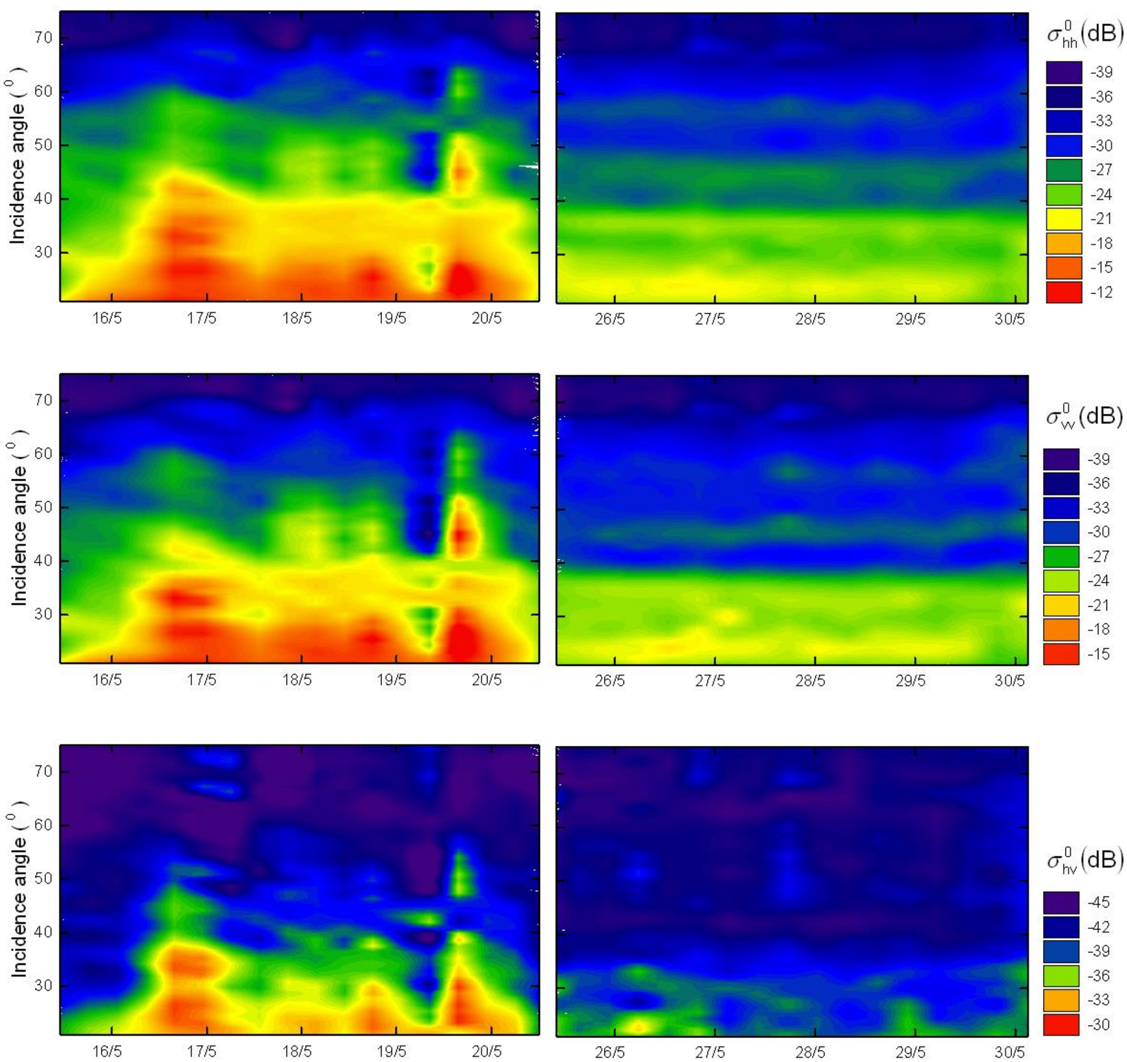

Figure 6.22. Time series polarimetric C-band microwave scattering properties of snow covered (thin, 6cm) smooth FYI from 15 May - 30 May, 2012. Properties were measured using surface-based C-band scatterometer. (Continued on next page.)

Figure 6.22 (Concluded.)

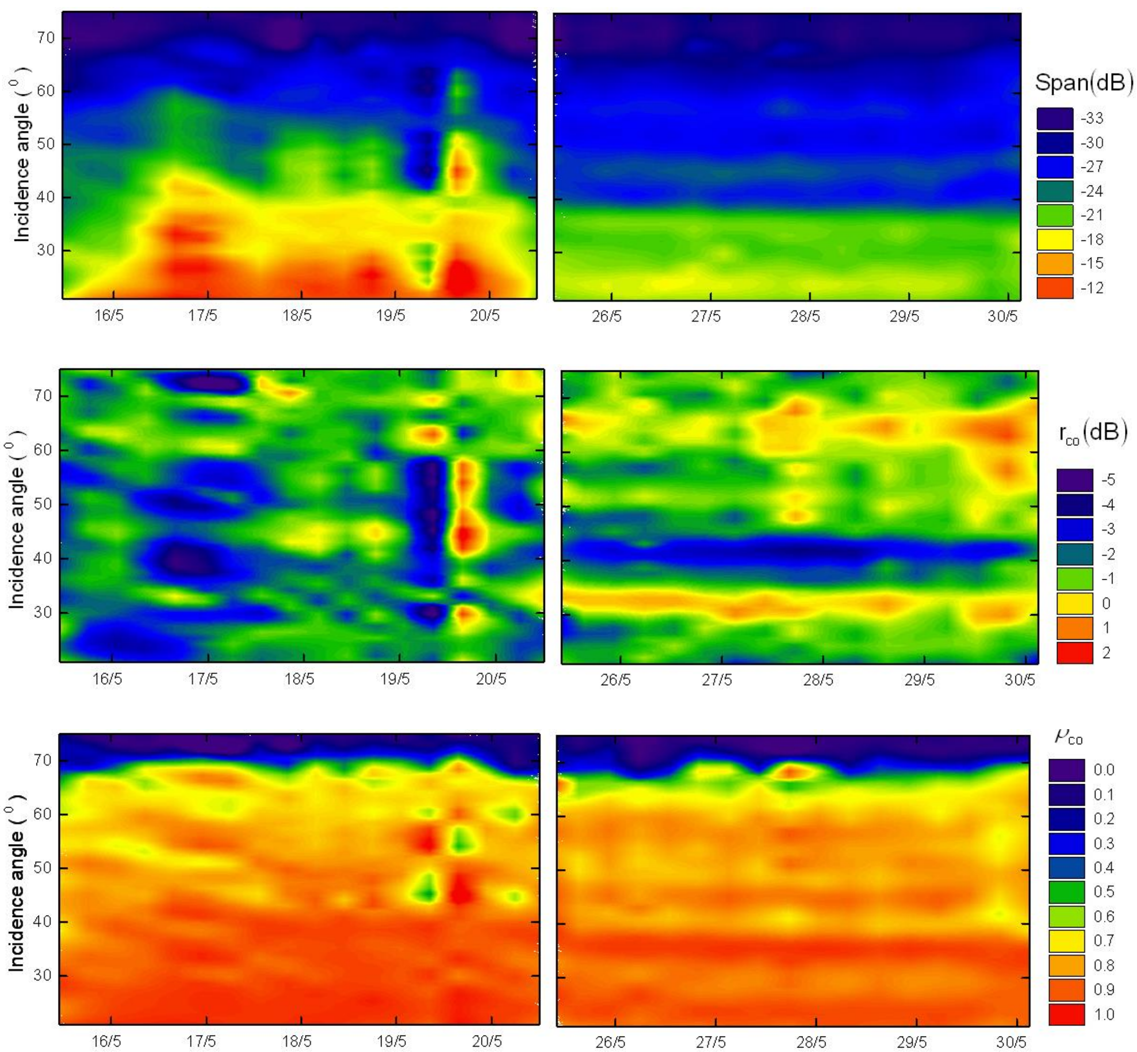

Figure 6.22. Time series polarimetric C-band microwave scattering properties of snow covered (thin, 6cm) smooth FYI from 15 May - 30 May, 2012. Properties were measured using surface-based C-band scatterometer.

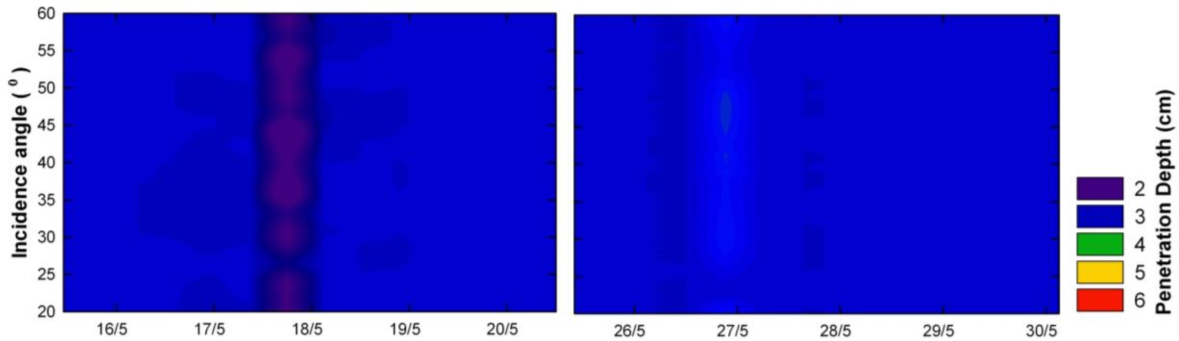

Figure 6.23. Time series penetration depth of polarimetric C-band microwave for thin snow covered (6cm) smooth FYI from 15 May - 30 May, 2012.

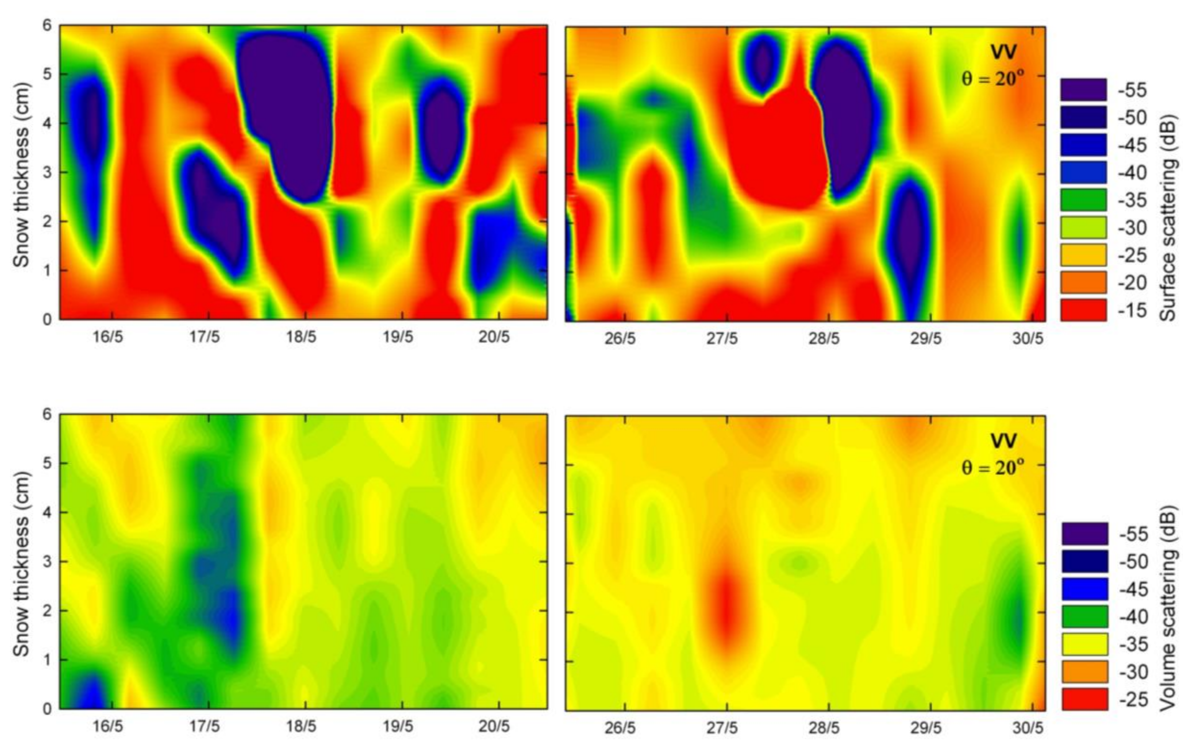

Figure 6.24. Time series modeled potential surface and potential volume scattering for C-band microwave at 20° incidence angle for thin snow covered (6cm) smooth FYI from 15 May - 30 May, 2012. (Note: Potential here means scattering from snow layer considering absence of any layer above it and also not taking scattering losses into account).

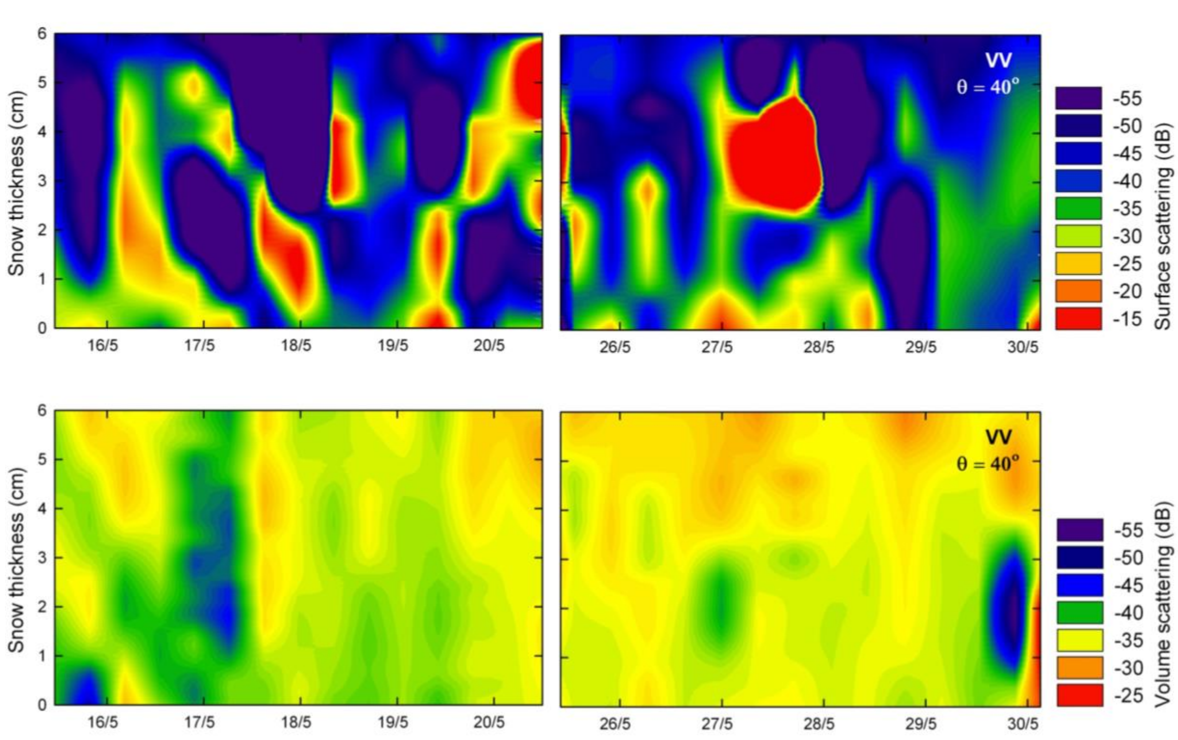

Figure 6.25. Time series modeled potential surface and potential volume scattering for C-band microwave at 40° incidence angle for thin snow covered (6cm) smooth FYI from 15 May - 30 May, 2012. (Note: Potential here means scattering from snow layer considering absence of any layer above it and also not taking scattering losses into account).

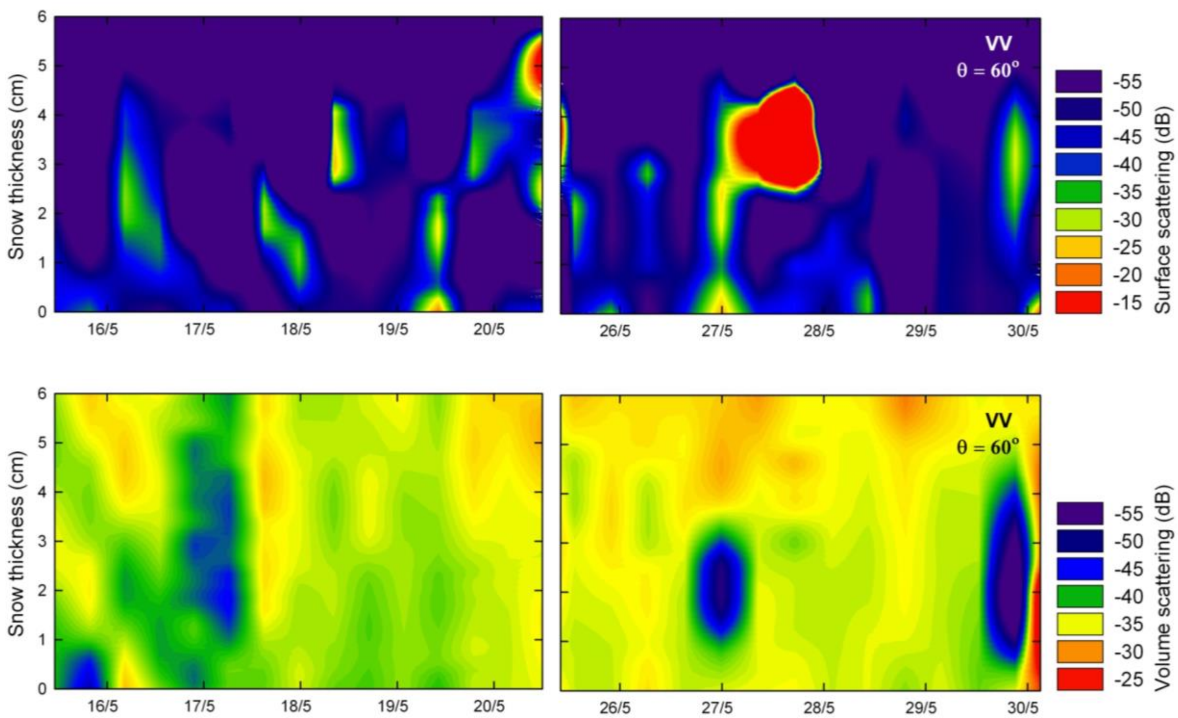

Figure 6.26. Time series modeled potential surface and potential volume scattering for C-band microwave at 60° incidence angle for thin snow covered (6cm) smooth FYI from 15 May - 30 May, 2012. (Note: Potential here means scattering from snow layer considering absence of any layer above it and also not taking scattering losses into account).

6.5 Conclusion

In study-1, coincident snow physical, dielectric and C-band microwave properties from thick snow (16 cm) covered smooth FYI were presented. The properties were acquired over a period of 24 hours for two temperature conditions: Case-1) early melt period; and Case-2) melt onset period. Polarimetric backscatter from Radarsat-2 SAR images for the two cases was also examined. For case-1, the snow properties changed during the diurnal temperature cycle. This change in snow properties was found closely associated with C-band polarimetric backscatter. The Radarsat-2 SAR backscatter from ascending and descending passes validated the influence of diurnal snow properties on C-band backscatter. For case-2, the snow properties did not change substantially over the 24 hour period. Therefore, no change in C-band polarimetric backscatter was observed. Similar results were demonstrated by the ascending and descending passes of the Radarsat-2 SAR images.

In study-2, coincident snow physical, dielectric and C-band microwave properties from thick (16 cm) and thin (6 cm) snow covered smooth FYI were presented. The properties were acquired in time series from early melt period to melt onset period. During the early melt period, the backscatter from both thick and thin snow covers showed similar association with snow properties and air temperature. Surprisingly, the backscatter from thin snow was higher than from thick snow. This was primarily due to the low microwave penetration depth of 3 cm in both of the snow covers. The presence of brine in the upper layers of thin snow provided a medium for interaction with microwaves, thus resulting in higher backscatter. During the melt onset period, the backscatter from thick snow was higher than thin snow. This was attributed to the early melting of thin snow when compared to thick snow. For the entire study period, the backscatter response from both snow covers was dominated by surface scattering at low incidence angles and volume scattering at high incidence angles. For thick snow, surface scattering increased and volume scattering decreased from early melt to melt onset, whereas the opposite was true for thin snow.

CHAPTER SEVEN:

CONCLUSIONS

7.1 Summary

In chapter 1, a scientific rationale and research objectives for this thesis were provided. In chapter 2, the pertinent nomenclature and a background on the polarimetric microwave remote sensing of snow covered sea ice was presented. Chapter 3 presented the C-band polarimetric microwave signatures of snow covered FYI at cold atmospheric temperatures. This chapter also investigated the classification potential of C-band polarimetric parameters derived after Cloude-Pottier (1997) decomposition, Touzi (2007) decomposition, Freeman-Durden (1998) decomposition, normalized radar cross section (NRCS) measurements, phase differences and statistical SAR correlation measures by relating them to three pre-identified sea ice types (smooth, rough and deformed) and wind roughened open water. Chapter 4 extended the analysis conducted in Chapter 3 to investigate the thermal dependence of snow covered FYI on SAR polarimetric parameter response and their classification consistency. Chapter 5 investigated the sensitivity of C-band linear and polarimetric parameters derived from synthesis and decomposition of Radarsat-2 SAR data with respect to snow covers of variable thickness on SFYI. In chapter 6, observations of diurnal and time series (early melt to melt onset) coincident geophysical and dielectric properties of thick and thin snow covers over SFYI and associated C-band polarimetric backscatter were investigated.

7.1.1 Detailed summary

Chapter 3 –Evaluation of C-band SAR polarimetric parameters for discrimination of first-year sea ice types at cold atmospheric conditions

1. C-band SAR polarimetric signatures of smooth, rough deformed FYI types and wind roughened open water are presented.
    a. Polarimetric parameters σ_{hh}^0, σ_{vv}^0, σ_{hv}^0, , $SPAN$, H, α, P_d, P_v, ψ and τ_s are positively related to snow covered FYI roughness.
    b. Polarimetric parameters $R_{hh/vv}$, $R_{hh/hv}$, r_{hhvv}, A, β and λ_s are negatively related to snow covered FYI roughness.
    c. Polarimetric parameters P_s, ϕ_s and α_s are neither positively nor negatively related to snow covered FYI roughness.
2. Classification potential of twenty SAR polarimetric parameters is evaluated.
    a. No polarimetric parameter in itself can classify all the ice types (SFYI, RFYI, DFYI and OW) with each class accuracy >60%.
    b. Pairing of two polarimetric parameters increases the classification accuracy by 10-22%.
    c. Polarimetric parameter combinations of H-P_v, σ_{vv}^0- H, P_v-λ_s and σ_{hv}^0-H derive the best classification results among the two-parameter combinations.
    d. Combining the third polarimetric parameter does not increase the classification accuracy in 50% of the cases.
    e. RFYI is the least accurately classified ice type.

3. Dependence of C-band SAR polarimetric parameters on radar incidence angle is evaluated.
    a. Polarimetric parameters σ^0_{hh}, σ^0_{vv}, σ^0_{hv}, $SPAN$, ϕ_{hh-vv} and A are negatively related to radar incidence angle.
    b. Polarimetric parameters H and α are positively related to radar incidence angle.

Chapter 4 –Analysis of consistency in first-year sea ice type classification potential of C-band SAR polarimetric parameters during the transition from cold to warm atmospheric conditions

1. The consistency in polarimetric C-band microwave signatures of snow covered FYI types and parameter classification potential during the transition from cold to warm atmospheric conditions is investigated.
2. Six categories of polarimetric parameters exist based on their sensitivity to variations in geophysical properties and their potential to classify ice types.
3. Category 1: Polarimetric parameters σ^0_{hh}, σ^0_{vv}, $SPAN$ and P_s are highly consistent in their ice type signature response and classification at different atmospheric temperatures. They produce high classification accuracy and are applicable for use in generalized sea ice classification scheme.
4. Category 2: Polarimetric parameters $R_{hh/vv}$, ϕ_{hh-vv}, β, P_d, ψ, α_s, ϕ_s and τ_s are highly consistent in their ice type signature response during transition from cold to warm atmospheric conditions, but produce low overall classification accuracies. These parameters are not useful for any sea ice classification schemes.

5. Category 3: Polarimetric parameters A and α are highly inconsistent in their ice type signature response and also produce low classification accuracy.
6. Category 4: Polarimetric parameters σ_{hv}^{0} and P_v are highly inconsistent in their ice type signature response but produce low classification accuracies during transition from cold to warm atmospheric conditions.
7. Category 5: Polarimetric parameters H and λ_s are somewhat consistent in their ice type signature response but produce high classification accuracy.
8. Category 6: Polarimetric parameters $AR_{hh/hv}$ and ρ_{hhvv} are somewhat consistent in their ice type signature response but produce low classification accuracy.

Chapter 5 – Sensitivity of C-band SAR polarimetric parameters to snow thickness over first-year sea ice during cold and warm temperature conditions

1. C-band polarimetric parameters are analyzed with respect to snow covers of variable thickness on smooth FYI and temperature change.
2. Polarimetric parameters σ_{hh}^{0}, σ_{vv}^{0}, σ_{hv}^{0}, $SPAN$, ϕ_{hh-vv}, P_v, P_s, H, P_d, γ_{var}, α, α_s, ψ and τ_s are positively related to snow thickness at cold temperature conditions (-7.9°C).
3. Polarimetric parameters $R_{hh/vv}$, ρ_{hhvv}, A, β, ϕ_s, P_{max}, P_{min}, λ_s are negatively related to snow thickness at cold temperature conditions (-7.9°C).
4. Volume, mixed or multiple scattering increases with snow thickness at cold temperature conditions (-7.9°C).

5. No relationship exists between polarimetric parameters and snow thickness at warm temperature conditions (-0.4°C).
6. Linear co- and cross-pol backscatter from thin and medium snow cover increases on transition from cold to warm temperature conditions (from -7.9°C to -0.4°C).
7. Linear co- and cross-pol backscatter from thick snow cover decreases on transition from cold to warm temperature conditions (from -7.9°C to -0.4°C).
8. Polarimetric parameters P_s, P_d, P_v, H and γ_{var} are positively related to atmospheric warming (from -7.9°C to -0.4°C) for thin and medium snow covers and negatively related to atmospheric warming (from -7.9°C to -0.4°C) for thick snow cover.
9. Polarimetric parameters P_{max}, P_{min} and f_p are negatively related to atmospheric warming (from -7.9°C to -0.4°C) for thin and medium snow covers and positively related to atmospheric warming (from -7.9°C to -0.4°C) for thick snow cover.
10. Volume, mixed or multiple scattering from thin and medium snow covers increases with atmospheric warming (from -7.9°C to -0.4°C).
11. Snow thickness estimation through the effect of snow thermodynamics on polarimetric SAR at warm conditions is not feasible.

Chapter 6 – Polarimetric C-band microwave signatures of snow cover over smooth first-year sea ice from early melt to melt onset

1. C-band polarimetric microwave backscatter coincident to snow geophysical and electrical properties is analyzed for thick snow (16 cm) at diurnal scale for early melt and melt onset period. Radarsta-2 SAR images are used to validate the findings.

a. Snow physical and electrical properties change during the 24 hour temperature cycle for early melt period.

b. C-band polarimetric backscatter is closely associated to the variations in snow geophysical and electrical properties at diurnal scale during the early melt period.

c. Radarsat-2 SAR backscatter from ascending and descending passes changes in response to variations in snow properties at diurnal scale during early melt period.

d. Snow physical, electrical properties do not change substantially at diurnal scale for melt onset period.

e. C-band polarimetric backscatter does not change at diurnal scale for melt onset period.

f. Radarsat-2 SAR ascending and descending images cannot be used as substitutes for each other during the early melt period but can be used as substitutes during the melt onset period.

2. Time series C-band polarimetric microwave backscatter coincident to snow geophysical and electrical properties is analyzed for thick (16 cm) and thin (6 cm) snow cover from early melt to melt onset period.

   a. Polarimetric microwave backscatter from thin snow is higher than from thick snow during the early melt period, if the microwave penetration depth is low and the scattering is largely from the top few centimeters of the snowpack.

b. Polarimetric microwave backscatter from thin snow is lower than from thick snow during the melt onset period, if the microwave penetration depth is low and the scattering is largely from the top few centimeters of the snowpack.
c. Surface scattering increases and volume scattering decreases for thick snow on transition from early melt to melt onset. The opposite is true for thin snow.
d. The brine wicking phenomenon in combination with microwave penetration depth defines the backscatter from variable snow covers over smooth FYI, during the early melt period.
e. The presence of liquid water in snow pack in combination with microwave penetration depth defines the backscatter from variable snow covers over smooth FYI, during the melt onset period.
f. Snow thickness discrimination using C-band microwaves is best achievable at low radar incidence angles (<30°) and at low temperature conditions (<10°C).

7.2 Limitations and recommendations

The results presented in chapter 3 and chapter 4 were limited by the use of a small range of incidence angle images. The dependence of polarimetric SAR signatures on θ_i was carried out at only four incidence angles (between 22° and 37°), therefore the results may not be valid outside this range. Also, the results may not be suitable for normalization of incidence angle effect on SAR backscatter in Radarsat-2 images, primarily adopted for multi-image comparison. The parameter specific classification analysis was performed at two radar incidence angles, thus the results are applicable only at θ_i = 23° and θ_i = 27°. Moreover, the interpretation of polarimetric signatures was not supported by intensive *in-situ* measured snow covered sea ice geophysical and electrical properties. The study also lacked in providing modeling evidence to the results.

It is recommended that the work presented in chapter 3 and chapter 4 be extended to other geophysical and temperature conditions with more intensively measured *in-situ* snow and sea ice properties. Similar analysis over a wider range of radar incidence angles also be investigated. A detailed modeling of polarimetric SAR response from snow covered sea ice types should be incorporated to add confidence in the interpretation of polarimetric microwave signatures of snow covered sea ice.

In chapter 5, the relationship between polarimetric SAR backscatter and snow thickness was investigated using discrete measurements of snow ranging between 6.3 cm and 37.6 cm. The sample size of snow measurements was small. Moreover, each snow site was on a different pan of ice, at times several kilometers apart. The investigation was carried out at only two temperature conditions (-7.9°C and -0.4°C). The results also lacked the support of modeling evidence.

An investigation of the relationship between polarimetric SAR backscatter and a complete range of snow thicknesses commonly encountered over FYI is recommended. The sample size of snow thickness measurements must be increased for accurate statistical analysis. Having all the snow sites on a single or similar pan of sea ice reduces the ambiguity in interpretation of microwave backscatter arising due to sea ice surface roughness and electro-thermo-physical properties. Therefore, similar SAR based studies must be supplemented with coincident on-ground microwave and geophysical measurements of homogeneous snow sites. The investigations over a wider range of temperature conditions are recommended for enhanced understanding of the microwave scattering properties from snow covered FYI.

Chapter 6 presented the coincident C-band scatterometer measurements and *in-situ* measured snow covered FYI geophysical and electrical properties at diurnal and temporal scale from early melt to melt onset period. Confidence in these results is limited to accurate geophysical parameterization, modeling and microwave backscatter measurements. Improvements in calculation of brine volume fraction and their validation with laboratory and/or field experiments are required. Enhanced understanding of the brine wicking phenomenon within snow covers of different thicknesses and at different temperatures is necessary for better understanding of scattering mechanisms in snow covered FYI. Improvements in snow density measurements and snow grain size/shape measurements are required for scattering model parameterizations. A comparison of different scattering model with same initial parameters is required for validation of results and enhanced understanding of scattering mechanisms. A comparison of the scatterometer backscatter measurements by gradually increasing the height for the same scan area is useful for understanding the effects of scale.

7.3 Concluding remarks

In the last two decades, most of the studies on Arctic snow and sea ice concentrated on single and/or dual polarized SAR data. This is because all of the early satellites such as Radarsat-1 (1995), ERS-1 (1991), ERS-2 (1995) and ENVISAT-ASAR (2002) were single or dual-polarized. Many of these studies highlighted the limitations of single and /or dual polarized data and stressed the need for full polarimetric SAR data. Therefore, full polarimetric Radarsat-2 (2007) and experimental modes of TerraSAR-X (2007) were brought onboard. Even before the potential of full polarimetric SAR data for snow and sea ice investigations is fully explored, the scientific community is already moving towards new generation of satellites (SENTINEL-1, Radarsat Constellation). These satellites possess or will possess single and /or dual polarized modes (SENTINEL-1) or will have advanced polarimetric modes such as compact polarimetry. Full polarimetry modes are or will not be included in these satellites.

This realization demonstrates that there is or will be a gap of knowledge on polarimetric microwave properties of snow and sea ice within the cryosphere community. The investigations conducted in this thesis, especially chapter 3 to chapter 5 provide much needed analysis on the relationship between C-band SAR polarimetric parameters and snow covered FYI geophysical properties. One of the major contributions of this thesis has been on building a library of polarimetric microwave signatures for different geophysical and temperature conditions, which will facilitate the development of improved sea ice classification and snow thickness estimation algorithms. The results presented in the thesis will provide a source for cross referencing and validating new or similar findings.

REFERENCES

Askne, J., and W. Dierking , 2008. *Remote Sensing of the European Seas*. Springer, Netherlands, pp. 383-398.

Assur, A., 1960. *Composition of sea ice and its tensile strength*. U.S. Army Cold Regions Research and Engineering Laboratory. Research Report 44. pp. 54.

Barber, D. G. and E. F. LeDrew., 1994a. On the Links between Microwave and Solar Wavelength Interactions with Snow-Covered First-Year Sea Ice, *Arctic,* 47(3): 298-309.

Barber, D. G., T. N. Papakyriakou and E. F. LeDrew., 1994b. On the relationship between energy fluxes, dielectric properties, and microwave scattering over snow covered first-year sea ice during the spring transition period, *Journal of Geophysical Research,* 99(C11): 22401-22411.

Barber, D. G., S. P. Reddan and E. F. LeDrew., 1995a. Statistical characterization of the geophysical and electrical properties of snow on landfast first-year sea ice, *Journal of Geophysical Research.* 100(C2): 2673-2686.

Barber, D. G., T. N. Papakyriakou, E. F. LeDrew and M. E. Shokr., 1995b. An examination of the relation between the spring period evolution of the scattering coefficient and radiative fluxes over landfast sea-ice, *International Journal of Remote Sensing,* 16(17): 3343-3363.

Barber, D. G., A. Fung, T. C. Grenfell, S. V. Nghiem, R. G. Onstott, V. Lytle, D. K. Perovich and A. J. Gow., 1998. The Role of Snow on Microwave Emission and Scattering over First-Year Sea Ice, *IEEE Transcations on Geoscience and Remote Sensing,* 36(5): 1750-1763.

Barber, D.G. and A. Thomas, 1998a. The influence of cloud cover on the radiation budget, physical properties, and microwave scattering coefficient ($\sigma°$) of first-year and multiyear sea ice. *IEEE Transactions on Geoscience and Remote Sensing*, 36(1): 38-50.

Barber, D.G., and Nghiem, S.V., 1999. The role of snow on the thermal dependence of microwave backscatter over sea ice, *Journal of Geophysical Research*, 104(C11): 25,789-25,803.

Barber, D.G., J. Yackel and J. Hanesiak, 2001. Perspectives on Sea Ice, RadarSat-1, and Arctic Climate Processes, *Canadian Journal of Remote Sensing, 27*(1): 51-61.

Barber, D.G., J. Iacozza and A.E. Walker, 2003. Estimation of snow water equivalent using microwave radiometry over Arctic first-year sea ice. *Hydrological Processes*, 17: 3,503-3,517.

Barber, D.G., J.K. Ehn , M. Pucko, S. Rysgaard, J.W. Deming, J.S. Bowman, T. Papakyriakou, R.J. Galley, and D.H. Soggard, 2014. Frost flowers on young Arctic sea ice: The climate, chemical, and microbial significance of an emerging ice type. *Journal of Geophysical Research*, 1-29: DOI: 10.1002/2014JD021736.

Barry, R. G., 1964. Weather conditions at Tanquary Fiord, summer 1963. D. Phys. R(G), Hazen 23, *Defence Research Board.Department of National Defence*, Ottawa, pp. 28.

Barry R.G., 1996. The parameterization of surface albedo for sea ice and its snow cover. *Progress in Physical Geography,* 20: 63-79.

Beaven, S. G., G. L. Lockhart, S. P. Gogineni, A. R. Hosseinmostafa, K. Jezek, A. J. Gow, D. K. Perovich, A. K. Fung and S. Tjuatja., 1995. Laboratory measurements of radar backscatter from bare and snow-covered saline ice sheets, *International Journal of Remote Sensing*, 16(5): 851-876.

Bredow, J. W. and S. Gogineni., 1990. "Comparison of Measurements and Theory for Backscatter from Bare and Snow-Covered Saline Ice, *IEEE Transactions on Geoscience and Remote Sensing*, 28(4): 456-463.

CAA (Canadian Avalanche Association), 1995. *Observation Guidelines and Recording Standards for Weather, Snowpack and Avalanches*. A revision of: National Research Council of Canada Technical Memorandum No. 132. Canadian Avalanche Association, Revelstoke, British Columbia. pp. 98.

Carlstrom, A., 1990. Discrimination of low salinity sea ice types using VV- and VH-polarization C-band SAR imagery. *Proc. of IGARSS'90*, College Park, Maryland, USA, pp. 2,233-2,236.

Carlstrom, A., 1997. A microwave backscattering model for deformed first-year sea ice and comparisons with SAR data. *IEEE Transactions on Geoscience and Remote Sensing*, 35(2): 378-391.

Carlstrom, A., and L. M. H Ulander, 1995. Validation of backscatter models for level and deformed ice sea ice in ERS-1 SAR images. *International Journal of Remote Sensing*, 16(7): 3,245-3,266.

Cavalieri, D.J., C. L. Parkinson, and K. Y. Vinnikov, 2003. 30-year satellite record reveals contrasting Arctic and Antarctic decadal sea ice variability, *Geophysical Research Letters*, 30(18), doi:10.1029/2003GL018031.

Cloude, S.R., and E. Pottier, 1997. An entropy based classification scheme for land applications of polarimetric SAR. *IEEE Transactions on Geoscience and Remote Sensing*, 35(1): 68-78.

Colbeck, S.C., E. Akitaya, R. Armstrong, H. Gubler, J. LaFeuille, K. Lied, D. McClung and E. Morris, 1990. *The International Classification for Seasonal Snow on the Ground*. The International Commission on Snow and Ice of the International Association of Scientific Hydrology. pp. 37.

Congalton, R.G., 1991. A Review of Assessing the Accuracy of Classifications of Remotely Sensed Data. *Remote Sensing of Environment*, 37(1): 35-46.

Cota G. F. and E. P. Horne., 1989. Physical controls of arctic ice algal production, *Marine Ecology Progress Series*, 52:111-121.

Cox, G. F. N. and W. F. Weeks., 1983. Equations for determining the gas and brine volumes in sea-ice samples, *Journal of Glaciology,* 29(12): 306-316.

Cox, G.F.N. and W.F. Weeks, 1975. *Brine drainage and initial salt entrapment in sodium chloride ice*. U.S. Army Cold Regions Research and Engineering Laboratory. Research Report 345. pp. 85.

Cunnigham, G., R. Kwok and B. Holt., 1992. Preliminary results from ASF/GPS ice classification algorithm, *IGARSS, Houstan*.

Curry, J. A., J. L. Schramm and E. E. Ebert., 1994. Sea Ice-Albedo Climate Feedback Mechanism, *Journal of Cliamte,* 8: 240-247.

Denoth, A., 1989. Snow dielectric measurements. *Advances in Space Research*, 9(1): 233-243.

Dierking, W. and J. Dall, 2007. Sea-ice deformation state from synthetic aperture radar imagery–Part 1: Comparison of C- and L-band and different polarization. *IEEE Transactions on Geoscience and Remote Sensing*, 45(11): 3,610-3,621.

Dierking, W., and J. Askne, 1998. Polarimetric L- and C-band SAR signatures of Baltic Sea ice observed during EMAC-95. In: *Future Trends in Remote Sensing*, P. Gudmandsen, Ed. Balkema, Rotterdam, pp. 329-336.

Dierking, W., H. Skriver and P. Gudmandsen, 2003. SAR polarimetry for sea ice classification. *Proceedings of POLinSAR 2003 Workshop on applications of SAR polarimetry and polarimetric interferometry*, January 14-16, 2003, Frascati, Italy. European Space Agency-ESRIN. 109-118.

Drinkwater, M. R., 1989. LIMEX ’87 ice surface characteristics: Implications for C-band SAR backscatter signatures. *IEEE Transactions on Geoscience and Remote Sensing*, 27(5): 501-513.

Drinkwater, M.R. and G.B. Crocker, 1988. Modeling changes in the dielectric and scattering properties of young snow covered sea ice at GHz frequencies. *Journal of Glaciology*, 34(118): 274-282.

Drinkwater, M.R. R. Kwok, E. Rignot, H. Israelsson, R.G. Onstott and D.P. Winebrenner, 1992. Potential application of polarimetry to the classification of sea ice. In: *Microwave remote sensing of sea ice*, Carsey F. (ed.). American Geophysical Union,Geophysical Monograph 68. Chapter 24: 419-430.

Drobot, S.D. and D.G. Barber, 1998. Towards development of a snow water equivalent (SWE) algorithm using microwave radiometry over snow covered first-year sea ice. *Photogrammetric Engineering & Remote Sensing*, 64(5): 415-423.

Evans, D.L., T.G. Farr, J.J. van Zyl, and H.A. Zebsker, 1988. Radar polarimetry: Analysis tools and applications, *IEEE Transactions on Geoscience and Remote Sensing*, 26: 774-789.

Feltham, D.L., 2008. Sea Ice Rheology, *Annual Review of Fluid Mechanics*, 40: 91-112.

Ferro-Famil, L., E. Pottier, and J.S. Lee, 2001. Unsupervised Classification of Multifrequency and Fully Polarimetric SAR Images Based on the H/A/Alpha-Wishart Classifier. *IEEE Transactions on Geoscience and Remote Sensing*, 39(11): 2332-2342.

Fetterer, F. and D. Generis, 1992 "ERS-1 SAR as a data source for operational ice analysis," *First ERS-1 symposium, Cannes, France*.

Fichaux, N., and T. Ranchin, 2002. Combined extraction of high spatial resolution wind speed and wind direction from SAR images: A new approach using wavelet transform. *Canadian Journal of Remote Sensing*, 28(3): 510-516.

Foucher, S. and Lopez-Martinez, C, 2009. An Evaluation of PolSAR Speckle Filters. *IGARSS'2009*, Cape Town, South Africa, 12-17 July.

Frankenstein, G. and R. Garner, 1967. Equations for determining the brine volume of sea ice from -0.5° to -22.9°C. *Journal of Glaciology*, 6(48): 943-944.

Freeman, T., and S.L. Durden, 1998. A Three-Component Scattering Model for Polarimetric SAR Data. *IEEE Transactions on Geoscience and Remote Sensing*, 36(3): 963-973.

Frolov, A., Y. Macheret, 1999. On dielectric properties of dry and wet snow. *Hydrological Processes*, 13: 1,755-1,760.

Fung, A.K, 1994. *Microwave scattering and emission models and their applications*. Artech House, Norwood, USA.

Fung, A.K. and K.S. Chen, 2004. An update on the IEM surface backscattering model. *IEEE Geoscience and Remote Sensing Letters*, 1(2): 75-77.

Geiger, R., 1957. The climate near the ground. Harvard University Press, Cambridge, Mass.

Geldsetzer, T., and J. J. Yackel, 2009. Sea Ice type and open water discrimination using dual co-polarized C-band SAR. *Canadian Journal of Remote Sensing*, 35(1): 73-84.

Geldsetzer, T., A. Langlois and J. J. Yackel, 2009a. Dielectric properties of brine-wetted snow on first-year sea ice, *Cold Regions Science and Technology* 58: 47-56.

Geldsetzer, T., 2009b. *Microwave Properties of Snow on Sea Ice*, PhD. Dissertation University of Calgary, Calgary, Alberta, Canada.

Geldsetzer, T., J. B. Mead, J. J. Yackel, R. K. Scharien and S. E. L. Howell, 2007. Surface-Based Polarimetric C-band Scatterometer for Field Measurements of Sea Ice. *IEEE Transactions on Geoscience and Remote Sensing*, 45(11): 3405-3416.

Gill, Jagvijay .P.S., and J.J. Yackel, 2012. Evaluation of C-band SAR polarimetric parameters for discrimination of first-year sea ice types. *Canadian Journal of Remote Sensing*, 38(3): 306-323.

Gill, Jagvijay. P. S., J. J. Yackel, and T. Geldsetzer, 2013. Analysis of consistency in first-year sea ice classification potential of C-band SAR polarimetric parameters," *Canadian Journal of Remote Sensing*, 39(2): 1-17.

Gill, R.S., 2003. *SAR ice classification using fuzzy screening method.* Workshop on SAR polarimetry and polarimetrc interferometry, Frascati, Italy.

Gogineni, S. P, 1986. Radar backscatter from sea ice, *IEEE National Radar Conference, Los Angeles, USA.*

Hallikainen, M. and M. Toikka, 1992 Classification of sea ice types with radar, *Second European Microwave Conference, Espoo, Finland*.

Hallikainen, M., and M. Toikka, 1992. *Classification of sea ice types with radar*. Proceedings of 22nd European Microwave Conference, Espoo, Finland, pp. 957-962.

Hallikainen, M., and M. Toikka, 1992. Radar backscatter signatures of Baltic Sea ice, *Proceedings IGARSS,* 92: 1,527-1,529.

Hallikainen, M.T. and D.P. Winebrenner, 1992. The physical basis for sea ice remote sensing. In: *Microwave Remote Sensing of Sea Ice,* Carsey, F. (ed.). Geophysical Monograph. American Geophysical Union. Chapter 3: 29-46.

Hersbach, H., 2008. *CMOD5.N: A C-band geophysical model function for equivalent neutral wind*. Technical Memorandum 554, European Centre for Medium-Range Weather Forecasts.

Hersbach, H., A. Stoffelen, and S. de Haan, 2007. An improved C-band scatterometer ocean geophysical model function: CMOD5. *Journal of Geophysical Research,* 112(C03006): 1-18.

Hibler, W. D., III; and W. B. Tucker III, 1977. Seasonal variations in apparent sea ice viscosity on the geophysical scale, *Geophysical Research Letters*, 4(2): 87-90.

Hollinger, J. P., B.E. Troy, R.O. Ramseier, K.W. Asmus, M.F. Harman and C.A. Luther, 1984. Microwave emission from high Arctic sea ice during freeze up. *Journal of Geophysical Research,* 89(C5): 8,104-8,122.

Holt, B. and S. Digby, 1985. Processes and imagery of first-year fast sea ice during the melt season, *Journal of Geophysical Research*, 90: 5,045-6,062.

Hyyppa , J., and M. Hallikainen, 1992. Classification of low-salinity sea ice types by ranging scatterometer. *International Journal of Remote Sensing*, 13: 2,399-2,413.

Iacozza, J. and D. G. Barber, 2010. An examination of snow redistribution over smooth land-fast sea ice, *Hydrological Processes,* 24: 850-865.

Iacozza, J. and D.G. Barber, 1999. An examination of the distribution of snow on sea ice. *Atmosphere-Ocean*, 37(1): 21-51.

Iacozza, J. and D.G. Barber, 2001. Ablation patterns of snow cover over smooth first-year sea ice in the Canadian Arctic. *Hydrological Processes,* 15: 3,559-3,569.

Johannessen, O. M., S. Sandven, W. J. Campbell and R. Shuchman, 1992. ERS-1 SAR ice signature validation during SIZEX-92, *First ERS-1 Symposium*, Cannes.

Karvonen, J., 2004. Baltic Sea Ice SAR segmentation and classification using modified pulse-coupled neural networks. *IEEE Transactions on Geoscience and Remote Sensing*, 42(7): 1,566-1,574.

Kendra, J.R., K. Sarabandi and F.T. Ulaby, 1998. Radar measurements of snow: experiment and analysis. *IEEE Transactions on Geoscience and Remote Sensing*, 36(3): 864-879.

Kim, Y.S., R.G. Onstott and R.K. Moore, 1984. The effect of a snow cover on microwave backscatter from sea ice. IEEE Journal of Oceanic Engineering, OE-9(5): 383-388.

Kwok, R., B. Panzer, C. Leuschen, S. Pang, T. Markus, B. Holt and S. Gogineni, 2011. Airborne surveys of snow depth over Arctic sea ice, *Journal of Geophysical Research* 116(C11018): 1-16.

Kwok, R., E. Rignot, B. Holt and R. G. Onstott, 1992. Identification of sea ice types in spaceborne synthetic aperture radar data. *Journal of Geophysical Research*, 97(C2): 2,391-2,402.

Kwok, R., G. F. Cunningham, M. Wensnahan, I. Rigor, H. J. Zwally, and D. Yi, 2009. Thinning and volume loss of the Arctic Ocean sea ice cover: 2003-2008, *Journal of Geophysical Research.* 114(C07005): 1-16.

Kwok, R., S.V. Ngheim, S. Martin, D. P. Winebrenner, A.J. Gow, D.K. Perovich, C. T. Swift, D.G. Barber, K.M. Golden, and E.J. Knapp, 1998. Laboratory Measurements of Sea Ice: Connections to Microwave Remote Sensing. *IEEE Transactions on Geoscience and Remote Sensing*, 36(5): 1,716-1,730.

Ledley, T. S., 1991. Snow on sea ice: Competing effects in shaping climate. *Journal of Geophysical Research*, 96(17): 17,195-17,208.

Lee, J.S., 1981. Refined Filtering of Image Noise Using Local Statistics, *Computer Graphics and Image Processing,* 15: 380-389.

Lee, J.S., Grunes, M.R. and De Grande, G., 1997. Polarimetric SAR speckle filtering and its impact on classification. *Proc. Geoscience and Remote Sensing, IGARSS 1997,* 2: 1038-1040.

Lepparanta, M., and R. Hakala, 1992. The structure and strength of first-year ice ridges in the Baltic Sea. *Cold Regions Science and Technology*, 20: 295-311.

Light, B., G.A. Maykut and T.C. Grenfell, 2003. Effects of temperature on the microstructure of first-year Arctic sea ice. *Journal of Geophysical Research*, 108(C2), doi: 10.1029/2001JC000887.

Lillesand, T. M. and Kiefer, R. W. *Remote Sensing and Image Interpretation*, John Wiley & Sons Inc. New York. Fourth Ed.

Livingstone, C.E. and M.R. Drinkwater, 1991. Springtime C-band SAR backscatter signatures of Labrador Sea marginal ice: measurements versus modeling predictions. *IEEE Transactions on Geoscience and Remote Sensing*, 29(1): 29-41.

Lopez-Martinez, C., L. Ferro-Famil, and E. Pottier, 2007. *Tutorials of POLSARPRO: The polarimetric SAR data processing and educational tool*. (http://earth.esa.int/polsarpro/, Accessed on October 25, 2009).

Lundhaug, M., 2002. ERS SAR studies of sea ice signatures in the Pechora Sea and Kara sea region. *Canadian Journal of Remote Sensing*, 28(2): 114-127.

Lytle, V. I., K. C. Jezek, A. R. Hosseinmostafa and S. P. Gogineni, 1993. Laboratory Backscatter Measurements over Urea Ice with Snow Cover at Ku Band, *IEEE Transactions on Geoscience and Remote Sensing,* 31(5): 1009-1016.

Mäkynen, M., 2007. *Investigation of the microwave signatures of the Baltic sea ice*. Helsinki University of Technology Laboratory of Space Technology Publications, Finland.

Mäkynen, M., A.T. Manninen, M.H. Simila, J.A. Karvonen and M. Hallikainen, 2002. Incidence angle dependence of the statistical properties of C-band HH-polarization backscattering signatures of the Baltic Sea ice. *IEEE Transactions on Geoscience and Remote Sensing*, 40(12): 2,593-2,605.

Mäkynen, M., and M. Hallikainen, 2004. Investigation of C- and X-band backscattering signatures of Baltic Sea ice. *International Journal of Remote Sensing*, 25(11): 2,061-2,086.

Markus, T., D. C. Powell and J. R. Wang, 2006. "Sensitivity of Passive Microwave Snow Depth Retrievals to Weather Effects and Snow Evolution," *IEEE Transactions on Geoscience and Remote Sensing* 44(1): 68-77.

Martin, S., 1979. A field study of brine drainage and oil entrapment in first-year sea ice. *Journal of Glaciology*, 22(88): 473-502.

Maykut, G. A., 1978. Energy Exchange Over Young Sea Ice in the Central Arctic, *Journal of Geophysical Research*, 83(C7): 3,646-3,658.

McGuffie, K. and A. Henderson-sellers, 2001. Forty years of climate modelling. *International Journal of Climatology*, 21: 1,067-1,109.

Mellor, M., 1964. Properties of snow, *Rep. III-AI*, U.S. Army Cold Reg. Res.and Eng. Lab., Hanover , N.H.

Mellor, M., 1977. Engineering properties of snow, *Journal of Glaciology*, 19(81): 15-66.

MSC (Meteorological Service of Canada), 2005. *Manual of standard procedures for observing and reporting ice conditions*, revised ninth edition. Environment Canada, Ottawa.

Nakamura, K., H. Wakabayashi, K. Naoki, T. Moriyama, and S. Uratsuka, 2005. Observation of Sea-Ice Thickness in the Sea of Okhotsk by Using Dual-Frequency and Fully Polarimetric Airborne SAR (Pi-SAR) Data. *IEEE Transactions of Geoscience and Remote Sensing*, 43(11): 2,460-2,469.

Nakawo, M. and N. K. Sinha, 1981. Growth Rate and Salinity Profile of the First-Year Sea Ice in the High Arctic, *Journal of Glaciology*, 27(96): 315-330.

Nghiem, S. V., R. Kwok, S. H. Yueh, A. J. Gow, D. K. Perovich, J. A. Kong, and C. Hsu, 1997. Evolution in polarimetric signatures of thin saline ice under constant growth. *Radio Science*, 32(1): 127-151.

Nghiem, S.V., and C. Bertoia, 2001. Study of Multi Polarization C-band backscatter Signatures for Arctic Sea Ice Mapping with Future Satellite SAR. *Canadian Journal of Remote Sensing*, 27(5): 387-402.

Nghiem, S.V., R. Kwok, S.H. Yueh and M.R. Drinkwater, 1995. Polarimetric signatures of sea ice 1. Theoretical model. *Journal of Geophysical Research*, 100(C7): 13,665-13,679.

Olson, C.E., Jr., and Z. Ma, 1989. Normality assumptions in supervised classification of remotely sensed terrain data, In, *Quantitative Remote Sensing: An Economic Tool for the Nineties*, *Proc. IGARSS'89*. *IEEE#89CH2768-0*, pp. 1,857-1,859.

Onstott, R.G., 1992. SAR and scatterometer signatures of sea ice. In: *Microwave Remote Sensing of Sea Ice*, Carsey, F. (ed.). Geophysical Monograph. American Geophysical Union. Chapter 5: 73-104.

Parkinson, C. L., D. J. Cavalieri, P. Gloerson, H. J. Zwally, and J. C. Comiso, 1999. Arctic sea ice extents, areas, and trends, 1978–1996. *Journal of Geophysical Research*, 104 (9): 20,837–20,856.

Parkinson, C.L. and W.M. Washington, 1979. A large scale numerical model of sea ice. *Journal of Geophysical Research*, 84: 311-337.

Partington, K. C., and M. Hanna, 1994. Modelling radar sea ice backscatter in support of ERS-1 SAR, *Advances in Remote Sensing,* 3(2): 9-23.

Poe, G., A. Stogryn and A.T. Edgerton, 1972. *A study of the microwave emission characteristics of sea ice*. Final Technical Report 1749R-2, Contract No. 2-35340, Aerojet Electrosystems Co., Azusa, California. Cited in Vant (1976) and Ulaby et al. (1986 p. 2045).

Pounder, E.R., 1965. *The Physics of Ice*. Pergamon: New York. pp. 151.

Rees, W.G., 2006. *Remote Sensing of Snow and Ice*. CRC Press, Boca Raton, FL. pp. 312.

Rignot, E. and M.R. Drinkwater, 1992. On the application of Polarimetric Radar Observations to Sea-ice Classification. *Proceedings on Geoscience and Remote Sensing, IGARSS'92,* pp. 576-578.

Rodrigues, A., D. Corr, K. Partington, E. Pottier, and L. Ferro-Famil, 2003. Unsupervised Wishart Classifications of Sea-Ice using Entropy, Alpha and Anisotropy Decompositions. *Proc POLinSAR*, Frascati, Italy, 14-16 January.

Rothrock, D. A., Y. Yu, and G. A. Maykut, 1999. Thinning of the Arctic sea-ice cover. *Geophysical Research Letters*, 29(23): 3,469–3,472.

Scharien, R. K. and J. J. Yackel, 2005. Analysis of surface roughness and morphology of first-year sea ice melt ponds: Implications for microwave scattering. *IEEE Transactions on Geoscience and Remote Sensing,* 43(12): 2,927-2,939.

Scheuchl B., Hajnsek I., I.G. Cumming, 2002. Model-Based Classification of Polarimetric SAR Sea Ice Data. *Proc. IGARSS'02*, Toronto, June 24-28.

Scheuchl, B., Caves, R., I.G. Cumming, and G. Staples, 2001. Automated Sea Ice Classification Using Spaceborne Polarimetric SAR data. *Proc. IGARSS'01*, Sydney, Australia.

Scheuchl, B., D. Flett, G. Staples, G. Davidson, and I.G. Cumming, 2003a. Preliminary Classification Results of Simulated RADARSAT-2 Polarimetric Sea Ice Data. *Proc. POLinSAR '03,* Frascati, Italy, 14-16 January.

Scheuchl, B., I. Hajnsek, and I.G. Cumming, 2003b. Classification strategies for fully polarimetric SAR data of sea ice. *Proc. POLinSAR*, Frascati, Italy, Jan 14-16.

Scheuchl, B., I. G. Cumming, and I. Hajnsek, 2005. Classification of Fully Polarimetric Single- and Dual-Frequency SAR Data of Sea Ice Using the Wishart Statistics. *Canadian Journal of Remote Sensing*, 31(1): 61–72.

Scheuchl, B., I.G. Cumming, and I. Hajnsek, 2002. Sea Ice Classification Using Multi-Frequency Polarimetric SAR Data. *Proc. Geoscience and Remote Sensing Symposium, IGARSS 2002*, pp. 1914-1916.

Schwerdtfeger, P., 1963. "The thermal properties of sea ice," *Journal of Glaciology,* 4(36): 789-807.

Serreze, M.C. and R.G. Barry, 2005. *The Arctic Climate System*, Cambridge University Press, Cambridge.

Shih, S., K. Ding, S.V. Ngheim, C. Hsu, J. A. Kong, and A. K. Jordan, 1998. Thin Saline Ice Thickness Retrieval Using Time-Series C-Band Polarimetric Radar Measurements. *IEEE Transactions on Geoscience and Remote Sensing.* 36(5): 1,589-1,598.

Shokr, M. and N.K. Sinha, 1994. Arctic sea ice microstructure observations relevant to microwave scattering. *Arctic*, 47(3): 265-279.

Simila, M., and J. Helminen, 1995. The identification of the deformed sea ice fields from ERS-SAR image by wavelets. *Proc. IGARSS'95*, Firenze, Italy, vol. 2, pp. 868-870.

Simila, M., J. Karvonen, C. Haas, and M. Hallikainen, 2006. C-band SAR based estimation of Baltic Sea ice thickness distributions. *Proc. Geoscience and Remote Sensing, IGARSS'06*, pp. 710-713.

Smith, T. G. and I. Sterling. 1978. Variation in the density of ringed sea (Phoca hispida) birth lairs in the Amundsen Gulf, Northwest Territories, *Canadian Journal of Zoology* 56: 1066-1070.

Strum, M., J. Holmgren and D. K. Perovich, 2002. Winter snow cover on sea ice of the Arctic Ocean at Surface Heat Budget of the Arctic Ocean (SHEBA): Temporal evolution and spatial variability, *Journal of Geophysical Research*, 107(C10): 1-17.

Sturm, M., J.A. Maslanik, D.K. Perovich, J.C. Sroeve, J. Richter-Menge, T. Markus, J. Holmgren, J.F. Heinrichs and K. Tape, 2006. Snow depth and ice thickness measurements from the Beaufort and Chukchi Seas collected during the AMSR-Ice03 campaign. *IEEE Transactions on Geoscience and Remote Sensing*, 44(11): 3,009-3,019.

Therrien, C.W., 1987. *Decision Estimation and Classification: An introduction to pattern recognition and related topics*. John Wiley & Sons, New York.

Tjuata, S., A.K. Fung, and J.C. Comiso, 1995. Effects of Snow Cover on Sea Ice Emission, *IEEE IGARSS'95 Digest*, vol. 1, pp. 697-699.

Touzi, R., 2007. Target Scattering Decomposition in Terms of Roll-Invariant Target Parameters. *IEEE Transactions on Geoscience and Remote Sensing*, 45(1): 73-84.

Touzi, R., S. Goze, T. L. Toan, A. Lopes and E. Mougin., 1992. Polarimetric Discriminators for SAR Images, *IEEE Transactions on Geoscience and Remote Sensing*, 30(5): 973-980.

Tremblay, L. B., and L. A. Nivsak, 1997. Modelling sea ice as a granular material including the dilatancy effect. *Journal of Physical Oceanography*, 27: 2342-2360.

Tucker III, W.B., D.K. Perovich, A.J. Gow, W.F. Weeks and M.R. Drinkwater, 1992. Physical properties of sea ice relevant to remote sensing. In: *Microwave Remote Sensing of Sea Ice*, Carsey, F. (ed.). Geophysical Monograph. American Geophysical Union. Chapter 2, 9-28.

Ulaby, F.T., H.W. Stiles and M. Abdelrazik, 1984. Snowcover influence on backscattering from terrain. *IEEE Transactions on Geoscience and Remote Sensing*, GE-22(2): 126-133.

Ulaby, F.T., R.K. Moore and A.K. Fung, 1986. *Microwave remote sensing: Active and passive. Volume III: From theory to applications*. Addison-Wesley Publishing Co. pp. 1,096.

Vachon, P.W. and J. Wolfe, 2011. C-band cross-polarization wind speed retrieval. *IEEE Geoscience and Remote Sensing Letters*, 8(3): 456-459.

van der Sanden, J.J., 2004. Anticipated applications potential of Radarsat-2 data. *Canadian Journal of Remote Sensing*, 30(3): 369-379.

van Zyl, J. J., H. A. Zebker and C. Elachi, 1987. Imaging radar polarization signatures: Theory and observation, *Radio Science,* 22(4): 529-543.

Wakabayashi, H., T. Matsuoka, K. Nakamura and F. Nishi., 2004. Polarimetric Characteristics of Sea Ice in the Sea of Okhotsk Observed by Airborne L-Band SAR, *IEEE Transactions on Geoscience and Remote Sensing,* 42(11): 2,412-2,425.

Wang, J.R., A.T.C. Chnag, A.K. Sharma, 2002. On the estimation of snow depth from microwave radiometric measurements. *IEEE Transactions on Geoscience and Remote Sensing.* 30(4): 785-792.

Weeks, W.F., and S.F. Ackley, 1986. The growth, structure and properties of sea ice. In: *The Geophysics of Sea Ice,* edited by N. Untersteiner, Martinus Nijhoff Publ., Dordrecht.

Williams, J., 1975. The influence of Snowcover on the Atmospheric Circulation and Its Role in Climate Change: An Analysis Based on Results from NCAR Global Circulation Model, *Journal of Applied Meteorology*, 14(2): 137-152.

Winebrenner, D. P., Farmer, L. D., and Joughin, I. R., 1995. On the response of polarimetric synthetic aperture radar signatures at 24 cm wavelength to sea ice thickness in Arctic leads. *Radio Science,* 30(2): 373-402.

Winebrenner, D.P. and 14 others, 1992, Microwave sea ice signature modeling. In: *Microwave Remote Sensing of Sea Ice*, Carsey, F. (ed.). Geophysical Monograph. American Geophysical Union. Chapter 8: 137-175.

Winebrenner, D.P., L. Tsang, B.Wen and R. West, 1989. Sea ice characterization measurements needed for testing of microwave remote sensing models. *IEEE Journal of Oceanic Engineering*, 14(2):149-158.

WMO (World Meteorological Organization), 2007. WMO sea ice nomenclature. WMO No. 259 Supplement No. 5. pp. 23. (http://www.jcomm-services.org/).

Woodhouse, I.H., 2006. *Introduction to Microwave Remote Sensing*. CRC Press, Boca, Raton, pp. 370.

Yackel J.J., and D. G. Barber., 2000. Melt ponds on sea ice in the Canadian Arctic Archipelago. Part 2. On the use of RADARSAT-1 synthetic aperture radar for geophysical inversion. *Journal of Geophysical Research,* 105(C9): 22061–22070.

Yackel, J. J. and D. G. Barber., 2007. Observations of Snow Water Equivalent Change on Landfast First-Year Sea Ice in Winter Using Synthetic Aperture Radar, *IEEE Transactions on Geoscience and Remote Sensing,* 45(4): 1005-1015.

Yackel, J. J., D. G. Barber, and J. M. Hanesiak, 2000. Melt Ponds on Sea Ice in the Canadian Arctic Archipelago: Part 1.Variability in morphological and radiative properties. *Journal of Geophysical Research*, 105(C9): 22,049-22,060.

Yackel, J. J., D. G. Barber, T. N. Papakyriakou and C. Breneman, 2007. First-year Sea ice spring melt transitions in the Canadian Arctic Archipelago from time-series synthetic aperture radar data, 1992-2002. *Hydrological processes*, 21(2): 253-265.

Yackel, J.J., and D. G. Barber, 1998. Measuring the thermodynamic state of sea ice using Synthetic Aperture Radar (SAR) time series data. *Proc. Geoscience and Remote Sensing Symposium*, Seattle, WA, USA. vol. 2, pp. 989-991. July 6-10.

Zebker, H. A., J. J. van Zyl and D. N. Held., 1987. Imaging Radar Polarimetry from Wave Synthesis, *Journal of Geophysical Research,* 92(B1): 683-701.

APPENDIX A:

VIOLATION OF DATA NORMALITY AND ITS IMPLICATIONS

The violation of normality can have implications on the results of classifications that assume Gaussian distribution.

We performed a classification test on raw images (un-normalized) and power transformed images (normalized using logarithm transformation) and found the results of the two datasets to be nearly similar. The transformation of raw images to log normal did not consistently increase the classification accuracy, rather for nearly 50% of the images the results were found to decrease. Table-A shows the classification accuracies of normalized data.

We also performed classification on images normalized using square root transformation, and found the results to be nearly same as the other two classification datasets (raw and normalized using logarithm transformation).

We acknowledge that there are several possible reasons for this. One of the main reasons could be that the two transformations used for normalization are not good for the data used in the current study. This certainly requires an intensive research on different transformation algorithms for data normalization. Considering the objectives of the current study, this is beyond its scope. The second reason could be the samples used for training and validation of classification. It has been reported that large number of random samples can attribute to higher classification results for un-normalized data. One reference is provided below.

Olson, C.E., Jr. and Z. Ma, 1989. Normality assumptions in supervised classification of remotely sensed terrain data, In, *Quantitative Remote Sensing: An Economic Tool for the Nineties*, IGARSS '89. IEEE#89CH2768-0, pp. 1857-1859.

Based on the comparative analysis of classifications (raw and normalized), where no significant advantage was achieved from data normalization, the original results in the paper were retained. At the same time, a discussion on the model assumption and the implications of the lack of data normality was included.

"Violation of assumption of normality or Gaussian model misfit in MLC can reduce the classification accuracy (Olson et al., 1989). In the current study a preliminary comparison of the results of classifications performed on raw and normalized polarimetric data was made. The data normalized using logarithm and square root transformation did not exhibit any significant improvement over the raw data. All classification results and signatures presented in the study were thus computed from original SAR data without normalization performed."

Table A: Classification accuracies of single polarimetric parameters derived from k-means classification. Significant classification accuracies (>60%) are highlighted in bold. The classification is performed on transformed images. Logarithm (base 10) transformation was applied. The values in red show that the overall classification decreased after normalization, whereas the values in blue show that the overall classification increased after normalization.

Polarimetric Parameter	Ice Type Classification Accuracy (%)				Overall Accuracy (%)	Kappa Coeff.
	OW	SFYI	RFYI	DFYI		
σ_{hh}^0	**60.28**	**81.20**	37.21	22.12	50.54	0.32
σ_{vv}^0	**75.41**	**82.20**	45.30	45.13	**63.69**	0.51
σ_{hv}^0	34.43	**90.60**	**60.33**	**90.81**	**68.26**	0.57
$R_{hh/vv}$	**92.62**	41.88	16.28	13.27	43.60	0.24
$R_{hh/hv}$	59.02	31.62	36.05	46.02	43.83	0.25
$SPAN$	50.00	**92.31**	58.14	30.97	57.99	0.43
ϕ_{hh-vv}	**81.80**	15.38	10.00	39.82	39.95	0.17
r_{hhvv}	04.92	57.26	25.58	02.65	22.37	-0.03
H	**89.34**	35.04	12.79	49.56	49.54	0.31
A	04.10	55.56	44.65	01.77	24.16	0.04
α	**88.52**	**64.10**	39.53	**67.26**	**66.89**	0.55
β	29.51	63.25	15.12	23.89	34.24	0.11
P_s	24.59	32.48	24.42	68.14	37.89	0.17
P_d	**71.31**	24.79	23.26	36.28	40.41	0.20
P_v	**64.75**	**88.03**	33.72	40.71	58.67	0.44
ψ	27.05	**90.60**	08.14	**66.37**	50.45	0.33
ϕ_s	50.00	**90.00**	**62.09**	**81.68**	**73.47**	0.50
τ_s	**50.82**	05.13	22.09	04.42	21.00	0.06
α_s	**86.89**	10.26	22.09	07.96	33.33	0.10
λ_s	47.38	21.71	12.56	27.52	23.74	0.01
σ_{hh}^0	14.10	01.71	**66.58**	50.21	29.90	0.09
σ_{vv}^0	**91.80**	**61.54**	36.05	**62.83**	**65.29**	0.53

APPENDIX B:

CONTRIBUTIONS AND SOFTWARE

Chapter 3-5

Dr. John Yackel, Dr. Torsten Geldsetzer, Dr. Randall Scharien, Mark Christopher Fuller collected and provided important pieces of the snow and sea ice geophysical and microwave data in the form of excel spreadsheets, pictures, images and ground truth coordinates. Dr. John Yackel and Dr. Torsten Geldsetzer provided valuable guidance with respect to data processing, data analysis and manuscript preparation.

The SAR polarimetric parameters were computed using PCI-Geomatica's Polarimetric Workstation (PWS). Additional testing and cross referencing of the parameter outputs was done using European Space Agency's NEST software and some programming in IDL on personal level. However, the parameters included in this thesis were computed using PCI-PWS.

Chapter 6

Dr. John Yackel, Mark Christopher Fuller, Carina Butterworth, Grant Gunn (University of Waterloo) and myself collected the geophysical and multi-frequency microwave data. Data organization, processing and analysis was done by myself. Important discussion on data analysis and processing was provided by Dr. John Yackel and Dr. Torsten Geldsetzer. Scattering model and working code was provided by Dr. Torsten Geldsetzer.